UNIVERSITY OF SOUTHAMPTON

EFFECTIVE COMPUTATION OF ACOUSTIC PROPAGATION IN TURBOFAN AERO-ENGINE DUCTS

Vincent Hii Jiu Ta

Thesis submitted in partial fulfilment of the requirements for the degree of
Doctor of Philosophy

Faculty of Engineering, Science and Mathematics
Institute of Sound and Vibration Research

September 2005

UNIVERSITY OF SOUTHAMPTON

ABSTRACT

FACULTY OF ENGINEERING, SCIENCE AND MATHEMATICS

INSTITUTE OF SOUND AND VIBRATION RESEARCH

Doctor of Philosophy

EFFECTIVE COMPUTATION OF ACOUSTIC PROPAGATION IN TURBOFAN BYPASS DUCTS

by Vincent Hii Jiu Ta

In this thesis, a numerical mode matching (MM) procedure is applied to the acoustic analysis of turbofan intake and bypass ducts. The expansion of the sound field in a duct in terms of modes forms the basis for many analytic and semi-analytic methods in duct acoustics. It has many attractive features such as reducing the dimension of the problem. By matching expansions of such eigensolutions at the interface between different uniform duct segments, the effect of axial variations of impedance can be modelled with far fewer parameters than would be required for a three-dimensional numerical transmission analysis. The current MM scheme can be applied readily to axially uniform ducts of arbitrary cross-section with non-uniform flow and impedance boundaries. This research focuses on predicting accurately the attenuation by the acoustic treatments within engine ducts in a computationally efficient way. Specially the main goal of the research is to ascertain the effectiveness of the MM method to study large three-dimensional ducts at realistic high frequencies within an engineering time scale.

A revised MM procedure has been proposed in this research. It is different to the existing approach employed by Beckemeyer [1], Cummings [2] and Sijtsma [3] in their studies of duct acoustics. When flow is present in the duct, the revised MM procedure yields solutions which give better agreement with the finite element (FE) transmission analysis than those using the existing approach. When no flow in the duct, both approaches are equivalent. The research has shown that the revised MM scheme has correctly modelled a range of benchmark problems and converged to the correct solutions with a small number of duct modes. The research has also shown that the revised MM procedure is capable of studying sound diffraction by a splitter in the two-dimensional flow duct. The MM scheme also shows less computation times and storage requirement than the FE transmission analysis when applied to study a three-dimensional problem.

Issues regarding the computation of duct eigenvalues and eigenfunctions in the presence of uniform and sheared flows have also been addressed in the research. An FE eigenvalue model has been developed for calculating the eigenmodes in ducts of arbitrary cross-section and with non-uniform impedance boundaries and flow. The accuracy and convergence of the FE eigenvalue model has been extensively validated using the analytical solutions and the results in the literatures obtained by other methods. The effects of non-uniform mean flow and acoustic impedance boundaries on the modal sound field in a duct have been studied using the validated FE eigenvalue model. The study has also shown that using an iterative routine (ARPACK), sets of propagating eigenmodes can be obtained at modest computational cost for frequencies and flow conditions which are characteristics of turbofan intake and bypass ducts.

Contents

List of Figures

List of Tables

Acknowledgements

This work would not have been possible without the help of many people. Firstly of all I would like to acknowledge my supervisor Professor Jeremy Astley, for his excellent support, guidance and encouragement throughout the completion of this work. I also would like to thank him for providing me with the opportunity to carry my research at the Institute of Sound and Vibration Research (ISVR).

I would also like to thank my examiners; Professor Hans Bodén from KTH, Sweden and Dr. Chris Jones from ISVR, Southampton, UK for taking their time to evaluate this work. I would also like to acknowledge the financial support from the University Technology Centre (UTC) Rolls-Royce. Also special thanks to Dr Brian Tester, Dr. Matthew Wright, Dr. Alan McApline, Dr. Rie Sugimoto and Dr. Pablo Gamallo for their valuable discussions and guidance.

Thank you to all my friends and workmates in Southampton, especially James, Alessandro, Juan, Chris L, Matt, Gary, Qiduo, Emmett, TzePei, Viswanah, Fabrice, Paul and Chris Brooks. Special thanks also goes to my wife, Jessie for being there for me through the good and bad times.

Special thanks to Professor Denys Mead for reviewing the draft thesis. I would like to express my gratitude to all the people who dedicated their time to develop the free and open source software which was essential for realizing this project.

Finally to my family. Dad, Mum, Michael and Anthony for all your love and support.

Vincent Hii Jiu Ta, September 2005

List of Symbols and Abbreviations

Symbols

N	Mesh resolution
η	Mode cut-off ratio
M, M_o	Mean flow Mach number
c_o	Speed of sound of an acoustic fluid
f	Frequency in Hertz
k	Acoustic wavenumber
k_x	Modal axial wavenumber
κ	Modal transverse wavenumber
ω	Angular frequency
W	Weighting functions
ε	Error
ρ	Acoustic fluid density
p	Acoustic pressure
$\mathbf{U}_0$	Mean flow
$\mathbf{u}, \mathbf{v}$	Particle velocity
Φ, Ψ	Mode eigenfunction
A	Acoustic admittance
Z	Acoustic impedance
λ	Eigenvalue

Abbreviations

FE	Finite element
IE	Infinite element
NMMM	New/revised mode matching method

TMMM	Existing mode matching method
MM	Mode matching

Chapter 1

Introduction

1.1 Overview

In this thesis, a numerical mode matching (MM) procedure is applied to the acoustic analysis of turbofan intake and bypass ducts. The expansion of the sound field in a duct in terms of modes forms the basis for many analytic and semi-analytic methods in duct acoustics. It has many attractive features such as reducing the dimension of the problem; propagation in a prismatic two-dimensional or axisymmetric duct reduces to a one-dimensional eigenvalue problem; propagation in a duct of arbitrary cross-section reduces to two-dimensional eigenvalue problem posed over the duct cross-section. By matching expansions of such eigensolutions at the interface between different uniform duct segments, the effect of axial variations of impedance can be modelled with far fewer parameters than would be required for a three-dimensional numerical transmission analysis.

In this thesis, the effectiveness of a revised mode matching procedure for studying sound transmission in high bypass ratio turbofan aero-engine ducts is investigated. The research focuses on predicting accurately the attenuation by the acoustic treatments within engine ducts in a computationally efficient way. The MM model developed in this study is capable of considering axially straight ducts of any cross-sections with non-uniform flow and locally reacting impedance boundaries.

To date, a number of other approaches, both exact and approximate, have been proposed for studying sound propagation in flow ducts. These include the finite element method (FEM), [7, 8, 9, 7, 10, 11, 12, 13], computational aeroacoustics (CAA) schemes [14, 15, 16, 17, 16], ray tracing methods [18, 19, 2], the multiple scales (MS) method [20, 21], the parabolic equation approximation (PEA) method [22, 23, 24], the discontinuous Galerkin method (DGM) [25, 26, 27] and the multi-modal method [28, 29, 30]. However it appears that there is no universal method which allows the solution of any kind of aeroacoustic problem with the best efficiency and accuracy. Each method has its own limitations either in term of modelling capabilities or computational cost when applied to realistic turbofan engine configurations with non-uniform impedance boundaries, non-uniform flows, complex duct geometries and at relatively high frequencies. The MM method is selected in this study because the method is computationally fast and requires low computing resources compared to other existing numerical methods. The method is therefore particularly suitable for parametric studies during the preliminary design stage of engine nacelles. The method is also robust and can be readily used to solve realistic engine duct problems with some geometric simplifications and assumptions.

The frequency range of interest in this study is from 0 to 2200 Hertz (Hz) which corresponds to values of kR from 0 to 40 where k is the acoustic wavenumber and R is the characteristic radius of the aero-engine duct. This frequency range corresponds approximately to the blade passing frequency (BPF) in the intake or bypass duct of a turbofan aero-engine at maximum power. Ideally it would be desirable to cover even higher frequencies, say up to 2 to 3 times BPF.

In this thesis, different aspects that have to be understood in order to develop the computational scheme are documented. These aspects include mathematics equations, physics, computer science and numerical analysis. The chapter continues with a list of the aims of this thesis and the contributions made in this thesis. The chapter ends with a plan of this thesis.

1.1.1 Outline

This chapter is arranged as follows. Section 1.2 presents a review of current prediction methods for flow duct acoustics. This review concentrates on the applications and limitations of each method in modelling acoustic propagation in turbofan aero-engines. The methods reviewed are; mode matching, the method of multiple scales, parabolic equation approximations, ray tracing, the finite element method, computational aeroacoustic schemes based on the linearized Euler equations, the discontinuous Galerkin method and the multi-modal method. The motivations and objectives of the research are outlined in Sections 1.3 and 1.4. The original contributions made in this thesis are presented in Section 1.5. Finally, Section 1.6 outlines the contents of the thesis.

1.1.2 Aircraft Noise and Reduction

Although individual aircraft have become quieter since the introduction of jet engines in the early 1960s, any reduction in noise levels around the major airports has been off-set by the huge increase in the number of planes. Since the main source of aircraft noise is engine-related noise, the quest for quieter skies has led to a major focus on reducing engine noise without sacrificing engine thrust and performance. For the early jet engines, the major noise source was mixing noise attributed to the jet exhaust mixing with the surrounding air. Mixing noise was reduced with the advent of high bypass ratio turbofan engines.

In the modern high bypass ratio engines, the fan is used to generate thrust and the core and fan exhausts are further mixed internally before being vented. This leads to a reduction of jet exhaust velocities hence the mixing noise. As a consequence, the emphasis on noise reduction has now shifted to fan related noise and the acoustics of the ducted fan system.

Fig. 1.1 shows a longitudinal cross-section of a typical high bypass ratio turbofan aircraft engine. Downstream of the fan, the duct of a turbofan engine splits into a bypass duct and an engine duct. In both ducts, radial stators are placed to cancel out the swirling effect of the flow and to recover the energy from the swirl.

One of the early studies of noise generating mechanisms in flow ducts is by Tyler and Sofrin [31]. They had classified noise generating mechanisms in axial flow systems as those due to the rotating blades, the interaction between the rotor and the stator and the interaction of the boundary layer and inlet disturbances with the rotor blades. The study found that the fundamental tonal noise generating mechanism is attributed to the rotating pressure patterns or spinning modes by the rotor or the fan at the BPF or its harmonics. The interaction of rotor wakes cutting through the stator blades produces noise at multiples of the BPF. As the fan size is increased with increasing bypass ratio engines, rotor-stator interactions play a more significant role as a noise generating mechanism. The interaction generates both broadband and tonal noise. In the duct, part of the rotor-stator interaction noise travels back towards the engine fan, which partly reflects it and partly transmits it. Downstream of the stators, the rotor-stator noise travels through the engine duct and the bypass duct before being radiated out to the atmosphere.

For high bypass ratio turbofan engines, aft-fan noise has became the largest or the second largest source of radiated noise under all three noise certification conditions; cutback, sideline and approach. Other sources of noise include noise from the inlet fan, airframe, jet, core turbine and low pressure compressor.

One of the most effective techniques of reducing aircraft noise is by using acoustic treatments in certain key areas of the duct. The relatively long and curved geometry of the engine duct makes an acoustic lining highly effective. Therefore, it is important to have an accurate, reliable and practical tool for acoustic analysis in predicting the effect of acoustic treatments in flow ducts. Other methods such as the negative scarf inlet [32] and optimal fan blade design [33] have also been proposed, however, the presence of appropriate acoustical linings is still an important way of reducing noise in engine ducts.

This research also focuses on studying sound diffraction by radial and circumferential splitters in the engine duct. Although splitters have not yet been implemented in commercial aero-engines, they have been considered as a potential way of reducing duct noise. Fig. 1.2 shows an experimental turbofan engine with a splitter ring installed in the inlet duct which had been tested as part of an experimental installation conducted by NASA in the early 1980s. However, no results have been published regarding the performance of the splitters. Fig. 1.3 shows an idealised 1/6 scale test rig used for SILENCE(R) [1] no flow tests with recommended arrangements

---

[1] SILENCE(R) - Significantly Lower Community Exposure To Aircraft Noise is the largest ever European aircraft noise research program. It is a four year program and involved 50 partners collaborate together to validate noise reduction technologies that will allow as of 2008 quieter aircraft operations by up to 6 dB. The program is part of the 5th framework program of the European Commission

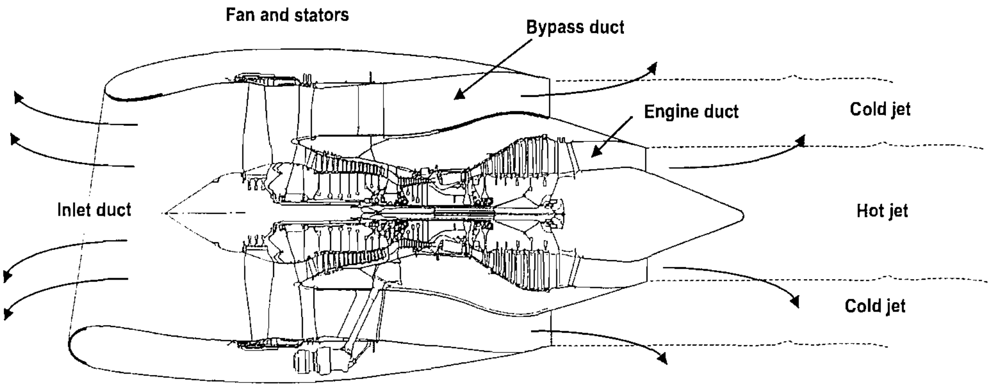

Figure 1.1: A cross-section cut of a typical high bypass ratio turbofan aero-engine and the major noise sources.

of radial and circumferential splitters for duct noise reduction by Institute of Sound and Vibration Research (ISVR). The experimental results have shown some encouraging noise reduction by the splitters. The waves that hitting the splitters are being reflected and scattered into other duct modes which may be more readily attenuated by the acoustic liner. The splitters also provide additional surface areas for acoustic treatments.

Modelling transmission of sound in a turbofan engine duct is a challenging problem because a real engine duct has a three-dimensional geometry and complex mean flow. The propagation of sound in the bypass duct is more complicated than in the inlet duct because the mean flow in the duct is strongly sheared, sometimes with swirl and increase geometry complexity. It therefore requires more precise modelling. However, this noise transmission problem can be simplified by assuming, to a first approximation, that the inlet duct has a circular cross-section containing uniform mean flow and the bypass duct has an annular cross-section containing uniform mean flow.

Fig. 1.4 shows two simplified bypass duct models. One with varying acoustic impedance boundaries in both axial and circumferential directions and the other with four radial splitters. These simplified bypass duct models can be represented in two-dimensions by rectangular ducts assuming the duct model is unwrapped as shown in Fig. 1.5 in which the height and width of the two-dimensional duct define the perimeter and radius of the three-dimensional duct. Figs. 1.4(b) and (d) show the two-dimensional representations of the two bypass duct models presented. Fig. 1.6 shows two simplified inlet duct models, one with an axially varying impedance. The other duct contains two liner splices. Their equivalent two-dimensional models are also shown.

These two-dimensional models are used in the initial development of the MM scheme before extending it to three-dimensional models. The two-dimensional models also provide good insight to the physics in the three-dimensional models. In most of the models, the splitters will be assumed to be infinitely thin so that the uniform flow assumption can be justified.

---

enabling a 50% funding of the total budget of more than 110 million Euro.

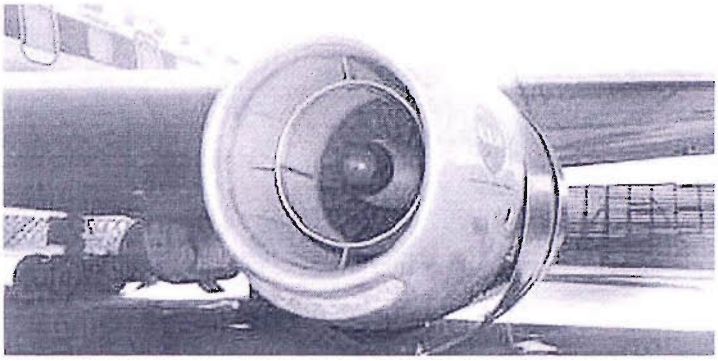

Figure 1.2: NASA experimental treated nacelle mounted on McDonnell Douglas DC-8 airplane. [4]

1.2 Methods Currently Available

In this section, current methods of analysis for flow duct acoustics are reviewed. The review focuses on the capabilities and limitations of each method in studying sound transmission in turbofan aero-engine ducts. The methods covered are MM techniques, the MS method, the PEA method, ray theory, the FEM, CAA, the DGM and the multi-modal method.

1.2.1 Mode Matching Method

The MM technique is a well known method for studying sound propagation in ducts [1, 2, 3, 34, 35, 36, 37]. Generally, the method matches solutions between uniform duct sections at geometric or impedance discontinuities. The MM procedure entails the expansion of unknown fields in the individual sections in terms of their respective duct modes. Since the eigenfunctions of the modes are known for each section, the problem reduces to the determination of the relationship between the modal coefficients associated with the field expansions in the different duct sections. This requires the application of the continuity conditions for the fields at the interfaces. Continuity of acoustic pressure and particle velocity are commonly assumed. This then leads to a finite set of linear simultaneous equations for the unknown modal coefficients.

In [1], the MM method was employed to study sound transmission in ducts with partial transverse baffles with and without flow. In the study, different matching conditions had been suggested to study the problems. However, only a few of the matching conditions had been tested with results presented. Alfredson [34] apllied the MM method to study sound transmission in a duct with axially varying cross-sectional areas for the case of zero flow and Joshi *et al.* [35] applied the method to a uniform duct with a uniform axially segmented linings and with uniform flow. In both studies, locally reacting liners were assumed.

In [3], the MM method was employed to study sound transmission in a cylindrical duct with non-locally reacting liners and the results compared well with the experimental measurements. Cummings [2] in his study of silencer transmission loss also showed good comparison between the MM results with those obtained by ray

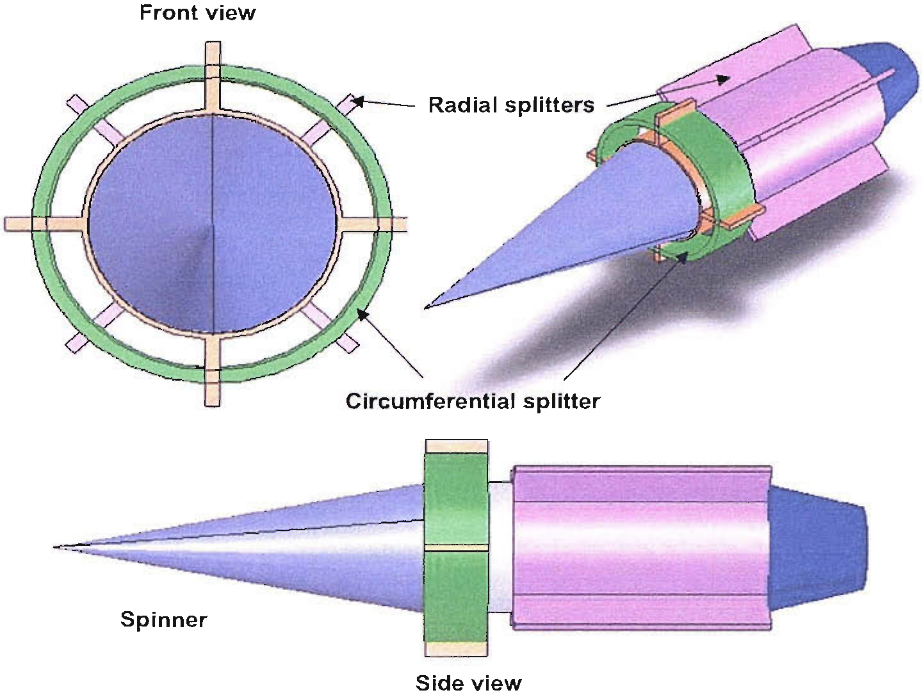

Figure 1.3: A potential arrangement of radial and circumferential splitters in an idealised 1/6 scale test rig for SILENCE(R) no flow test.

acoustics and experimental measurements. A two-dimensional duct with zero flow was considered in the study.

The drawback of the MM method is its inability to represent non-uniform duct geometries and flows in the duct axial direction. The method can only be apply to study axially straight ducts. However, the method is capable of representing ducts of any arbitrary duct cross-section with non-uniform impedance boundaries and mean flows.

From the present literature research, there appears to be little published or documented on the application of the MM method to study sound transmission in flow ducts with three-dimensional geometry. Although work has been published recently on ducts with circular geometry containing circumferentially varying liner impedance [38].

1.2.2 Multiple Scales Method

In recent years, the method of MS has been employed to study acoustic propagation in flow ducts with slowly varying geometries [21, 20, 39, 40]. The MS approach allows the sound transmission to be represented by a summation of slowly-varying modes. The amplitudes and phases of the modes are determined by slowly changing parameters such as the axial slope of the duct walls and the mean flow. For some aero-engine ducts, the MS method can be suitable because the slope of the duct wall is small for aerodynamic reasons. These variations are necessarily gradual over a length scale much larger than typical acoustic wavelengths to preserve

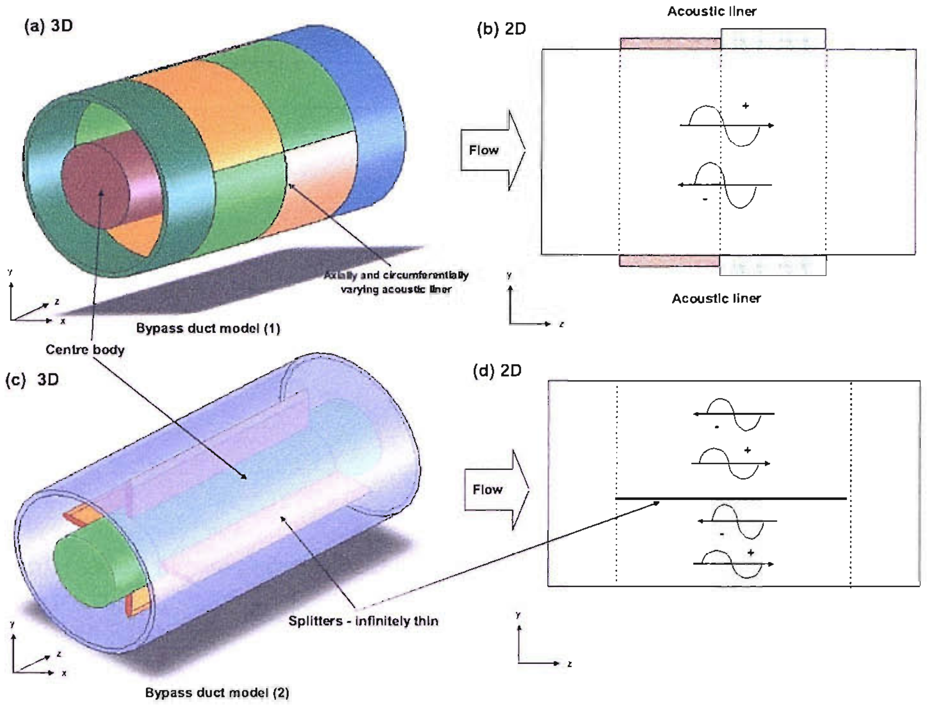

Figure 1.4: (a)-(b) An idealised bypass duct model with a circumferentially and axially varying acoustic liner and its two-dimensional model. (c)-(b) An idealised bypass duct model with radial splitters and its two-dimensional model.

the aerodynamic of the mean flow.

The method of MS was first applied to the case of a variable geometry duct by Nayfeh [40] without flow. Later, Rienstra [21, 20] applied the method to the case of a slowly varying circular duct and an slowly varying annular duct with irrotational mean flow. The method was then applied to the case of mean swirling flow by Cooper and Peake [39]. In [20], a comparison of solutions obtained by the MS and the FEM for an axisymmetric lined turbofan inlet duct in irrotational mean flow, was presented and general good agreement was shown between the two methods. Recently, Rienstra [41] has published the mathematical theory on extending the method to three-dimensional problems. However no results are presented.

A complication of the MS is the 'turning point' problem. This is when the geometry of the duct varies in such a way that the propagating mode vanishes (the cut-on mode becomes cut-off) and causes the break down of the solution. These phenomena can be overcome by a special adjustment to the formulation in the turning point region. This transition type phenomena of duct modes in a slowly varying cylindrical duct has been investigated by Rienstra [42] for hard walls and by Ovenden [43] for soft walls. Recently, Ovenden [44] has derived an explicit solution for an acoustic mode undergoing cut-on cut-off transition for an arbitrary duct with mean irrotational flow. The analytical solution is a composite solution, encompassing both the inner boundary layer solution in the neighbourhood of the transition point and the outer slowly varying modal solution far

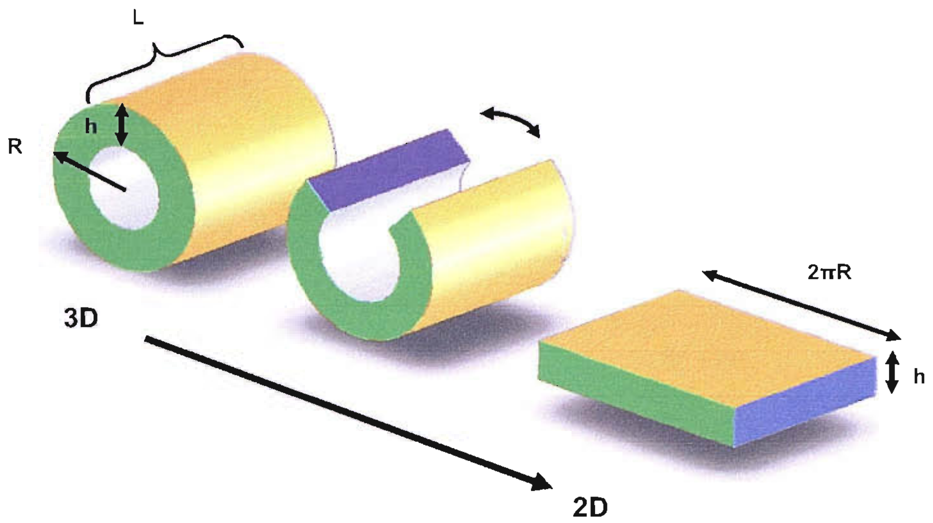

Figure 1.5: An idealised bypass duct model can be represented in two-dimensions by a rectangular duct.

upstream and downstream.

The drawback of the MS approach is that there is no interaction between the various acoustic modes in the duct. The method is therefore unsuitable for our study here as predicting accurately the acoustic scattering due to impedance discontinuities and sound diffraction by splitters in the duct form a major part of this research. The method is limited to ducts with slowly varying geometries. However, the method is computationally fast and requires low computing resources compared to other numerical schemes. The method permits the inclusion of acoustic impedance boundaries and mean flow.

1.2.3 Parabolic Equation Approximation Method

The PEA method has been employed to study sound propagation in ducts in [22, 23, 24, 45, 46]. A comprehensive review of the application and development of the PEA method for different research areas including duct acoustics is given by Lee *et al.* [47].

The PEA method approximates the second order wave equation into two first order equations. The method changes the boundary value problem to an initial value problem so that it can be solved by the marching algorithm, which is computationally cheap to perform. However, by this, reflections that couple downstream propagation waves to upstream propagation waves are neglected.

In [48], Lan employed the PEA method in his study of sound propagation in an axisymmetric circular duct in the presence of uniform axial mean flow. In [22, 23], Dougherty employed the method in his investigation of flow effects on sound propagation in nonuniform, soft-walled ducts. Dallois *et al.* [24] employed the wide angle PEA method to investigate sound diffraction by a core vortex in moving media. In [45], the PEA method was employed to predict the attenuation provided by an outer fan duct liner in an aft fan duct and in [46], to

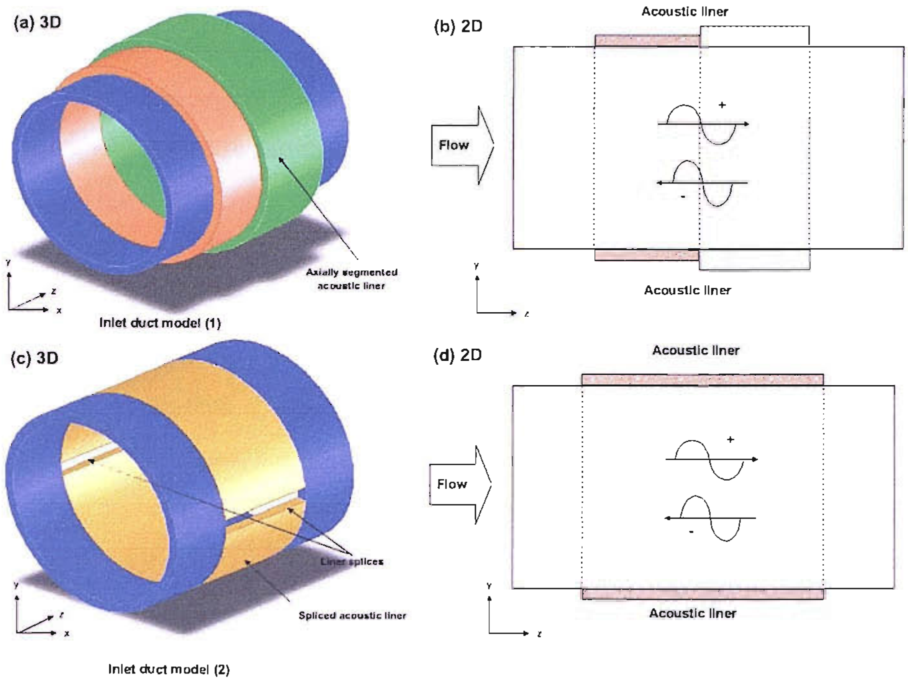

Figure 1.6: (a)-(b) An idealised inlet duct model with an axially varying acoustic liner and its two-dimensional model. (c)-(d) An idealised inlet duct model with two liner splices and its two-dimensional model.

study the effects on aft fan noise propagation due to geometry changes e.g. bifurcation and pylons. The study found that bifurcations and pylons clearly affect modal content in both propagation and radiation calculations.

The PEA method is only accurate for uniform ducts or weakly varying ducts where reflection and mode interaction are not critical. For axially non-uniform ducts with non-uniform acoustic impedance boundaries, decoupling the upstream and downstream propagation waves might yield inaccuracy in the solution. The method can represent three-dimensional ducts with three-dimensional mean flows and impedance boundaries and remains computationally efficient under these conditions.

1.2.4 Ray Theory

Ray theory is a high frequency approximation model [18, 19, 2]. When the wavelength of a sound wave is small compared to other characteristic lengths of the system, the sound may be considered to be propagating locally as a plane wave, resulting in a characteristic line or ray path.

The ray acoustic technique was first employed to study sound propagation in an inlet duct by Kempton and Smith [49]. In the study, the reciprocity principle was applied in which rays were traced backwards from the measurement or microphone locations to the source. The source was taken to be a distribution of incoherent monopoles or dipoles. Tester [18] later studied the case of a two-dimensional lined duct with a point and a line source. Dougherty [19] employed the ray acoustic technique to nacelle acoustic design in three dimensions with nonuniform mean flow. In [2], Cummings used a forward ray tracing method in his investigation of the transmission loss of duct silencers and the ray results compared well with those obtained by a mode matching model and experimental measurements. In the study, rays were traced forwards from the source regions to the microphone locations.

The advantages of the ray theory are its simplicity and versatility in application to complex geometries and its computational robustness and rapidity. It permits implementation of a broadband source and is able to represent non-uniform ducts with non-uniform acoustic boundaries and mean flows. The disadvantages of the method are that an accurate source model is difficult to define and it is only accurate for high frequencies. For this research, the ray technique is not regarded as accurate enough for the typical duct geometries within the frequency range of interest.

1.2.5 Finite/Infinite Element Methods

The finite element/infinite element (FE/IE) method is among the most widely used numerical methods for studying acoustic propagation and radiation problems at low and mid frequencies [32, 9, 7, 10, 11, 50, 51, 52, 53, 54, 55, 56, 57, 13, 58, 59]. The focus of this research is on in-duct sound propagation and infinite elements are not required. No further details on the IE will therefore be given.

In the FEM, the solution domain is divided into sub-domains (or elements) in which suitable basis functions (or element shape functions) are defined. The shape functions interpolate the acoustic field within each element on the basis of the value of the acoustic field at discrete nodes within and on the boundary of the element.

Although, there are a lot of publications about the application of FEM to study transmission of sound in ducts, due to high computational cost, two-dimensional or axisymmetric duct models are generally assumed [32, 9, 7, 10, 11, 50, 51, 60]. The only three-dimensional duct studies found are those by Regan *et al.* [13], by Tester *et al.* [58] and by McAlphine *et al.*[59]. All these studies are related to the investigation of acoustic liner non-uniformities on duct modes.

In [9], Eversman and Okunbor had proposed a method of treating the flow shear layer at the exit of a bypass duct by assuming continuity of particle velocity and acoustic pressure at a vortex sheet in their investigation of aft-fan duct acoustic radiation with irrotational mean flow.

The FEM can represent non-uniform ducts with non-uniform irrotational mean flows and with non-uniform locally and non-locally reacting frequency dependent impedance boundaries. The method has good dispersion characteristics when high order elements are used. The drawback of the method is that it is computationally expensive. Therefore, the practicability of the method in application to large three-dimensional problems is restricted to low and mid frequencies.

To overcome the high computational cost, methods such as domain decomposition [61], a time domain formulation with an iterative solver [62] and parallel computing [13] have been proposed. However, there are other issues associated with these methods such as matrix ill-conditioning and complex implementation.

Recently, Listerud and Eversman [63] explored the use of cubic 'serendipity' elements to study sound propagation in a non-uniform duct model in a moving medium. In [64], the serendipity elements were used to model acoustic radiation in a non-uniform moving medium. Both studies showed that cubic serendipity elements outperform the common quadratic serendipity elements in terms of computational efficiency. A disadvantage of cubic elements is that they create a greater bandwidth in the stiffness matrix than the quadratic elements, given the same nodal density along element boundaries. However, the study showed that the penalty in numerical accuracy incurred by using serendipity elements rather than Lagrangian elements in most of the FE models is far outweighed by the gains in problem size.

1.2.6 The Discontinous Galerkin Method

The DGM is quite a recent method developed to study flow duct acoustic problems [26, 25, 27]. The DGM is somewhere between a finite element and a finite volume method and has many good features of both. The method provides a practical framework for the development of high-order accurate methods using unstructured or structured grids. The method is well suited to large-scale time-dependent computations in which high accuracy is required. An important distinction between the DGM and the conventional FEM is that the local solution is discontinuous at element boundaries. The solution within each element is not related to neighbouring elements. The local elements are related to each other by energy flux through the element boundaries. Since they only require to communicate through the elements that have common boundaries, the method is well suited for parallelization using message passing. In the DGM, the type of the element used and the choice of the governing equations can be varied from element to element without loss of rigour in the method [26].

In [25], the dispersion and dissipation properties of the DGM for acoustic wave propagation were studied by Hu *et al.* . The study found that the dispersion relation and the dissipation rate depended on the energy flux formulation used to connect the discontinuous domains. The study also showed that the DGM requires less storage and computational time than the conventional FEM. Hu and Atkins carried out a study of the convergence rate of the DGM and found that higher order basis functions gave better dispersion and dissipation results [27].

The DGM is capable of representing non-uniform ducts with rotational and irrotational flows. The method also permits the inclusion of acoustic impedance boundaries. However, the method suffers from large computational time and resources when applied to large three-dimensional problems at high frequencies.

1.2.7 Linearized Euler Equations (LEE) Computation Aeroacoustics Scheme

The rapid growth of computer processing power has led to a new and active field of research called computational aeroacoustics (CAA) which combines the traditional disciplines of acoustics and computational fluid dynamics (CFD) [65, 66, 67, 68, 68].

The CAA schemes generally solved the linearized Euler equations (LEE) for the acoustic field. In general, the CAA problems can be classified into problems of propagation, scattering and radiation, linear interaction noise problems and vortex generated broadband noise fully coupled to the mean flow [67, 69]. For sound propagation, scattering and radiation problems, a stationary mean flow field is calculated by solving the Reynolds-averaged Navier-Stokes equations. The Euler equations are then linearized around this mean flow to simulate the sound field.

One of the greatest advantages offered by the CAA schemes is their ability to solve non-linear problems of sound generation. This is achieved by solving together the unsteady flow and the sound generation by using only the conservation equations that govern the fluid motions. This means that the unsteady flow and the sound field are regarded as different but related to the same flow field. Because the amplitude of the acoustic pressure waves generated by a flow field is orders of magnitude smaller than the dynamic pressures, solving the coupled problem would be very demanding in spatial and temporal accuracy. Most of the past studies were at low frequencies or two-dimensional or axisymmetric duct models were assumed.

There are a handfull of CAA schemes which have been developed to study duct acoustic problems. In this thesis, two of the most commonly used CAA schemes are reviewed; the Dispersion-Relation-Preserving (DRP) finite difference scheme [66, 70] and the high order compact scheme [71, 68]. Each scheme has its advantages and disadvantages when applied to different problems.

The CAA schemes are capable of studying sound propagation in non-uniform ducts with rotational and irrotational mean flows and with vortical disturbances. The schemes also permit the inclusion of acoustic impedance boundaries. Although the CAA schemes have capabilities to study a wider range of aeroacoustic problems than other numerical methods, for large three-dimensional problems at high frequencies they are extremely computationally demanding and unsuitable for parametric studies. Besides these, there are also a number of other issues concerning the CAA schemes [65, 66, 67]:

- large disparity between energy levels in the unsteady flow and in the sound field;
- large disparity between the length scales of the fluid dynamics and of the propagation sound field;
- a wide range of frequency of acoustic interest;
- numerical dissipation and dispersion;

- special boundary conditions required for the acoustic part of the solution;
- convergency and grid topologies.

These issues need to be solved before the CAA schemes can be used as a reliable and accurate engineering tool.

Dispersion-Relation-Preserving Finite Difference Scheme

The DRP finite difference scheme of Tam and Webb [66] is based on optimized finite difference approximations of space and time derivatives in the wavenumber and frequency domains. It is a high order scheme which is specially designed to reduce dissipation and dispersion. It is a fully explicit scheme and thus can be easily parallelized. The formulation of the DRP scheme can be found in [66, 72].

In [14], the DRP scheme was employed to solve the Navier Stokes equations to predict the ducted fan engine acoustics. In [15], Ozyoruk, Ahuja and Long employed the DRP scheme in their predictions of forward and aft radiated noise from a turbofan engine. In the study, a Kirchhoff formulation is used for calculating the noise radiation. A high-order explicit time marching algorithm was used to advance the solutions in time and a domain decomposition method was applied to parallelize the codes.

The Compact Scheme

The compact scheme is also a high-order finite difference method [71, 72]. The scheme requires narrower computational grid stencils, has better fine-scale resolution and yields better global accuracy than standard finite difference schemes with the same order [71].

A typical sixth-order compact scheme is expressed as follows [73]:

$$\alpha f'_{i-1} + f'_i + \alpha f'_{i+1} = a\frac{f_{i+1} - f_{i-1}}{2h} + b\frac{f_{i+2} - f_{i-2}}{4h} \tag{1.1}$$

where f'_i is the derivative of the function at point i and f_i is the value of the function at the same point. h is the distance between adjacent points in the mesh. $a.b$ and α are coefficients to be determined depending on the order of the scheme. The formulation indicates that the value of the derivative of a function at a given point depends not only on the values of f at neighbouring points but also on the values of the derivatives at these points. This highlights another difference between the compact scheme and the conventional scheme. Fig. 1.7 illustrates another difference between a conventional sixth-order scheme and a sixth-order compact scheme. To approximate the solution of node $x_{i,j}$, the conventional sixth-order scheme incorporates seven points in each direction while the sixth-order compact scheme is formulated on a compact set of nine grid points around the node.

Two key issues encountered in the compact scheme are (a) boundary treatments (e.g. in areas near the boundaries in which the scheme cannot be applied because the stencil extends outside the computational domain) and (b) grid nonuniformity [74]. Both issues are still active research fields at present [75, 76, 73].

In [68], a high-order compact scheme was employed to study fan noise radiation through a realistic engine exhaust geometry with flow. In the study, for efficient computation and accurate modelling of features such as liner wall condition, the in-duct sound propagation was modelled by using a multiple scales method [21, 20]. An integral solution of the Ffowcs Williams-Hawkings (FW-H) equation was implemented numerically to determine the far field noise levels efficiently.

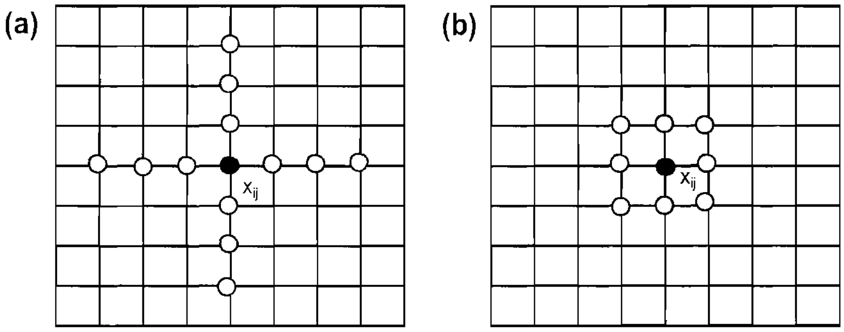

Figure 1.7: Stencils at the reference node $x_{i,j}$ for (a) the conventional sixth-order scheme and (b) the sixth-order compact scheme.

1.2.8 Multi-modal Method

A multi-modal method has been proposed by Pagneux and others [29, 30, 28] for studying sound propagation in flow ducts. The method segments the duct at the impedance and geometric changes. The method then projects the first order mass and momentum conservation equations over the eigenfunctions of a rigid uniform duct. Mode coupling effects are then explicitly expressed by the inverse Fourier transformation of liner admittance. A scattering matrix that relates the reflection and transmission coefficients of each segmented duct section is set up. From these scattering matrices, a global scattering matrix can be constructed and solved. The rigid duct modes are used in the method because they are known a priori.

The method can represent non-uniform ducts containing non-uniform impedance boundaries when no flow is present in the duct. When flow is present in the duct, the method can only be applied to axially uniform ducts. The drawback of the method is that the eigenfunctions of the rigid duct modes used in the method sometimes do not satisfy the true boundary condition for acoustic linings and the complex duct cross-section and this can lead to poor solution convergence and inaccurate results [28]. For rigid ducts, the method is accurate as long as the duct cross-section variations are not very abrupt.

Summary

Table 1.1 presents a summary of the modelling capabilities of each prediction method in application to sound transmission studies in turbofan aero-engine ducts. The FEM, the DGM and the LEE-CAA schemes can represent complex duct geometries with non-uniform mean flows and impedance boundaries but they are computationally demanding for large three-dimensional problems at high frequencies. Ray theory is not accurate enough for the frequency range of interest in this research. The PEA method is only accurate for uniform ducts or weakly varying ducts where reflection and mode interaction are not critical. The MS method does not allow modal scattering between acoustic modes in the duct and is only accurate for ducts with slowly varying geometries. The MM method is restricted to axially uniform ducts. In the multi-modal method, the eigenfunctions of the rigid duct modes used do not always satisfy the true boundary condition for acoustic linings and the complex duct cross-section. This can lead to poor solution convergence and inaccurate results.

Numerical Scheme Proposed

The scattering and attenuation of the sound field within aero-engine ducts is strongly dependent on duct geometry, the acoustic impedance and placement of the liners and the convective and refractive effects of the non-uniform mean flow. It is therefore important that the method that is chosen for the development of an engineering tool for studying sound transmission in high bypass ratio turbofan aero-engines is capable of considered these features. In this research, the MM method is selected rather than other methods because it is computationally fast and requires a low computational storage. This also makes the scheme particularly suitable for parametric studies during the preliminary design stage.

The research will be examining the validity of the MM method for studying transmission of sound in flow ducts, in particular three-dimensional ducts. The MM method will be validated against analytical and numerical solutions obtained by other methods to establish its accuracy. Its general modelling characteristics, strengths and limitations are explored in two and three-dimensional cases. The two-dimensional models are used in the initial development of the scheme before extending it to three-dimensional models.

The ability of the method for studying sound diffraction by radial and circumferential splitters in the duct is also explored in this thesis although this is only touched upon briefly.

1.3 Motivations

The impact of high noise levels associated with jet propulsion systems has been felt by people living in communities surrounding airports and the flight paths. The introduction of no-frill airlines in recent years has resulted in an increased frequency of aircraft operations at most major airports e.g. London Heathrow Airport and

Method	Mean Flow	Geometry	Frequency	Mesh	Acoustic Liner	Computation Cost	Splitter
FEM	Non-uniform irrotational flow	Non-uniform duct	Low, mid	Structured and unstructured	Yes	High	Yes
CAA-LEE	Non-uniform rotational flow	Non-uniform duct	Low, mid	Structured	Yes	High	Yes
Ray theory	Yes in theory	Non-uniform duct	High	Not required	Yes	Low	Yes
MM	Non-uniform irrotational flow over duct cross-section	Axially uniform duct with arbitrary cross-section	Low, mid, high	Not required	Yes	Low	Yes
MS	Non-uniform irrotational flow	Duct with slowly varying geometries	Low, mid	Not required	Yes	Medium	No
DGM	Non-uniform rotational flow	Non-uniform duct	Low, mid	Structured and unstructured	Yes	High	Yes
PEA	Non-uniform irrotational flow	Duct with slowly varying geometries	Low, mid	Structured	Yes	Medium	Yes
Multi-modal	Uniform irrotational flow	Axially uniform duct with arbitrary cross-section	Low, mid, high	Not required	Yes	Low	No

Table 1.1: Modelling capabilities of each prediction method in studying acoustic propagation and attenuation in turbofan aero-engine ducts.

Luton Airport. The noise problems have became so severe that stringent airport noise restrictions have been introduced to control the noise generated by turbofan aircraft during landing and take off.

Although a significant reduction in the noise generated by turbofan engines has been achieved since the introduction of turbofan aero-engines to commercial aviation in the early 1960s, a significant further reduction of aircraft noise is still required. These restrictions are difficult to meet even by the current high bypass ratio turbofan engines which already have advanced noise reduction technologies implemented on them. Aero-engine manufacturers are under great pressure to meet these stricter noise restrictions.

This research aims to develop an effective acoustic analysis tool that is capable of modelling sound propagation in aero-engine ducts realistically, effectively and accurately. Ideally, the method should compute the solution within a reasonable engineering time scale (in hours rather than days, weeks or months) with modest computing resources and architecture. The computational tool should consider the following features in order of importance:

- attenuation by acoustic linings at the bounding surfaces and splitters;
- non-uniform duct geometry;
- sound diffraction by splitters (radial and circumferential);
- sound refraction by the mean flow and
- wakes and vorticities generated in the duct.

1.4 Research Objectives

Having chosen the most effective method of analysis to be the MM method, the main objectives of this research are:

- to develop and validate a numerical scheme based on mode matching for studying transmission of sound in high bypass ratio turbofan aircraft engine ducts;
- to consider features such as non-uniform mean flows, radial and circumferential splitters, non-uniform acoustic impedance boundaries in the duct and any arbitrary duct cross-sections, and
- to be used by engine nacelle manufacturers during preliminary design stages at reasonable computing time and storage requirement.

Other objectives for this research are

- to compare the performance of the MM scheme proposed with alternative methods;
- to employ the MM scheme proposed to study acoustic scattering due to impedance discontinuities in the duct;
- to employ the MM scheme proposed to study the influence of acoustic liner non-uniformities on duct modes;
- to employ the MM scheme proposed to gain better understanding of sound diffraction by splitters (radial and circumferential) in the duct;
- to employ the MM scheme proposed to gain better understanding of propagation of surface waves in the duct, and
- to add to the 'knowledge base' regarding the validity of MM techniques for studying transmission of sound in two and three-dimensional ducts.

1.5 Original Contributions

In the accomplishment of the research objectives the following original contributions have been made:

- A numerical scheme using finite elements has been proposed to solve for duct eigenvalues and eigenfunctions in the presence of uniform and sheared flow. The FE eigenvalue model is capable of representing ducts of any arbitrary duct cross-sections with non-uniform impedance boundaries and mean flows. From the results computed, different types of duct modes are identified unambiguously and no modes are repeated. An FE mesh resolution of 8-10 nodes per wavelength has been found to be adequate to resolve the duct modes of interest in this research (duct modes having cut-off ratios greater than 0.8) .

- For large three-dimensional problems, an iterative eigenvalue routine (ARPACK) has been employed to solve the eigenvalue problems. A performance study has demonstrated that the iterative routine can result in significant improvement in computation times and storage requirement when compared with a direct eigenvalue routine.
- The FE eigenvalue model has been employed to study the modal sound field in an idealised inlet duct with spliced liners of different widths with and without the presence of mean flow in the duct.
- A new Galerkin MM procedure has been developed for studying transmission of sound in flow ducts. The scheme matches solutions between duct segments using continuity of mass flux and momentum flux at the matching interface. The conventional MM procedure matches solutions between duct segments using continuity of acoustic pressure and velocity. When flow is present in the duct, the solutions obtained using the revised MM procedure show better agreement with the FE solutions than those obtained using the pre-existing approach. Both MM procedures are equivalent when no flow is present in the duct.
- The new MM scheme is capable of studying acoustic effects in axially uniform ducts of any arbitrary cross-section with non-uniform mean flows and impedance boundaries. A study into the efficiency of the scheme has shown that large savings in both computational storage and computation times may be achieved compared to an FE transmission analysis. The savings will be more significant for large three-dimensional problems at high frequencies. The study also shows that the resulting solution times are such that a parametric study of the geometrical parameters may be performed within an engineering time scale.
- The new MM scheme has been employed to study acoustic scattering due to impedance discontinuities in the duct.
- The new MM scheme has been employed to study sound diffraction by a infinitely thin splitter in a two-dimensional flow duct.
- The new MM scheme has been employed to study propagation of surface waves in the duct.
- The new MM scheme has been employed to study transmission of sound in an idealised aircraft engine intake with spliced liners of varying width and length at a frequency of practical interest.

- The new MM scheme has been employed to conduct a broadband multi-mode analysis of the effect of liner splices in a circular flow duct.

The main point of originality of the work presented in this thesis lies in the development and application of a reliable and efficient engineering tool for studying sound transmission in turbofan aero-engine ducts.

1.6 Thesis Outline

This thesis is arranged as follows. Chapter 1 reviews the current prediction methods for flow duct acoustics. The motivations and objectives of the research, as well as contributions of the thesis to the analysis of flow duct acoustics are presented.

In Chapter 2, theories used in the development of a numerical method using finite elements to solve for duct eigenvalues and eigenfunctions in the presence of uniform and sheared flow are presented. The formulation of two and three-dimensional eigenvalue problems as well as the boundary conditions of the problems are presented.

Chapter 3 presents the results of the two-dimensional eigenvalue problems. Issues regarding the accuracy and convergence of the FE eigenvalue model are investigated and discussed. The numerical results for various duct configurations have been presented which show the validity of the analysis and computer code.

In Chapter 4, results of the three-dimensional eigenvalue problems are presented. Issues regarding the accuracy and convergence of the FE model for three-dimensional problems are investigated and discussed. The numerical results for various waveguides have been presented. These show the validity of the analysis and computer code. Results of a study of the modal sound field in an idealised inlet engine duct with spliced liners are presented.

Chapter 5 is devoted to the application of MM techniques to study sound transmission in flow ducts. In this chapter, two MM procedures; the conventional approach and the revised approach, are described using a test problem. The formulation of two and three-dimensional MM problems is also presented.

In Chapter 6, the formulation of an FE transmission model for studying sound transmission in two-dimensional flow ducts is presented. Also presented is the formulation of an FE flow model for computing the steady compressible potential flow in the duct. Some validation results of the FE transmission model are then presented.

Chapter 7 examines the validity of a MM model based on a revised MM procedure for studying sound transmission in two-dimensional flow ducts. Ducts with acoustic impedance discontinuities and a infinitely thin splitter are being considered. Issues regarding the accuracy and convergence of the MM model for two-dimensional problems are investigated and documented.

In Chapter 8, the validity of the MM model for studying sound transmission in three-dimensional flow ducts is examined. Issues regarding the accuracy and convergence of the MM model especially for three-dimensional problems are investigated and discussed. The MM model has been employed to study transmission of sound in an idealised turbofan inlet duct with spliced liners at a realistic frequency. The main observable results are highlighted. Engine order tone and broadband analysis are carried out.

In Chapter 8, concluding remarks, contributions of the thesis and future work are put forward.

Chapter 2

Theory: Eigenvalues and Eigenfunctions of Flow Ducts

2.1 Introduction

Sound propagation in acoustically lined flow ducts is a problem which is relevant to the acoustic design of aero-engine nacelles. It is of considerable practical interest due to stringent noise levels required for quiet commercial aircraft engines. The expansion of the sound field in a duct in terms of modes forms the basis for many analytic and semi-analytic methods in duct acoustics. It is not only an effective way of reducing the dimension of the problem; propagation in a prismatic two-dimensional or axisymmetric duct reduces to a one-dimensional eigenvalue problem; propagation in a duct of arbitrary cross-section reduces to a two-dimensional eigenvalue problem. It is also a useful way of understanding the sound attenuation in acoustically lined ducts by analysis of their modal solutions. The mode axial wavenumber indicates the mode attenuation rate and the modal propagation speed, and the duct eigenfunction represents the mode pressure field. By matching expansions of such eigensolutions at the interface between different uniform duct segments, the effect of axial variations of impedance can be modelled with far fewer parameters than would be required for a three-dimensional numerical transmission analysis.

To date, both exact and approximate methods have been developed for studying sound propagation in attenuated ducts with and without flow. These methods have been used not only for solving practical problems but also as a tool for fundamental understanding of the problem.

In this chapter, a numerical model using finite element (FE) for computing the eigenmodes in ducts of arbitrary cross-section with nonuniform mean flow and locally reacting impedance boundaries is described. The FE method has been employed to solve these kind of problems in the early 1980s [77, 12, 78]. These are based on the linearised Euler equations. However, the application was limited to low frequencies and coarse meshes because of the computational resources available at that time. In this research, this general approach is revisited.

For two-dimensional and axisymmetric ducts, the FE method may be computationally expensive as the solutions can also be obtained analytically [79]. For three-dimensional problems, when the mean flow and impedance boundary in the duct are non-uniform, some form of numerical procedure must be used, either to solve an analytical eigenvalue relationship, or to form an equivalent discrete problem. In the later instance, a FE representation of the duct cross-section is commonly used.

In this research, the FE eigenvalue model is used for computing the axial wavenumbers and eigenfunctions of the duct modes required for duct transmission analysis using mode matching techniques. This work also seeks to gain further understanding of the effect of the boundary layer on the attenuation of sound in the duct. The problem is formulated so that a boundary layer can be included near to the duct wall if this is required. The influence of acoustic liner non-uniformities on duct modes is also considered. In particular the effect of hard axial strips inside a lined duct on the attenuation characteristics of the liner. In some engine nacelles, the existence of hard axial strips is inevitable in order to hold the liners in place.

In this chapter, the equation describing the propagation of sound waves in an acoustically lined duct with a sheared flow is derived from first principles. The formulation of the eigenvalue problem with the relevant boundary conditions is then presented along with two methods for the solution of the eigenvalue problems. Although only simplified geometries are considered in this thesis, the extension of the central ideas to complex duct geometries is straightforward.

2.1.1 Outline

Section 2.2 presents a review of currently available techniques for solution of the duct eigenvalue problem. The different types of duct modes presence in a duct and the identification of these modes from the eigensolutions are then described and presented. In Section 2.3, the problem specification is put forward followed by a derivation of the equations describing the propagation of sound waves in a duct with a sheared flow and a uniform flow. In Section 2.4, the formulation of the duct eigenvalue problem for an acoustically lined two-dimensional duct containing a sheared flow and a uniform flow is presented. Finally in Section 2.5, methods for the solution of the eigenvalue problem are described.

2.2 Acoustic Modes In A Duct

2.2.1 Uniform Flow

Sound propagation in a duct can be described by modes. For uniform mean flow, these modes are found by solving the convected wave equation for the perturbed pressure as an eigenvalue problem. The derivation of the convected wave equation is presented later in this chapter. The eigenvalue problem has two sets of discrete eigenvalues as solutions which correspond to duct modes that propagate in the positive and negative duct axial directions. These are also termed 'positive' and 'negative' acoustic modes in this thesis. For hardwalled ducts, these duct modes form a complete, orthogonal set. Every pressure perturbation can be described by a combination of these eigenfunctions.

Numerous investigations on sound propagation and attenuation in ducts with uniform flow have been reported. The studies by Eversman [80], by Astley [12] and by Ko [81] are some of the representatives. The techniques developed for the solution of the duct eigenvalue problem include the Newton-Raphson iteration scheme, the FEM [12, 10], Rienstra's tracking method [5], the Muller method [2], Eversman's numerical integration scheme [80, 79], the multi-modal method [28] and the point matching method [38]. Each method has its advantages and disadvantages. However, only some of these methods can be used to represent three-dimensional geometries with non-uniform impedance boundaries and mean flows. The FEM is one of them.

2.2.2 Non-Uniform flow

For non-uniform flow in the duct, the duct modes that describe the propagation of sound in the duct are found by solving the Pridmore-Brown equation [82] for the perturbed pressure as an eigenvalue problem. The derivation of the Pridmore-Brown equation is presented later in this chapter. The eigenvalue problem will yield three sets of discrete eigenvalues as solutions which correspond to positive acoustical modes, negative acoustical modes and hydrodynamic modes. Physically, hydrodynamic modes represent rotational disturbances which are convected with the mean flow and they are almost pressureless [83]. Details of the different types of duct modes are presented in Chapter 3.

The effects of non-uniform mean flow on the propagation and attenuation of sound in ducts were first considered by Pridmore-Brown [82] for inviscid flow and by Mungur and Gladwell [84] for viscous flow. In both studies, a two-dimensional duct was considered and the influence of the boundary layer on the duct walls was approximated by treating the duct flow as a sheared flow with a characteristic boundary-layer velocity profile as shown in Fig. 2.2. Pridmore-Brown observed that for the case of rigid walls, for acoustic waves that propagate with the mean flow, the effect of the velocity gradient is to refract the sound into a narrow layer near the walls - see Fig. 2.1(a). This effect is found to be frequency dependent and is only important at high frequencies. Because the effect of shear flow is an important issue for the study of sound propagation and attenuation in ducts, the Pridmore-Brown equation has formed the basis for numerous subsequent studies. In [85], Hersh and Catton have observed that for acoustic waves that propagate against the flow, the effect of the velocity gradient is to refract the sound into the centre of the duct - see Fig. 2.1(b). The studies by Pridmore-Brown [82] and Hersh and Catton [85] have shown that the effect of refraction is found to be important for boundary layer flows when the ratio of boundary layer height to acoustic wavelength is equal to or greater than unity.

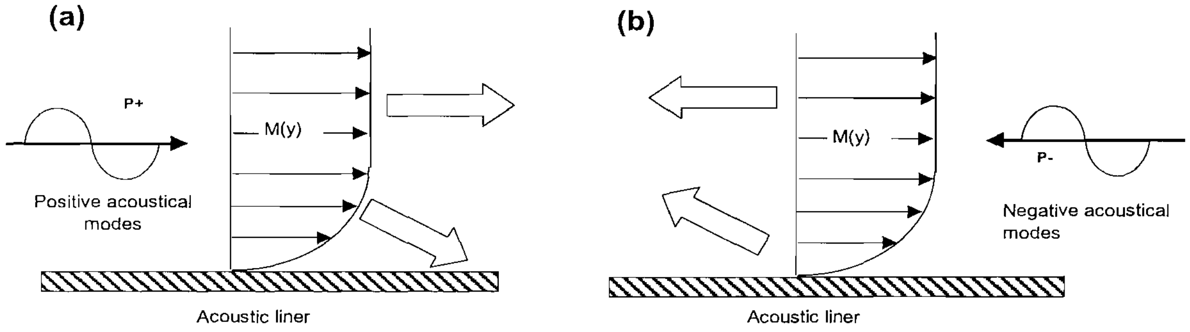

Figure 2.1: Schematic of downstream and upstream sound propagation. (a) For downstream wave propagation, wavefront is refracted into the duct walls by the velocity gradient. (b) For upstream wave propagation, wavefront is refracted away from the duct walls.

In [86], Tack and Lambert have employed a power series solution to the Pridmore-Brown's two-dimensional formulation in their study of the influence of shear flow on the attenuation of sound in lined ducts. Comparison between the theoretical and experimental results fails to give satisfactory results at mid and high frequencies. Syeb *et al.* [87] employs a finite difference iteration scheme to study sound attenuation in an acoustically lined circular duct containing a sheared flow. In [88, 89], a Galerkin weighted residual method is employed to investigate the transmission of sound in an acoustically treated rectangular duct with boundary layers and in [90], a Runge-Kutta integration scheme combined with a Newton-Raphson iteration is employed to study the effect of the boundary layer on the transmission and attenuation of sound in an acoustically treated circular duct. In [91], the same problem is studied using a method of weighted residuals with trigonometric basic functions and a perturbation approach is employed in [92]. In [12], a FEM is employed for the solutions of the flow duct eigenvalue problems. The FE solution agreed well with those obtained using the Galerkin weighted residual method [93]. The study found that the number of accurately computed modes is roughly equal to the number of quadratic Lagrangian elements used to discretize the duct width. Sometimes, the FE solution shows occurrence of spurious modes which are eigen-solutions that do not correspond to any of the physical acoustic modes. Their eigenvectors reveal very rapid oscillation. Later in [77], the same problems are studied using higher order elements with slope continuity and the spurious modes are eliminated. The FEM is later employed to compute eigenvalues and eigenfunctions of a circular duct with swirling flow [78].

Although the eigenvalue model proposed in this research is also based on FE analysis, it is different to those by Astley and Eversman [12, 77] and by Nijboer [78]. In this study, a weak form of the Pridmore-Brown equation forms the basis for the current eigenvalue formulation in acoustic pressure. In [77, 12, 78], the eigenvalue problem is formulated from the Euler equations in terms of primitive variables of velocity and acoustic pressure.

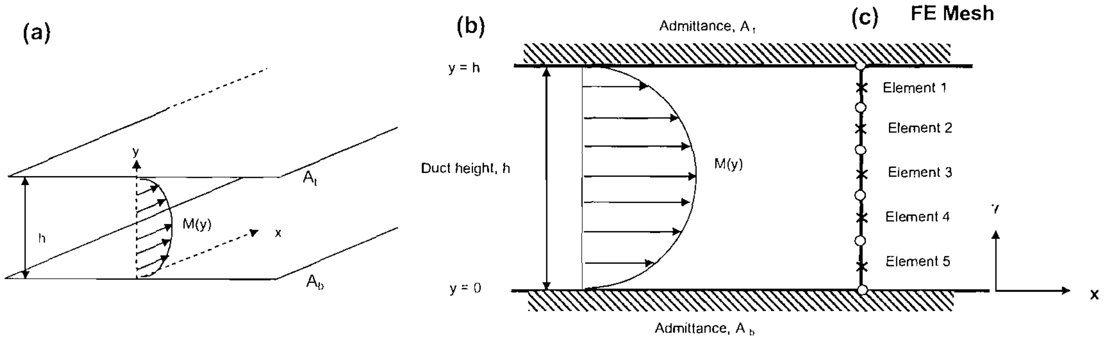

Figure 2.2: (a)-(b) Duct models. (c) FE mesh

2.3 Derivation of The Pridmore-Brown Equation

In this section, equations describing the propagation of sound waves in a lined duct with a sheared flow and a uniform flow are derived from first principles. The derivation is same as those presented in [82]. It is presented here because it is important to the understanding of this work. To reduce the complexity of the problem, the present analysis will be confined to two-dimensions only. The two-dimensional duct geometry is shown in Fig. 2.2(a). The duct walls at $y = 0$ and h are lined with a locally reacting acoustic liner whose admittances on the bottom and top surfaces are A_b and A_t respectively. The width of the duct is given by h and the duct is assumed to be infinitely long. The mean flow in the duct, $M(y)$ will be taken in the x direction and will be assumed to be a function of y only. Inviscid mean flow is assumed.

The fluid motion in the duct is governed by the Euler equations for the conservation of mass, momentum and energy which are expressed as follows [84]:

$$\text{Momentum } x \text{ direction:} \quad \rho'\left(\frac{\partial u'}{\partial t} + u'\frac{\partial u'}{\partial x} + v'\frac{\partial u'}{\partial y}\right) = -\frac{\partial p'}{\partial x} \tag{2.1}$$

$$\text{Momentum } y \text{ direction:} \quad \rho'\left(\frac{\partial v'}{\partial t} + u'\frac{\partial v'}{\partial x} + v'\frac{\partial v'}{\partial y}\right) = -\frac{\partial p'}{\partial y} \tag{2.2}$$

$$\text{Conservation of mass equation:} \quad \frac{\partial \rho'}{\partial t} + u'\frac{\partial \rho'}{\partial x} + v'\frac{\partial \rho'}{\partial x} + \rho_o'\left(\frac{\partial u'}{\partial x} + \frac{\partial v'}{\partial y}\right) = 0 \tag{2.3}$$

where ρ', u', v' and p' are the total fluid density, flow velocity in the x direction, flow velocity in the y direction and acoustic pressure respectively. These variables can be expressed as:

$$p' = p_o + p \; ; \; u' = u_o + u \; ; \; v' = v \quad \text{and} \quad \rho' = \rho_o + \rho \tag{2.4}$$

where ρ_o and ρ are the static and fluctuating density of the medium, p_o and p are the mean and fluctuating acoustic pressure, u_o is the mean flow velocity in the x direction and is assumed to be a function of y and u is the fluctuating velocity in the x direction. v is the fluctuating velocity in the y direction. $v' = v$ because there is no mean flow in the y direction $v_o = 0$. The pressure and density are adiabatically related by $p = c_o^2\rho$ where c_o is the speed of sound. ρ_o, p_o and c_o are steady state values which do not vary with y. The acoustic part of the Euler equation can be obtained by subtracting the time-average of Eqs. (2.1) to (2.3) from the original equations and neglecting the products of fluctuating components. The linearized momentum and mass equations are:

$$\text{Momentum } x \text{ direction:} \quad \rho_o\left(\frac{\partial u}{\partial t} + u_o\frac{\partial u}{\partial x} + v\frac{\partial u_o}{\partial y}\right) = -\frac{\partial p}{\partial x} \tag{2.5}$$

$$\text{Momentum } y \text{ direction:} \quad \rho_o\left(\frac{\partial v}{\partial t} + u_o\frac{\partial v}{\partial x}\right) = -\frac{\partial p}{\partial y} \tag{2.6}$$

$$\text{Conservation of mass equation:} \quad \frac{\partial \rho}{\partial t} + u_o\frac{\partial \rho}{\partial x} + \rho_o\left(\frac{\partial u}{\partial x} + \frac{\partial v}{\partial y}\right) = 0 \tag{2.7}$$

Let $\phi = (\partial u/\partial x + \partial v/\partial y)$ so that Eq. (2.7) can be rewritten as

$$\phi = -\frac{1}{\rho_o}\left(\frac{\partial \rho}{\partial t} + u_o\frac{\partial \rho}{\partial x}\right) \tag{2.8}$$

Differentiating Eqs. (2.5), (2.6) and (2.7) with respect to x, y and t respectively to yield:

$$\rho_o\left[\frac{\partial^2 u}{\partial x\partial t} + u_o\frac{\partial^2 u}{\partial x^2} + \frac{\partial v}{\partial x}\frac{\partial u_o}{\partial y}\right] = -\frac{\partial^2 p}{\partial x^2} \tag{2.9}$$

$$\rho_o\left[\frac{\partial^2 v}{\partial y\partial t} + \frac{\partial u_o}{\partial y}\frac{\partial v}{\partial x} + u_o\frac{\partial^2 v}{\partial x\partial y}\right] = -\frac{\partial^2 p}{\partial y^2} \tag{2.10}$$

$$\frac{\partial^2 \rho}{\partial t^2} + u_o\frac{\partial^2 \rho}{\partial x\partial t} + \rho_o\frac{\partial \phi}{\partial t} = 0 \tag{2.11}$$

The two momentum equations, Eqs. (2.9) and (2.10) are then added and equated to Eq. (2.11) to give

$$\rho_o\left[\frac{\partial^2 u}{\partial x\partial t} + u_o\frac{\partial^2 u}{\partial x^2} + \frac{\partial u_o}{\partial y}\frac{\partial v}{\partial x} + \frac{\partial^2 v}{\partial y\partial t} + \frac{\partial u_o}{\partial y}\frac{\partial v}{\partial x} + u_o\frac{\partial^2 v}{\partial x\partial y}\right] + \nabla^2 p = \frac{\partial^2 \rho}{\partial t^2} + u_o\frac{\partial^2 \rho}{\partial x\partial t} + \rho_o\frac{\partial \phi}{\partial t} \tag{2.12}$$

where $\nabla^2 = (\partial^2/\partial x^2 + \partial^2/\partial y^2)$. Eq. (2.12) can be further simplified to

$$\rho_o\left[u_o\frac{\partial \phi}{\partial x} + 2\frac{\partial u_o}{\partial y}\frac{\partial v}{\partial x}\right] + \nabla^2 p = \frac{\partial^2 \rho}{\partial t^2} + u_o\frac{\partial^2 \rho}{\partial x\partial t} \tag{2.13}$$

Using Eq. (2.8) and its derivative with respective to x and also the relation $p = c_o^2\rho$, ϕ can be eliminated from Eq. (2.13) to yield

$$\frac{1}{c_0^2}\frac{\partial^2 p}{\partial t^2} = (1 - M^2)\frac{\partial^2 p}{\partial x^2} + \frac{\partial^2 p}{\partial y^2} + 2\rho_o c_o\frac{\partial M}{\partial y}\frac{\partial v}{\partial x} - 2\frac{M}{c_o}\frac{\partial^2 p}{\partial x\partial t} \tag{2.14}$$

where $M = u_o/c_o$ is the local mean flow Mach number and it is a function of y only. Differentiating Eq. (2.6) with respect to x and substituting it into Eq. (2.14), the following expression is yielded:

$$\left(\frac{\partial}{\partial t}+Mc_o\frac{\partial}{\partial x}\right)^3 p-c_o^2\left(\frac{\partial}{\partial t}+Mc_o\frac{\partial}{\partial x}\right)\left(\frac{\partial^2}{\partial x^2}+\frac{\partial^2}{\partial y^2}\right)p+2c_o^3\frac{\partial^2 p}{\partial x\partial y}\frac{\partial M}{\partial y}=0 \tag{2.15}$$

This is the Pridmore-Brown equation that governs the propagation of sound with shear flow in acoustic pressure. In the expression, the interaction of shear flow with the acoustic wave is represented by the term involving $\partial M/\partial y$.

In the case of uniform flow, $\partial M/\partial y=0$, the Pridmore-Brown equation, Eq. (2.15) simplifies to the convected wave equation:

$$\left(\frac{\partial}{\partial t}+u_o\frac{\partial}{\partial x}\right)^2 p-c_o^2\left(\frac{\partial^2}{\partial x^2}+\frac{\partial^2}{\partial y^2}\right)p=0 \tag{2.16}$$

For uniform flow in the duct, the Pridmore-Brown equation, a third order partial differential equation simplifies to the convected wave equation which is a second order partial differential equation. By this, a group of solutions have been eliminated from the complete solutions. In [94], Eversman shows that these solutions are solutions which correspond to $\nabla\times\mathbf{V}\neq 0$ and they are known as the hydrodynamic disturbances. They propagate at the mean flow velocity with axial wavenumber $k_x=\omega/u_o$.

2.3.1 Acoustic Boundary Condition

At the duct wall, for a uniform admittance wall, the acoustic pressure, p must satisfy the boundary condition derived by Myers [95]. The pressure is related to the wall admittance, A by the following relation:

$$\frac{\partial p}{\partial \mathbf{n}}=-ikA(1-i\frac{M_o}{k}\frac{\partial}{\partial x})^2 p \tag{2.17}$$

where $\mathbf{n}$ is the unit normal directed out of the duct wall, $\omega=2\pi f$ is the angular frequency and f is the frequency in Hertz. M_o is the mean flow Mach number at the duct wall. For a no-slip boundary condition or zero flow, $M_o=0$, Eq. (2.17) simplifies to

$$\frac{\partial p}{\partial \mathbf{n}}=-ikAp \tag{2.18}$$

and for a rigid wall, $A=0$, Eq. (2.17) becomes

$$\frac{\partial p}{\partial \mathbf{n}}=0 \tag{2.19}$$

2.4 Formulation Of Eigenvalue Problems

2.4.1 Sheared Flow With No-Slip Boundary Conditions

In this section, the formulation of a duct eigenvalue problem based on the Pridmore-Brown equation for a two-dimensional duct containing a sheared flow is presented. Consider a two-dimensional duct as shown in Fig. 2.2 (a). The duct walls at $y = 0$ and h are acoustically lined with admittances on the bottom and top surfaces A_b and A_t respectively. The sound propagation in the duct is governed by the Pridmore-Brown equation expressed as follows:

$$\left(\frac{\partial}{\partial t}+Mc_o\frac{\partial}{\partial x}\right)^3 p - c_o^2\left(\frac{\partial}{\partial t}+Mc_o\frac{\partial}{\partial x}\right)\left(\frac{\partial^2}{\partial x^2}+\frac{\partial^2}{\partial y^2}\right)p + 2c_o^3\frac{\partial^2 p}{\partial x\partial y}\frac{\partial M}{\partial y} = 0 \tag{2.20}$$

Solutions to the acoustic pressure are sought in the form:

$$p = p(y)e^{-i\lambda kx}e^{i\omega t} \tag{2.21}$$

where λ are eigenvalues to be computed and $k\lambda = k_x$ are the corresponding duct axial wavenumbers. Substitute Eq. (2.21) into the Pridmore-Brown equation, Eq. (2.20), to obtain a cubic eigenvalue equation for λ:

$$\frac{\partial^2 p}{\partial y^2}(1-M\lambda) + 2\lambda\frac{\partial M}{\partial y}\frac{\partial p}{\partial y} + \left(k^2 - 3M\lambda k^2 + 3M^2\lambda^2k^2 - k^2\lambda^2 - k^2M^3\lambda^3 + k^2M\lambda^3\right)p = 0 \tag{2.22}$$

At the duct walls, at $y = 0$ and h, the non-slip boundary conditions are applied:

$$\begin{aligned} \left.\frac{\partial p}{\partial n}\right|_{y=0} &= -ikA_b p \\ \left.\frac{\partial p}{\partial n}\right|_{y=h} &= -ikA_t p \end{aligned} \tag{2.23}$$

Eq. (2.22) with the boundary conditions, Eq. (2.23) completes an eigenvalue problem which can then be solved to yield the duct axial wavenumbers and the corresponding duct eigenfunctions for a given shear flow profile. If $A_b = A_t$, the problem can be simplified to consider only half of the duct for symmetric modes.

2.4.2 Uniform Flow With Slip Boundary Conditions

For uniform flow in the duct, the duct eigenvalue problem is formulated based on the convected wave equation in acoustic pressure expressed as follows:

$$\left(\frac{\partial}{\partial t}+u_o\frac{\partial}{\partial x}\right)^2 p - c_o^2\left(\frac{\partial^2}{\partial x^2}+\frac{\partial^2}{\partial y^2}\right)p = 0 \tag{2.24}$$

Similarly, solutions to the acoustic pressure are sought in the form:

$$p = p(y)e^{-i\lambda kx}e^{i\omega t} \tag{2.25}$$

Substituting Eq. (2.25) into the convected wave equation, Eq. (2.24), to yield a quadratic eigenvalue equation for λ:

$$\frac{\partial^2 p}{\partial y^2} + k^2[(1 - M\lambda)^2 - (\lambda)^2]p = 0 \tag{2.26}$$

At the duct walls, at $y = 0$ and h, the slip boundary conditions are applied

$$\begin{aligned} \left.\frac{\partial p}{\partial \mathbf{n}}\right|_{y=0} &= -ikA_b(1 - M\lambda)^2 p \\ \left.\frac{\partial p}{\partial \mathbf{n}}\right|_{y=h} &= -ikA_t(1 - M\lambda)^2 p \end{aligned} \tag{2.27}$$

Eq. (2.26) with the boundary conditions, Eq. (2.27), completes an eigenvalue problem which can be solved to yield the duct axial wavenumbers and the corresponding duct eigenfunctions for a given uniform mean flow.

Engine Duct Flow Condition

The mean flow in the inlet duct is generally assumed to be uniform because the real flow is almost uniform with vorticity concentrated in the thin boundary layer at the duct walls. In the bypass duct, the mean flow is strongly sheared and sometimes with swirl. The acoustic disturbances in the duct are no longer irrotational and are coupled with the hydrodynamic disturbance due to entropy and vorticity waves. For an acoustic study of bypass duct, the acoustic modes can not be studied independently from the hydrodynamic modes as in the inlet duct with uniform flow.

2.5 Methods for the Solutions of Eigenvalue Problems

In this section, an FE algorithm and an analytical method for the solution of the eigenvalue problem formulated in Section 2.4 are presented.

2.5.1 The Finite Element Method

Sheared Flow With Non-Slip Boundary Conditions

In this section, the duct eigenvalue problem posed by Eq. (2.22) with the non slip boundary conditions is solved by the use of FE analysis. The FEM is based on a weak variational statement constructed by multiplying the duct eigenvalue equation, Eq. (2.22), by weighting functions, W and integrating over the duct width, h to give:

$$\int_0^h W \left\{ \frac{\partial^2 p}{\partial y^2}(1 - M\lambda) + 2\lambda \frac{\partial M}{\partial y}\frac{\partial p}{\partial y} + \left(k^2 - 3M\lambda k^2 + 3M^2\lambda^2 k^2 - k^2\lambda^2 - k^2 M^3\lambda^3 + k^2 M\lambda^3\right) p \right\} dy = 0 \tag{2.28}$$

Apply the divergence theorem to Eq. (2.28) to yield:

$$\int_0^h \left\{ \frac{\partial W}{\partial y}\frac{\partial p}{\partial y}(1-M\lambda) - 3W\frac{\partial M}{\partial y}\frac{\partial p}{\partial y}\lambda - W\left(k^2 - 3Mk^2\lambda + 3M^2k^2\lambda^2 - k^2\lambda^2 - k^2M^3\lambda^3 + k^2M\lambda^3\right)p \right\} dy - \left[W(1-M\lambda)\frac{\partial p}{\partial n}\right]_0^h = 0 \tag{2.29}$$

Apply the non-slip boundary conditions at $y = 0$ and h through the last term of Eq. (2.29) to yield:

$$\int_0^h \left\{ \frac{\partial W}{\partial y}\frac{\partial p}{\partial y}(1-M\lambda) - 3W\frac{\partial M}{\partial y}\frac{\partial p}{\partial y}\lambda - W\left(k^2 - 3Mk^2\lambda + 3M^2k^2\lambda^2 - k^2\lambda^2 - k^2M^3\lambda^3 + k^2M\lambda^3\right)p \right\} dy + \left[W(1-M\lambda)ikAp\right]_0^h = 0 \tag{2.30}$$

The FE discretization is achieved by dividing the duct height, h into m elements. The trial solution of the pressure is assumed to be of the form:

$$p = \sum_{j=1}^{n} N_j(y)\,p_j \tag{2.31}$$

where $j = 1, 2, \ldots n$, n is the number of nodes and $N_j(y)$ is the element shape function that connects the pressure at the nodes of the element. In this study, quadratic line elements are used to discretize the duct width. The elements produce trial functions that are continuous at all points in the region $0 \le y \le h$ with discontinuities in their y derivatives at element boundaries. Each element has two end nodes and one midside node. Fig. 2.2(b) shows a typical example of a FE mesh constructed for the two-dimensional duct. The shape functions of the element in natural coordinates are expressed as follows:

$$\begin{aligned} N_1(\xi) &= \tfrac{\xi}{2}(\xi - 1) \\ N_2(\xi) &= (1 - \xi^2) \\ N_3(\xi) &= \tfrac{\xi}{2}(\xi + 1) \end{aligned} \tag{2.32}$$

The shape function is equal to 1 at its associated node and 0 at the other nodes.

$$N_i(\xi_j) = \begin{cases} 1 & if\ i = j \\ 0 & if\ i \neq j \end{cases} \tag{2.33}$$

The Galerkin procedure then yields a solution by selecting weighting functions, W equal to N_i, the trial functions. Substitute Eq. (2.31) into Eq. (2.30) to give:

$$\int_0^h \left\{ \frac{\partial N_i}{\partial y}\frac{\partial N_j}{\partial y}(1-M\lambda) - 3N_i\frac{\partial M}{\partial y}\frac{\partial N_j}{\partial y}\lambda - N_iN_j\left(k^2 - 3Mk^2\lambda + 3M^2k^2\lambda^2 - k^2\lambda^2 - k^2M^3\lambda^3 + k^2M\lambda^3\right) \right\} p_j\, dy + \left[N_iN_j(1-M\lambda)ikAp_j\right]_0^h = 0$$

$$\tag{2.34}$$

Eq. (2.34) can be written as a function of eigenvalue, λ as:

$$[\mathbf{A}]\{p\}+[\mathbf{B}]\lambda\{p\}+[\mathbf{C}]\lambda^2\{p\}+[\mathbf{D}]\lambda^3\{p\}=0 \tag{2.35}$$

where

$$\mathbf{A}_{ij}=\int_0^h\left(\frac{\partial N_i}{\partial y}\frac{\partial N_j}{\partial y}-N_iN_jk^2\right)dy+\left[ikN_i(h)N_j(h)A_{y=h}-ikN_i(0)N_j(0)A_{y=h}\right]$$

$$\mathbf{B}_{ij}=-\int_0^h\left(\frac{\partial N_i}{\partial y}\frac{\partial N_j}{\partial y}M-3N_i\frac{\partial N_j}{\partial y}\frac{\partial M}{\partial y}+3Mk^2N_iN_j\right)dy-\left[ikN_i(h)N_j(h)M(h)A_{y=h}-ikN_i(0)N_j(0)M(0)A_{y=0}\right]$$

$$\mathbf{C}_{ij}=\int_0^h\left(-3N_iN_jk^2M^2+N_iN_jk^2\right)dy$$

$$\mathbf{D}_{ij}=\int_0^h\left(N_iN_jk^2M^3-N_iN_jk^2M\right)dy$$

By defining

$$\lambda^2\{p\}=\{Q\}\quad\text{and}\quad\lambda\{p\}=\{R\} \tag{2.36}$$

Eq. (2.35) can be re-written in a linear function of λ:

$$[\mathbf{A}]\{p\}+[\mathbf{B}]\lambda\{p\}+[\mathbf{C}]\lambda\{R\}+[\mathbf{D}]\lambda\{Q\}=0 \tag{2.37}$$

which can then be written in the form of a standard eigenvalue problem:

$$[\mathbf{G}]\{\delta\}=\lambda[\mathbf{H}]\{\delta\} \tag{2.38}$$

where the entries of $[\mathbf{G}]$ and $[\mathbf{H}]$ matrices are:

$$[\mathbf{G}]=\begin{bmatrix}\mathbf{I}&\mathbf{0}&\mathbf{0}\\\mathbf{0}&\mathbf{I}&\mathbf{0}\\\mathbf{C}&\mathbf{B}&\mathbf{A}\end{bmatrix}\;;\;[\mathbf{H}]=\begin{bmatrix}\mathbf{0}&\mathbf{I}&\mathbf{0}\\\mathbf{0}&\mathbf{0}&\mathbf{I}\\-\mathbf{D}&\mathbf{0}&\mathbf{0}\end{bmatrix}\;;\;\{\delta\}=\begin{Bmatrix}Q\\R\\P\end{Bmatrix} \tag{2.39}$$

$[\mathbf{I}]$ is an identity matrix. The matrices $[\mathbf{G}]$ and $[\mathbf{H}]$ are assembled from the appropriate element sub-matrices [96]. Solving the system will yield $3n$ eigenvalues λ; n positive acoustical modes, n negative acoustical modes and n hydrodynamic modes and also the corresponding mode eigenvectors.

Uniform Flow With Slip Boundary Conditions

For uniform flow in the duct, $\partial M/\partial y = 0$, the eigenvalue problem posed by Eq. (2.26) with the slip boundary conditions is solved. The weak variational statement is constructed by multiplying Eq. (2.26) by weighting functions, W and integrating over the duct width, h to yield:

$$\int_0^h W\left\{\frac{\partial^2 p}{\partial y^2}+k^2[(1-M_o\lambda)^2-\lambda^2]p\right\}dy=0 \tag{2.40}$$

where M_o is the uniform mean flow Mach number. The trial solutions of the pressure are assumed to be of the form:

$$p=\sum_{j-1}^{n} N_j(y)\,p_j \tag{2.41}$$

Apply the divergence theorem, the following expression is yielded:

$$\int_0^h \left\{\frac{\partial W}{\partial y}\frac{\partial p}{\partial y}-k^2 W\left[(1-M_o\lambda)^2-\lambda^2\right]p\right\}dy-\left[W\frac{\partial p}{\partial \mathbf{n}}\right]_0^h=0 \tag{2.42}$$

The Galerkin procedure selects weighting functions, $W = N_i$. Substitute the slip boundary condition terms, Eq (2.27) into Eq. (2.42). The following expression is yielded:

$$\int_0^h \left\{\frac{\partial N_i}{\partial y}\frac{\partial N_j}{\partial y}-k^2N_iN_j\left[(1-M_o\lambda)^2-\lambda^2\right]\right\}p_j\,dy+\left[N_iN_jikA(1-M_o\lambda)^2p_j\right]_0^h=0 \tag{2.43}$$

Write Eq. (2.43) into a function of λ:

$$[\mathbf{A}]\{p\}+[\mathbf{B}]\lambda\{\mathrm{p}\}+[\mathbf{C}]\lambda^2\{\mathrm{p}\}=0 \tag{2.44}$$

where

$$\mathbf{A}_{ij}=\int_0^h\left(\frac{\partial N_i}{\partial y}\frac{\partial N_j}{\partial y}dy-k^2N_iN_j\right)dy-\left[ikN_i(h)N_j(h)A_{y=h}+ikN_i(0)N_j(0)A_{y=0}\right]$$

$$\mathbf{B}_{ij}=\int_0^h(2N_iN_jM_ok^2)\,dy-\left[2ikM_oN_i(h)N_j(h)A_{y=h}-2ikM_oN_i(0)N_j(0)A_{y=0}\right]$$

$$\mathbf{C}_{ij}=\int_0^h(N_iN_jk^2-N_iN_jk^2M_o^2)\,dy+\left[ikM_o^2N_i(h)N_j(h)A_{y=h}-ikM_o^2N_i(0)N_j(0)A_{y=0}\right]$$

By defining $\lambda\{p\}=\{R\}$, Eq. (2.44) can be written in the form of a standard eigenvalue problem:

$$\begin{bmatrix}\mathbf{0} & \mathbf{I}\\ \mathbf{A} & \mathbf{B}\end{bmatrix}\begin{Bmatrix}p\\ R\end{Bmatrix}=\begin{bmatrix}\mathbf{I} & \mathbf{0}\\ \mathbf{0} & \mathbf{C}\end{bmatrix}\lambda\begin{Bmatrix}p\\ R\end{Bmatrix} \tag{2.45}$$

It can be seen that the resultant eigen-matrix is smaller than for the non-uniform flow case. Solving the system will yield $2n$ eigenvalues; n positive acoustic modes and n negative acoustic modes and the corresponding mode eigenfunctions.

2.5.2 Three-dimensional Problems

For three-dimensional problems, the FE algorithm for solving the eigenvalue problems will be similar to the two-dimensional case specified in this chapter. For three-dimensional ducts, the duct cross section is discretized using surface elements. For two dimensional ducts, the width of the duct is discretized using line elements. The entries in matrices [**A**], [**B**], [**C**] and [**D**] consist of area integrals rather than line integrals as in the two-dimensional case and the boundary conditions of the problem will be associated with the line integral terms in the matrices.

For three-dimensional ducts, 8-noded quadrilateral elements or 6-noded triangular elements as shown in Fig. 2.3 are used to discretize the duct cross-section. The mesh can be structured or unstructured. Fig. 2.4 shows a structured FE mesh constructed from 8-noded quadrilateral elements and an unstructured FE mesh constructed from 6-noded triangular elements. The element shape functions for an eight-noded quadrilateral element are:

$$\begin{aligned}
N_1(\xi,\eta) &= (1/4)\xi(1-\xi)\eta(1-\eta)\\
N_2(\xi,\eta) &= -(1/2)\xi(1-\xi)(1+\eta)(1-\eta)\\
N_3(\xi,\eta) &= (1/4)\xi(1-\xi)\eta(1+\eta)\\
N_4(\xi,\eta) &= -(1/2)(1+\xi)(1-\xi)\eta(1+\eta)\\
N_5(\xi,\eta) &= (1/4)\xi(1+\xi)\eta(1+\eta)\\
N_6(\xi,\eta) &= -(1/2)\xi(1+\xi)(1+\eta)(1-\eta)\\
N_7(\xi,\eta) &= (1/4)\xi(1+\xi)\eta(1-\eta)\\
N_8(\xi,\eta) &= -(1/2)(1+\xi)(1-\xi)\eta(1-\eta)
\end{aligned} \tag{2.46}$$

where ξ and η are the local coordinates. The element shape functions for a six-noded triangular element are:

$$\begin{aligned}
N_1(\xi,\eta) &= 1-\xi-\eta\\
N_2(\xi,\eta) &= \xi\\
N_3(\xi,\eta) &= \eta\\
N_4(\xi,\eta) &= 4\xi(1-\xi-\eta)\\
N_5(\xi,\eta) &= 4\eta(1-\xi-\eta)\\
N_6(\xi,\eta) &= 4\xi\eta
\end{aligned} \tag{2.47}$$

The element shape functions imply that the acoustic pressure is continuous at all points in the duct region but

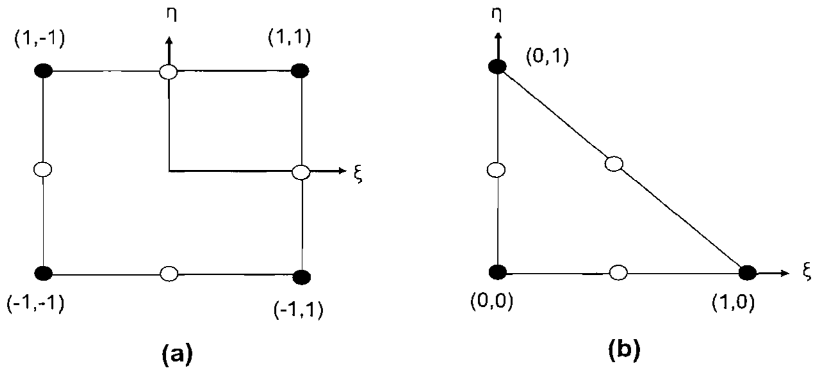

Figure 2.3: (a) 8-noded quadrilateral element, (b) 6-noded triangular element. • - interelement node and ○ - midside node.

discontinuities in the derivative are permitted at element boundaries.

Another important aspect of the FE analysis when solving three-dimension problems is the mapping from local coordinates to global coordinates. This is needed for a systematic way of integrating different elements of different sizes and shapes throughout the meshed model. The relation between the local and global coordinates is given by

$$dXdY = |J|\,d\eta d\xi \tag{2.48}$$

where $|J|$ is the Jacobian which is the determinant of

$$J = \begin{bmatrix} \frac{\partial X}{\partial \xi} & \frac{\partial Y}{\partial \xi} \\ \frac{\partial X}{\partial \eta} & \frac{\partial Y}{\partial \eta} \end{bmatrix} \tag{2.49}$$

where X and Y are the global coordinates defined as

$$\mathrm{X} = \sum N_i \mathrm{X_i} \qquad \mathrm{Y} = \sum N_i \mathrm{Y_i} \tag{2.50}$$

N_i is the shape function for node i and X_i and Y_i are the global coordinates x and y of node i.

2.5.3 Eigenvalue Routines

For two-dimensional problems, a standard complex eigenvalue routine uses the QZ algorithm, a complex implementation of the common QR algorithm for complex, non Hermitian matrices is employed to compute the eigen-solutions. For large three-dimensional problems, an iterative eigenvalue routine (*ARPACK*) developed by Lehoucq, Maschhoff, Soresen and Yang [97, 98] is employed for computing the eigen-solutions. ARPACK is a collection of Fortran77 subroutines designed to solve large scale eigenvalue problems [97, 98]. It is a free

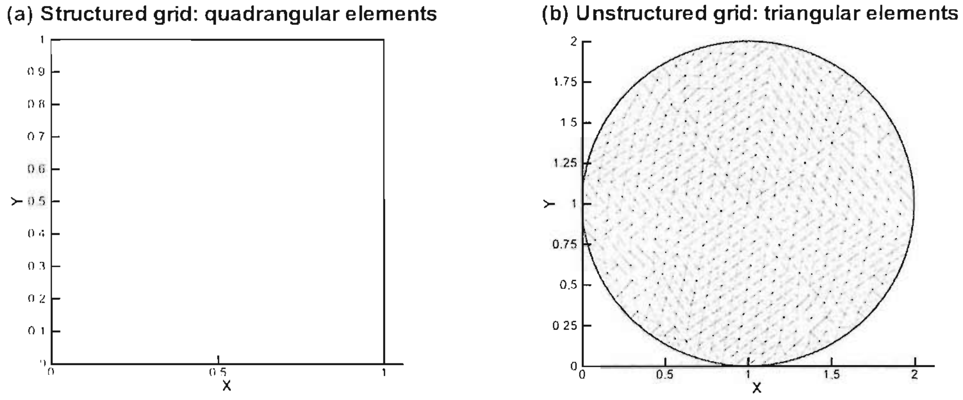
(a) Structured grid: quadrangular elements

(b) Unstructured grid: triangular elements

Figure 2.4: (a) A structured FE mesh constructed from 8-noded quadrilateral elements. (b) An unstructured FE mesh constructed from 6-noded triangular elements.

software which can be downloaded from *www.caam.rice.edu*. Rather than computing the complete eigenvalues, it computes a certain number of eigenvalues with user specified features such as those of the largest real part, largest imaginary part or largest absolute. Generally the number of eigenvalues computed is of the order of 10% for matrices that may typically be of order of around 10,000.

2.5.4 Analytical Method

Uniform Mean Flow

For two-dimensional and axisymmetric ducts, the duct eigen-solution can be computed analytically. In this section, an analytical method of solving the duct eigenvalue problem for a two-dimensional ducts with uniform mean flow is described [79, 80]. The present analysis will be confined to two-dimensional ducts only as the extension of the method to axisymmetric ducts is straightforward. The duct configuration considered is shown in Fig. 2.5. M_o is the uniform mean flow Mach number, A is the acoustic admittance at the duct wall at $y = 0$ and h is the duct width. In this study, the analytical model is used to provide a validation to the FE eigenvalue model for some two-dimensional and axisymmetric ducts.

The acoustic pressure in the duct is assumed to be represented by a superposition of acoustic modes of the form

$$p_i = \sum_{i=1}^{\infty} A_i e^{i\omega t} e^{-ik_{x,i}x} \cos(\kappa_i y) \tag{2.51}$$

where κ_i is the duct transverse wavenumber of ith mode and $k_{x,i}$ and A_i are the corresponding duct axial wavenumber and the coefficient of the mode respectively. κ_i is related to the duct axial wavenumber, $k_{x,i}$

by the dispersion equation:

$$\frac{k_{x,i}}{k} = \frac{1}{1-M_o^2}\left[-M_o \pm \sqrt{1-(1-M_o^2)\left(\frac{\kappa_i}{k}\right)^2}\right] \tag{2.52}$$

Substitute Eq. (2.51) into the convected wave equation, Eq. (2.16), an eigenvalue equation for κ_i is yielded:

$$kh\left(\frac{\kappa_i}{k}\right)\tan kh\left(\frac{\kappa_i}{k}\right) = iAkh(1-M_o\frac{k_{x,i}}{k})^2 = iAkh\omega^2 \tag{2.53}$$

The eigenvalue equation, Eq. (2.53), is then transformed into a first order non-linear ordinary differential equation by differentiating with respect to a non dimensional parameter ζ where $(0 \le \zeta \le 1)$ and this yields

$$\frac{\partial}{\partial\zeta}\left(\frac{\kappa_i h}{kh}\right) = \frac{i\omega^2 A_f}{\left[\tan kh\left(\frac{\kappa_i h}{kh}\right) + kh\left(\frac{\kappa_i h}{kh}\right)\sec^2 kh\left(\frac{\kappa_i h}{kh}\right) \mp 2i\frac{A\omega}{\upsilon^{1/2}}M_o\left(\frac{\kappa_i h}{kh}\right)\right]} \tag{2.54}$$

where the admittance $A(\zeta)$ is now taken as a function of the non dimensional parameter ζ. If A_f is the admittance for which the eigenvalues are required, then

$$A = \zeta A_f \qquad \text{and} \qquad \frac{dA}{d\zeta} = A_f$$

Eq. (2.54) is then integrated from suitable initial conditions with $A = 0$ over $(0 \le \zeta \le 1)$ to yield the eigenvalue solutions of the equation. In [79, 80], hard-walled eigenvalues $\kappa_i h/kh = (i-1)\pi/kh$ were used as initial values. A fourth-order Runga-Kutta integration scheme was then used to perform the integration from $\zeta = 0$ to $\zeta = 1$, a Newton-Raphson iteration was later performed to refine the solution. For each eigenvalue, κ_i/k, the corresponding duct axial wavenumber, $k_{x,i}/k$ can be computed using Eq. (2.52). When the acoustic admittance has a positive imaginary part, $Im(A) > 0$, two extra eigenvalues appear. These are known as the surface wave modes. They can be found using the following initial values:

$$\frac{\kappa_i h}{kh} = \frac{1-M_o^2}{M_o^2}\frac{1}{A} \pm 2i/M_o(1-M_o^2)^{1/2} \tag{2.55}$$

2.6 Surface Waves

In a three-dimensional acoustically lined duct, the duct modes can be classified into two categories; the three-dimensional acoustic modes and the two-dimensional surface waves that exist only near the lined wall [5].

For an axisymmetric duct, per frequency and per circumferential order, there are, at most four surface waves that can be present in the duct depending on the acoustic impedance value and the mean flow. There are two kinds of surface waves; two acoustic surface waves that exist with and without mean flow, and two hydrodynamic surface waves that exist when flow is present in the duct. The surface waves can be identified by

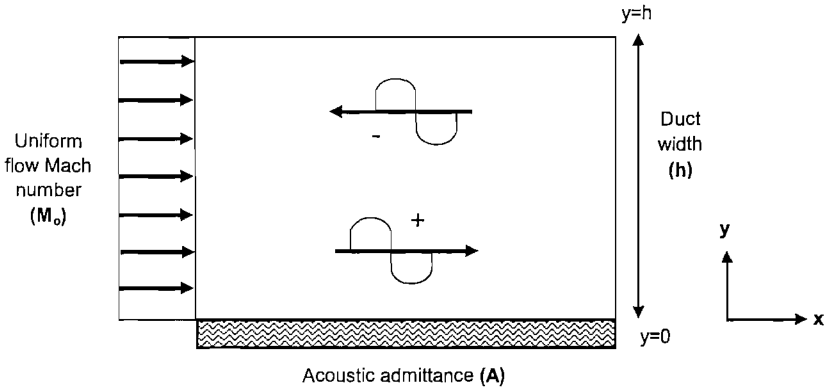

Figure 2.5: Duct model.

their axial wavenumbers with large imaginary parts, $Re(k_x) < Im(k_x)$ or by their transverse wavenumbers with large real parts, $Re(\kappa) > Im(\kappa)$.

In [5], Rienstra used a complex impedance to identify the presence of different types of surface waves in the duct according to the liner impedance. He presented a complex impedance plane with five regions showing the presence of different types of surface waves in each region - see Fig. 2.6. The plot is unique for different flow Mach number which is uniform mean flow of Mach number 0.5 in this case. In region I, no surface waves exist, in region II, only hydrodynamic instability mode (*HI*) exists, in region III, only *HI* and right propagating surface modes (*SR*) exist, in region VI, only *HI*, *SR* and left propagating surface modes (*SL*) exist and in region V, all four surface waves exist: *HI*, *SR*, *SL* and hydrodynamic stable mode (*HS*).

Rienstra's study found that for certain flow conditions, and impedance values, *HI* can be unstable. The mode propagates in one direction and exponentially decays in the opposite direction. The modal intensity of the mode indicated that the the actual propagation direction of the mode can be different for different flow and impedance values. This also suggests that in order to identify the positive and negative propagating modes correctly, the modal intensity should be used instead of the imaginary part of the duct axial wavenumber which is what is suggested in [80]. The expression of the modal intensity is presented in Chapter 5.

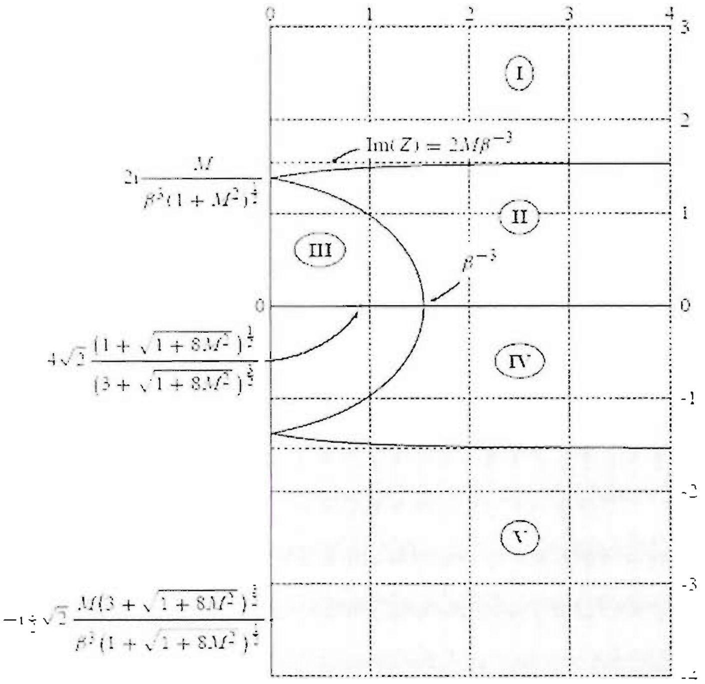

Figure 2.6: A complex impedance plane with five regions showing the presence of different types of surface waves for $M_o = 0.5$ [5].

Chapter 3

Results: Two-dimensional Eigenvalue Problems - Validation and Application

3.1 Introduction

In this chapter, the propagation and attenuation of modes in two-dimensional ducts with uniform and sheared flows are studied using an FE eigenvalue model. Details of the FE eigenvalue model are presented in Chapter 2. This work aims to establish the accuracy and convergence of the FE eigenvalue model for solutions of the duct eigenvalue equations presented in Chapter 2. The accuracy of the solutions computed by the FE eigenvalue model is checked against those obtained using other methods, either numerically or analytically. This work is also to indicate whether the two-dimensional results are favorable. If so, the generalization and assessment of the FE eigenvalue model for three-dimensional problems would be warranted.

Some issues regarding the validity of the FEM for solution of the duct eigenvalue problems have been addressed in the past [12, 77]. The eigenvalue problems considered were different to the problems considered in this study. Astley-Eversman eigenvalue model is formulated in terms of primitive variables of velocity and acoustic pressure and at low frequencies. The eigenvalue model considered in this study is formulated from the Pridmore-Brown equation for sheared flow and from the convected wave equation for uniform flow in terms of acoustic pressure.

In this research, we are interested in applications at relatively high frequencies relevant in high bypass ratio turbofan engine ducts. The reduced frequency range of interest corresponds to kh between 15 to 30 where k is the acoustic wavenumber and h is a characteristic width of the duct. This reduced frequency range corresponds approximately to blade passing frequency (BPF) for an equivalent circular duct in a turbofan aero-engine. Ideally the ability to calculate solutions for greater kh values would be desirable e.g. up to 60 or 70.

The objectives of this chapter are:

- to show that the FE eigenvalue model gives *correct* results. That is to say that the duct eigen-solutions computed correspond to the analytical solutions which should include hydrodynamic modes, acoustic modes and surface wave modes;

- to assess the accuracy of the FE eigenvalue model and to determine the FE mesh resolution which is required to obtain solutions for a given number of modes particularly at high frequencies;
- to gain further insight into the modelling characteristic of the FE eigenvalue model and the possible structure of the modal solutions;
- to investigate the advantages of the FEM over other methods currently available, and
- to study the effect of the boundary layer on the attenuation of sound in the duct.

3.1.1 Outline

The outline of this chapter is as follows. In Section 3.2, the problem specification is put forward, including the test problems that have been used and details of the numerical models. In Section 3.3, a description of the different types of duct modes presence in a duct and the identification of these modes from the eigen-solutions are presented. In Section 3.4.1, the accuracy of the FE eigenvalue model is checked by comparing with the analytical and numerical solutions obtained by other methods for a lined duct containing uniform flow. Section 3.4.2 presents results of a convergence study of the FE eigenvalue model using meshes of different resolutions. In Section 3.4.3, results of a comparison of the FE solutions with previous computed results obtained using other methods for a lined duct with uniform flow are presented. In Sections 3.5.1 and 3.5.2, the accuracy and convergence of the FE eigenvalue model for a lined duct with sheared flow are presented. Section 3.4.3 presents results of a comparison of the FE solutions with previously computed results obtained using other methods for a lined duct with various sheared flow profiles. Finally, in Section 3.6, some conclusions of the study are presented.

3.2 Problem Specification

3.2.1 Test Problems

This section presents the details of the test cases considered in this study. The results have been produced for the particular test cases of a uniform two-dimensional duct containing uniform flow and a uniform two-dimensional duct containing sheared flow - see Figs. 3.2(a) and 3.3(a). The shear flow profile shown in Fig. 3.3(a) is considered because it corresponds to a known test case in [93, 12]. The FE eigenvalue model is capable of considering any arbitrary flow profile.

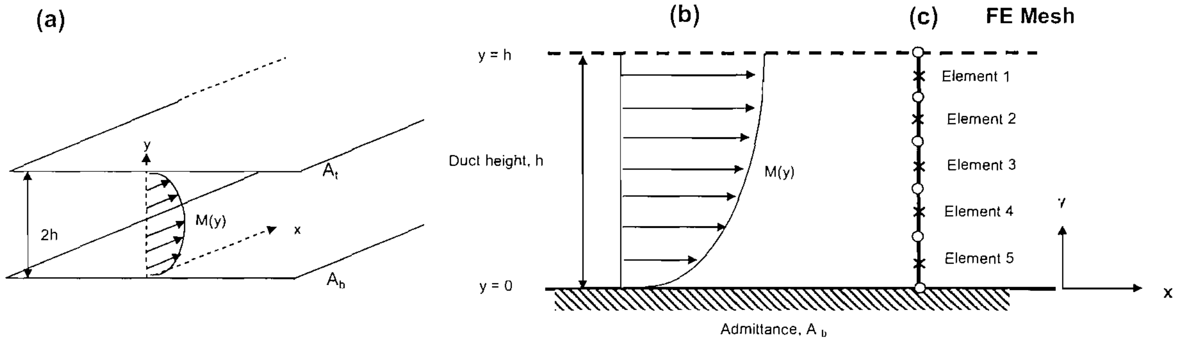

Figure 3.1: (a)-(b) Sketches of a two-dimensional duct geometry and the coordinate system for the duct, (c) Finite element grid.

The top and bottom of the duct walls are lined with locally reacting acoustic linings whose acoustic admittances are defined by A_t and A_b. The mean flow Mach number in the duct, M_o will be taken in the x direction and is assumed to be a function of y only. If $A_t = A_b$, the problem can be simplified to consider only half of the duct geometry for symmetric modes with hard boundary at $y = h$ - see Fig. 3.1(b).

3.3 Eigen-Solution

3.3.1 Acoustic Modes

For ducts with sheared flow, the eigenvalue problem for the Pridmore-Brown equation is solved for the acoustic pressure. The eigen solution yields three distinct sets of duct modes; positive acoustic modes, negative acoustic modes and hydrodynamic modes. For ducts with uniform flow, the eigenvalue problem for the convected wave equation is solved for the acoustic pressure. The eigen-solution yields two distinct sets of duct modes; positive acoustic modes and negative acoustic modes. The different types of duct modes can be identified based on the duct axial wavenumber and the duct modal intensity.

A mode with a negative modal intensity represents a negative acoustic mode. The mode decays or propagates in the negative x direction. Similarly, a mode with a positive modal intensity represents a positive acoustic mode. The mode decays or propagates in the positive x direction. The hydrodynamic modes are identified by their axial wavenumbers, $k_{x,h}$ which are predominantly real with small imaginary values. The $k_{x,h}$ value lies in the range bounded by k/M_{max} and k/M_{min} where M_{max} and M_{min} are the maximum and minimum mean flow Mach number values in the duct. $k = \omega/c_o$ is the acoustic wavenumber, ω is the angular frequency and c_o is the speed of sound. In the case of uniform flow in the duct, the axial wavenumbers of the hydrodynamic modes are represented by multiple solutions with $k_{x,h} = k/M_o$. Physically, the hydrodynamic modes represent rotational disturbances which are convected with the mean flow and they are almost pressureless [83].

In this study, the positive and negative acoustic modes are ordered on the basis of their cut-off ratios in descending order. The mode cut-off ratio, η is defined by:

$$\eta = \frac{k}{|\kappa|\sqrt{1-M_o^2}} \tag{3.1}$$

where κ is the duct transverse wavenumber and it is related to the eigenvalue, λ by the dispersion equation:

$$\kappa = k\sqrt{\frac{1}{1-M_o^2} - \frac{1}{1-M_o^2}(M_o + (1-M_o^2)\lambda)^2} \tag{3.2}$$

For shear flow, M_o is taken to be the maximum mean flow Mach number in the duct.

In a hardwalled duct, the duct modes having cut-off ratios greater than 1 are cut-on and propagate unattenuated in the axial direction upstream and downstream from their point of origin and carry acoustic energy. When the mode cut-off ratios are less than 1, the associated acoustic modes are cut-off. The cut-off modes decay exponentially along the axial direction of the duct and carry no acoustic energy. In a softwalled duct where acoustic modes are neither cut-on nor cut-off, the mode cut-off ratio can still be used to indicate the degree to which the mode propagates within the duct. The smaller the mode cut-off ratio, the greater the rate of which the acoustic mode decays along the duct.

For the shear flow case, an FE subdivision with n degrees of freedom yields an eigen-matrix of order $3n$. For uniform flow, the order of the eigen-matrix decreases to $2n$ because the Pridmore-Brown equation, a third order differential equation simplifies to the convected wave equation, a second order differential equation. Details of the discrete eigenvalue problem are presented in Chapter 2.

In this work, the eigenvalue problems are solved using the generalized eigenvalue routines in the IMSL library [99]. The routines use the QZ algorithm which is a complex implementation of the common QR algorithm for complex and non Hermitian matrices. The eigenvalue routines calculate all the eigenvalues.

Surface Waves

In lined ducts, besides the acoustic modes, the eigen-solutions can include up to four surface waves depending on the liner impedance and flow condition. The surface waves arise when part of the sound wave is scattered by the impedance wall and confined to a thin layer near the wall [100]. The characteristics of the surface waves are their pressure field is localized near the lined walls. Details regarding the surface waves are presented in Chapter 2. Part of the validation study is to ensure that the FE eigenvalue model is capable of resolving correctly the surface waves of different types. Some of the test cases have been deliberately set up to include different types of surface waves in the solutions.

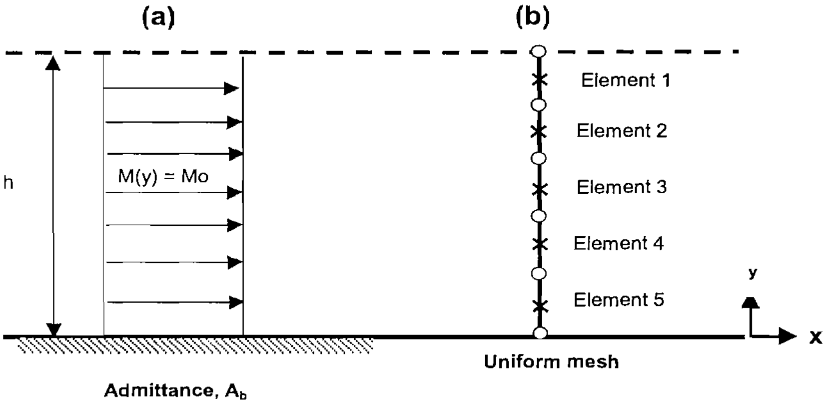

Figure 3.2: (a) A softwalled duct with uniform mean flow. (b) Finite element subdivision of the duct with using a uniform mesh. o interelement node, × midside node.

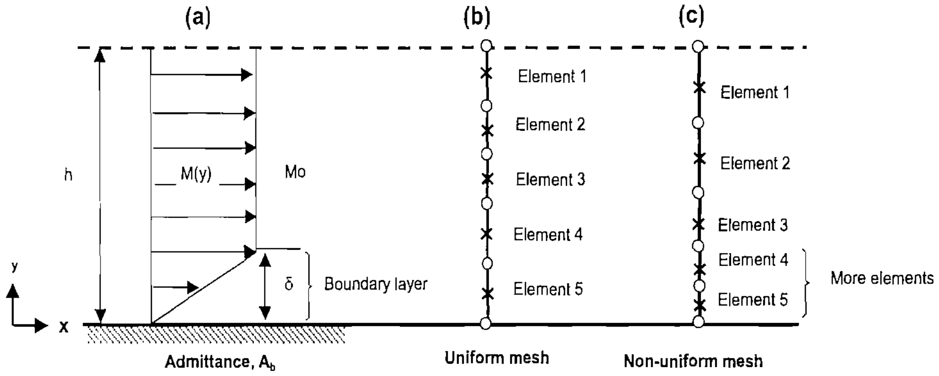

Figure 3.3: (a) A softwalled duct with a sheared mean flow. (b) Finite element subdivision of the duct width using a uniform mesh. (c) Finite element subdivision of the duct width using a nonuniform mesh. o interelement node. × midside node.

Numerical Model

The duct width is discretized using quadratic Langrangian line elements as shown in Fig. 3.1(c). For uniform flow, uniform meshes are used for the discretization of the duct width - see Fig. 3.2(b). For sheared flow, uniform and non-uniform meshes are used to discretize the duct width - see Figs. 3.3(b) and (c). Both meshes have the same number of elements but the non-uniform grid has more elements at the boundary layer than the uniform grid. This intends to resolve the pressure in that region more accurately. The linear shear flow profile shown in Fig. 3.3(a) is considered here because previous results are available for comparison. The FE eigenvalue model is capable of considering any arbitrary flow profile.

3.3.2 Benchmark Results

In this study, the validity of the FE eigenvalue model is examined by comparing with the exact and approximate results obtained by other methods. Some of these results are computed by the author and some are previously computed results. For uniform flow, the exact solutions are computed using an integration scheme [80, 79]. The scheme are detailed in Chapter 2. The approximate results are those previously computed by Unruh and Eversman [88] using the method of weighted residuals (MWR) and by Astley and Eversman [12] using the FEM. Although the eigenvalue model proposed in this research is also based on FE analysis, it is different to those by Astley and Eversman [12, 77]. The current FE eigenvalue model is formulated from the Pridmore-Brown equation in acoustic pressure. The Astley-Eversman FE eigenvalue model is formulated from the Euler equations in terms of primitive variables of velocity and acoustic pressure.

For sheared flow, the exact results are those previously computed by Hersh [85]. The approximate results are those previously computed by Unruh and Eversman [88] using the MWR and by Astley and Eversman [12] using the FEM.

3.4 Uniform Flow Results

This section presents results for uniform flow in the duct. Section 3.4.1 presents results of an assessment of accuracy of the FE eigenvalue model for a fixed mesh. Section 3.4.2 presents results of a convergence study of the FE eigenvalue model using meshes of different resolutions. In Section 3.4.3, results of a comparison of the FE solutions against previously computed results. Finally Section 3.4.4, results of a study into the treatment of surface waves by the FE eigenvalue model are presented.

3.4.1 Assessment of Accuracy of the FE Solutions for a Fixed Mesh - Uniform Flow

In this section, the accuracy of the FE eigenvalue model is checked by comparing with the analytical solutions computed by the author. The test duct as shown in Fig. 3.2(a) has an acoustically lined wall at $y = 0$ and a hard boundary at $y = h$. The duct is studied for kh =5, 10 and 20 with uniform mean flow at $M_o = 0.5$. The non-dimensional acoustic impedance at the lined wall is taken to be $2.0 - 2.34i$, $2.0 - 1.14i$, and $2.0 + 1.26i$ respectively. These values are derived for a simple model for a single cavity liner which consists of a porous facing sheet with resistance R and rigid back plate. They are separated by a honeycomb mesh with cavity depth d and mass reactance m. The non-dimensional specific acoustic impedance, Z of the lining is expressed as follows:

$$Z = R + i[X_m - X_c] \tag{3.3}$$

Duct width	h	0.5m
Reduced frequency	kh	5, 10, 20
Non-dimensional acoustic impedance	Z_b	$2-2.344i$, $2-1.144i$, $2+1.256i$
Mean flow Mach number	M_o	0.4

Table 3.1: Model duct specification.

where the mass reactance $X_m = km_r$ and the cavity reactance $X_c = -cot(kd)$. For the results presented here, the resistance is taken to be 2, and the mass reactance and liner depth are taken to be $m = 0.24$ and $d = 27.5mm$. These are typical values for a turbofan aero-engine liner. In Table 3.1, the values of the parameters used in this analysis are presented.

A uniform mesh constructed from 5 quadratic Lagrangian line elements as shown in Fig. 3.2(b) was used to discretize the duct width. Table 3.2 presents the axial wavenumbers of the positive and negative propagating modes computed by the FE eigenvalue model and also the corresponding mode cut-off ratios evaluated by using Eq. (4.2).

To assess the accuracy of the FE solution, the error percentage between the FE and the benchmark solutions is calculated using the following expression:

$$\varepsilon = \frac{\left|k^{\pm}_{x,n} - k^{\pm}_{x,e}\right|}{\left|k^{\pm}_{x,e}\right|} \times 100\% \tag{3.4}$$

where $k^{\pm}_{x,n}$ is the duct axial wavenumber computed by the FE eigenvalue model and $k^{\pm}_{x,e}$ is the duct axial wavenumber computed analytically. The superscripts $\pm$ are associated with duct modes propagate in the positive and negative x direction.

Figs. 3.4 to 3.6 show plots of error versus mode number for the three frequency cases. The mode number in the plots is obtained by ordering the modes according to their cut-off ratios in descending order so that those modes on the left are well cut-on and those on the right are effectively cut-off. In the plots, modes having cut-off ratios greater than 0.8 are represented by unfilled symbols and modes having cut-off ratios less than 0.8 are represented by filled symbols.

In this study, the comparison is only made for modes having cut-off ratios greater than 0.8 because these modes have been found to be adequate when incorporated with the mode matching method for duct transmission study. This would include all the cut-on modes and a few evanescent modes as in a hardwalled duct.

Results presented in Fig. 3.4 show that at the low frequency of $kh = 5$, all the duct modes having cut-off ratios greater than 0.8 are computed accurately by the FE eigenvalue model with errors less than 5% when compared with the exact solutions. For $kh = 10$, three out of the five positive acoustic modes and four out of the five negative acoustic modes having cut-off ratios greater than 0.8 show errors less than 5% when compared with the exact solutions. At the high frequency of $kh = 20$, only half of the duct modes having cut-off ratios greater than 0.8 show errors less than 5% when compared with the exact solutions - see Fig. 3.6. The gradual deterioration in the solution accuracy with increasing mode order illustrates the inability of the current mesh resolution to cope with the more complicated mode shapes. The mesh resolution, N defines the number of nodes which are required to represent the solution over one wavelength:

$$N = \frac{c_o}{f\Delta} \tag{3.5}$$

where f is the frequency in Hertz and Δ is the average distance between nodes. For many engineering applications, for a given frequency, a mesh resolution of 8 to 10 nodes per wavelength is the general rule of thumb.

Using Eq. (3.5), the FE mesh resolution is calculated to be 11 nodes per wavelength for $kh = 5$, 6 nodes per wavelength for $kh = 10$ and 3 nodes per wavelength for $kh = 20$. For $kh = 10$ and 20, the mesh resolution is less than the recommended resolution of 8 to 10 nodes per wavelength which explains the poor agreement between the two methods.

The large error observed of mode 7+ in Fig. 3.6(a) is because of the sign difference between the FE and the analytical solutions; $k^+_{x,7,n} = -3.575 - 3.678i$ and $k^+_{x,7,e} = 2.044 - 0.675i$. Using the error expression in Eq. (3.4), a large error is being computed because a large value is divided by a small value.

Table 3.2 shows that for $kh = 20$, the number of softwalled duct modes having cut-off ratios greater than 0.8 is equal to the number of hardwalled duct modes having cut-off ratios greater than 0.8. As the mode order increases, the cut-off ratios of the softwalled duct modes converge to those of the hardwalled duct. A similar characteristic has been observed for $kh = 5$ and 10. This observation justifies the use of the cut-off ratio to refer to duct modes in both rigid and lined ducts.

In Figs. 3.7 to 3.9, plots show the locations of the duct axial wavenumbers in the complex plane for the three frequency cases. Results obtained by the FE eigenvalue model and by the exact method are presented. In the plots, duct modes having cut-off ratios greater than 0.8 are represented by unfilled symbols and duct modes having cut-off ratios less than 0.8 are represented by filled symbols. The results are consistent with those observed in Fig. 3.4 to 3.6. For $kh = 5$ and 10, the agreement between the FE and the exact solutions for modes having cut-off ratios greater than 0.8 is generally good. At the high frequency of $kh = 20$, only half the duct modes having cut-off ratios greater than 0.8 agree well with the exact solutions. In Fig. 3.9(a), FE mode 7+ has a different imaginary sign from its exact counterpart.

3.4.2 Convergence of the FE Solutions - Uniform Flow

In this section, results that demonstrate the convergence of the FE solutions to the exact solutions are presented. The aim of this study is to determine the FE mesh resolution required to obtain solutions for a given number of

Mode	Exact	FEM	cut-off ratio, η	Exact	FEM	cut-off ratio, η
		kh=5.0			kh=10.0	
1+	$(3.636 - 0.077i)$	$(3.636 - 0.077i)$	8.10	$(7.096 - 0.142i)$	$(7.096 - 0.142i)$	6.31
2+	$(2.682 - 0.153i)$	$(2.682 - 0.153i)$	1.83	$(6.802 - 0.257i)$	$(6.802 - 0.257i)$	3.76
3+	$(-2.038 - 2.575i)$	$(-2.041 - 2.596i)$	0.90	$(5.165 - 0.290i)$	$(5.159 - 0.292i)$	1.80
4+	$-2.493 - 7.970i$	$-2.500 - 8.058i$	0.59	$(1.690 - 0.595i)$	$(1.582 - 0.622i)$	1.17
5+	$-2.603 - 12.045i$	$-2.616 - 12.361i$	0.44	$(-4.085 - 5.891i)$	$(-4.146 - 6.473i)$	0.90
6+	$-2.675 - 15.834i$	$-2.956 - 17.647i$	0.35	$-4.851 - 11.687i$	$-4.560 - 13.655i$	0.71
7+	$-2.734 - 19.504i$	$-3.237 - 21.519i$	0.29	$-4.736 - 16.223i$	$-4.805 - 18.290i$	0.59
8+	$-2.787 - 23.113i$	$-3.666 - 26.984i$	0.25	$-4.829 - 20.336i$	$-5.044 - 24.217i$	0.51
9+	$-2.835 - 26.685i$	$-4.643 - 32.829i$	0.22	$-4.898 - 24.241i$	$-5.316 - 30.529i$	0.44
10+	$-2.881 - 30.236i$	$-4.418 - 37.243i$	0.19	$-4.956 - 28.023i$	$-5.383 - 36.394i$	0.39
11+	$-2.925 - 33.772i$	$-2.653 - 41.184i$	0.17	$-5.006 - 31.727i$	$-4.900 - 40.043i$	0.35
1−	$(-7.986 + 0.128i)$	$(-7.703 + 0.116i)$	2.22	$(-16.534 + 0.020i)$	$(-16.534 + 0.020i)$	6.67
2−	$(-8.227 + 2.035i)$	$(-8.743 + 0.292i)$	2.39	$(-15.398 + 0.222i)$	$(-15.396 + 0.223i)$	2.21
3−	$(-3.366 + 3.036i)$	$(-2.692 + 3.079i)$	0.89	$(-12.408 + 1.069i)$	$(-12.350 + 1.140i)$	1.28
4−	$-2.836 + 8.480i$	$-2.591 + 8.344i$	0.58	$(-12.583 + 4.242i)$	$(-12.497 + 4.128i)$	1.09
5−	$-2.709 + 12.562i$	$-2.566 + 12.403i$	0.43	$(-6.148 + 6.842i)$	$(-6.013 + 7.465i)$	0.87
6−	$-2.633 + 16.349i$	$-2.550 + 16.214i$	0.35	$-5.479 + 12.597i$	$-5.442 + 15.252i$	0.69
7−	$-2.578 + 20.013i$	$-2.538 + 19.957i$	0.29	$-5.261 + 17.108i$	$-5.574 + 20.207i$	0.57
8−	$-2.533 + 23.613i$	$-2.526 + 23.709i$	0.25	$-5.139 + 21.208i$	$-5.415 + 26.453i$	0.49
9−	$-2.494 + 27.173i$	$-2.512 + 27.513i$	0.22	$-5.057 + 25.105i$	$-5.222 + 33.392i$	0.43
10−	$-2.460 + 30.709i$	$-2.481 + 31.329i$	0.19	$-4.994 + 28.884i$	$-4.881 + 39.441i$	0.38
11−	$-2.429 + 34.228i$	$-2.487 + 37.626i$	0.17	$-4.943 + 32.586i$	$-5.855 + 46.583i$	0.34

Mode	Exact	FEM	Softwalled duct cut-off ratio, η	Hardwalled duct cut-off ratio, η
		kh=20.0		
1+	$(14.241 - 0.016i)$	$(14.241 - 0.016i)$	28.017	∞
2+	$(13.889 - 0.104i)$	$(13.889 - 0.105i)$	6.481	6.946
3+	$(13.118 - 0.175i)$	$(13.113 - 0.176i)$	3.405	3.473
4+	$(11.783 - 0.221i)$	$(11.743 - 0.226i)$	2.293	2.315
5+	$(9.746 - 0.279i)$	$(9.540 - 0.281i)$	1.725	1.737
6+	$(6.744 - 0.387i)$	$(4.424 - 0.599i)$	1.383	1.389
7+	$(2.044 - 0.675i)$	$(-3.575 - 3.678i)$	1.153	1.158
8+	$(-7.117 - 5.198i)$	$(-6.595 - 15.154i)$	0.988	0.992
9+	$(-8.391 - 13.800i)$	$(-7.083 - 23.339i)$	0.865	0.868
10+	$-8.675 - 19.563i$	$-8.035 - 30.096i$	0.770	0.772
11+	$-8.833 - 24.491i$	$-9.292 - 34.320i$	0.693	0.695
1−	$(-33.275 + 0.004i)$	$(-33.275 + 0.004i)$	17.10	∞
2−	$(-32.799 + 0.038i)$	$(-32.799 + 0.039i)$	5.52	6.95
3−	$(-31.824 + 0.112i)$	$(-31.615 + 0.115i)$	3.20	3.47
4−	$(-30.292 + 0.238i)$	$(-30.229 + 0.260i)$	2.23	2.32
5−	$(-28.095 + 0.432i)$	$(-27.900 + 0.495i)$	1.70	1.74
6−	$(-24.994 + 0.720i)$	$(-22.643 + 0.704i)$	1.37	1.39
7−	$(-20.282 + 1.194i)$	$(-13.677 + 4.401i)$	1.15	1.16
8−	$(-11.174 + 5.855i)$	$(-10.270 + 16.931i)$	0.99	0.99
9−	$(-9.973 + 14.536i)$	$(-9.769 + 26.311i)$	0.87	0.87
10−	$-9.751 + 20.338i$	$-9.513 + 33.559i$	0.77	0.77
11−	$-9.639 + 25.284i$	$-8.188 + 39.411i$	0.69	0.70

() - mode having cut-off ratio, $\eta > 0.8$

Table 3.2: Axial wavenumbers of the positive and negative acoustic modes computed by the FE eigenvalue model and by the analytic model. $M_o = 0.4$, kh =5, 10 and 20. The duct wall at $y = h$ is acoustically lined and the duct wall at $y = 0$ is acoustically hard.

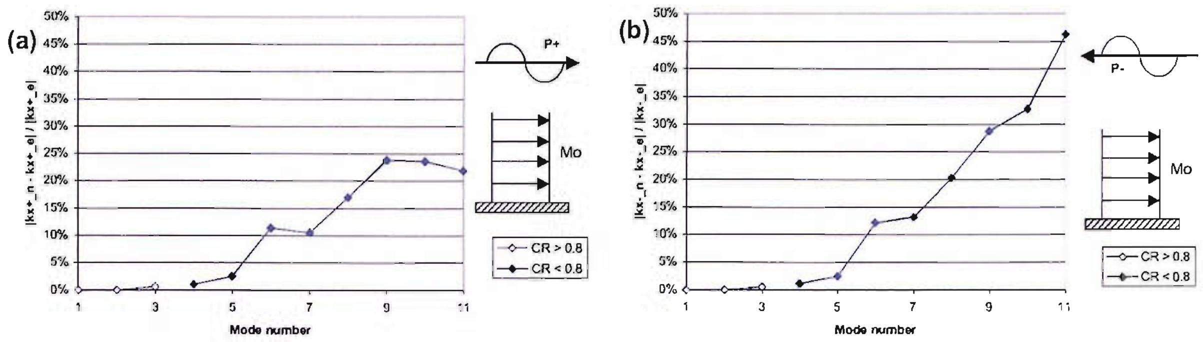

Figure 3.4: Error plotted against mode number for $kh = 5$. $M_o = 0.4$, $Z_b = 2 - 2.34423i$ and $Z_t = \infty + \infty i$. (a) Positive acoustic modes, (b) Negative acoustic modes

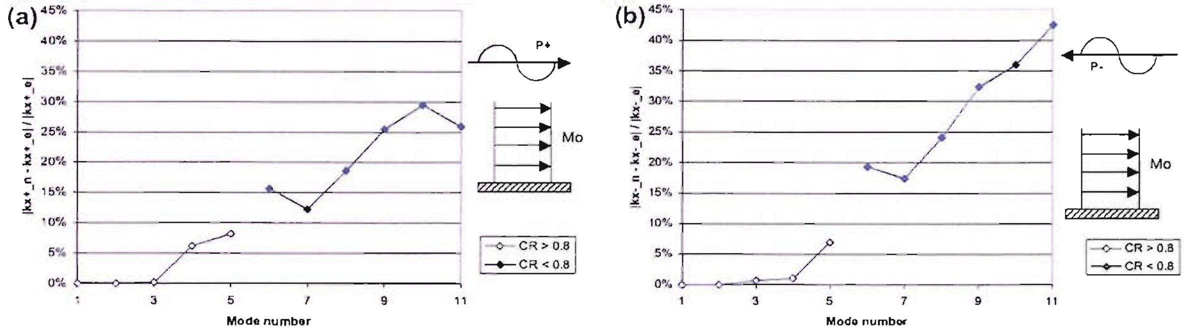

Figure 3.5: Error plotted against mode number for $kh = 10$. $M_o = 0.4$, $Z_b = 2 - 1.14423i$ and $Z_t = \infty + \infty i$. (a) Positive acoustic modes, (b) Negative acoustic modes

duct modes particularly at high frequencies. The same test duct as in Section 3.4.1 is considered here. The duct is only studied for $kh = 20$ with uniform mean of Mach number 0.4.

In Fig. 3.10, the errors between the FE and the exact solutions are plotted against the mode number for different mesh resolutions. The error is calculated using Eq. (3.4). The mode number in the plots is obtained by ordering the modes according to their cut-off ratios in descending order. In the plots, errors of the duct modal wavenumbers having cut-off ratios greater than 0.8 are denoted by unfilled symbols and errors of the duct modal wavenumbers having cut-off ratios less than 0.8 are denoted by filled symbols.

As expected, the FE solutions converge to the exact solutions as the mesh resolution increases. The errors of the duct modes having cut-off ratios greater than 0.8 drop below 6% when the mesh resolution is equal to 8 nodes per wavelength and drop below 4% when the mesh resolution is equal to 10 nodes per wavelength. In general, the error decreases with increasing mesh resolution.

This study has shown that an FE mesh resolution of 8 to 10 nodes per wavelength is found to be adequate to resolve the duct modes of interest in this research.

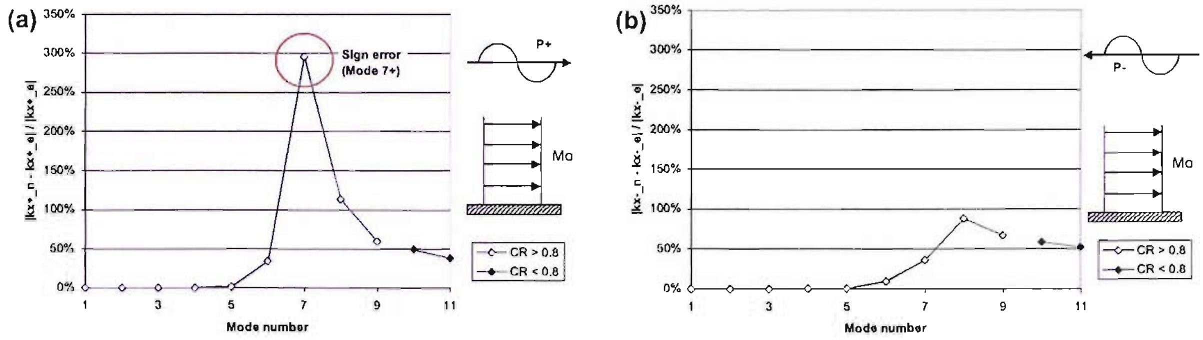

Figure 3.6: Error plotted against mode number for $kh = 20$. $M_o = 0.4$, Z_b=$2+1.25576i$ and Z_t=$\infty + \infty i$. (a) Positive acoustic modes, (b) Negative acoustic modes

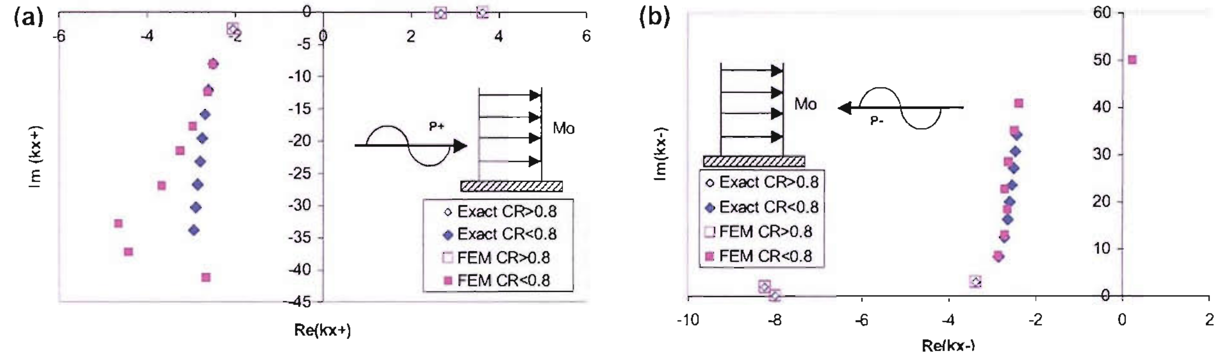

Figure 3.7: Duct axial wavenumbers in the complex plane for $kh = 5$. FE and exact solutions are presented. $M_o = 0.4$, Z_b=$2 - 2.34423i$ and Z_t=$\infty + \infty i$. (a) Positive acoustic modes (b) Negative acoustic modes.

3.4.3 Comparison with Previously Computed Results - Uniform Flow

The FE solutions are compared against the previously computed results for a uniform mean flow of Mach number 0.4 in the negative x direction. This comparison is not intended to validate the current FE eigenvalue model but is to indicate how the resolution required for the current FE eigenvalue model compares to that of previous formulations.

Fig. 3.2(a) shows the duct geometry used in the production of the results. The duct has a lined wall at $y = 0$ and a hard wall at $y = h$. The non-dimensional admittance of the liner is taken to be $A_b = 0.72 + 0.42i$. The duct is studied for $kh = 6$. The duct width is discretized using a uniform mesh of five Lagrangian quadratic line elements.

Table 3.3 presents the duct axial wavenumbers obtained by the exact method, by the MWR with the use of ten basis functions, by the Astley-Eversman FE eigenvalue model and by the current FE eigenvalue model. The previously computed results are taken from a known test case in [12]. In the table, duct modes having cut-off ratios greater than 0.8 are bracketed.

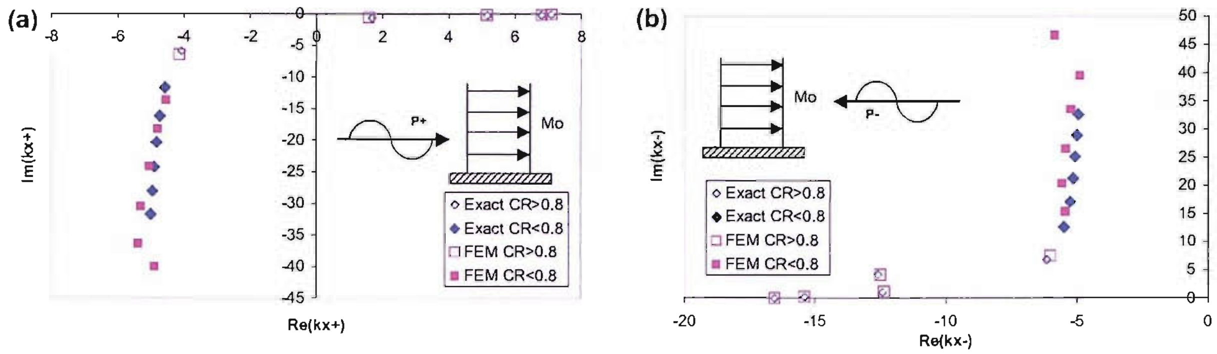

Figure 3.8: Duct axial wavenumbers in the complex plane for $kh = 10$. FE and exact solutions are presented. $M_o = 0.4$, Z_b=2 $-$ 1.14423i and Z_t=$\infty + \infty i$. (a) Positive acoustic modes, (b)Negative acoustic modes.

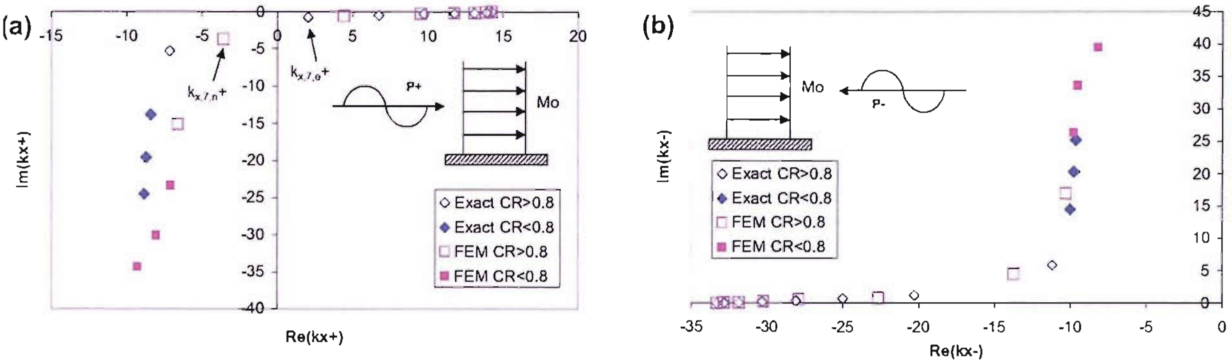

Figure 3.9: Duct axial wavenumbers in the complex plane for $kh = 20$. FE and exact solutions are presented. $M_o = 0.4$, Z_b=2$+$ 1.25576i and Z_t=$\infty + \infty i$. (a) Positive acoustic modes, (b) Negative acoustic modes.

In Fig. 3.11, the errors of the three approximation solutions when compared with the exact solutions are plotted against the mode number. The error is calculated using the error expression in Eq. (3.4). The results show that the accuracy of the current FE eigenvalue model is found to be comparable to the MWR and the Astley-Eversman FE eigenvalue model, and is of good agreement with the exact solutions.

The results also show that the number of accurately predicted duct modes by the current FE eigenvalue model is about equal to the number of quadratic elements. This agrees with the estimate of accuracy established by Astley and Eversman in [12]. This estimate of accuracy is found equivalent to a mesh resolution of 6 to 7 nodes per wavelength which is close to the 8 to 10 nodes per wavelength established for the current FE eigenvalue model in this research.

The current FE solutions show no occurrence of spurious modes as observed in the Astley-Eversman FE eigenvalue model [12]. Spurious modes are eigen-solutions that do not correspond to any of the physical acoustic modes and their eigenvectors reveal very rapid oscillation. This is supported by the mode shape plots presented in Fig. 3.12. In the figure, the eigenvectors of modes 1+ to 11+ obtained by the current FE eigenvalue

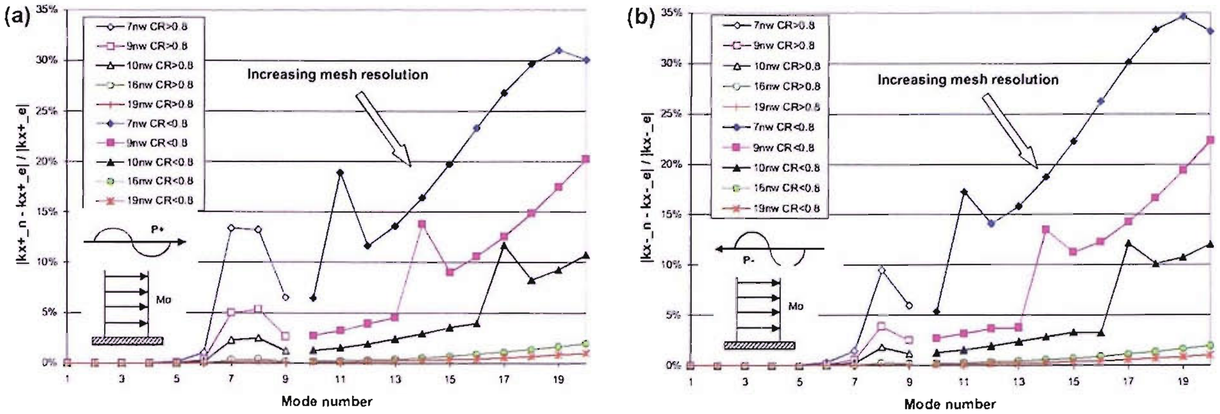

Figure 3.10: Convergence study of the FE eigenvalue model. Error plotted against mode number for different mesh resolutions. $kh=20$, $M_o=0.4$, $Z_b=2+1.25576i$ and $Z_t=\infty+\infty i$. (a) Positive acoustic modes, (b) Negative acoustic modes.

model and by the analytic model are plotted against the width of the duct. Solid lines denote the exact solutions and dotted lines denote the FE solutions. Fig. 3.12 shows a gradual deterioration in the accuracy of the current FE solution as the mode order increases. This illustrates the growing inability of the current mesh to cope with the more complicated mode shapes. Mode 8+ in Fig. 3.13(h) is a surface wave and the mode shape shows the pressure is localised near the lined wall.

The conclusions can be drawn from this study are:

- the accuracy of the FE eigenvalue model proposed in this research is found to be comparable to the MWR and the Astley-Eversman FE eigenvalue model;
- the solutions obtained by the current FE eigenvalue model are found to be of good accuracy with the exact solutions when adequate mesh resolution is used;
- the solutions obtained by the current FE eigenvalue model show no occurrence of spurious modes with no modes repeated and
- an FE mesh resolution of 8 to 10 nodes per wavelength is found to be adequate to resolve accurately the modes of interest in this research. This estimate of accuracy is found to be comparable to those established by Astley and Eversman in their FE eigenvalue model study [12].

In terms of application to general problems, the current FE eigenvalue model has the advantages of representing any duct cross section with non-uniform mean flows and impedance boundaries compared to the analytical method and the MWR.

Mode	Exact	MWR	FEM (Astley-Eversman)	FEM (Current)
1+	$(1.964-0.003i)$	$(1.96-0.004i)$	$(1.964-0.003i)$	$(1.964-0.003i)$
2+	$(1.622-0.051i)$	$(1.62-0.050i)$	$(1.622-0.051i)$	$(1.621-0.051i)$
3+	$(0.979-0.736i)$	$(0.96-0.770i)$	$(0.980-0.738i)$	$(0.983-0.743i)$
4+	$(0.831-1.500i)$	$(0.82-1.550i)$	$(0.831-1.507i)$	$(0.835-1.521i)$
5+	$(0.753-2.219i)$	$(0.75-2.280i)$	$(0.741-2.181i)$	$(0.753-2.274i)$
6+	$0.715-2.901i$	$(0.70-2.970i)$	$(\ddagger 0.679-2.368i)$	$0.692-3.250i$
7+	$0.691-3.560i$	$0.68-3.660i$	$0.714-2.908i$	$0.680-4.106i$
8+	$-5.918-4.078i$	$-1.51-5.390i$	$-4.588-4.912i$	$-4.607-5.118i$
9+	$0.675-4.206i$	$0.66-4.340i$	$0.681-3.515i$	$0.656-5.161i$
10+	$0.663-4.844i$	$0.65-5.030i$	$0.674-3.633i$	$0.646-6.316i$
11+	$0.654-5.476i$		$0.667-5.617i$	$0.662-7.199i$
1−	$(-0.655+0.045i)$	$(-0.66+0.050i)$	$(-0.655+0.045i)$	$(-0.655+0.045i)$
2−	$(-0.592+0.074i)$	$(-0.59+0.060i)$	$(-0.592+0.074i)$	$(-0.592+0.074i)$
3−	$(-0.112+0.152i)$	$(-0.11+0.150i)$	$(-0.111+0.152i)$	$(-0.110+0.153i)$
4−	$(0.609+0.973i)$	$(0.60+0.990i)$	$(0.609+0.979i)$	$(0.610+0.990i)$
5−	$(0.685+1.820i)$	$(0.67+1.840i)$	$(0.684+1.824i)$	$(0.690+1.871i)$
6−	$(0.719+2.526i)$	$(0.69+2.550i)$	$(0.754+2.232i)$	$(0.780+2.698i)$
7−	$0.744+3.183i$	$0.70+3.220i$	$(\ddagger 0.672+2.331i)$	$0.752+3.438i$
8−	$0.762+3.815i$	$0.70+3.870i$	$(0.718+2.550i)$	$0.786+4.340i$
9−	$0.775+4.433i$	$0.70+4.510i$	$0.674+3.591i$	$0.786+5.354i$
10−	$0.782+5.042i$	$0.69+5.150i$	$0.963+3.897i$	$0.742+6.423i$
11−	$0.784+5.647i$		$0.667+5.617i$	$0.679+7.215i$

( ) - mode with cut-off ratio, $\eta > 0.8$

$\ddagger$ - spurious mode

Table 3.3: Duct axial wavenumbers obtained by the exact method, by the MWR, by the Astley-Eversman FE eigenvalue model and by the current FE eigenvalue model for an acoustically lined duct. $M_o = -0.5$, $kh = 6$, $A_b = 0.72 + 0.42i$ and $A_t = 0 + 0i$

3.4.4 Surface Waves - Uniform Flow

This work investigates the capability of the current FE eigenvalue model to resolve the correct number of surface waves of different types. It is carried out by applying different acoustic impedances at the lined walls at the bottom ($y = 0$) and top ($y = h$) of the duct. Fig. 3.2(a) shows the duct geometry used in the production of the results. The duct is studied for $kh = 18$ with uniform mean flow at $M_o = 0.5$. Table 3.4 outlines three configurations with different acoustic impedances at the top and bottom of the duct along with the different types of surface waves expected according to the location of the impedance in the complex impedance plane [5]. The duct width is discretized using a uniform mesh of 30 quadratic Lagrangian line elements for which the mesh resolution is calculated to be 10 nodes per wavelength.

Table 3.5 presents the axial and transverse wavenumbers of the surface waves computed by the FE eigenvalue model and by an integration scheme [79]. The results show that both methods predict the correct number of surface waves of different types expected. Configuration 1 results show the existence of eight surface modes; two hydrodynamic instability modes (H_I), two hydrodynamic stable modes (H_S), two right propagating surface modes (S_R) and two left propagating surface modes (S_L). Configuration 2 results show the existence of six

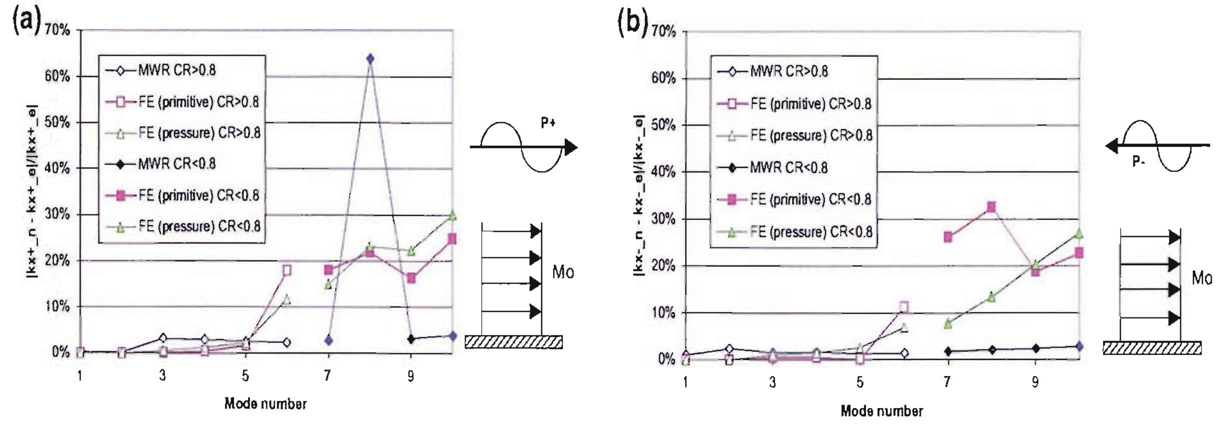

Figure 3.11: Comparison of FE solutions with previously computed results. Error plotted against mode number for uniform mean flow of Mach number 0.4 in the positive x direction. $kh = 6, A_b = 0.72+0.42i$ and $A_t = 0+0i$. (a)Positive acoustic modes (b)Negative acoustic modes

surface waves; two H_I, two S_R, one S_I and one H_S. Configuration 3 results show the existence of one S_I, one S_R, one H_I and one H_S.

For all three cases, general good agreement is observed between the FE and the exact solutions except the HI mode because of insufficient mesh resolution to resolve the localized pressure field at the lined walls. This has been verified by the results obtained using a finer mesh.

Fig. 3.13 presents the eigenvectors of the eight surface waves of Configuration 1 plotted against the width of the duct. The eigenvectors have been normalized to the maximum absolute pressure. The eigenvector plots show that the pressure field of the surface wave is localized near to the lined walls especially the HI mode. This suggests that a finer mesh is required near to the lined walls in order to model the localized pressure accurately and effectively.

Although the problem studied is symmetric, the eigenvector plots presented in Fig. 3.13 show that the surface waves with an identical axial wavenumber show asymmetry in the mode shapes. No further investigation is carried out at the time of the research, but it has been suggested as future research, to gain a better understanding of the characteristics of the surface waves.

The results presented in Table 3.5 also show that the axial wavenumbers of the surface waves computed in the three configurations are very close to each other when an identical impedance is used. This might suggest that the propagation characteristics of the surface waves are very acoustic impedance dependent. This can be expected as most of the acoustic energy of the surface wave is localised near to the lined walls. This also means that the surface waves will influence only the sound field near the lined walls and have small influence on the sound field away from the walls.

The FE eigenvalue model developed in this study has been shown to be capable of resolving the surface

	Specific impedance	S_L	S_R	H_l	H_S	Region in complex Z-plane
Configuration 1	Top: $0.1-3.0i$	√	√	√	√	V
	Bottom: $0.1-3.0i$	√	√	√	√	V
Configuration 2	Top: $0.1-3.0i$	√	√	√	√	V
	Bottom: $0.1-1.0i$	-	√	√	-	III
Configuration 3	Top: $0.1-3.0i$	√	√	√	√	V
	Bottom: $0.1+3.0i$	-	-	-	-	I

Table 3.4: Non-dimensional acoustic impedance at the top and bottom of the duct and the location of the impedance in the complex impedance plane according to Rienstra [6]. $M_o = 0.5$ and $kh = 18$.

waves of different types if sufficient mesh resolution is used. The propagation characteristics of the surface waves are found to be very acoustic impedance dependent.

3.5 Sheared Flow Results

This section presents results for shear flow in the duct. Section 3.5.1 examines the accuracy of the FE eigenvalue model by comparing the FE solutions with the exact or reference solutions. Section 3.5.2 presents results of a convergence study of the FE eigenvalue model. In Section 3.5.3, the effect of mesh uniformity to the accuracy of the FE solution is investigated. Section 3.5.5 presents results of a comparison of the FE solutions with previously computed results.

Due to limited results available for validation especially at high frequencies, an approach adopted in this study is to use converged FE solutions computed using a high resolution mesh such as 100 quadratic Lagrangian elements as the reference solutions. This should be a reasonable approximation to the exact solutions at least for the low order modes e.g. modes having cut-off ratios greater than 0.8. The hydrodynamic modes are omitted in the results because they are almost pressureless and their contribution to the acoustic field is insignificant [83].

3.5.1 Assessment of Accuracy of the FE Solutions for a Fixed Mesh - Sheared Flow

This work examines the accuracy of the FE eigenvalue model for determination of duct eigen-modes in sheared flow. Fig. 3.3(a) shows the test duct used in the production of the results. It has a soft wall at $y = 0$ and a hard wall at $y = h$. The non-dimensional acoustic admittance at the lined wall is taken to be $1.14 - 0.55i$ and $0.07 - 0.18i$ respectively. The duct is studied for $kh = 1.1$ and 10. For the low frequency case of $kh = 1.1$, a constant gradient boundary layer is considered - see Fig. 3.14(a). This flow profile corresponds to a known test case in [93, 12]. For the high frequency case of $kh = 10$, a more realistic flow profile in a turbofan aero-engine

Mode	Exact method		FEM	
	k_x	κ	k_x	κ
Configuration 1, A_t=0.1-3.0i, A_b=0.1-3.0i, 0.5 Mach number				
SR_1	$25.545-0.033i$	$0.277+4.495i$	$25.545-0.033i$	$0.277+4.495i$
SR_2	$25.762-0.024i$	$0.152+6.063i$	$25.762-0.024i$	$0.152+6.063i$
SL_1	$-129.687+61.453i$	$58.265+82.589i$	$-130.083+62.801i$	$59.443+83.043i$
SL_2	$-129.687+61.453i$	$58.265+82.589i$	$-130.083+62.801i$	$59.443+83.043i$
HI_1	$551.813+13.573i$	$11.800-497.857i$	$860.265+55.709i$	$48.324-765.658i$
HI_2	$551.813+13.573i$	$11.800-497.857i$	$860.265+55.709i$	$48.324-765.658i$
HS_1	$-144.445-75.000i$	$69.395+96.592i$	$-144.514-78.159i$	$72.188+96.823i$
HS_2	$-144.445-75.000i$	$69.395+96.592i$	$-144.514-78.159i$	$72.188+96.823i$
Configuration 2, A_t=0.1-3.0i, A_b=0.1-1.0i, 0.5 Mach number				
SR_1	$25.667-0.028i$	$0.198+5.433i$	$25.667-0.028i$	$0.198+5.433i$
SR_2	$28.110-0.449i$	$1.207+14.898i$	$28.110-0.449i$	$1.207+14.897i$
SL_1	$-129.687+61.452i$	$58.265+82.589i$	$-130.083+62.801i$	$59.443+83.043i$
HI_1	$272.104+14.850i$	$13.050-253.802i$	$284.528+17.879i$	$15.693-264.717i$
HI_2	$551.813+13.573i$	$11.800-497.857i$	$860.265+55.709i$	$48.324-765.658i$
HS_1	$-144.446-75.000i$	$69.395-96.592i$	$-144.514-78.159i$	$72.188-96.823i$
Configuration 3, A_t=0.1-3.0i, A_b=0.1+3.0i, 0.5 Mach number				
SR_1	$25.680-0.026i$	$0.180+5.523i$	$25.680-0.026i$	$0.180+5.523i$
SL_1	$-129.687+61.452i$	$58.265-82.590i$	$-130.083+62.801i$	$59.443-83.043i$
HI_1	$551.813+13.573i$	$11.800-497.857i$	$860.265+55.709i$	$48.324-765.658i$
HS_1	$-144.446-75.000i$	$69.359-96.592i$	$-144.514-78.159i$	$72.188-96.823i$

Table 3.5: Exact and FE computed duct axial and transverse wavenumbers of the surface waves.

is considered - see Fig. 3.14(b). The thickness of the boundary layer is $\delta/h = 0.2$. The remaining flow is uniform at $M_o = 0.3$. For both frequencies, a uniform mesh of 5 quadratic line elements is used to discretize the duct width. For these results, the error of the FE solutions when compared to the exact or reference solutions is computed using the error expression in Eq. (3.4).

In Table 3.6, the axial wavenumbers of the first nine positive and negative acoustic modes for $kh = 1.1$ and 10 are listed. For comparison, the exact solutions are obtained using an integration scheme [93] and the reference solutions are FE solutions computed using a uniform mesh of 100 quadratic Lagrangian elements - see Table 3.6. The modes are arranged based on the mode cut-off ratios in descending order and those having cut-off ratios greater than 0.8 are bracketed. The mode cut-off ratio is calculated using the expression in Eq. (3.1) with the maximum shear flow value.

In Figs. 3.15 and 3.16, plots of error versus mode number for $kh = 1.1$ and 10 are presented. The mode number is obtained by ordering the modes according their cut-off ratios in descending order. In the plots, duct modes having cut-off ratios greater than 0.8 are denoted by unfilled symbols and those having cut-off ratios less than 0.8 are denoted by filled symbols.

At the low frequency of $kh = 1.1$, all the duct modes having cut-off ratios greater than 0.8 show good agreement with the exact solutions with less than 5% error. For $kh = 10$, only half the duct modes having cut-

Mode	Exact	FEM	Reference	FEM
	kh=1.1, $A_b = 1.14 - 0.5447i, A_t = 0 + 0i$		kh=10, $A_b = 0.0734 - 0.177i, A_t = 0 + 0i$	
1+	$(0.6673 - 0.3610i)$	$(0.6673 - 0.3611i)$	$(0.7684 - 0.0001i)$	$(0.7684 - 0.0001i)$
2+	$0.1678 - 2.9181i$	$0.1678 - 2.9180i$	$(0.7516 - 0.0001i)$	$(0.7516 - 0.0001i)$
3+	$0.0165 - 5.8060i$	$0.0158 - 5.8066i$	$(0.7040 - 0.0003i)$	$(0.7039 - 0.0003i)$
4+	$-0.0379 - 8.7080i$	$-0.0437 - 8.7109i$	$(0.6214 - 0.0004i)$	$(0.6210 - 0.0004i)$
5+	$-0.0701 - 11.608i$	$-0.0827 - 11.627i$	$(0.4956 - 0.0007i)$	$(0.4938 - 0.0007i)$
6+	$-0.0906 - 14.542i$	$-0.1197 - 14.565i$	$(0.3020 - 0.0012i)$	$(0.2945 - 0.0013i)$
7+	$-0.1058 - 17.487i$	$-0.1598 - 17.542i$	$(-0.2888 - 0.5886i)$	$(-0.2887 - 0.6320i)$
8+	$-0.1159 - 20.459i$	$-0.1179 - 20.579i$	$(-0.2887 - 0.8803i)$	$(-0.2848 - 0.9388i)$
9+	$-0.1177 - 23.452i$	$-0.2242 - 23.711i$	$(-0.2905 - 1.1204i)$	$(-0.2676 - 1.1797i)$
1−	$(-0.8107 + 0.5024i)$	$(-0.8105 + 0.5022i)$	$(-1.4247 + 0.0000i)$	$(-1.4247 + 0.0000i)$
2−	$-0.4795 + 3.0143i$	$-0.4796 + 3.0143i$	$(-1.3930 + 0.0000i)$	$(-1.3930 + 0.0000i)$
3−	$-0.3379 + 5.8343i$	$-0.3387 + 5.8348i$	$(-1.3282 + 0.0000i)$	$(-1.3281 + 0.0000i)$
4−	$-0.2796 + 8.7209i$	$-0.2837 + 8.7232i$	$(-1.2274 + 0.0000i)$	$(-1.2269 + 0.0000i)$
5−	$-0.2513 + 11.625i$	$-0.2639 + 11.633i$	$(-1.0860 + 0.0002i)$	$(-1.0837 + 0.0002i)$
6−	$-0.2366 + 14.547i$	$-0.2652 + 14.569i$	$(-0.8854 + 0.0007i)$	$(-0.8776 + 0.0007i)$
7−	$-0.2285 + 17.491i$	$-0.2808 + 17.544i$	$(-0.4676 + 0.0045i)$	$(-0.3808 + 0.0010i)$
8−	$-0.2221 + 20.461i$	$-0.2989 + 20.581i$	$(-0.2929 + 0.5880i)$	$(-0.2930 + 0.6311i)$
9−	$-0.2111 + 23.454i$	$-0.3058 + 23.716i$	$(-0.2940 + 1.1200i)$	$(-0.2742 + 1.1807i)$

() - mode with cut-off ratio, $\eta > 0.8$

Table 3.6: Duct axial wavenumbers for a soft-walled duct containing sheared flows. Exact, reference and FE solutions.

off ratios greater than 0.8 show less than 5% error with the reference solutions. The error is due to inadequate mesh resolution.

In Figs. 3.17 and 3.18, plots show the location of the duct axial wavenumbers in the complex plane for $kh = 1.1$ and 10 are presented. Duct modes having cut-off ratios greater than 0.8 are denoted by unfilled symbols and duct modes having cut-off ratios less than 0.8 are denoted by filled symbols. Figs. 3.17 and 3.18 show reasonably good agreement between the two solutions especially for acoustic modes having cut-off ratios greater than 0.8. For modes having cut-off ratios less than 0.8, the FE solutions start to deviate significantly from the exact or reference solutions as the mode number increases, which is consistent with the results presented in Figs. 3.15 and 3.16. This illustrates the growing inability of the current mesh to cope with the more complicated mode shapes at high frequencies.

The results presented in this section have shown that the FE eigenvalue model is capable for determination of duct eigen-modes in sheared flow with impedance boundaries if an adequate mesh resolution is used.

3.5.2 Convergence of the FE Solutions - Sheared Flow

In this section, results that demonstrate the convergence of the FE solutions to the exact solutions are presented. This study aims to determine the FE mesh resolution required to obtain solutions for a given number of duct modes particularly at high frequencies. The same test duct as in Section 3.5.1 is considered here. The duct is studied for $kh = 20$ and the non-dimensional acoustic impedance at the lined wall is taken to be $Z_b = 2.00 + 5.80i$. In the duct, a sheared flow with a boundary layer of thickness $\delta/h = 0.2$ as shown in Fig. 3.14(b) is considered.

Fig. 3.19 presents the errors between the FE and the reference solutions. These are plotted against the mode number for different mesh resolutions. The error is calculated using the error expression in Eq. (3.4). Fig. 3.19 shows that the error decreases with increasing mesh resolution. The errors of the modes having cut-off ratios greater than 0.8 drop below 5% when the mesh resolution is 8 nodes per wavelength. The error drops below 2% when the mesh resolution is 10 nodes per wavelength.

This study has concluded that for sheared flow in the duct, an FE mesh resolution of 8 to 10 nodes per wavelength is found to be adequate to resolve the duct modes (cut-off ratio greater than 0.7) of interest in this research. This convergence criteria are similar to those established in the uniform flow problems in Section 3.4.2.

3.5.3 FE Mesh Uniformity

This study examines the effect of mesh uniformity on the accuracy of the FE solution. An acoustically lined duct containing a sheared flow with a boundary layer of thickness $\delta/h = 0.2$ as shown in Fig. 3.14(b) is considered. The remaining flow is uniform at $M_o = 0.3$. The duct is studied for $kh = 20$ and the acoustic impedance at the lined wall is taken to be $Z_b = 2.0 + 5.804i$.

The duct width is discretized using uniform and non-uniform meshes of different mesh resolutions as shown in Fig. 3.20. The nonuniform mesh has more elements at the boundary layer aiming to resolve the sound field at the boundary layer more accurately and effectively. The FE solutions obtained using different meshes are then compared with the reference solutions and the errors between the two solutions are computed using Eq. (3.4). Fig. 3.21 presents plots of error versus mode number for the different meshes. The results show that the uniform meshes yield solutions with better accuracy than those obtained using non-uniform meshes. Uniform mesh is therefore used in all the analysis carried out in this study.

3.5.4 Effect of Shear Flow on the Propagation and Attenuation of Acoustic Modes In Ducts

In this study, the effect of the boundary layer on sound attenuation in the duct is investigated. A duct containing a sheared flow with a boundary layer of thickness $\delta/h = 0.2$ and uniform flow at $M_o = 0.5$ is considered. The duct is studied for $kh = 10$. The duct has a soft wall at $y = 0$ whose impedance is $Z_b = 2.00 + 5.80i$ and a hard wall at $y = h$.

In Table 3.7, the duct axial wavenumbers of the uniform flow case and of the sheared flow case are pre-

	Positive acoustic mode			Negative acoustic mode	
Mode	Uniform flow	Shear flow		Uniform flow	Shear flow
1+	$7.653 - 0.011i$	$7.749 - 0.033i$	1−	$-14.205 + 0.012i$	$-14.157 + 0.001i$
2+	$7.079 - 0.041i$	$7.237 - 0.044i$	2−	$-13.495 + 0.074i$	$-13.134 + 0.019i$
3+	$5.346 - 0.062i$	$5.437 - 0.066i$	3−	$-11.711 + 0.132i$	$-11.134 + 0.091i$
4+	$1.130 - 0.167i$	$1.158 - 0.173i$	4−	$-7.480 + 0.254i$	$-7.082 + 0.235i$
5+	$-3.052 - 7.520i$	$-2.945 - 7.520i$	5−	$-3.291 + 7.617i$	$-3.156 + 7.569i$
6+	$-3.101 - 12.387i$	$-3.012 - 12.364i$	6−	$-3.239 + 12.487i$	$-3.138 + 12.404i$
7+	$-3.122 - 16.497i$	$-3.067 - 16.435i$	7−	$-3.217 + 16.600i$	$-3.162 + 16.471i$
8+	$-3.135 - 20.318i$	$-3.134 - 20.217i$	8−	$-3.203 + 20.423i$	$-3.209 + 20.247i$
9+	$-3.144 - 23.995i$	$-3.172 - 23.887i$	9−	$-3.192 + 24.101i$	$-3.234 + 23.910i$
10+	$-3.152 - 27.591i$	$-3.181 - 27.499i$	10−	$-3.183 + 27.698i$	$-3.235 + 27.519i$
11+	$-3.158 - 31.144i$	$-3.199 - 31.052i$	11−	$-3.176 + 31.251i$	$-3.248 + 31.071i$
12+	$-3.164 - 34.676i$	$-3.244 - 34.558i$	12−	$-3.169 + 34.785i$	$-3.288 + 34.576i$
13+	$-3.168 - 38.206i$	$-3.291 - 38.063i$	13−	$-3.164 + 38.315i$	$-3.331 + 38.079i$
14+	$-3.173 - 41.746i$	$-3.317 - 41.612i$	14−	$-3.158 + 41.856i$	$-3.353 + 41.624i$
15+	$-3.178 - 45.310i$	$-3.330 - 45.204i$	15−	$-3.153 + 45.419i$	$-3.362 + 45.216i$
16+	$-3.182 - 48.905i$	$-3.350 - 48.821i$	16−	$-3.150 + 49.014i$	$-3.379 + 48.832i$
17+	$-3.188 - 52.538i$	$-3.379 - 52.463i$	17−	$-3.148 + 52.645i$	$-3.405 + 52.474i$
18+	$-3.197 - 56.204i$	$-3.402 - 56.155i$	18−	$-3.151 + 56.306i$	$-3.424 + 56.166i$
19+	$-3.211 - 59.871i$	$-3.410 - 59.879i$	19−	$-3.165 + 59.961i$	$-3.428 + 59.889i$
20+	$-3.244 - 63.357i$	$-3.386 - 63.407i$	20−	$-3.212 + 63.415i$	$-3.396 + 63.414i$

Table 3.7: Duct axial wavenumbers for a lined duct containing a uniform flow and a sheared flow.

sented. In Fig. 3.22, the locations of these axial wavenumbers are plotted in the complex plane. The duct axial wavenumber provides a good understanding of the mode characteristics. The real part of the duct axial wavenumber indicates the axial propagation speed of the mode and the imaginary part of the duct axial wavenumber indicates the axial decay rate of the mode.

Results presented in Fig. 3.22 and Table 3.7 show that in this particular case, the boundary layer does not have significant effect on the sound attenuation in the duct; however, there are still some effects. The duct modes that propagate with the flow show greater drop in axial decay rates than those that propagate against the flow. This is due to the velocity gradient of the boundary layer which refracts the sound that propagates in the direction of the flow into a narrow layer near the lined wall results in greater attenuation - see Fig. 3.23. Similarly, for duct modes that propagate against the flow, the velocity gradient of the boundary layer refracts the sound away from the lined wall and this results in smaller attenuation [85] - see Fig. 3.23.

3.5.5 Comparison with Previously Computed Results - Sheared Flow

Results of a comparison of the FE solutions against previously computed results are presented in this section. Previous results are those computed by Hersh using an integration scheme [85], by Unruh and Eversman [88] using a MWR and by Astley and Eversman [12] using an FEM. This comparison is not intended to validate the current FE eigenvalue model but is to indicate how the resolution required for the current FE eigenvalue model compares to that of previous formulations.

The configuration of the test duct is illustrated in Fig. 3.14(a). The duct is studied for $kh = 1$, 5 and 10 with a linear sheared layer of 20% of the duct width. The remainder of the flow is uniform at $M_o = 0.3$. This test problem is chosen here because it was previously presented as a test problem for the MWR in [93]. The non-dimensional acoustic admittance at the lined wall is taken to be $-0.06+0.27i$, $0.16+0.45$ and $1.39+0.10i$ respectively.

Table 3.8 presents the duct axial wavenumbers obtained by the exact method, by the MWR, by the Astley-Eversman FE eigenvalue model and by the current FE eigenvalue model. The current FE solutions are computed using a uniform mesh of 5 quadratic Lagrangian elements. For each test case, only the first three positive and negative acoustic modes are presented as these are the only results available for comparison. In the table, duct modes having cut-off ratios greater than 0.8 are bracketed.

Figs. 3.24 to 3.26 present the errors of the solutions obtained by the three approximate methods when compared with the exact solutions. Results show that at low frequencies of $kh = 1$ and 5, the current FE eigenvalue model is observed to yield solutions with better accuracy than those of the MWR. At the high frequency of $kh = 10$, the current FE eigenvalue model performed poorer than the MWR and the Astley-Eversman FE eigenvalue model especially for the high order modes. This is due to insufficient mesh resolution to resolve the more complicated mode shape at high frequencies. The current mesh resolution of 6 nodes per wavelength is less than the recommended resolution of 8 to 10 nodes per wavelength.

3.6 Conclusions

In this chapter, the validity of the FE eigenvalue model for computation of duct eigen-solutions in shear and uniform flows has been examined. The accuracy of the FE eigenvalue model has been checked by comparing with the analytical and approximate solutions obtained by other methods. The numerical results for various duct configurations have been presented. These show the validity of the analysis and computer code.

The study has shown that a mesh resolution of 8 to 10 nodes per wavelength is found to be adequate to resolve the duct modes of interest in this research. This mesh resolution is found to be comparable to those established by Astley and Eversman for their FE eigenvalue model [12].

The current FE solutions show no occurrence of spurious modes as observed in the Astley-Eversman FE eigenvalue model. The current FE eigenvalue model is capable of resolving the correct number of surface modes of different types if sufficient mesh resolution is used. Comparison with previously computed results using other methods shows that the accuracy of the current FE eigenvalue model is comparable to the MWR and the Astley-Eversman FE eigenvalue model. It is also of good standard relative to the exact solutions.

The results presented in this chapter have shown that it is worthwhile to extend the FE eigenvalue model to

Mode	Exact	MWR	FEM	FEM
			$(m = 5, n = 11)$	$(m = 5, n = 11)$
		(10 basis functions)	(Astley - Eversman)	(Current)
$kh = 1.0, A_t = -0.0551 + 0.2722i, A_b = 0.0 + 0.0i$				
1+	$(0.8659 - 0.0162i)$	$(0.8656 - 0.0161i)$	$(0.8659 - 0.0161i)$	$(0.8658 - 0.0162i)$
2+	$-0.7256 - 2.6574i$	$-0.7586 - 2.7215i$	$-0.7279 - 2.6564i$	$-0.7554 - 2.6467i$
3+	$-0.6519 - 5.7880i$	$-0.9511 - 5.9204i$	$-0.6470 - 5.7775i$	$-0.7753 - 5.6590i$
1−	$(-1.6090 + 0.0580i)$	$(-1.6111 + 0.0580i)$	$(-1.6087 + 0.0580i)$	$(-1.6081 + 0.0577i)$
2−	$-0.7821 + 2.6943i$	$-0.8177 + 2.7628i$	$-0.7846 + 2.6933i$	$-0.8136 + 2.6810i$
3−	$-0.6736 + 5.7890i$	$-0.9864 + 5.9211i$	$-0.6685 + 5.7781i$	$-0.7947 + 5.6529i$
$kh = 5.0, A_t = 0.1607 + 0.4463i, A_b = 0.0 + 0.0i$				
1+	$(0.6428 - 0.0215i)$	$(0.6448 - 0.0208i)$	$(0.6427 - 0.0215i)$	$(0.6427 - 0.0214i)$
2+	$(0.8553 - 0.0415i)$	$(0.8598 - 0.0428i)$	$(0.8551 - 0.0410i)$	$(0.8550 - 0.0410i)$
3+	$(-0.2853 - 0.5558i)$	$(-0.2858 - 0.5600i)$	$(-0.2854 - 0.5565i)$	$(-0.2863 - 0.5594i)$
1−	$(-1.4200 + 0.0452i)$	$(-1.4193 + 0.0420i)$	$(-1.4198 + 0.0448i)$	$(-1.4194 + 0.0436i)$
2−	$(-1.2946 + 0.0596i)$	$(-1.2903 + 0.0612i)$	$(-1.2945 + 0.0596i)$	$(-1.2931 + 0.0598i)$
3−	$(-0.3995 + 0.5634i)$	$(-0.4011 + 0.5701i)$	$(-0.3996 + 0.5641i)$	$(-0.4006 + 0.5668i)$
$kh = 10.0, A_t = 1.3929 + 0.0997i, A_b = 0.0 + 0.0i$				
1+	$(0.7586 - 0.0038i)$	$(0.7587 - 0.0039i)$	$(0.7586 - 0.0038i)$	$(0.7586 - 0.0038i)$
2+	$(0.6666 - 0.0297i)$	$(0.6665 - 0.0298i)$	$(0.6666 - 0.0298i)$	$(0.6666 - 0.0298i)$
3+	$(0.4295 - 0.0902i)$	$(0.4297 - 0.0901i)$	$(0.4295 - 0.0914i)$	$(0.4283 - 0.0935i)$
1−	$(-1.4140 + 0.0003i)$	$(-1.4142 + 0.0003i)$	$(-1.4140 + 0.0003i)$	$(-1.4140 + 0.0003i)$
2−	$(-1.2929 + 0.0051i)$	$(-1.2932 + 0.0051i)$	$(-1.2929 + 0.0051i)$	$(-1.2928 + 0.0051i)$
3−	$(-1.0132 + 0.0382i)$	$(-1.0138 + 0.0378i)$	$(-1.0124 + 0.0384i)$	$(-1.0100 + 0.0390i)$

( ) - mode with cut-off ratio greater than 0.8

Table 3.8: Duct axial wavenumbers obtained by the exact method, by the MWR, by the Astley-Eversman FE eigenvalue model and by the current FE eigenvalue model for an acoustically lined duct with a sheared flow.

three dimensions to explore its ability to represent ducts of arbitrary cross sections with non-uniform impedance boundaries and mean flow.

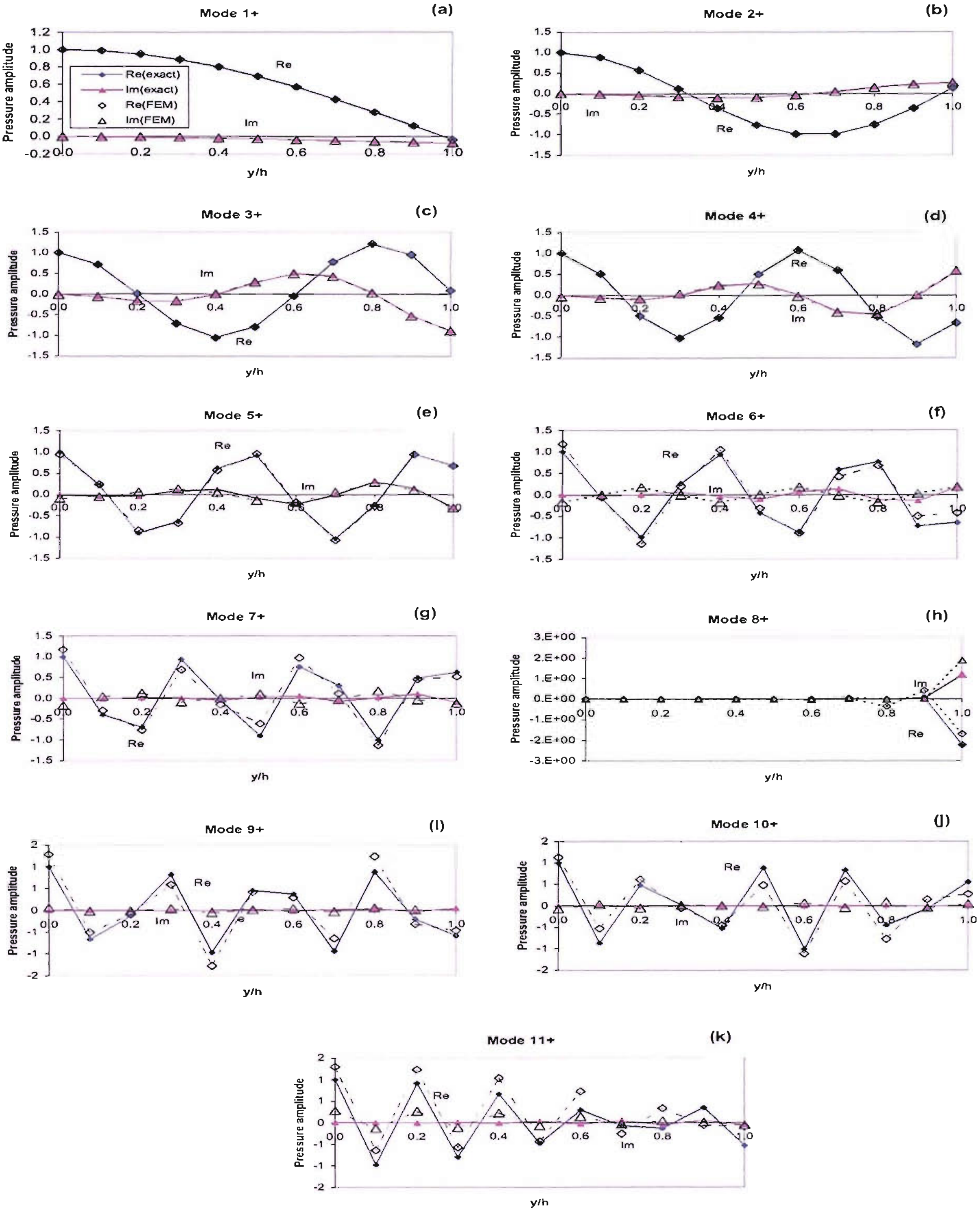

Figure 3.12: Comparison of exact and FE computed eigenvectors of mode 1+ to mode 11+ for a two-dimensional lined duct with uniform mean flow of Mach number 0.4 in the positive x direction. $kh = 6.0$, $A_h = 0.72 + 0.42i$ and $A_t = 0 + 0i$. Duct mode 6+ in (h) is a surface wave. —◇—, Real(FEM), —♦—, Real(Exact), — o —, Imaginary(FEM), — • —, Imaginary(Exact).

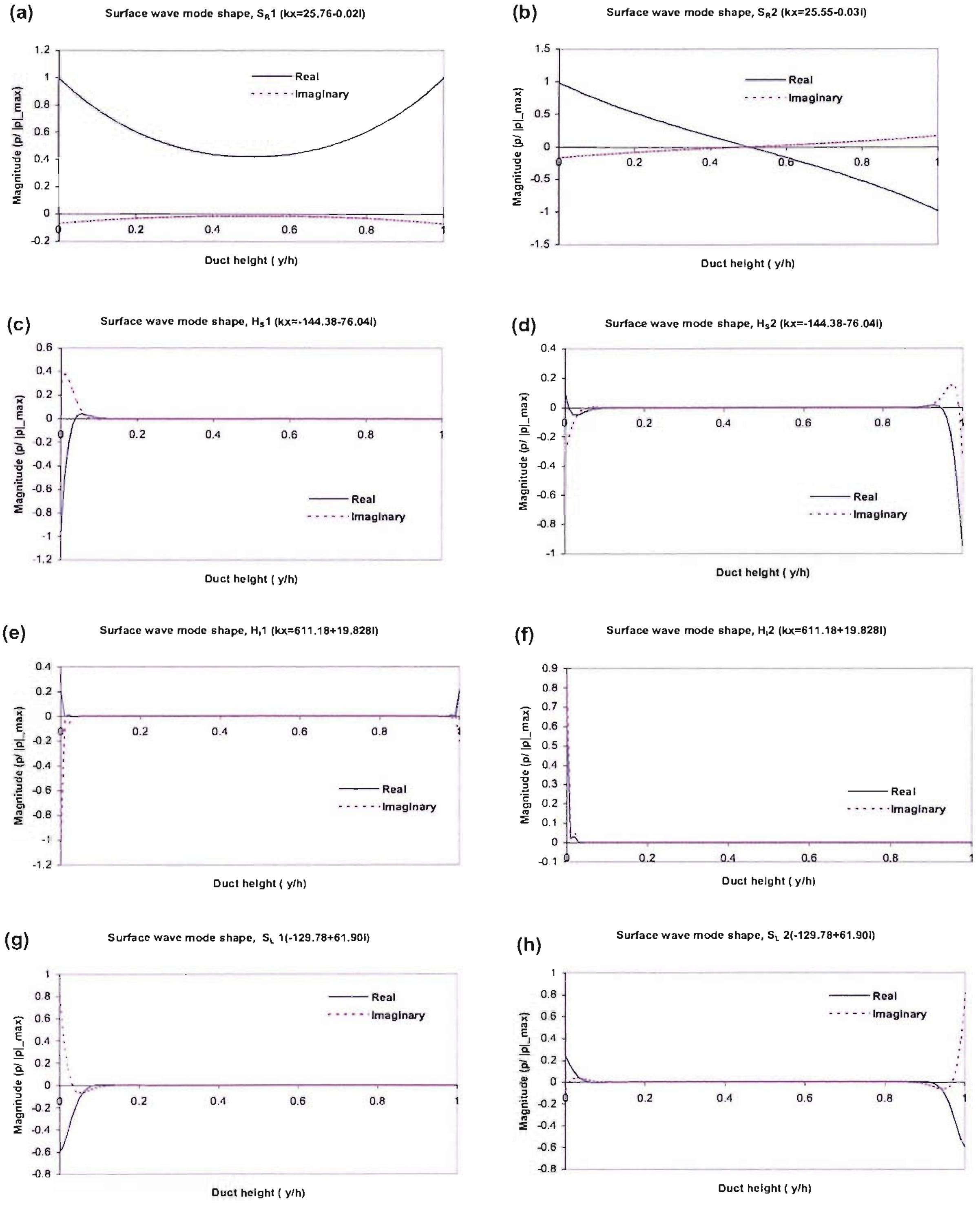

Figure 3.13: Eigenvectors of the surface waves - Configuration 1. $Z_t = 0.1 - 3i$, $Z_b = 0.1 - 3i$, $M_o = 0.5$ and $kh = 36$. The eigenvectors have been normalized to the maximum absolute pressure.

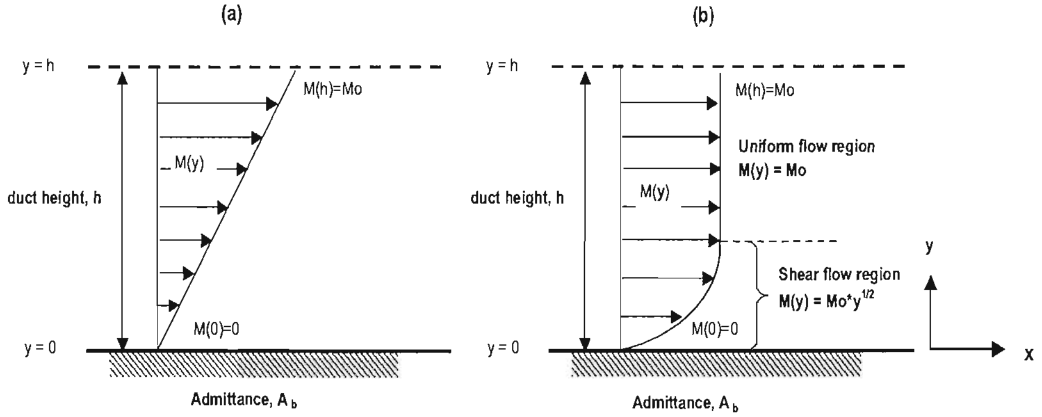

Figure 3.14: (a) A constant gradient boundary layer, (b) A sheared flow with a boundary layer thickness δ.

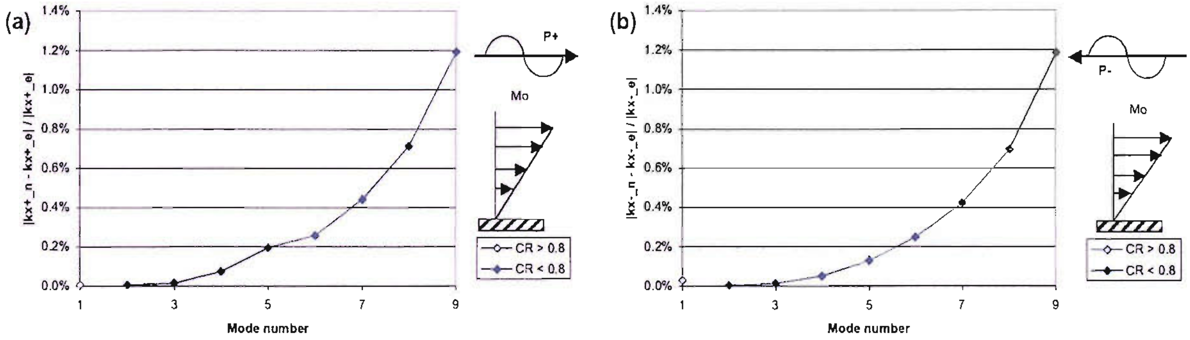

Figure 3.15: Error plotted against mode number for a lined duct containing a sheared flow with a constant gradient boundary layer. $kh = 1.1$, $M_o = 0.3$, A_b=$1.14 - 0.5447i$ and A_t=$0 + 0i$. (a) Positive acoustic modes (b) Negative acoustic modes

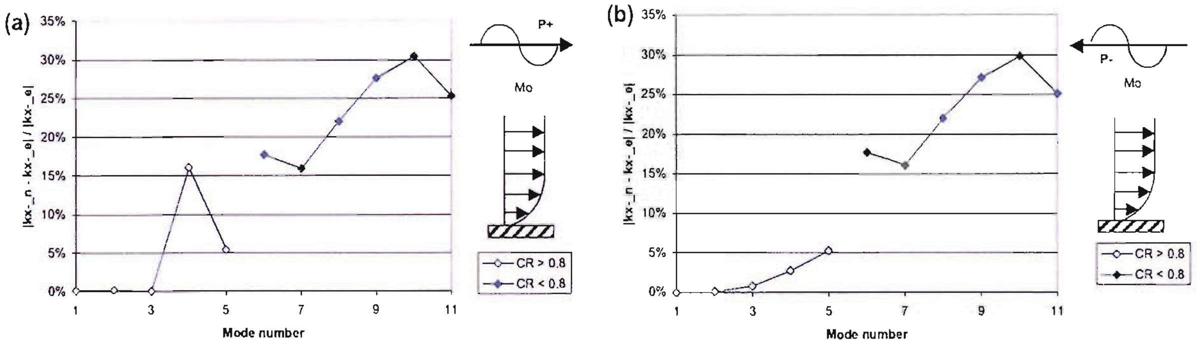

Figure 3.16: Error plotted against mode number for a lined duct containing a sheared flow with a boundary layer of thickness $\delta/h = 0.2$. $kh = 10$, $M_o = 0.3$, A_b=$0.073 - 0.177i$ and A_t=$0 + 0i$. (a) Positive acoustic modes, (b) Negative acoustic modes.

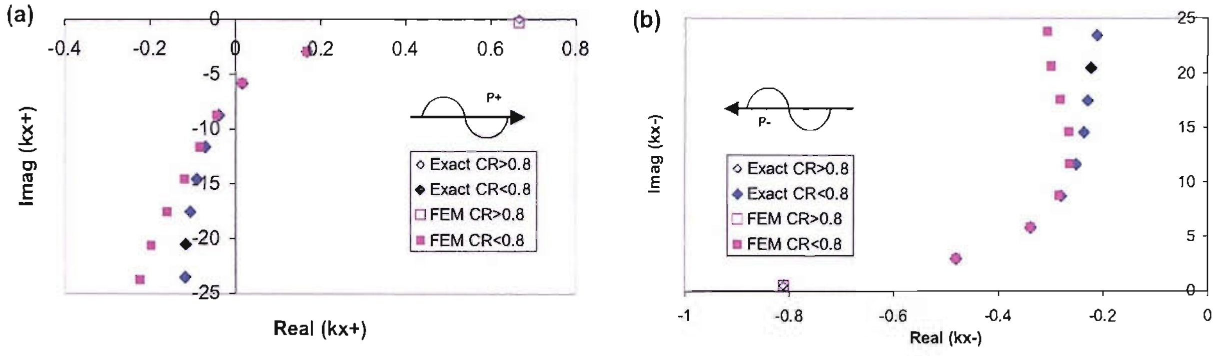

Figure 3.17: Duct axial wavenumbers in the complex plane for a lined duct containing a sheared flow with a constant gradient boundary layer. FE and exact solutions are presented. $kh = 1.1$, $M_o = 0.3$, A_b=$1.14 - 0.5447i$ and A_t=$0 + 0i$. (a) Positive acoustic modes, (b) Negative acoustic modes.

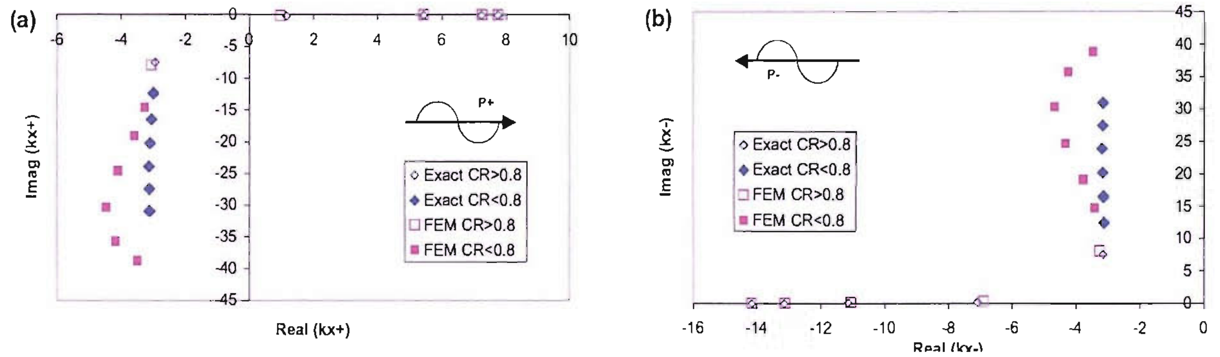

Figure 3.18: Duct axial wavenumbers in the complex plane for a lined duct containing a sheared flow with boundary layer of thickness $\delta/h = 0.2$. $kh = 10$, $M_o = 0.3$, A_b=$0.07 - 0.18i$ and A_t=$0 + 0i$. (a) Positive acoustic modes, (b) Negative acoustic modes.

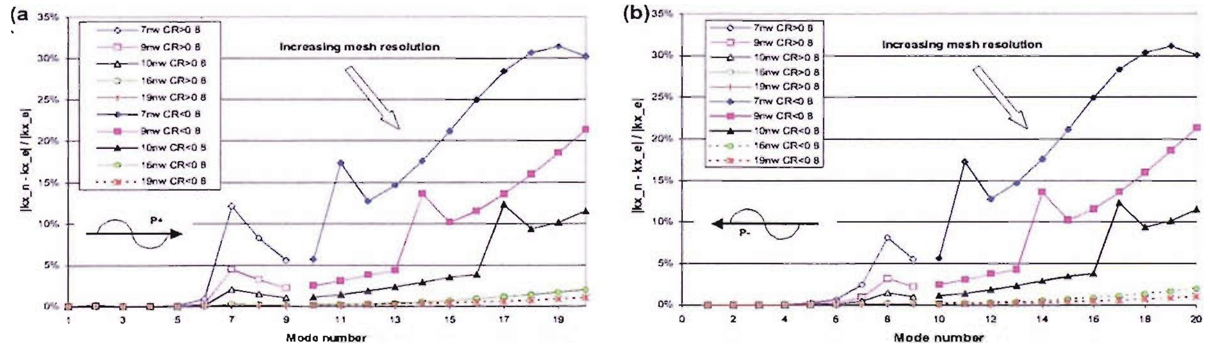

Figure 3.19: Convergence study of the FE solutions. Error plotted against mode number for different FE mesh resolutions. Sheared flow with a boundary layer of thickness $\delta/h = 0.2$. kh =20, $M_o = 0.3$, Z_b=$2.0 + 5.804i$ and Z_t=$\infty + \infty i$. (a) Positive acoustic modes, (b) Negative acoustic modes

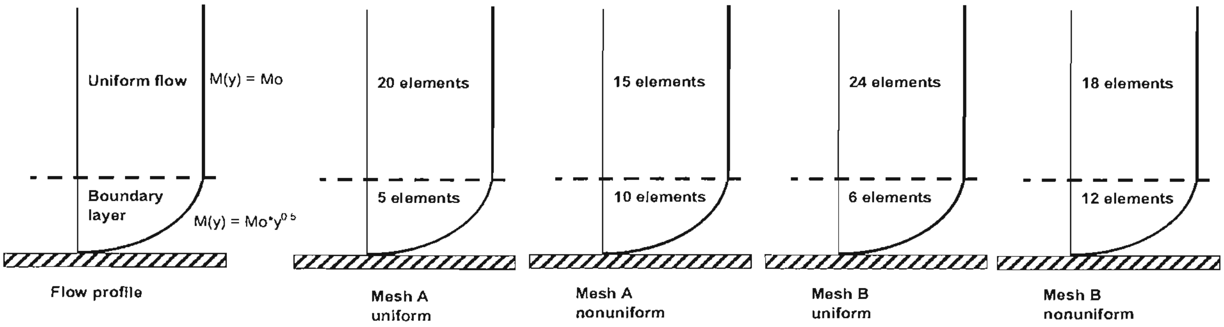

Figure 3.20: Uniform and nonuniform meshes.

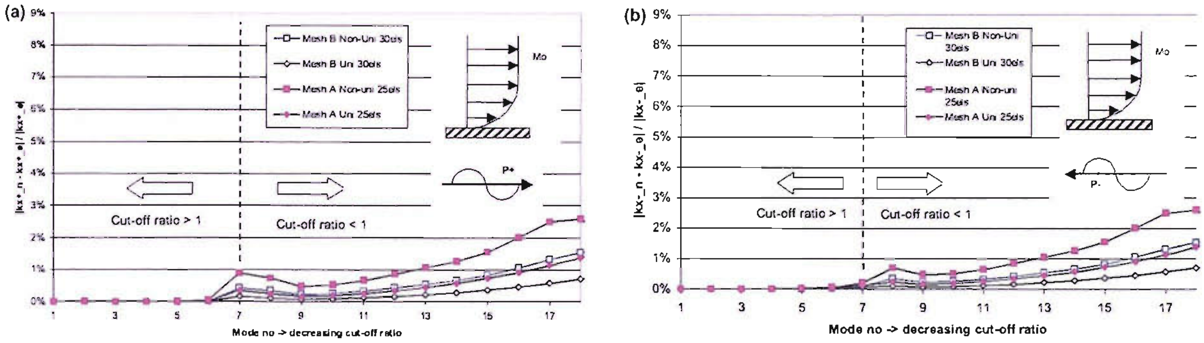

Figure 3.21: Comparison between the FE solutions obtained using uniform and nonuniform meshes. Error plotted against mode number for a lined duct containing a sheared flow with a boundary layer of thickness $\delta/h = 0.2$. $M_o = 0.3$, $kh = 20$, $Z_b = 2 + 5.804i$ and $Z_t = \infty + \infty i$. (a) Positive acoustic modes, (b) Negative acoustic modes

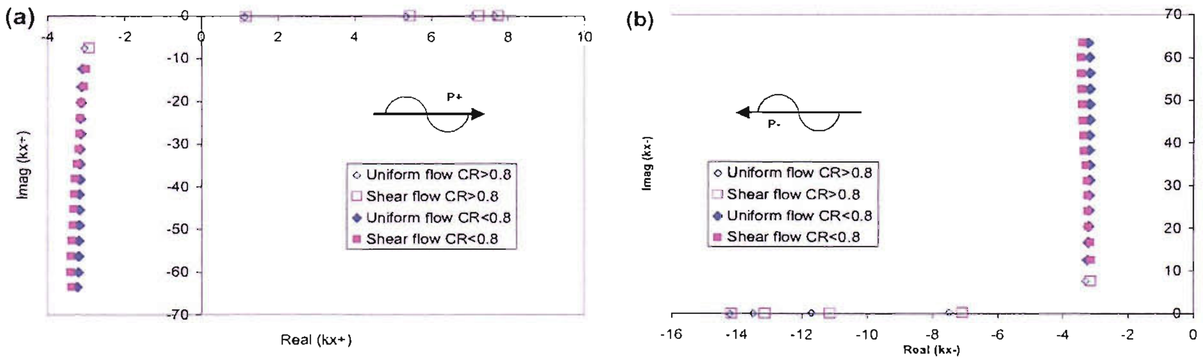

Figure 3.22: Duct axial wavenumbers of an acoustically lined duct containing a uniform flow and a sheared flow in the complex plane. $kh = 10$, $Z_b = 2 + 5.80i$ and $Z_t = \infty + \infty i$ (a)Positive acoustic modes, (b) Negative acoustic modes

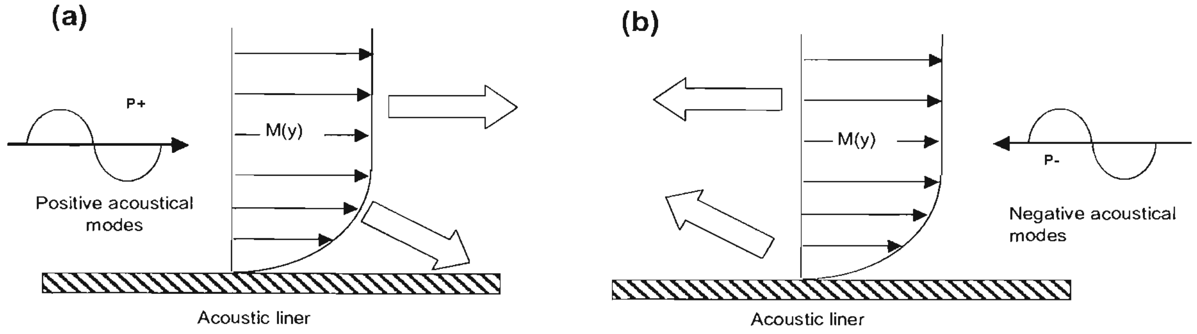

Figure 3.23: (a) Velocity gradient of the boundary layer refracts the sound that propagates with the flow into a narrow layer near the lined wall, (b) Velocity gradient of the boundary layer refracts the sound that propagates against the flow away from the lined wall.

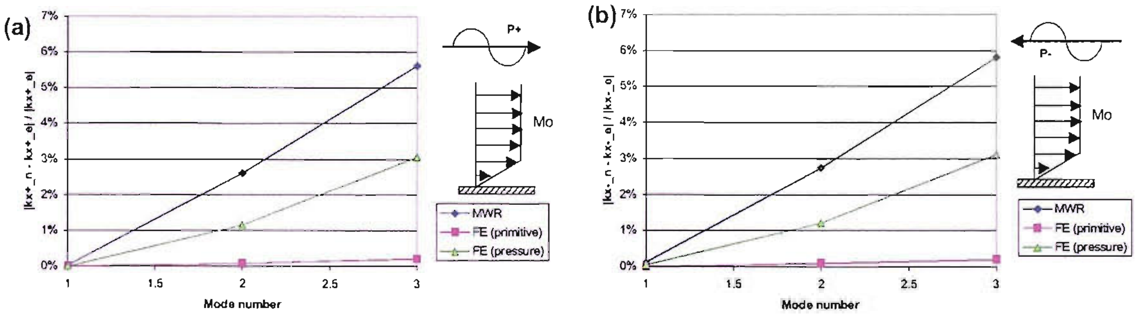

Figure 3.24: Comparison of the current FE solutions with the previously computed results. Errors of the Astley-Eversman FE eigenvalue model, of the current FE eigenvalue model and of the MWR plotted against the mode number for a lined duct containing a sheared flow with a boundary layer thickness $\delta/h = 0.2$. $kh = 1$, $M_o = 0.3$, $A_t = -0.055 + 0.272i$ and $A_b = 0 + 0i$. (a) Positive acoustic modes, (b) Negative acoustic modes.

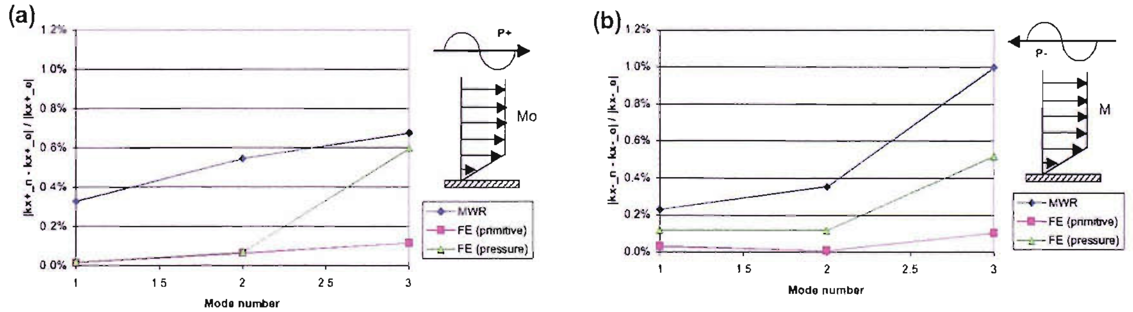

Figure 3.25: Comparison of the current FE solutions with the previously computed results. Errors of the Astley-Eversman FE eigenvalue model, of the current FE eigenvalue model and of the MWR solutions plotted against the mode number for a lined duct containing a sheared flow with a boundary layer thickness $\delta/h = 0.2$. $kh = 5$, $M_o = 0.3$, $A_t = 0.161 + 0.446i$ and $A_b = 0 + 0i$. (a) Positive acoustic modes, (b) Negative acoustic modes.

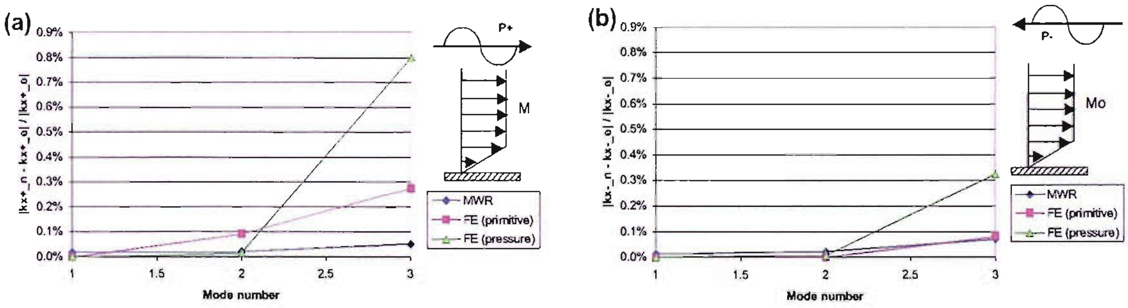

Figure 3.26: Comparison of the current FE solutions with previously computed results. Errors of the Astley-Eversman FE eigenvalue model, of the current FE eigenvalue model and of the MWR plotted against the mode number for a lined duct containing a sheared flow with a boundary layer thickness $\delta/h = 0.2$. $kh = 10$, $M_o = 0.3$, A_t=$1.393 + 0.100i$ and A_b=$0 + 0i$. (a) Positive acoustic modes, (b) Negative acoustic modes.

Chapter 4

Results: Three-Dimensional Eigenvalue Problems - Validation And Application

4.1 Introduction

In this chapter, the validity of the finite element (FE) eigenvalue model for computation of duct eigen-solutions in three-dimensional ducts is assessed. Chapter 3 has shown that the FE eigenvalue model is accurate, robust and efficient for two-dimensional ducts. In this chapter, the accuracy of the FE eigenvalue model is examined by comparing with those obtained analytically using an integration method [79, 80].

Due to the large problem size for the three-dimensional problems, the use of a direct eigenvalue routine as in Chapter 3 will require a large amount of computing resources and time. To circumvent this problem, an iterative eigenvalue routine, ARPACK is employed to compute the eigen-solutions. ARPACK is a collection of Fortran77 subroutines designed to solve large scale eigenvalue problems [97, 98]. The number of eigenvalues computed is user specified with features such as those of the largest real part, largest imaginary part or largest absolute. Generally the number of eigenvalues computed is many fewer than the size of the eigen-matrix. This is an advantage here because only a number of the duct modes e.g. duct modes having cut-off ratios greater than 0.8 are of interest in this research. ARPACK also computes the eigenvectors on request. The program is also capable for parallel computing to speed up the computation time but this is not implemented in this study.

ARPACK is based upon an algorithmic variant of the Arnoldi process called the Implicitly Restarted Arnoldi Method (IRAM). When the eigen matrix is symmetric, the method reduces to a variant of the Lanczos process called the Implicitly Restarted Lanczos Method (IRLM). These variants may be viewed as a synthesis of the Arnoldi/Lanczos process with the Implicitly Shifted QR technique that is suitable for large scale problems. More details about ARPACK can be found in [97, 98].

The aspects that have been specifically considered in this study are:

- to examine the accuracy of the FE solution by comparison with the analytical solution. The FE solutions should correspond to the exact solutions which should include hydrodynamic modes, acoustic modes and surface modes;

- to asses the convergence of the FE eigenvalue model. This aims to determine the FE mesh resolution required to obtain accurate solutions for a given number of modes, particularly at high frequencies;
- to assess the performance of ARPACK compared to a direct eigenvalue routine in terms of computation time and storage requirement; and
- to demonstrate the feasibility of the FE eigenvalue model for large scale three-dimensional problems particularly at high frequencies.

For simplicity and validation purposes, only uniform mean flow is considered in this study. The uniform flow problem is smaller in terms of problem size compared to the non-uniform flow problems. Hence less computation time and resources are required to solve the problems. The FE eigenvalue model is capable of considering ducts of any arbitrary cross-section with non-uniform flow and impedance boundaries.

4.1.1 Outline

In Section 4.2, the problem specification is put forward, including the test problems that have been used and details of the numerical models. Section 4.2.2 describes the different types of duct modes present in a duct along with the identification of these modes from the eigen-solutions. Section 4.3.2 presents results of an investigation of the performance of different FE meshes to the accuracy of the FE solution. Results of an assessment of accuracy of the FE eigenvalue model are presented in Section 4.3.3. In Section 4.3.4, results of a convergence study of the FE model are presented. In Section 4.4, results of a modal study of a cylindrical duct containing spliced liners of varying widths are presented. Section 4.5 presents results of a performance study of a direct routine and an iterative routine. Finally, in Section 4.6 the conclusions of the study are presented.

4.2 Problem Specification

The results have been produced for the particular test cases of an infinitely long rectangular duct and an infinitely long circular duct as shown in Fig. 4.1. The width and height of the rectangular duct are defined by d and h respectively. The duct walls at $y = 0$ and h are lined with a locally reacting acoustic lining whose acoustic impedance is defined by Z_b and Z_t respectively. The radius of the cylindrical duct is denoted by R and the duct wall is lined with a locally reacting acoustic lining whose acoustic impedance is denoted by Z_c. For both ducts, uniform mean flow of Mach number, M_o is assumed.

Although the duct geometries considered in this study are that of rectangular and circular ducts, the FE eigenvalue model is sufficiently general for it to represent any cross-sectional geometry with any mean flow profile and impedance boundary. The reason these duct geometries are considered here is because exact solutions are available for comparison.

4.2.1 Numerical Model

The duct cross-section is discretized using meshes constructed from either 8-noded quadrilateral elements or 6-noded triangular elements. The meshes are created using the *ICEMCFD* [101] mesh generator. The mesh can be structured or unstructured. Fig. 4.2 shows a structured mesh constructed from 8-noded quadrilateral elements for the rectangular duct and an unstructured mesh constructed from 6-noded triangular elements for the circular duct. Details of the element shape functions are presented in Chapter 2.

The resolution of the mesh is based on the number of nodes which are required to represent the solution accurately over one wavelength. The resolution of the mesh, N is defined as:

$$N = \frac{c_o}{f\Delta} \tag{4.1}$$

where c_o is the local speed of sound, f is the frequency in Hertz and Δ is the average distance between nodes.

Rectangular duct

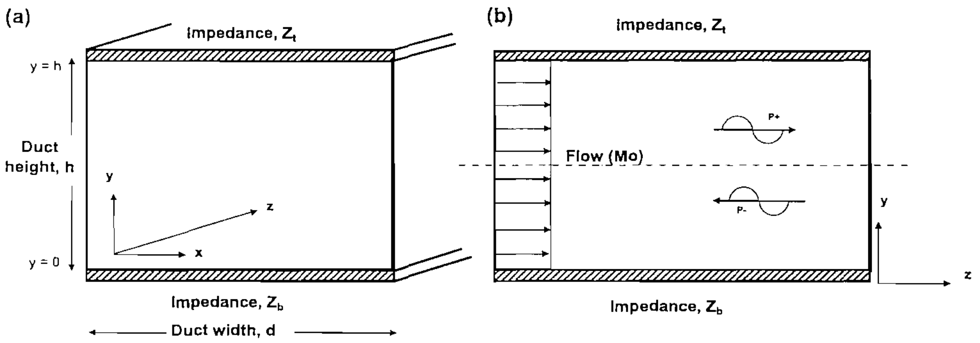

Circular duct

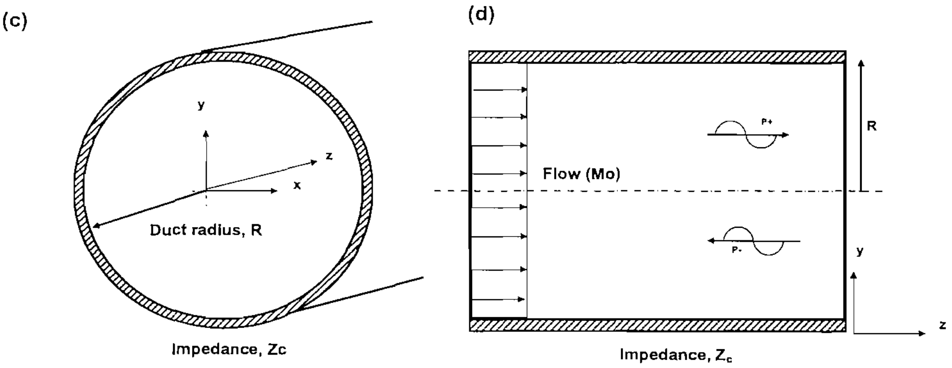

Figure 4.1: (a)-(b) A rectangular duct geometry and the coordinate system for the duct. (c)-(d) A circular duct geometry and the coordinate system for the duct.

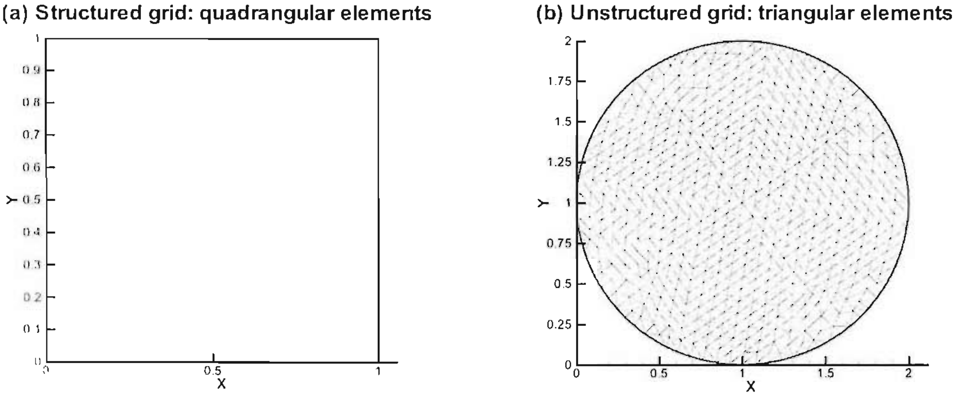
(a) Structured grid: quadrangular elements

(b) Unstructured grid: triangular elements

Figure 4.2: (a) A structured FE mesh constructed from 8-nodedd quadrilateral elements. (b) An unstructured FE mesh constructed from 6-nodedd triangular elements.

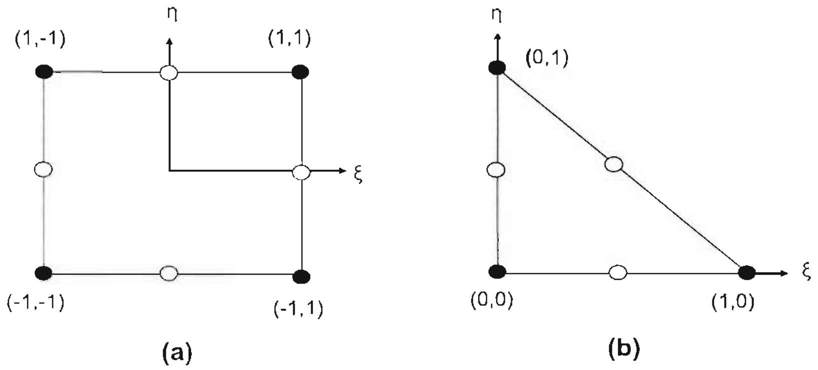

Figure 4.3: (a) 8-noded quadrilateral element, (b) 6-noded triangular element. • - interelement node and o - midside node.

For many engineering purposes, a mesh resolution of 8 to 10 nodes per wavelength is the general rule of thumb reference.

4.2.2 Duct Mode Classification

For uniform flow in the duct, the duct modes are found by solving the convected wave equation for acoustic pressure as an eigenvalue problem. The eigen-solution yields two distinct sets of duct modes; positive acoustic modes and negative acoustic modes. The different types of duct modes can be identified based on their axial wavenumbers and the modal intensities.

A mode with a negative modal intensity represents a negative acoustic mode. The mode decays and propagates in the negative z direction. Similarly, a mode with a positive modal intensity represents a positive acoustic mode. The mode decays or propagates in the positive z direction. The Morfey [102] expression of acoustic intensity with the Eversman [103] boundary condition term is used to calculate the modal intensity. The expression of the modal intensity is presented in Chapter 5.

The positive and negative acoustic modes are ordered on the basis of their cut-off ratios in descending order. The mode cut-off ratio, η is defined as:

$$\eta = \frac{k}{|\kappa|\sqrt{1-M_o^2}} \tag{4.2}$$

where κ is the duct transverse wavenumber and it is related to the eigenvalue, λ by the dispersion equation:

$$\kappa = k\sqrt{\frac{1}{1-M_o^2} - \frac{1}{1-M_o^2}(M_o + (1-M_o^2)\lambda)^2} \tag{4.3}$$

4.3 Results

Results are first presented of a study of the effect of different FE meshes on the accuracy of the FE solutions. This is followed by results of an assessment of accuracy of the FE eigenvalue model. In Section 4.3.4, results of a convergence study of the FE eigenvalue model are presented. Section 4.4 presents results of a study of the modal sound field in a circular duct with spliced liners of varying widths. Finally in Section 4.5 results of a performance study of an iterative eigenvalue routine (ARPACK) against a direct eigenvalue routine are presented.

4.3.1 Benchmark Results

Analytical solutions obtained by an integration scheme [79] are used to benchmark the FE solutions. The details of the integration scheme are presented in Chapter 2.

4.3.2 Performance of Different Finite Element Meshes To the Accuracy of the FE Solution

This work investigates the performance of different FE meshes in terms of the accuracy of the FE solution. A rectangular duct and a circular duct, as shown in Fig. 4.1, were considered. Both ducts were studied for reduced frequency of 15 with rigid boundaries and uniform mean flow at $M_o = 0.4$. The FE solutions obtained using different types of grids are compared with the exact solutions and the error between the two solutions is calculated using the following expression:

$$\varepsilon = \frac{\left|k^{\pm}_{z,n} - k^{\pm}_{z,e}\right|}{\left|k^{\pm}_{z,e}\right|} \times 100\% \tag{4.4}$$

where $k^{\pm}_{z,n}$ are the FE computed duct axial wavenumbers and $k^{\pm}_{z,e}$ are the analytical solutions. The FE solutions are obtained using ARPACK.

For the rectangular duct, two structured and two unstructured meshes constructed from either 8-noded quadrilateral elements or 6-noded triangular elements with an average mesh resolution of 10 nodes per wavelength are considered - see Figs. 4.4(a)-(d). For the circular duct, two unstructured meshes constructed from 6-noded triangular with an average mesh resolution of 10 nodes per wavelength are considered - see Figs. 4.4 (e)-(f).

In Fig. 4.5, plots of errors versus mode number for the circular duct are presented. The mode number in the plots is obtained by ordering the modes according to their cut-off ratios in descending order. Modes having cut-off ratios greater than 1 are represented by unfilled symbols and modes having cut-off ratios less than 1 are represented by filled symbols. In Fig. 4.6, similar plots are presented for the rectangular duct. In this study, the comparison is only made for duct modes having cut-off ratios greater than 0.8 because these are the modes of interest in this research. These would include all the cut-on modes and a few evanescent modes as in a hardwalled duct.

Figs. 4.5 and 4.6 show that triangular meshes, either structured and unstructured yield solutions with better accuracy than those obtained using quadrilateral meshes. For quadrilateral meshes, structured meshes out perform unstructured meshes. For triangular meshes, both structured and unstructured meshes yield solutions with comparable accuracy when compared with the analytical solutions. These results are found contradictory to the other FE studies which shown that quadrilateral elements are more effective than triangular elements. This behaviour is therefore a function of the FE eigenvalue model and does not apply to other software. In this thesis, quadrilateral elements are used for the FE transmission analysis and triangle elements are used for the FE eigenvalue model.

The results presented show very similar error trend to those observed in the two-dimensional problems in Chapter 3. The large error observed of modes 64+ and 65+ in Fig. 4.5(a) and of mode 26+ in Fig. 4.6(a) is because of the sign difference between the FE and the exact solutions as described in Chapter 2. This results in a large error being computed using the error expression - Eq. (4.4).

4.3.3 Assessment of Accuracy of the FE Solutions

This section examines the accuracy of the FE eigenvalue model by comparing with the exact solutions for a rectangular duct and a circular duct. The details of the rectangular and circular ducts are presented in Table 4.1. Both ducts are studied with uniform flow at Mach number $M_o = 0.4$ for reduced frequency of 15. The duct cross-sections are discretized using meshes constructed from 6-noded triangular elements with an average mesh resolution of 8 nodes per wavelength. The error between the FE and the exact solutions is computed using Eq. (4.4)

In Figs. 4.7 and 4.8, plots of error versus mode number for the rectangular and circular ducts are presented. In the plots, cut-on modes are represented by unfilled symbols and cut-off modes are represented by filled symbols.

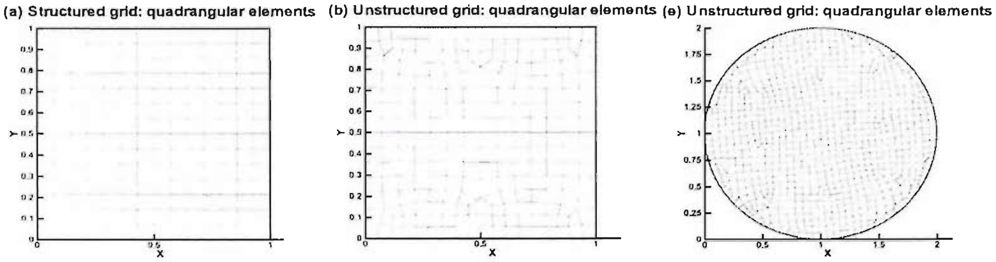
(a) Structured grid: quadrangular elements (b) Unstructured grid: quadrangular elements (e) Unstructured grid: quadrangular elements

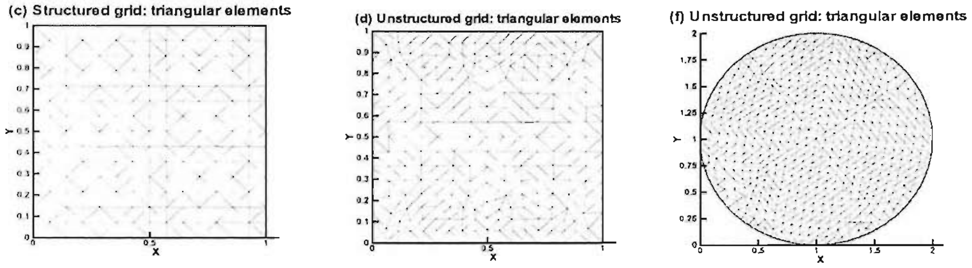
(c) Structured grid: triangular elements (d) Unstructured grid: triangular elements (f) Unstructured grid: triangular elements

Figure 4.4: FE grids constructed for the circular and rectangular ducts.

	Rectangular duct	Circular duct
Geometry	h=1.0, w=1.0	R=1.0
Impedance	$Z_t = 2-1i$, $Z_b = 2-1i$	Z_c = 2.02+0.01i
Flow	+ 0.4 Mach number	+ 0.4 Mach number
Frequency	kh =15.0	kR = 15.0

Table 4.1: Test models specification.

Results for the circular duct show that all the duct modes having cut-off ratios greater 0.8 have been computed to within 9% error. Similar results are observed for the rectangular duct in which all the duct modes having cut-off ratios greater than 0.8 have been computed to within 1% error - see Fig. 4.8.

In Figs. 4.9 and 4.10, the locations of the duct axial wavenumbers in the complex plane for the rectangular and circular ducts are presented. The results show generally good agreement between the two solutions which is consistent with the results presented in Figs. 4.7 and 4.8.

4.3.4 Convergence of the FE Solutions

This study is to examine the convergence of the FE eigenvalue model. The aim of the study is to determine the FE mesh resolution required to obtain solutions for a given number of modes particularly at high frequencies. The circular duct in Section 4.3.3 is considered here. The duct is studied for $kR = 15$ with uniform mean flow at $M_o = -0.4$.

The FE solutions obtained using FE meshes of different resolutions are compared against the exact solutions and the error between the two solutions is computed. Six unstructured meshes constructed from 6-noded triangular elements with resolutions of 6, 8, 10, 12, 14 and 20 nodes per wavelength as shown in Fig. 4.11

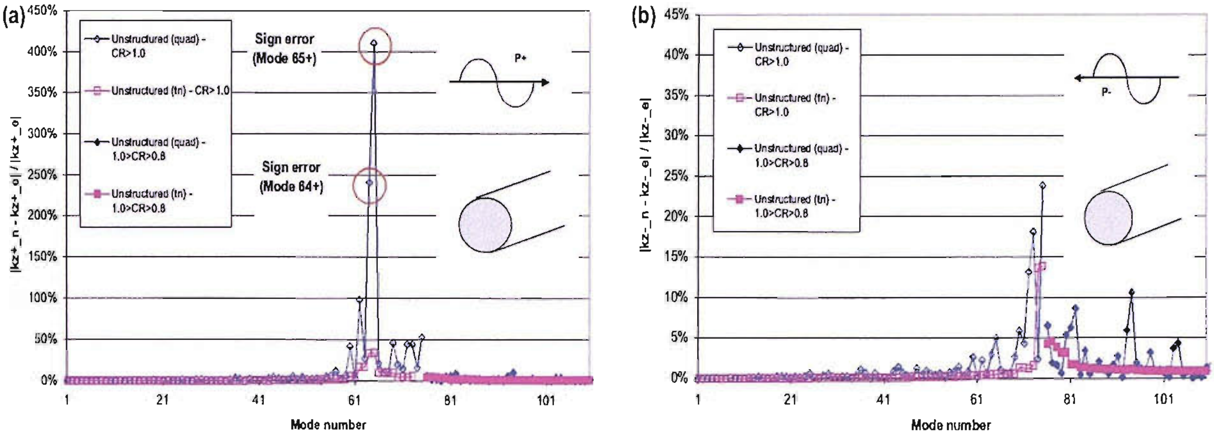

Figure 4.5: Error plotted against mode number for the circular duct. kR=15 and $M_o = 0.4$. Hardwalled. (a) Positive acoustic modes, (b) Negative acoustic modes.

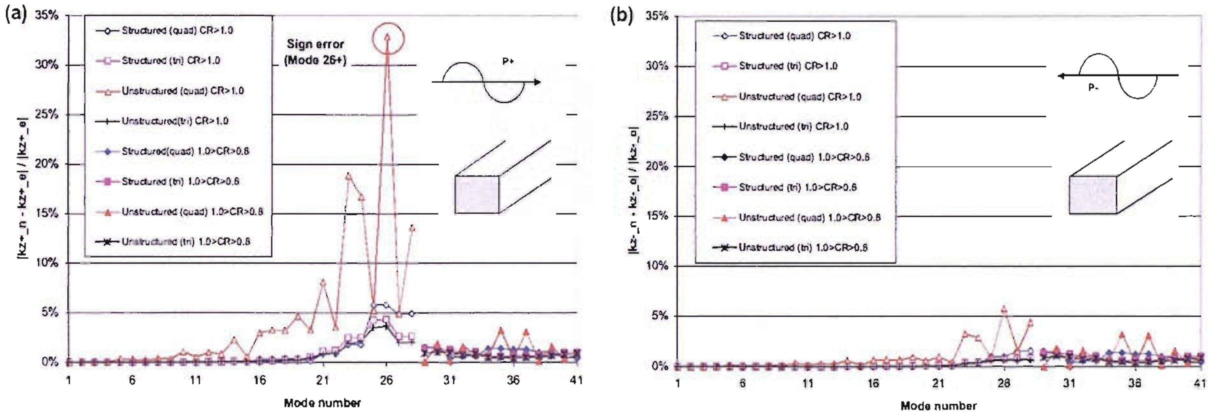

Figure 4.6: Error plotted against mode number for the rectangular duct. kh=15 and $M_o = 0.4$. Hardwalled. (a) Positive acoustic modes, (b) Negative acoustic modes.

sound field in the duct. Therefore, the mesh near to the splices is been refined.

In Fig. 4.12, plots of error versus mode number for different mesh resolutions are presented. Modes having cut-off ratio greater than 1 are denoted by unfilled symbols and modes having cut-off ratio less than 1 are denoted by filled symbols. The results show that the error decreases with increasing mesh resolution. The errors fall below 10% when the mesh resolution is equal to 8 nodes per wavelength and below 6% when the mesh resolution is equal to 10 nodes per wavelength. For mesh resolution greater than 10 nodes per wavelength, small improvement in the accuracy of the solution is observed. This indicates that convergency in solution has been achieved.

This study has shown that an FE mesh resolution of 8 to 10 nodes per wavelength has been found to be adequate to resolve the duct modes of required interest in this research. This convergence criteria is similar to

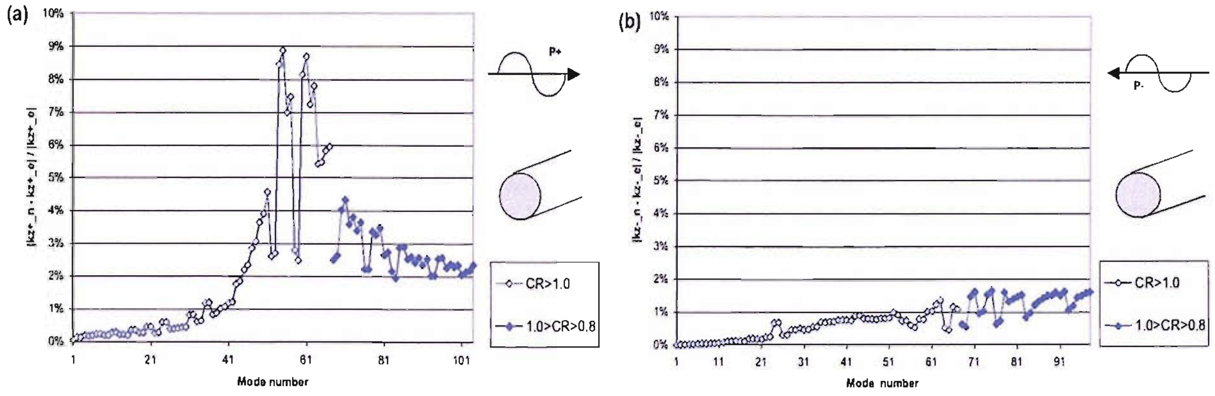

Figure 4.7: Error plotted against mode number for the circular duct. $M_o = 0.4$, kR=15 and $Z_c = 2.02 + 0.01i$. (a) Positive acoustic modes, (b) Negative acoustic modes.

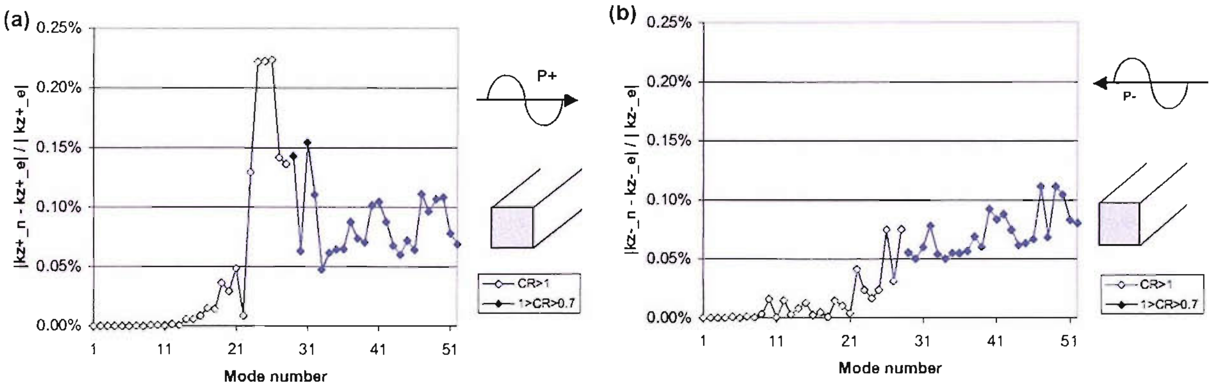

Figure 4.8: Error plotted against mode number for the rectangular duct. $M_o = 0.4$, kR=15, $Z_t = 2 - 1i$ and $Z_b = 2 - 1i$. (a) Positive acoustic modes, (b) Negative acoustic modes.

those established for two-dimensional problems in Chapter 3.

4.4 Application: Spliced Liners Study

Knowledge of the modal content of the sound field in a turbofan engine duct is important for source characterization and for helping to determine noise generation mechanisms in the engine. In this section, the modal solutions in a circular duct with liner splices of different widths are investigated using the FE eigenvalue model. In modern turbofan engines, acoustic lining is commonly used to absorb sound generated by the fan. The acoustic liner is usually manufactured in sections and each covers part of the duct's circumference. The sections are joined together by longitudinal hard strips or liner splices which are acoustically hard. Although the area covered by the splices is small, the discontinuities in the acoustic impedance around the circumference of the duct cause modal scattering of high order modes into other low order modes which are less attenuated by

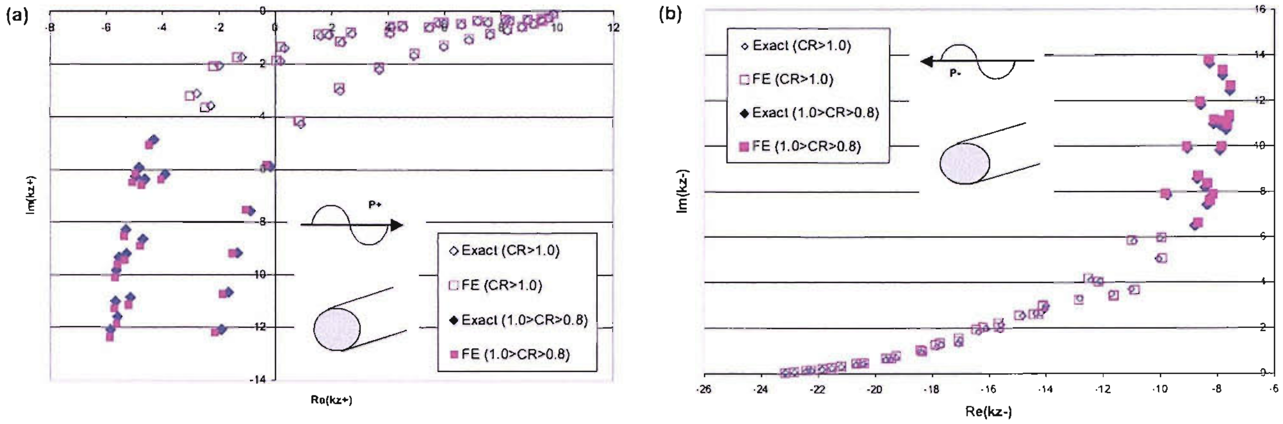

Figure 4.9: Comparison of duct axial wavenumber between the FE and exact solutions for the circular duct. $M_o = 0.4$, $kR = 15$ and $Z_c = 2.02 + 0.01i$. (a) Positive acoustic modes, (b) Negative acoustic modes.

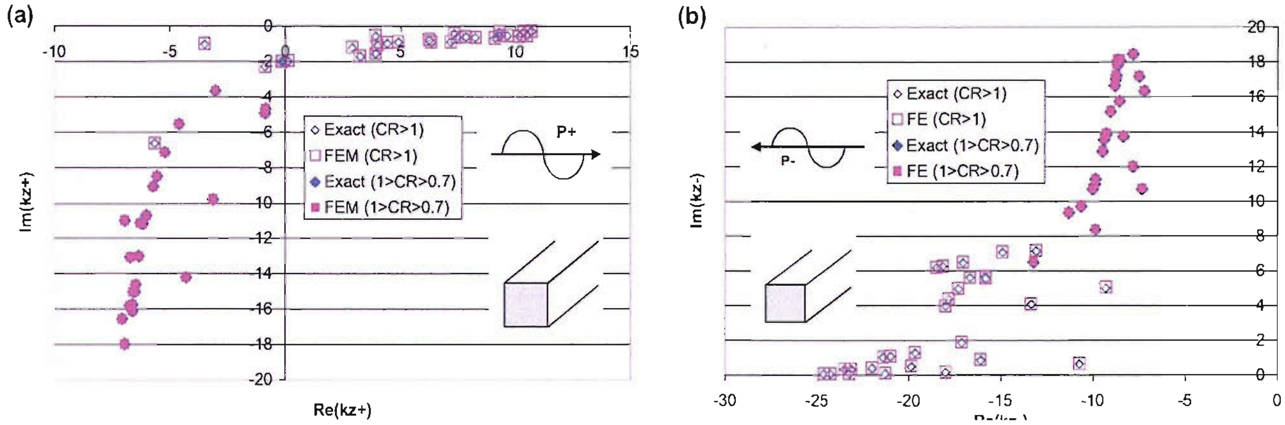

Figure 4.10: Comparison of duct axial wavenumber between the FE and exact solutions for the rectangular duct. $M_o = 0.4$, $kR = 15$, $Z_t = 2 - 1i$ and $Z_b = 2 - 1i$. (a) Positive acoustic modes, (b) Negative acoustic modes

the acoustic liner. This can result in a significant reduction in the liner performance.

The objectives of this study are to investigate how the acoustic modes in the duct are modulated by the presence of the liner splices and also by the presence of mean flow in the duct. This is achieved by making comparisons between a uniform liner and a liner with splices of different widths on the modal axial attenuation rate, $\triangle SPL$, the mode axial propagating speed, $Re\{k_z^{\pm}\}$ and the mode shape. The $\triangle SPL$ defines the rate of change in the sound pressure level (SPL) over a duct radius. It is calculated using the following expression [94]:

$$\triangle SPL = 20\log(e)\beta Im\{kx_z^{\pm}\}R = 8.686\beta R \tag{4.5}$$

where β is negative if the propagation is in the positive axial direction and vice versa. The higher the $\triangle SPL$,

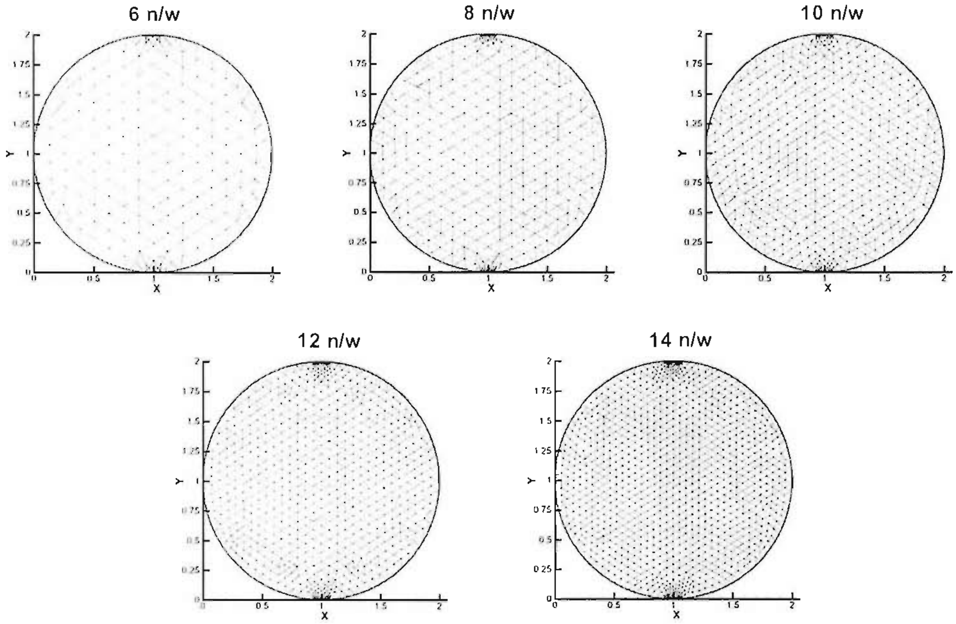

Figure 4.11: FE grids used in the convergence study.

Duct radius	$R = 1m$
Splice width	s = 3.8 cm, 5.7 cm, 7.6 cm, 9.5 cm, 11.4 cm
Impedance	$Z_c = 2.12 + 0.01i$
Flow	$M_o = -0.4$
Frequency	$kR = 14$

Table 4.2: Test models specification for a circular duct with liner splices.

where β is negative if the propagation is in the positive axial direction and vice versa. The higher the $\triangle SPL$, the greater the rate of attenuation of the acoustic mode along the duct. The outcome of this work is to identify and quantify the potential noise benefit that could be gained by manufacturing a uniform acoustic lining with no splices.

The geometry of the test model is shown in Fig. 4.13. The duct contains two liner splices whose width, s varies from 3.8 cm to 11.4 cm and the duct is assumed to be infinitely long. The splices are 180 degrees apart from each other. The duct is studied for $kR = 15$ with and without flow in the duct. In Table 4.2, the values of the parameters used in this analysis are presented. The duct cross-section is discretized using an FE mesh constructed from 6-noded triangular elements with an average mesh resolution of 10 nodes per wavelength and the mesh near the vicinity of the splices is refined - see Fig. 4.14.

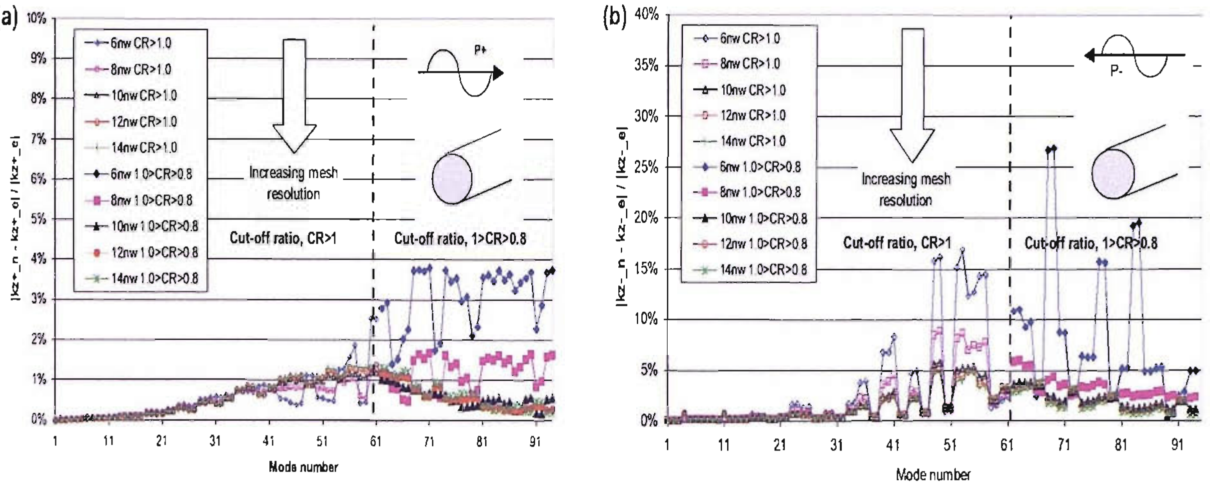

Figure 4.12: Error plotted against mode number for different mesh resolutions. $M_o = -0.4$, $kR = 15$ and $Z_c = 2.02 + 0.01i$. (a) Positive acoustic modes, (b) Negative acoustic modes.

propagation direction. In Table 4.3, the duct axial wavenumbers of the corresponding $\triangle SPL$ presented in Fig. 4.15 are presented. The results show that the modes in the duct with liner splices show smaller attenuation than those in the duct without splices. This is due to the reduction in the effective lining area for the spliced liner case. However, only one of the coupled azimuthal modes shows reduction in $\triangle SPL$. The other azimuthal mode shows $\triangle SPL$ values very close to those of the uniform liner - see Fig. 4.15. For zero splice width, both coupled azimuthal modes show identical $\triangle SPL$ as well as $Re\{k_z\}$.

In Fig. 4.16, the mode shapes of the positive acoustic mode ($\pm 20, 1$) highlighted in Fig. 4.15 for different splice widths are plotted. Inspection of the mode shapes found that only the mode with a maximum pressure at the splices shows reduction in the $\triangle SPL$ - see Fig. 4.16. The other azimuthal mode which has a minimum pressure at the splices shows $\triangle SPL$ very similar to those of zero splice width. The splices have only a small effect on the modal propagation speed as the coupled modes show very similar $Re\{k_z^+\}$.

The results also show that high order modes are more affected by the discontinuity in the acoustic impedance than low order modes. The reduction can be as high as 5 to 6 dB per duct radius for high order modes and 1 to 2 dB per radius for low order modes. The FE results also show no occurrence of additional modes or spurious modes in the duct with splices.

4.4.2 Uniform Flow Case

In Figs. 4.17 and 4.18, plots of $\triangle SPL$ versus $Re\{k_z^\pm\}$ for different splice widths in the presence of uniform flow are presented. Fig. 4.17 presents modes that propagate with the flow and Fig. 4.18 presents modes that propagate against the flow. In Tables. 4.4 and 4.5, the numerical values of the axial wavenumbers and $\triangle SPL$

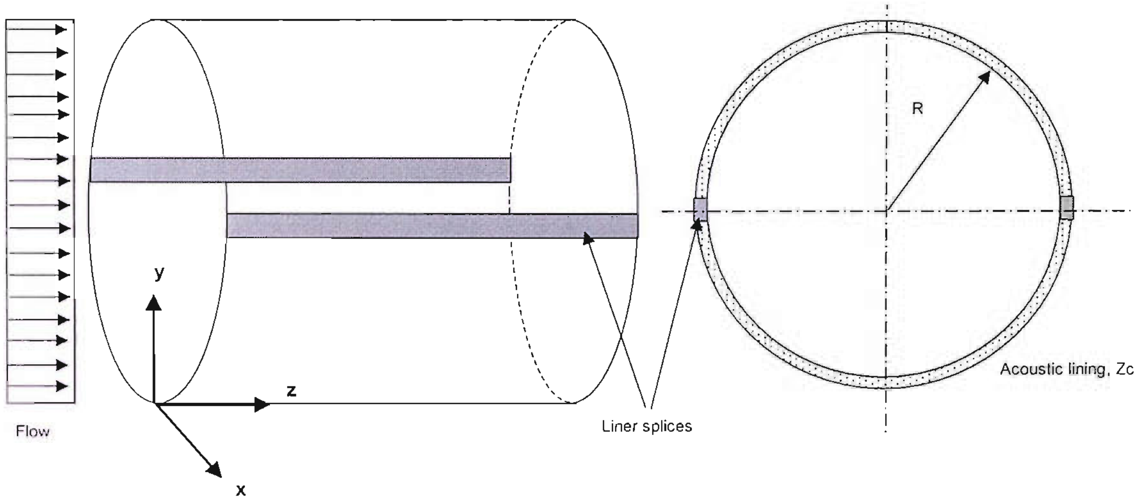

Figure 4.13: A circular duct containing two liner splices and the coordinates of the system.

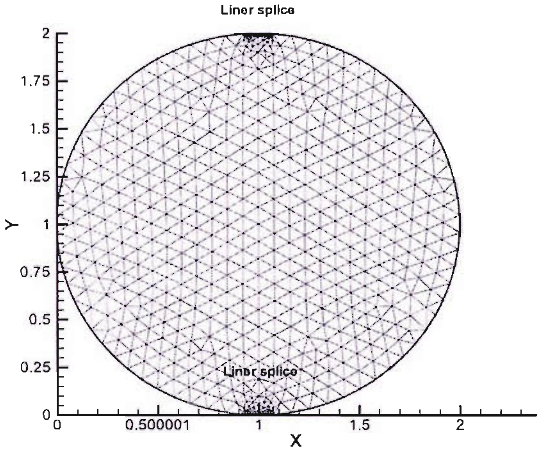

Figure 4.14: A circular duct cross-sectional mesh with two splices.

4.4.2 Uniform Flow Case

In Figs. 4.17 and 4.18, plots of $\triangle SPL$ versus $Re\{k_z^{\pm}\}$ for different splice widths in the presence of uniform flow are presented. Fig. 4.17 presents modes that propagate with the flow and Fig. 4.18 presents modes that propagate against the flow. In Tables. 4.4 and 4.5, the numerical values of the axial wavenumbers and $\triangle SPL$ of the duct modes are presented.

Results for the uniform flow case are very similar to those observed in the no flow case. The modes in the duct with liner splices show a smaller rate of attenuation than those in the duct with no splices. This is only observed on one of the coupled azimuthal modes. The other azimuthal mode shows rates of attenuation very similar to those of zero splice width.

In Figs. 4.19 and 4.20, the mode shapes of the positive acoustic modes (+/-10,3) and of the negative acoustic

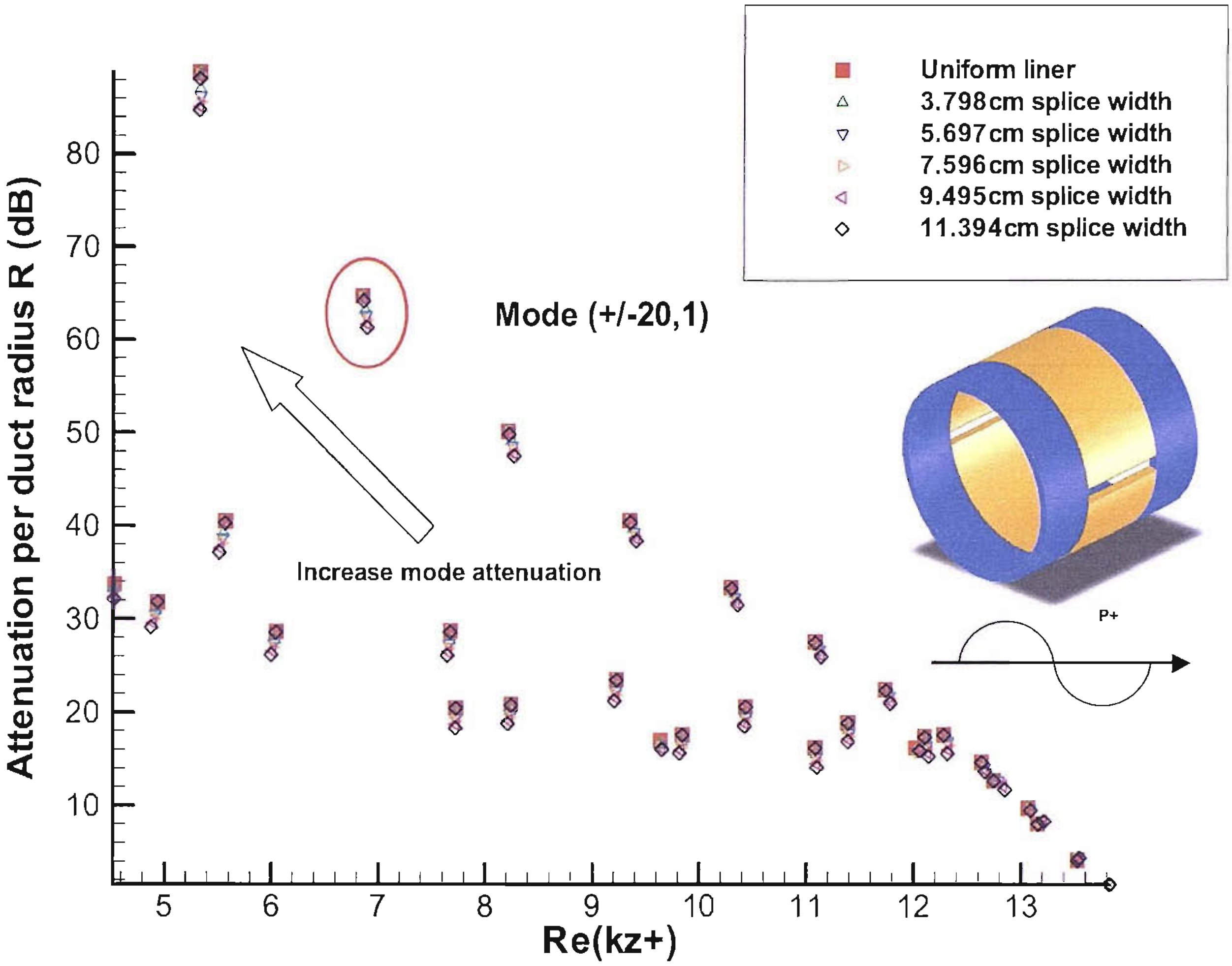

Figure 4.15: ΔSPL plotted against $Re\{k_z^+\}$ for different splice widths. Positive acoustic modes. $M_o = 0$, $kR = 14$ and $Z_c = 2.02 + 0.01i$.

propagation speed as both coupled modes show very similar propagation speed $Re\{k_z^{\pm}\}$.

The FE results also show no occurrence of additional modes or spurious modes in the duct with liner splices. Comparison with the zero flow results shows that the presence of flow in the duct further reduces the liner performance and high order modes are more affected than low order modes. Generally, the results have shown that the presence of liner splices in a duct decreases the liner performance.

4.5 Performance Study

Results of a performance study of a direct eigenvalue routine compared to an iterative eigenvalue routine (ARPACK) are presented. This study aims to assess the feasibility of using the FE eigenvalue model for studying three-dimensional problems at high frequencies.

Liner width	Plot	k_z^+	$\triangle SPL$	Plot	k_z^+	$\triangle SPL$
0cm	A1	6.849-2.935i	64.76 dB/R	A2	6.845-2.934i	64.72 dB/R
3.798cm	B1	6.870-2.870i	63.31 dB/R	B2	6.846-2.933i	64.71 dB/R
5.697cm	C1	6.876-2.842i	62.70 dB/R	C2	6.846-2.931i	64.66 dB/R
7.596cm	D1	6.880-2.818i	62.17 dB/R	D2	6.848-2.927i	64.58 dB/R
9.495cm	E1	6.883-2.798i	61.74 dB/R	E2	6.850-2.921i	64.44 dB/R
11.394cm	F1	6.886-2.783i	61.39 dB/R	F2	6.853-2.912i	64.24 dB/R

Table 4.3: Axial wavenumbers and attenuation of the positive acoustic mode $(\pm 20, 1)$ highlighted in Fig. 4.15. $M_o = 0$, $kR = 14$ and $Z_c = 2.02 + 0.01i$.

Liner width	Plot	k_z^+	$\triangle SPL$	Plot	k_z^+	$\triangle SPL$
0cm	A1	12.766-3.351i	73.92 dB/R	A2	12.761-3.351i	73.93 dB/R
3.798cm	B1	12.800-3.225i	71.14 dB/R	B2	12.762-3.351i	73.93 dB/R
5.697cm	C1	12.787-3.153i	69.57 dB/R	C2	12.762-3.350i	73.91 dB/R
7.596cm	D1	12.750-3.087i	68.11 dB/R	D2	12.763-3.349i	73.88 dB/R
9.495cm	E1	12.722-3.028i	66.80 dB/R	E2	12.764-3.346i	73.82 dB/R
11.394cm	F1	12.677-2.976i	65.66 dB/R	F2	12.766-3.342i	73.72 dB/R

Table 4.4: Axial wavenumbers and mode attenuations of the positive acoustic mode $(\pm 10, 3)$ indicated in Fig. 4.19. $M_o = -0.4$, $kR = 14$ and $Z_c = 2.02 + 0.01i$.

Liner width	Plot	k_z^-	$\triangle SPL$	Plot	k_z^-	$\triangle SPL$
0cm	A1	-2.284+3.050i	67.30 dB/R	A2	-2.277+3.049i	67.26 dB/R
3.798cm	B1	-2.277+2.975i	65.65 dB/R	B2	-2.277+3.047i	67.23 dB/R
5.697cm	C1	-2.272+2.945i	64.97 dB/R	C2	-2.277+3.045i	67.17 dB/R
7.596cm	D1	-2.269+2.919i	64.40 dB/R	D2	-2.276+3.039i	67.06 dB/R
9.495cm	E1	-2.266+2.897i	63.91 dB/R	E2	-2.275+3.031i	66.87 dB/R
11.394cm	F1	-2.265+2.879i	63.52 dB/R	F2	-2.273+3.019i	66.61 dB/R

Table 4.5: Axial wavenumbers and mode attenuations of the negative acoustic modes $(\pm 22, 1)$ indicated in Fig. 4.20. $M_o = -0.4$, $kR = 14$ and $Z_c = 2.02 + 0.01i$.

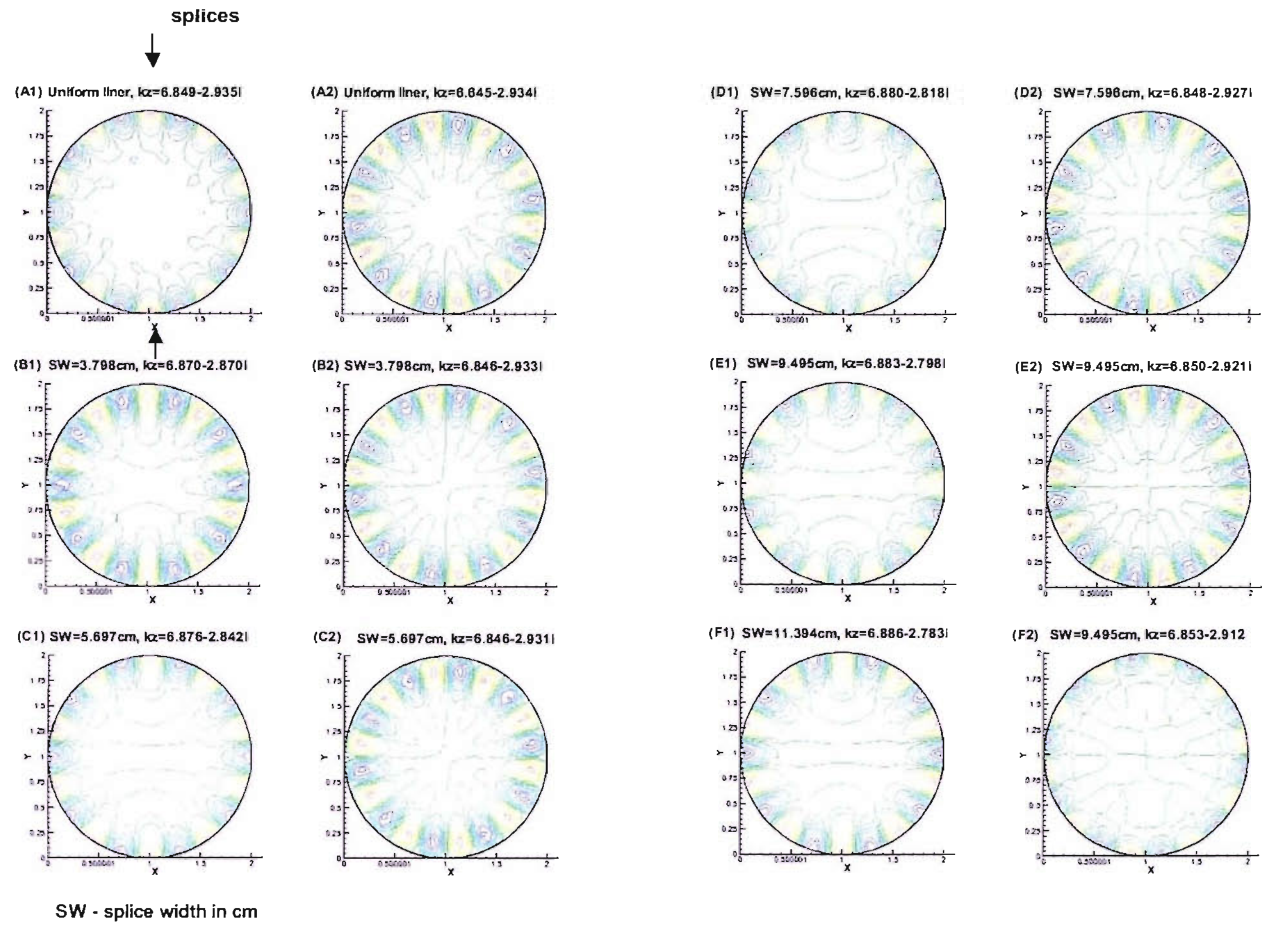

Figure 4.16: Mode shapes of the positive acoustic mode (+/-20,1) highlighted in Fig. 4.16. $M_o = 0$, $kR = 14$ and $Z_c = 2.02 + 0.01i$.

4.5 Performance Study

Results of a performance study of a direct eigenvalue routine compared to an iterative eigenvalue routine (ARPACK) are presented. This study aims to assess the feasibility of using the FE eigenvalue model for studying three-dimensional problems at high frequencies.

A rigid circular duct as shown in Fig. 4.1 is considered in this study. The duct is studied for $kR = 15$ without flow in the duct. In Fig. 4.21, the times taken to compute the solutions by the direct eigenvalue routine and by the iterative eigenvalue routine are plotted against the problem size. The problem size is defined in terms of the number of nodal point used to discretize the duct cross-section. All the results are computed on a 1GHz Pentium III computer with 1G bytes of RAM. The FE eigenvalue model either using the direct eigenvalue routine or the iterative eigenvalue routine is written in Fortran language operating under Window 2000. The main difference between the two routines is that the direct eigenvalue routine computes all the solutions and

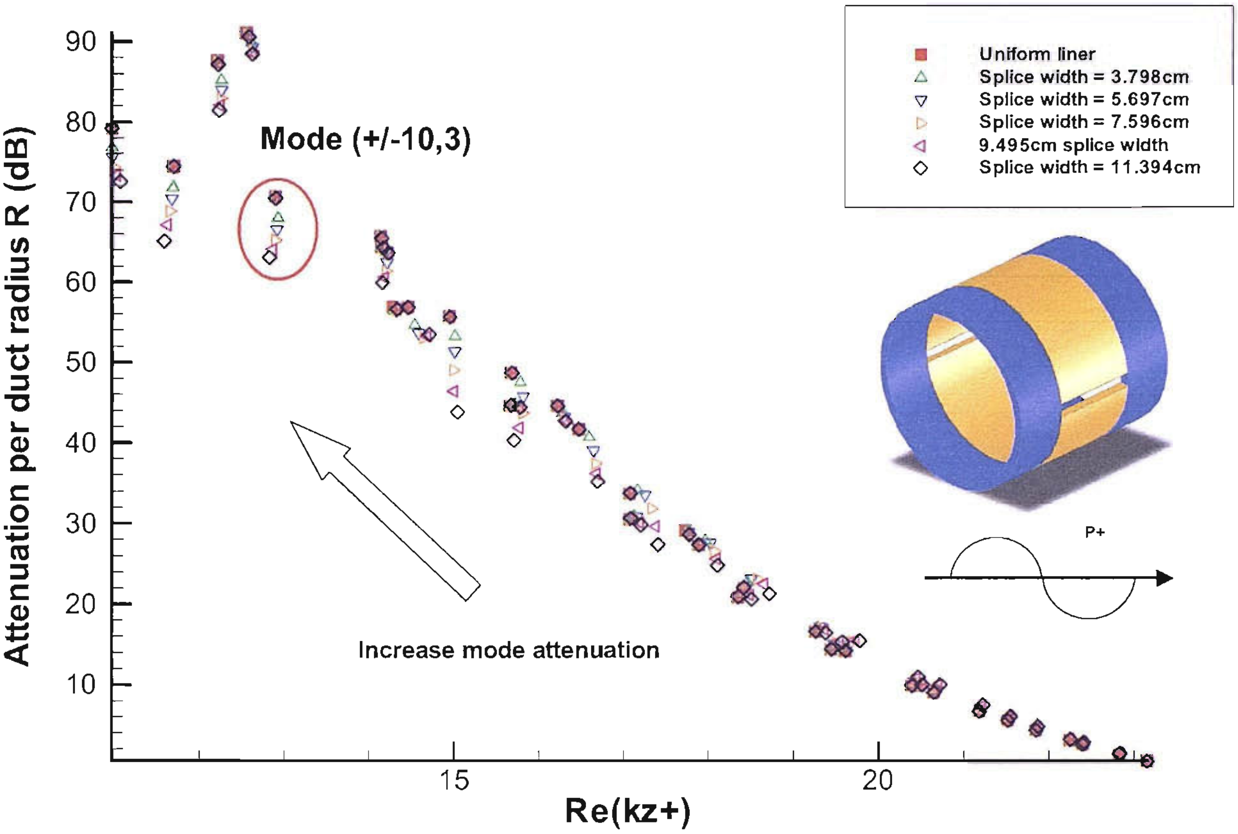

Figure 4.17: $\triangle SPL$ plotted against $Re\{k_z^+\}$ for different splice widths. Positive acoustic modes. $M-o=-0.4$, $kR=14$ and $Z_c=2.02+0.01i$.

which correspond to the different number of eigenvalues computed. In Fig. 4.21(b), the number of eigenvalues, N computed by ARPACK is plotted against the computation time, T on a logarithmic scale base 10. The plot shows that the computation time, T scales as $N^{1.7}$ where N is the number of eigenvalues sought.

The results presented have shown that ARPACK offers significant savings in computation time over the direct eigenvalue routine. The slopes of the timing curves indicate that these savings should be more significant with increasing problem size. ARPACK is also a better choice for this work as only a specific number of eigenvalues are required to be computed.

4.6 Conclusions

In this chapter, the validity of the FE eigenvalue model for computation of eigenmodes in three-dimensional ducts has been assessed. The numerical results for various duct cross sections and the mode shape for various modes have been presented which show the validity of the analysis and computer code. Simple waveguide shapes are chosen for the study here because their field distributions are well known. The study found that

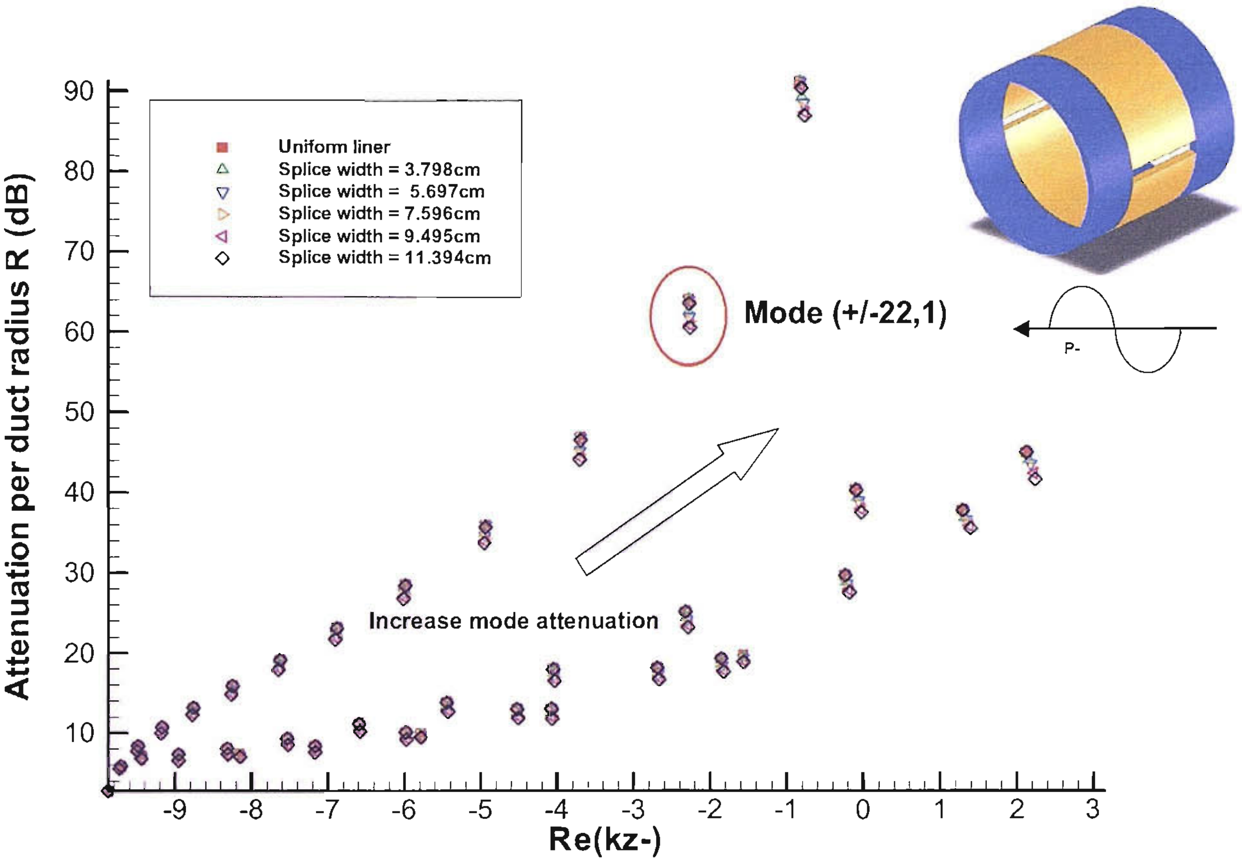

Figure 4.18: $\triangle SPL$ plotted against $Re\{k_z^-\}$ for different splice widths. Negative acoustic modes. $M_o = -0.4$, $kR = 14$ and $Z_c = 2.02 + 0.01i$.

complete sets of propagating eigenmodes can be obtained at modest computational cost for frequencies and flow conditions which are characteristic of turbofan intake and bypass ducts.

The results presented in this study have concluded that:

- The FE eigenvalue model yield solutions which exhibit good accuracy when compared with the exact solutions when an adequate FE mesh resolution is used. The FE solutions show no modes are repeated or missing.

- The FE solutions obtained using triangular meshes show better accuracy than those obtained using quadrilateral meshes.

- An FE mesh resolution of 8 to 10 nodes per wavelength is found to be adequate to resolve the duct modes of interest in this research which is modes having cut-off ratio greater than 0.8.

- This study has demonstrated that the FE eigenvalue model is capable of studying three-dimensional ducts with non-uniform impedance boundaries and uniform flow.

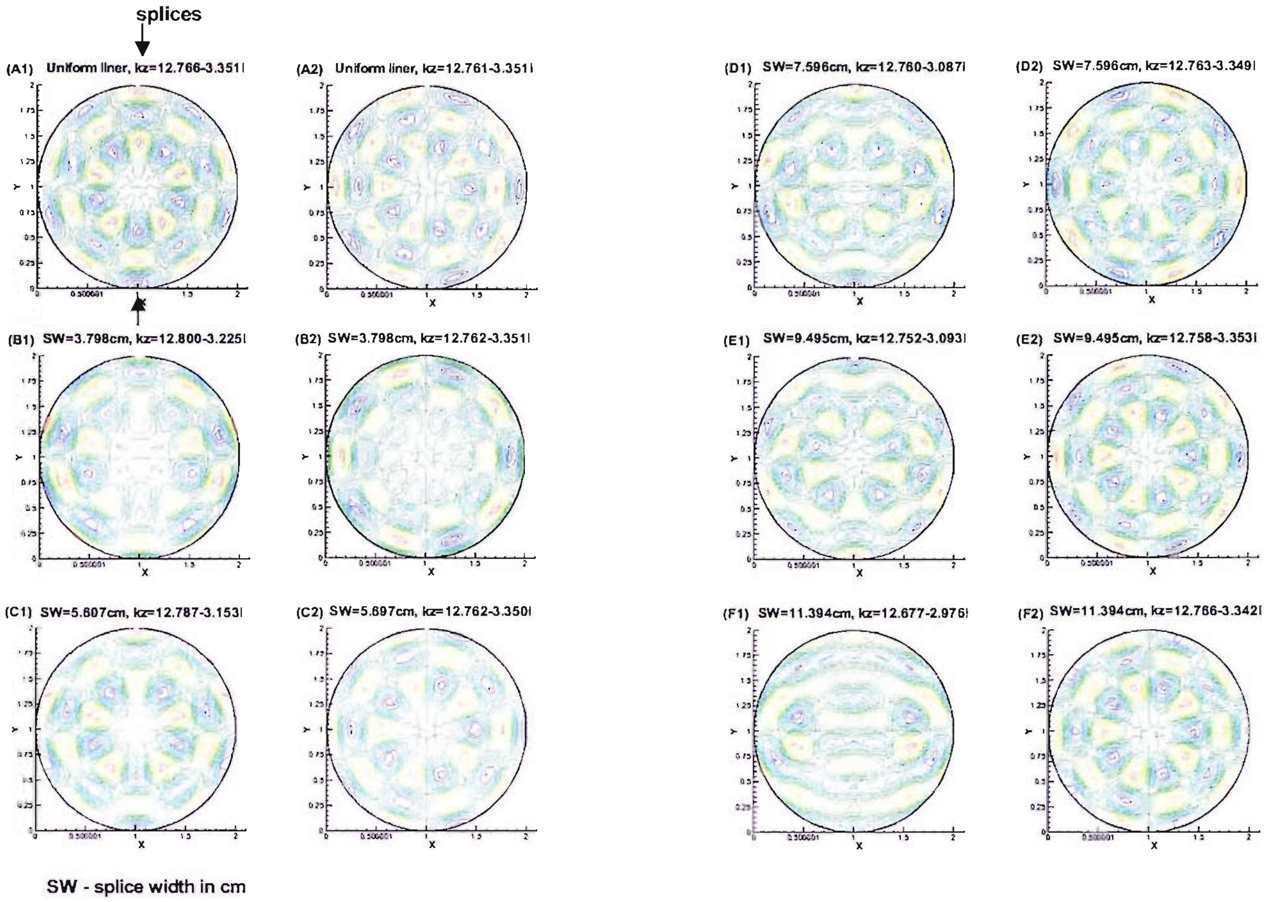

Figure 4.19: Mode shapes of the positive acoustic mode ($\pm 10,3$) highlighted in Fig. 4.17. $M_o = -0.4$, $kR = 14$ and $Z_c = 2.02 + 0.01i$.

lateral meshes.

- An FE mesh resolution of 8 to 10 nodes per wavelength is found to be adequate to resolve the duct modes of interest in this research which is modes having cut-off ratio greater than 0.8.
- This study has demonstrated that the FE eigenvalue model is capable of studying three-dimensional ducts with non-uniform impedance boundaries and uniform flow.
- The modal study of a circular duct with liner splices showed that an increase in splice width decreases the liner performance. The FE solutions also show no occurrence of additional duct modes or spurious modes in the duct with the introduction of liner splices.
- The iterative routine (ARPACK) offers significant savings in computation time over the QR direct eigenvalue routine and these savings should be more significant with increasing problem size.

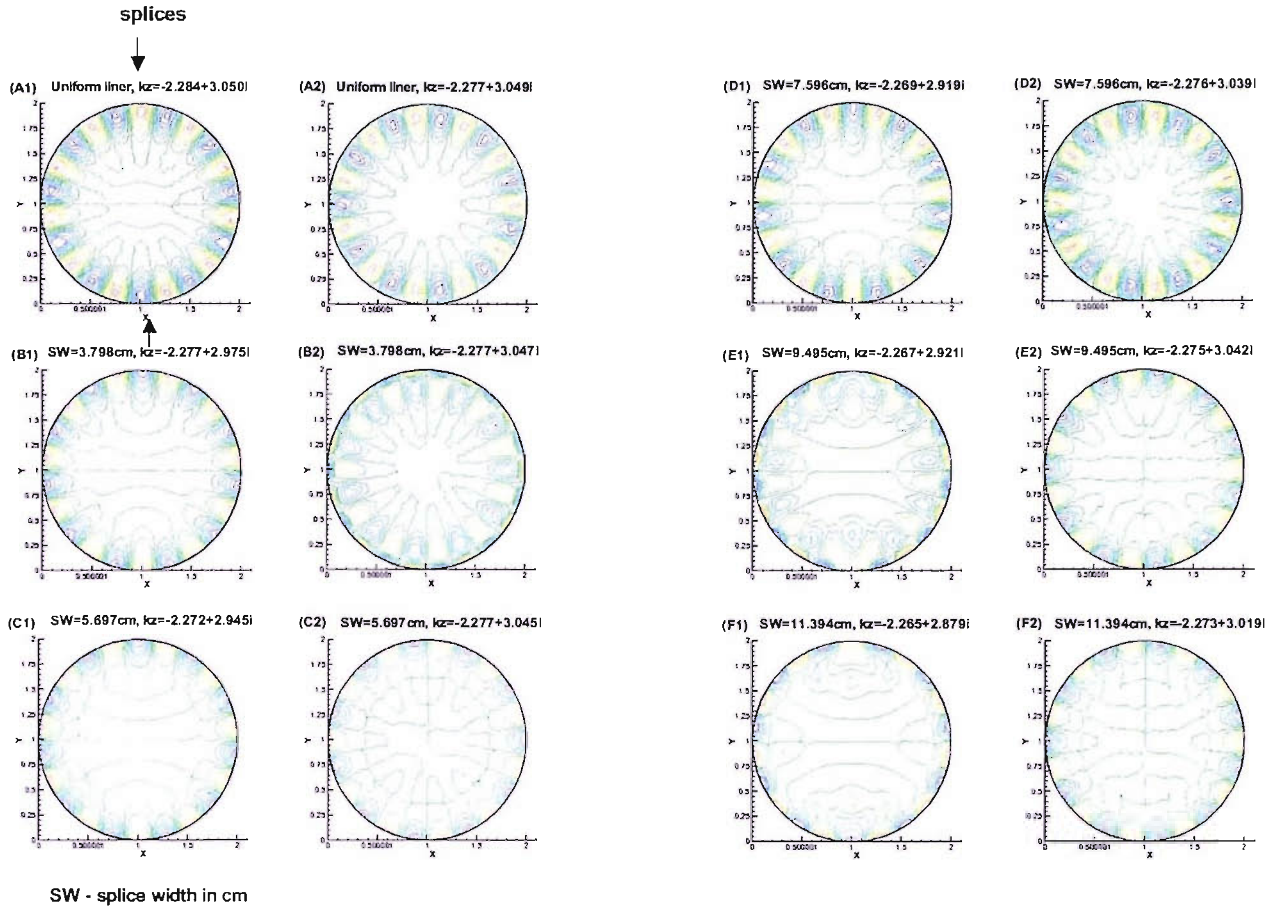

Figure 4.20: Mode shape of the negative acoustic mode (±22, 1) highlighted in Fig. 4.18. $M_o = -0.4$, $kR = 14$ and $Z = 2.02 + 0.01i$.

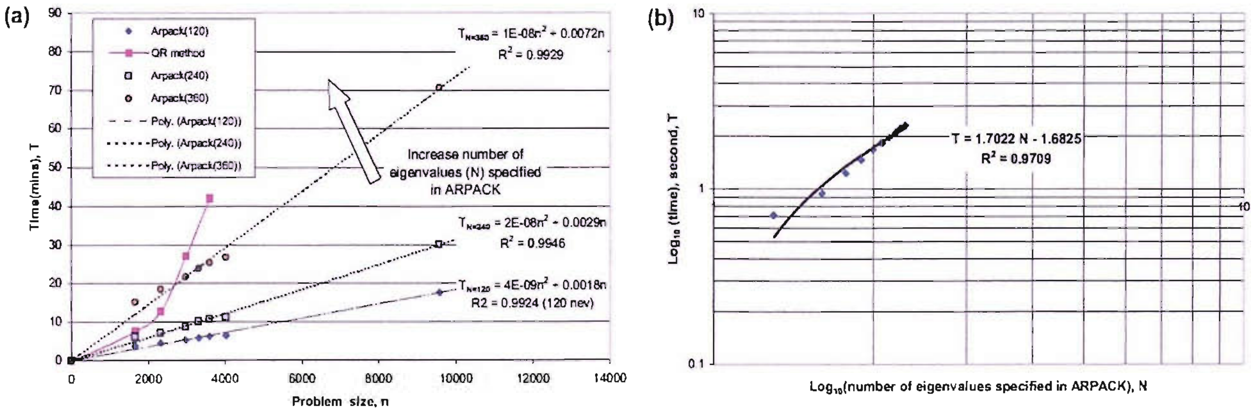

Figure 4.21: (a) Computation time plotted against problem size for the QR direct method and ARPACK. (b) The number of eigenvalues, N computed by ARPACK plotted against the computation time, T in an logarithmic (base 10) scale

Chapter 5

Application of Mode Matching Techniques To Study Sound Transmission in Flow Ducts.

5.1 Introduction

This chapter is about the application of mode matching (MM) techniques to study transmission of sound in flow ducts. The essence of the mathematics is that the duct is segmented into different sections at boundaries where changes of acoustic impedance or geometry take place. The duct modes which propagate in each section, including some evanescent modes, are computed. The complex amplitudes of the duct modes are then matched across the interface of the section with that of the next section. This yields a series of equations which can then be solved to yield the complex amplitudes of the duct modes in each section.

This chapter will describe two MM procedures: the existing and the revised MM procedures. The revised MM procedure is different to the existing MM procedure which has been employed by Beckmeyer [1], Cummings [2] and Sijtsma [3] in their studies of duct acoustics. The revised MM procedure matches solutions between segmented sections using continuity of axial momentum flux and mass flux across the matching interface. The existing MM procedure matches solutions between segmented sections using continuity of acoustic pressure and axial particle velocity across the matching interface. Fig. 5.1 shows the different matching criteria implied at a matching interface by the two procedures. Note that the revised MM procedure is also known as the new mode matching method (NMMM) and the existing MM procedure is also known as the traditional mode matching method (TMMM) in the thesis. The NMMM is proposed because during the course of the study, it was found that when traditional mode matching solutions were compared to a full FE transmission analyses, discrepancies were found in the vicinity of a liner discontinuity when flow is present in the duct. These persisted as the resolution of each model was increased and led to significant differences in transmitted and reflect acoustic power. In this work, FE solutions are used as the benchmark solutions for validating the MM solutions.

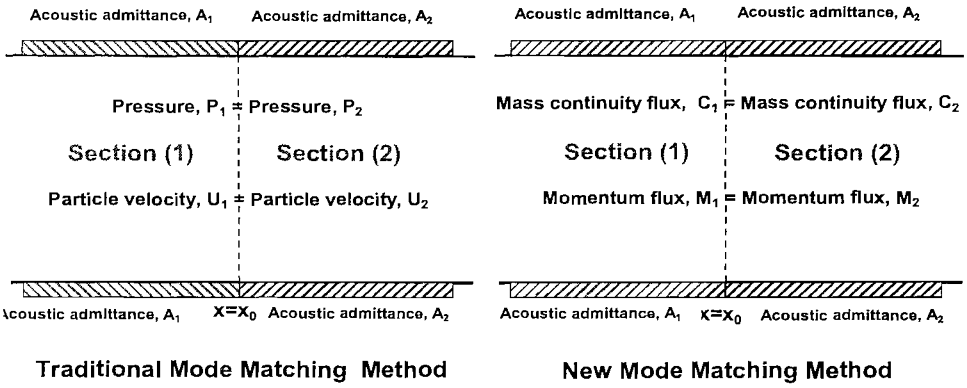

Figure 5.1: Different matching criteria. (a) TMMM, (b) NMMM.

Outline

In Section 5.2, the problem specification is presented. Section 5.3 describes the two MM procedures using a test problem. In Section 5.5.2, an iterative procedure for solving the formulated MM problems is described. In Section 5.5, the application of the MM procedures for studying transmission of sound in a two-dimensional flow duct with and without the presence of an infinitely thin splitter is described.

5.2 Specification of the problem

5.2.1 General Case

Modelling transmission of sound in an acoustically lined turbofan engine duct is a challenging problem. Not only a real engine duct has a three-dimensional geometry and flow, the problem becomes rather complicated in the bypass duct because of growing boundary layer thickness, the presence of vorticity, swirling flow and increased geometrical complexity.

However, this noise transmission problem can be simplified, to a first approximation, by assuming that the inlet duct is a circular-section axisymmetric duct with uniform mean flow and the bypass duct is an annular-section axisymmetric duct with uniform mean flow as described in Chapter 1. Finite thickness splitters (radial and circumferential) can be included into the MM model if it can be assumed that they are sufficiently thin for the uniform flow assumption to be justified.

In this study, two duct models as shown in Fig. 5.2 are considered. Both ducts consist of a short hard Section (a) with length L_1, a lined Section (b) with impedance Z and length L_2 and another short hard Section (c) with length L_3. In duct (B), an infinitely thin splitter with length L_2 is positioned at $y = h_1$ in Section (b). The uniform mean flow in both ducts is given by u_o. At the source plane at $x = 0$, a single harmonic mode or a multi-mode source with equal energy per mode can be specified as the input source. The outlet of the duct at

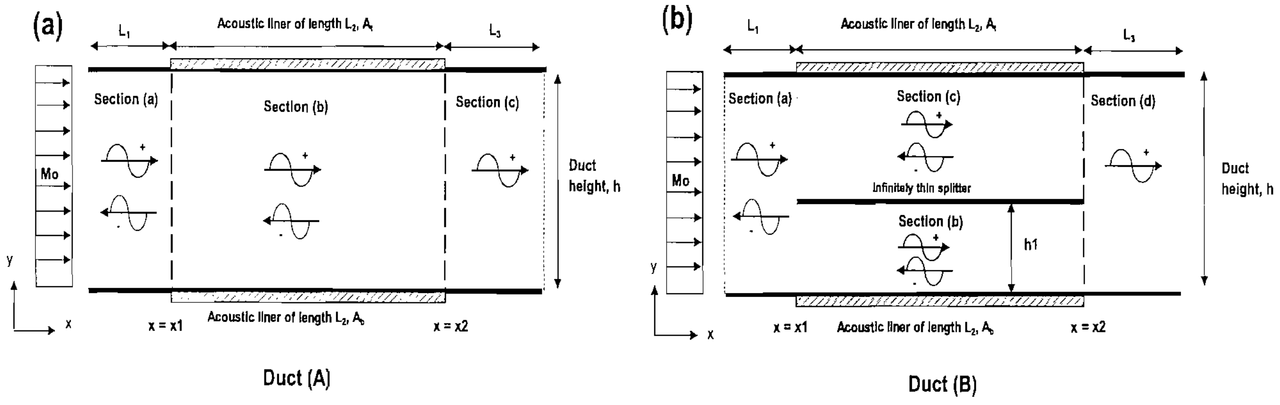

Figure 5.2: (a) Duct (A) with an impedance discontinuity, (b) Duct (B) with an infinitely thin splitter.

$x = L$ is anechoically terminated.

5.3 Mode Matching Methods

In this section, two MM procedures; the existing and the revised are described using a general test model. The test model consists of an axially uniform duct with an impedance discontinuity at $z = z_o$ - see Fig. 5.3. The uniform mean flow in the duct is given by u_o and the flow is assumed to be parallel with the z axis of the duct.

To study the acoustic scattering due to the impedance discontinuity at $z = z_o$, the duct is segmented into two sections; Section (1) and Section (2) - see Fig. 5.3(a). The duct modes that represent the harmonic sound field in each section are computed numerically using the FE eigenvalue solver described in Chapter 2. The harmonic sound field in each section is expressed as:

$$p_N = \sum_{i=0}^{\infty} \left\{ A^+_{N,i}\ \psi^+_{N,i}(\mathbf{x}) e^{-ik^+_{z,N,i} z} + A^-_{N,i}\ \psi^-_{N,i}(\mathbf{x}) e^{-ik^-_{z,N,i} z} \right\} \tag{5.1}$$

where $N = 1,2$ denotes the duct section, the superscript $+$ and $-$ signs are associated with duct modes propagating in the positive and negative z direction and $A^{\pm}_N$ are the complex amplitudes of the duct modes. The eigenfunctions and the axial wavenumbers of the duct modes in each duct section are denoted by $\psi^{\pm}_{N,i}$ and $k^{\pm}_{z,N,i}$ respectively. The FE computed eigenfunctions are represented by a series of nodal pressures and element shape functions:

$$\psi_i(\mathbf{x}) = \sum_{j=1}^{m} N_j(\mathbf{x}) p_{i,j} \tag{5.2}$$

where $N_j(\mathbf{x})$ is the element shape function and $p_{i,j}$ is the nodal pressure of mode i at node j. Solving the eigenvalue numerically will allow the consideration of ducts of any cross-section with non-uniform mean flows and impedance boundaries.

For prismatic ducts e.g. two-dimensional and axisymmetric ducts, the duct modes can also be computed analytically. For two-dimensional ducts, the eigenfunctions of the duct modes are expressed by a series of cosine functions $\psi(y)_i = \cos_i(\kappa_i y)$, where κ_i are the mode transverse wavenumbers. For axisymmetric ducts, the duct eigenfunctions are expressed in terms of Bessel functions.

Similarly the axial particle velocity in each duct section can be expressed as a superposition of positive and negative acoustic modes:

$$U_N = \sum_{i=0}^{\infty} \left\{ B_{N,i}^{+}\ \psi_{N,i}^{+}(\mathbf{x}) e^{-ik_{z,N,i}^{+} z} + B_{N,i}^{-}\ \psi_{N,i}^{-}(\mathbf{x}) e^{-ik_{z,N,i}^{-} z} \right\} \tag{5.3}$$

$B_{N,i}^{\pm}$ can be related to $A_{N,i}^{\pm}$ using the acoustic momentum equation:

$$B_{N,i}^{\pm} = \frac{k_{z,N,i}^{\pm}}{\rho_o(\omega - k_{z,N,i}^{\pm} u_o)} A_{N,i}^{\pm} \tag{5.4}$$

where $\omega = 2\pi f$ is the angular frequency, f is the frequency in Hertz, $k = \omega / c_o$ is the local wavenumber, c_o is the local speed of sound and ρ_o is the local fluid density.

The acoustic pressure and axial particle velocity for each duct section are described by a truncated set of modes, m; $m1$ in Section 1 and $m2$ in Section 2 expressed in the following form:

$$P_N^{(m)} = \{A_N^{+}\}^T \{\Psi_N^{+}\} + \{A_N^{-}\}^T \{\Psi_N^{-}\} \tag{5.5}$$

$$U_N^{(m)} = \{B_N^{+}\}^T \{\Psi_N^{+}\} + \{B_N^{-}\}^T \{\Psi_N^{-}\} \tag{5.6}$$

where,

$$\begin{aligned} \Psi_{N,i}^{\pm} &= \psi_{N,i}^{\pm}(\mathbf{x}) e^{-ik_{z,N,i}^{\pm} z} \\ B_{N,i}^{\pm} &= \tfrac{k_{z,N,i}^{\pm}}{\rho_o(\omega - k_{z,N}^{\pm} u_o)} A_{N,i}^{\pm} \end{aligned} \tag{5.7}$$

Neither the revised nor the existing MM procedure is an exact matching procedure, both procedures involve a weighted residual approach in which the residuals are minimised over the area of the duct for three-dimensions or over the width of the duct for two-dimensions. The existing approach minimises the residuals of acoustic pressure and axial particle velocity over the interface between the two regimes using mode eigenfunctions as weighting functions. The revised procedure minimises the residuals of the mass continuity equation and the axial momentum equation over a duct volume enclosing the duct cross section where the impedance discontinuity occurs. Once again transverse eigenfunctions are used as weighting functions. The crucial difference between the two MM procedures is that the volume integral of the revised procedure introduces an integral over the lined surface of the duct which does not necessarily vanish as the control volume shrinks to contain only the matching plane.

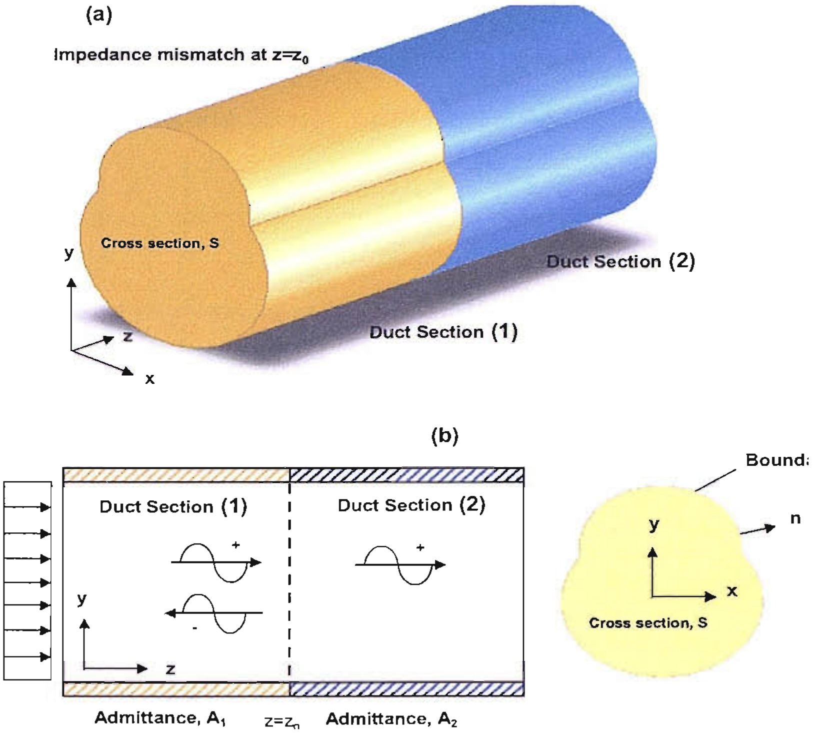

Figure 5.3: An axially uniform duct with an acoustic impedance discontinuity at $x = x_o$. (a) Three-dimensional view, (b) Two-dimensional view.

5.4 Traditional Mode Matching By The Galerkin Weighted Residual Method

The existing MM procedure minimises the residuals of $(P_1^{m1} - P_2^{m2})$ and $(U_1^{m1} - U_2^{m2})$ over the interface between Section (1) and Section (2) using mode eigenfunctions as weighting functions. This yields the following two weak statements:

$$\int_S W\,(P_1^{m1} - P_2^{m2})dS \tag{5.8}$$

$$\int_S W\,(U_1^{m1} - U_2^{m2})dS \tag{5.9}$$

where S is the area of the duct cross section. The Galerkin method selects weighting functions to be from the same class of approximation functions, Ψ_1^+. Substitute Eqs. (5.5) and (5.6) into Eqs. (5.8) and (5.9) to yield:

$$\int_S W\,(\{A_1^+\}^T\{\Psi_1^+\} + \{A_1^-\}^T\{\Psi_1^-\} - \{A_2^+\}^T\{\Psi_2^+\})\,dS = 0 \tag{5.10}$$

$$\int_S W\,(\{B_1^+\}^T\{\Psi_1^+\} + \{B_1^-\}^T\{\Psi_1^-\} - \{B_2^+\}^T\{\Psi_2^+\})\,dS = 0 \tag{5.11}$$

It is given that the coefficients A_1^+ are known and $A_2^- = 0$ as there is an anechoic termination at the exit plane. This yields a system of $2m$ equations with $2m$ unknowns which are then written in the following partition form:

$$\left\{ \begin{array}{c} A_1^- \\ A_2^+ \end{array} \right\} = \left[\mathbf{T}_{1-2}^{\mathrm{GWR}} \right] \left\{ \begin{array}{c} A_1^+ \\ A_2^- \end{array} \right\} \tag{5.12}$$

$\mathbf{T}_{1-2}^{\mathrm{GWR}}$ is the transfer matrix which relates the acoustic pressure and axial particle velocity in Sections (1) and (2) and **GWR** stands for Galerkin weighted residual method. In reaching these equations, the coefficients $B_{N,i}^{\pm}$ have been eliminated in terms of the coefficients $A_{N,i}^{\pm}$. The matrix entries are

$$T_{1-2}^{GWR} = \begin{bmatrix} \mathbf{a}^- & -\mathbf{b}^+ \\ \mathbf{g}^- & -\mathbf{f}^+ \end{bmatrix}^{-1} \begin{bmatrix} \mathbf{a}^+ & -\mathbf{b}^- \\ \mathbf{g}^+ & -\mathbf{f}^- \end{bmatrix} \tag{5.13}$$

where

$$\begin{aligned} a_{i,j}^{\pm} &= \int_S \left(\psi_{1,i}^+ \psi_{1,j}^{\pm} \right) dS \\ b_{i,j}^{\pm} &= \int_S \left(\psi_{1,i}^+ \psi_{2,j}^{\pm} \right) dS \\ g_{i,j}^{\pm} &= \frac{k_{z,1,j}^{\pm}}{\rho_o(\omega - k_{z,1,j}^{\pm} u_o)} \int_S \left(\psi_{1,i}^+ \psi_{1,j}^{\pm} \right) dS \\ f_{i,j}^{\pm} &= \frac{k_{z,2,j}^{\pm}}{\rho_o(\omega - k_{z,2,j}^{\pm} u_o)} \int_S \left(\psi_{1,i}^+ \psi_{2,j}^{\pm} \right) dS \end{aligned} \tag{5.14}$$

$a^{\pm}$, $b^{\pm}$, $g^{\pm}$ and $f^{\pm}$ are each $(N \times N)$ matrices as $N = m1 = m2$. The system is then solved to yield the complex amplitudes of the modes in each duct section for a given A_1^+.

5.4.1 Traditional Mode Matching By The Least Squares Method

The residuals of $(P_1^{m1} - P_2^{m2})$ and $(U_1^{m1} - U_2^{m2})$ over the interface between Section (1) and Section (2) can also be solved by the least squares (LS) method. The residuals $(P_1^m - P_2^m)$ and $(U_1^m - U_2^m)$ are squared and integrated across the duct cross sectional area, S to yield the following two functions:

$$\mathbb{F}_p = \int_S \left| (P_1^{m1} - P_2^{m2}) \right|^2 dS \tag{5.15}$$

$$\mathbb{F}_u = \int_S \left| (U_1^{m1} - U_2^{m2}) \right|^2 dS \tag{5.16}$$

Substitute Eqs. (5.5) and (5.6) into Eqs. (5.15) and (5.16), this yields:

$$\mathbb{F}_p = \int_S \left| \{A_1^+\}^T \{\psi_1^+\} + \{A_1^-\}^T \{\psi_1^-\} - \{A_2^+\}^T \{\psi_2^+\} \right|^2 dS \tag{5.17}$$

$$\mathbb{F}_u = \int_S \left| \{B_1^+\}^T \{\psi_1^+\} + \{B_1^-\}^T \{\psi_1^-\} - \{B_2^+\}^T \{\psi_2^+\} \right|^2 dS \tag{5.18}$$

Both equations are then differentiated with respect to a selected coefficient which is A_1^- in this case. At minimum, the derivatives of $\mathbb{F}_p$ and $\mathbb{F}_u$ are equal to zero:

$$\frac{\partial \mathbb{F}_p}{\partial A_1^{R,-}} + i\frac{\partial \mathbb{F}_p}{\partial A_1^{I,-}} = 0 \ ; \qquad \frac{\partial \mathbb{F}_u}{\partial A_1^{R,-}} + i\frac{\partial \mathbb{F}_u}{\partial A_1^{I,-}} = 0 \tag{5.19}$$

where the subscripts, R and I denote the real and imaginary parts of the coefficients A_1^-. A system of $m1 + m2$ equations with $m1 + m2$ unknowns is yielded which can then be written in the following partition form:

$$\left\{ \begin{array}{c} A_1^- \\ A_2^+ \end{array} \right\} = \left[\mathbf{T}_{1-2}^{\mathbf{LS}} \right] \left\{ \begin{array}{c} A_1^+ \\ A_2^- \end{array} \right\} \tag{5.20}$$

where $\mathbf{T}_{1-2}^{\mathbf{LS}}$ is the transfer matrix which relates the acoustic pressure and axial particle velocity in Sections (1) and (2) and **LS** denotes the least squares method. In reaching these equations, the coefficients $B_{N,i}^{\pm}$ have been eliminated in terms of the coefficients $A_{N,i}^{\pm}$. The matrix entries are:

$$T_{1-2}^{LS} = \begin{bmatrix} \mathbf{a}^- & -\mathbf{b}^+ \\ \mathbf{g}^- & -\mathbf{f}^+ \end{bmatrix}^{-1} \begin{bmatrix} \mathbf{a}^+ & -\mathbf{b}^- \\ \mathbf{g}^+ & -\mathbf{f}^- \end{bmatrix} \tag{5.21}$$

where

$$\begin{aligned} a_{i,j}^{\pm} &= \int_S \left(\psi_{1,i}^- \psi_{1,j}^{*,\pm} \right) dS \\ b_{i,j}^{\pm} &= \int_S \left(\psi_{1,i}^- \psi_{2,j}^{*,\pm} \right) dS \\ g_{i,j}^{\pm} &= \frac{k_{z,1,j}^{\pm}}{\rho_o(\omega - k_{z,1,j}^{\pm} u_o)} \int_S \left(\psi_{1,i}^- \psi_{1,j}^{*,\pm} \right) dS \\ f_{i,j}^{\pm} &= \frac{k_{z,2,j}^{\pm}}{\rho_o(\omega - k_{z,2,j}^{\pm} u_o)} \int_S \left(\psi_{1,i}^- \psi_{2,j}^{*,\pm} \right) dS \end{aligned} \tag{5.22}$$

$a^{\pm}$, $b^{\pm}$, $g^{\pm}$ and $f^{\pm}$ are each $(N \times N)$ square matrices as $N = m1 = m2$. The system is then solved to yield the complex amplitudes of the duct modes in each section for a given A_1^+.

In this particular case, $m1 = m2$ as both functions are minimized with respect to the same coefficient A_1^-. If $\mathbb{F}_p$ and $\mathbb{F}_u$ are minimized with respect to different coefficients, then $m1 \neq m2$. This is the main difference between the two MM models. If the Galerkin weighted residual method is used, $m1 = m2$ so that there are enough equations to solve for the number of unknowns.

5.4.2 New Mode Matching Method By The Galerkin Weighted Residuals

This section describes solving the same problem by the revised MM procedure. The revised procedure minimises the residuals of the mass continuity equation and the axial momentum equation over a duct volume enclosing the duct cross section where the impedance discontinuity occurs. The eigenfunctions are used as weighting functions. In each duct section, the acoustic field governing equations in dimensional form are given by:

$$\text{Momentum equation in the x-direction : } \quad i\omega w + u_o\frac{\partial w}{\partial z} + \frac{1}{\rho_o}\frac{\partial p}{\partial x} = 0 \tag{5.23}$$

$$\text{Momentum equation in the y-direction : } \quad i\omega v + u_o\frac{\partial v}{\partial z} + \frac{1}{\rho_o}\frac{\partial p}{\partial y} = 0 \tag{5.24}$$

$$\text{Momentum equation in the z-direction : } \quad i\omega u + u_o\frac{\partial u}{\partial z} + \frac{1}{\rho_o}\frac{\partial p}{\partial z} = 0 \tag{5.25}$$

$$\text{Mass continuity equation : } \quad i\omega p + u_o\frac{\partial p}{\partial z} + \rho_o c_o^2\left(\frac{\partial w}{\partial x} + \frac{\partial v}{\partial y} + \frac{\partial u}{\partial z}\right) = 0 \tag{5.26}$$

where u, v and w are the acoustic particle velocity in the x, y and z directions respectively and p is the acoustic pressure.

At the impedance discontinuity at $z = z_o$, consider a control volume, V bounded by surfaces $S_{z_o+\delta}$, $S_{z_o-\delta}$ and S_c as shown in Fig. 5.4(a). The surfaces $S_{z_o+\delta}$ and $S_{z_o-\delta}$ are bounded by perimeters $\Gamma_{z_o+\delta}$ and $\Gamma_{z_o-\delta}$ at $z = z_o + \delta$ and $z_o - \delta$ respectively. The control volume encloses the duct cross section where the impedance discontinuity occurs. Let the acoustic admittance, A vary smoothly from A_1 at $z = z_o - \delta$ to A_2 at $z_o + \delta$ at $z = z_o$ as shown in Fig. 5.4(b).

First, consider the weighted form of the axial momentum equation integrated over the control volume, V gives

$$\int_V W\left\{i\omega u + \frac{\partial}{\partial x}(0) + \frac{\partial}{\partial y}(0) + \frac{\partial}{\partial z}(u_o u + \frac{p}{\rho_o})\right\} dV = 0 \tag{5.27}$$

Apply the divergence theorem to give

$$\int_V W i\omega u \, dV + \int_{S_{z_o+\delta}} W(u_o u + \frac{1}{\rho_o}p)\, dS - \int_{S_{z_o-\delta}} W(u_o u + \frac{1}{\rho_o}p)\, dS = 0 \tag{5.28}$$

$\partial W/\partial z = 0$ as W is chosen so that it depends only on the transverse coordinates. Take the limit:

$$\lim_{\delta \to 0}\left\{\int_V W i\omega u \, dV + \int_{S_{z_o+\delta}} W(u_o u + \frac{1}{\rho_o}p)\, dS - \int_{S_{z_o-\delta}} W(u_o u + \frac{1}{\rho_o}p)\, dS\right\} = 0 \tag{5.29}$$

This statement is only true if u is finite or has an integrable singularity at the impedance discontinuity as shown in Fig. 5.5. If the limit of Eq. (5.29) is now taken as δ tends to zero,

$$u_o\int_S W U_2^{m2} dS + \frac{1}{\rho_o}\int_S W P_2^{m2} dS = u_o\int_S W U_1^{m1} dS + \frac{1}{\rho_o}\int_S W P_1^{m1} dS \tag{5.30}$$

where $P_{1,2}^{m1,m2}$ and $U_{1,2}^{m1,m2}$ are the pressure and velocity solutions to the left and right of matching interface, S.

Now let consider the weighted form of the mass continuity equation

$$\int_V W\left\{i\omega p + \frac{\partial}{\partial x}(\rho_o c_o^2 w) + \frac{\partial}{\partial y}(\rho_o c_o^2 v) + \frac{\partial}{\partial z}(u_o p + \rho_o c_o^2 u)\right\} dV = 0 \tag{5.31}$$

Apply the divergence theorem to give:

$$\int_V W(i\omega p - \rho_o c_o^2 \frac{\partial w}{\partial x} - \rho_o c_o^2 \frac{\partial v}{\partial y})dV + \int_{S_{z_o+\delta}} W(u_o p + \rho_o c_o^2 u)dS - \int_{S_{z_o-\delta}} W(u_o p + \rho_o c_o^2 u)dS + \int_{S_c} (\rho_o c_o^2 W \mathbf{u}\cdot\mathbf{n})dS = 0 \tag{5.32}$$

$\partial W/\partial z = 0$ as W is chosen so that it depends only on the transverse coordinates. The last integral term in the equation is associated to the boundary condition of the problem. On the duct boundary, the solution must satisfy the Myers boundary condition [95]:

$$\mathbf{u}\cdot\mathbf{n} = Ap - \frac{iu_o}{\omega}\frac{\partial}{\partial z}(Ap) \tag{5.33}$$

where A is the acoustic admittance, **u** is the particle velocity and **n** denotes the direction normal to the surface S_c. Substitute the Myers boundary condition, Eq. (5.33) into Eq. (5.32) this gives:

$$\begin{aligned} &\int_V W(i\omega p - \rho_o c_o^2 \frac{\partial w}{\partial x} - \rho_o c_o^2 \frac{\partial v}{\partial y})dV + \int_{S_{z_o+\delta}} W(u_o p + \rho_o c_o^2 u)dS - \\ &\int_{S_{z_o-\delta}} W(u_o p + \rho_o c_o^2 u)dS + \int_{S_c} \rho_o c_o^2 W\left[Ap - \frac{iu_o}{\omega}\frac{\partial}{\partial z}(Ap)\right] dS = 0 \end{aligned} \tag{5.34}$$

The last integral in Eq. (5.34) can be rewritten as:

$$\int_{S_c} \rho_o c_o^2 W\left[Ap - \frac{iu_o}{\omega}\frac{\partial}{\partial z}(Ap)\right] dS = \int_{S_c} (\rho_o c_o^2 WAp)dS - \int_{\Gamma_{z_o+\delta}} (i\rho_o c_o^2 \frac{u_o}{\omega} WA_2 p)d\Gamma + \int_{\Gamma_{z_o-\delta}} (i\rho_o c_o^2 \frac{u_o}{\omega} WA_1 p)d\Gamma \tag{5.35}$$

where the last two line integrals are evaluated at the duct perimeters $\Gamma_{z_o+\delta}$ and $\Gamma_{z_o-\delta}$ respectively. Take the limit:

$$\begin{aligned} \lim_{\delta \to 0} \Bigg\{ &\int_V W(i\omega p - \rho_o c_o^2 \frac{\partial w}{\partial x} - \rho_o c_o^2 \frac{\partial v}{\partial y})dV + \int_{S_{z_o+\delta}} W(u_o p + \rho_o c_o^2 u)dS - \int_{S_{z_o-\delta}} W(u_o p + \rho_o c_o^2 u)dS \\ &+ \int_{S_c} (\rho_o c_o^2 WAp)dS - \int_{\Gamma_{z_o+\delta}} (i\rho_o c_o^2 \frac{u_o}{\omega} WA_2 p)d\Gamma + \int_{\Gamma_{z_o-\delta}} (i\rho_o c_o^2 \frac{u_o}{\omega} WA_1 p)d\Gamma \Bigg\} = 0 \end{aligned} \tag{5.36}$$

This statement is only true if p, v and w are finite or have integrable singularities at the impedance discontinuity as shown in Fig. 5.5. If the limit of Eq. (5.29) is now taken as δ tends to zero,

$$\int_S W(u_o P_2^{m2} + \rho_o c_o^2 U_2^{m2})dS - \int_S W(u_o P_1^{m1} + \rho_o c_o^2 U_1^{m1})dS - \int_\Gamma i\rho_o c_o^2 \frac{u_o}{\omega} WA_2 P_2^{m2} d\Gamma + \int_\Gamma i\rho_o c_o^2 \frac{u_o}{\omega} WA_1 P_1^{m1} d\Gamma = 0 \tag{5.37}$$

where $P_{1,2}^{m1,m2}$ and $U_{1,2}^{m1,m2}$ are the pressure and velocity solutions to the left and right of S. For zero flow $(u_o = 0)$, Eqs. (5.30) and (5.37) is equivalent to the corresponding equations from the existing MM procedure. However, when flow is present in the duct, the MM equations from the revised MM procedure show an additional boundary condition term at the matching interface where the impedance discontinuity occurs.

The Galerkin method selects testing functions, $W = \psi_1^+$, from the same class of approximation functions. Substitute Eqs. (5.5) and (5.6) into Eqs. (5.37) and (5.30) to yield

$$\begin{aligned}
&\int_S \left\{\psi_1^+\right\}\left[u_o\left(\left\{A_2^+\right\}^T\left\{\psi_2^+\right\}+\left\{A_2^-\right\}^T\left\{\psi_2^-\right\}\right)+\rho_o c_o^2\left(\left\{B_2^+\right\}^T\left\{\psi_2^+\right\}+\left\{B_2^-\right\}^T\left\{\psi_2^-\right\}\right)\right]dS\\
&-\int_S \left\{\psi_1^+\right\}\left[u_o\left(\left\{A_1^+\right\}^T\left\{\psi_1^+\right\}+\left\{A_1^-\right\}^T\left\{\psi_1^-\right\}\right)+\rho_o c_o^2\left(\left\{B_1^+\right\}^T\left\{\psi_1^+\right\}+\left\{B_1^-\right\}^T\left\{\psi_1^-\right\}\right)\right]dS\\
&-\int_\Gamma i\rho_o c_o^2 \tfrac{u_o}{\omega}\left\{\psi_1^+\right\}A_2\left(\left\{A_2^+\right\}^T\left\{\psi_2^+\right\}+\left\{A_2^-\right\}^T\left\{\psi_2^-\right\}\right)d\Gamma\\
&+\int_\Gamma i\rho_o c_o^2 \tfrac{u_o}{\omega}\left\{\psi_1^+\right\}A_1\left(\left\{A_1^+\right\}^T\left\{\psi_1^+\right\}+\left\{A_1^-\right\}^T\left\{\psi_1^-\right\}\right)d\Gamma=0
\end{aligned} \tag{5.38}$$

The coefficients A_1^+ is known and $A_2^- = 0$ as there is an anechoic termination at the exit plane. A system of $2m$ unknowns with $2m$ equations is yielded which is then written in the following partition form:

$$\begin{Bmatrix} A_1^- \\ A_2^+ \end{Bmatrix} = \left[\mathrm{T}_{1-2}^{\mathrm{N-GWR}}\right]\begin{Bmatrix} A_1^+ \\ A_2^- \end{Bmatrix} \tag{5.39}$$

where T_{1-2}^{N-GWR} is the transfer matrix which relates the momentum flux and mass flux in Sections (1) and (2) and $\mathbf{N-GWR}$ denotes the new MM procedure by the Galerkin weighted residual method. In reaching these equations, the coefficients $B_{N,i}^{\pm}$ have been eliminated in terms of the coefficients $A_{N,i}^{\pm}$. The matrix entries are

$$T_{1-2}^{N-GWR} = \begin{bmatrix} \mathbf{a}^- & -\mathbf{b}^+ \\ \mathbf{g}^- & -\mathbf{f}^+ \end{bmatrix}^{-1}\begin{bmatrix} \mathbf{a}^+ & -\mathbf{b}^- \\ \mathbf{g}^+ & -\mathbf{f}^- \end{bmatrix} \tag{5.40}$$

where

$$\begin{aligned}
a_{i,j}^{\pm} &= \left(\frac{k_{z,1,j}^{\pm}}{\rho_o(\omega-k_{z,1,j}^{\pm}u_o)}+\frac{1}{\rho_o}\right)\int_S\left(\psi_{1,i}^+\psi_{1,j}^{\pm}\right)dS\\
b_{i,j}^{\pm} &= \left(\frac{k_{z,2,j}^{\pm}}{\rho_o(\omega-k_{z,2,j}^{\pm}u_o)}+\frac{1}{\rho_o}\right)\int_S\left(\psi_{1,i}^+\psi_{2,j}^{\pm}\right)dS\\
g_{i,j}^{\pm} &= \left(\frac{k_{z,1,j}^{\pm}c_o^2}{(\omega-k_{z,1,j}^{\pm}u_o)}+u_o\right)\int_S\left(\psi_{1,i}^+\psi_{1,j}^{\pm}\right)dS-\int_\Gamma\left(i\rho_o c_o^2 u_o\omega^{-1}A_1\psi_{1,i}^+\psi_{1,j}^{\pm}\right)d\Gamma\\
f_{i,j}^{\pm} &= \left(\frac{k_{z,2,j}^{\pm}c_o^2}{(\omega-k_{z,2,j}^{\pm}u_o)}+u_o\right)\int_S\left(\psi_{1,i}^+\psi_{2,j}^{\pm}\right)dS-\int_\Gamma\left(i\rho_o c_o^2 u_o\omega^{-1}A_2\psi_{1,i}^+\psi_{2,j}^{\pm}\right)d\Gamma
\end{aligned} \tag{5.41}$$

$a^{\pm}$, $b^{\pm}$, $g^{\pm}$ and $f^{\pm}$ are each $(N \times N)$ square matrices as $N = m1 = m2$. The system is then solved to yield the coefficients of the duct modes for a given A_1^+.

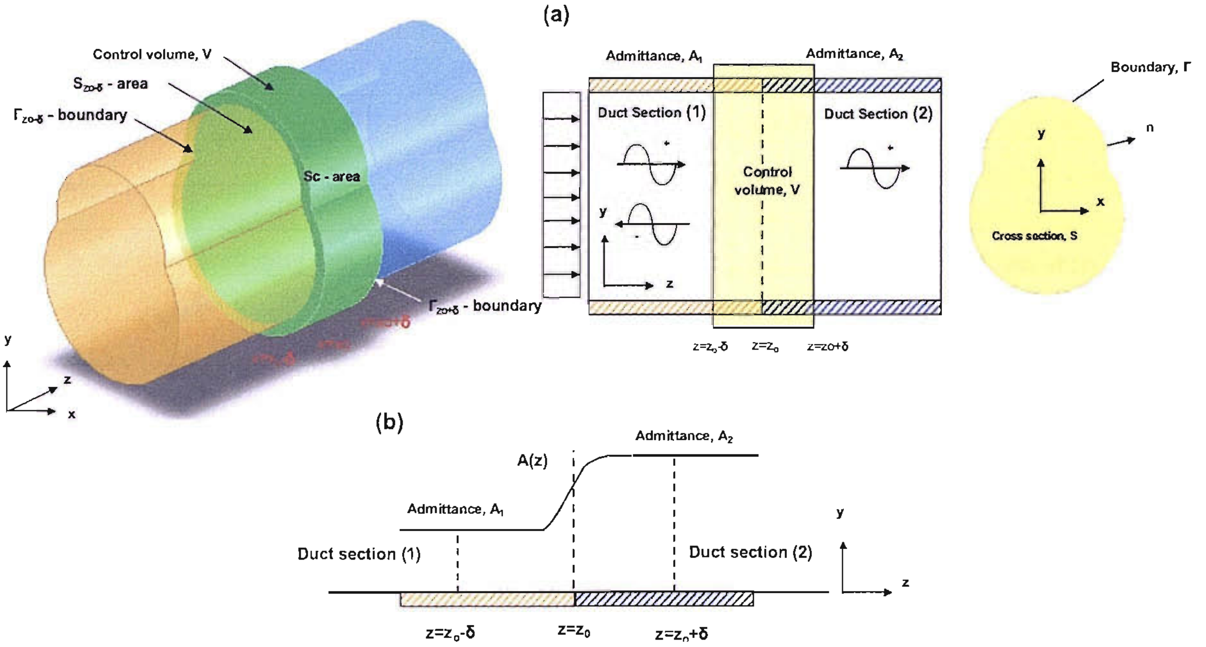

Figure 5.4: (a) Control volume, V bounded by surface areas $S_{z_o+\delta}$, $S_{z_o-\delta}$ and S_c. Surface area $S_{z_o\pm\delta}$ is bounded by perimeter $\Gamma_{z_o\pm\delta}$. (b) Acoustic admittance, A varies smoothly from A_1 at $z=z_o-\delta$ to A_2 at $z_o+\delta$.

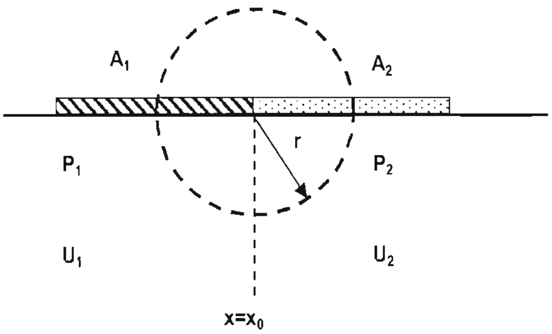

Figure 5.5: Acoustic pressure, p and particle velocity, u behave as $r^{-1/2}$ at the acoustic impedance discontinuity at $z=z_o$ where r is the radius from the discontinuity.

5.5 Application of NMMM To Study Sound Transmission In Flow Ducts

In this section, the revised MM procedure is employed to study transmission of sound in two-dimensional flow ducts with and without the presence of a splitter. The ducts are assumed to be anechoically terminated at both ends and at the inlet of the duct at $x = 0$, a single harmonic mode is incident.

Mode Matching Model

To study acoustic scattering due to the impedance discontinuity, Duct (A) is segmented into three sections; Section (1), Section (2) and Section (3) at $x = x_1$ and x_2 - see Fig. 5.2(a). To study sound diffraction by a splitter, Duct (B) is segmented into four sections; Section (1), Section (2), Section (3) and Section (4) at $x = x_1$ and x_2 - see Fig. 5.2(b).

The superposition of positive and negative acoustic modes that represent the harmonic pressure field in each section are truncated into a finite number of duct modes, N_m. Typically to ensure good accuracy, $N_m >> n_c$, where n_c is the number of cut-on modes as in a hardwalled duct [59]. In practice if $n_c < 5$, then $N_m \geqslant 20$ appears sufficient [59]. The duct modes are numerically computed using the FE eigenvalue model described in Chapter 2. The acoustic field in each section is expressed as:

$$P_N^{N_m} = \sum_{i=0}^{N_m} \left\{ A^+_{N,i} \psi^+_{N,i} e^{-ik^+_{x,N,i}x} + A^-_{N,i} \psi^-_{N,i} e^{-ik^-_{x,N,i}x} \right\} \tag{5.42}$$

where $N = 1,2,3,4$ denotes the duct section, the superscripts $+$ and $-$ signs are associated with duct modes that propagate in the positive and negative x directions and $A^\pm_N$ are the complex amplitudes of the duct modes. The duct eigenfunctions and axial wavenumbers are denoted by $\psi^\pm_N$ and $k^\pm_{x,N}$. The $\psi^\pm_{N,i}$ are represented by a series of nodal pressure and element shape functions:

$$\psi_{N,i}(y) = \sum_{j=1}^{m} N_j(y) p_{j,i} \tag{5.43}$$

where $N_j(y)$ is the element shape function and $p_{j,i}$ is the nodal pressure computed for mode i. The axial particle velocity in each section is expressed as:

$$U_N^{N_m} = \sum_{i=0}^{N_m} \left\{ B^+_{N,i} \psi^+_{N,i} e^{-ik^+_{x,N,i}x} + B^-_{N,i} \psi^-_{N,i} e^{-ik^-_{x,N,i}x} \right\} \tag{5.44}$$

$B^\pm_N$ is related to $A^\pm_N$ using the momentum equation:

$$B^\pm_{N,i} = \frac{k^\pm_{x,N,i}}{\rho_o(\omega - k^\pm_{x,N,i} u_o)} A^\pm_{N,i} \tag{5.45}$$

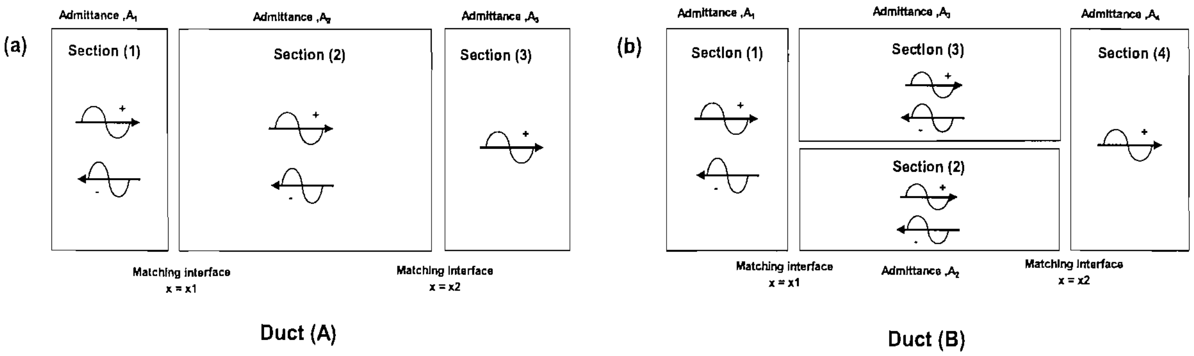

Figure 5.6: Mode matching models (a) Model (A), (b) Model (B).

5.5.1 Duct (A) With Impedance Discontinuities

The revised MM procedure minimises the residual of the mass continuity equation and the axial momentum equation over a duct area enclosing the duct width where the impedance discontinuities occur at $x = x_1$ and x_2. The residuals are minimised using mode eigenfunctions as weighting functions. At $x = x_1$, the following weak statements are yielded:

$$\int_0^h W\left(u_o U_1^{m1} + \frac{1}{\rho_o}P_1^{m1}\right)dy - \int_0^h W\left(u_o U_2^{m2} + \frac{1}{\rho_o}P_2^{m2}\right)dy = 0 \qquad (5.46)$$

and

$$\begin{aligned}&\textstyle\int_0^h W\left(u_o P_1^{m1} + \rho_o c_0^2 U_1^{m1}\right)dy - i\rho_o c_0^2 u_o \omega^{-1}\left[W(h)A_{1,y=h}P_1^{m1}(h) - W(0)A_{1,y=0}P_1^{m1}(0)\right] - \\ &\textstyle\int_0^h W\left(u_o P_2^{m2} + \rho_o c_0^2 U_2^{m2}\right)dy - i\rho_o c_0^2 u_o \omega^{-1}\left[W(h)A_{2,y=h}P_2^{m2}(h) - W(0)A_{2,y=0}P_2^{m2}(0)\right] = 0\end{aligned} \qquad (5.47)$$

where A_1 and A_2 are acoustic admittances of the boundary of Sections (1) and (2). $m1$ and $m2$ are the number of truncated duct modes in Sections (1) and (2) and $m1 = m2$. At $x = x_2$, a further two weak statements are yielded by matching solutions between Sections (2) and (3) using continuity of mass flux and axial momentum flux.

$$\int_0^h W\left(u_o U_2^{m2} + \frac{1}{\rho_o}P_2^{m2}\right)dy - \int_0^h W\left(u_o U_3^{m3} + \frac{1}{\rho_o}P_3^{m3}\right)dy = 0 \qquad (5.48)$$

and

$$\begin{aligned}&\textstyle\int_0^h W\left(u_o P_2^{m2} + \rho_o c_0^2 U_2^{m2}\right)dy - i\rho_o c_0^2 u_o \omega^{-1}\left[W(h)A_{2,y=h}P_2^{m2}(h) - W(0)A_{2,y=0}P_2^{m2}(0)\right] - \\ &\textstyle\int_0^h W\left(u_o P_3^{m3} + \rho_o c_0^2 U_3^{m3}\right)dy - i\rho_o c_0^2 u_o \omega^{-1}\left[W(h)A_{3,y=h}P_3^{m3}(h) - W(0)A_{3,y=0}P_3^{m3}(0)\right] = 0\end{aligned} \qquad (5.49)$$

where A_3 is the acoustic admittance of the boundary of Section (3). $m3$ is the number of truncated duct modes in Section (3) and $m3 = m2 = m1$. The weighting functions are from the same class of approximation functions, $W = \psi_1^+$, the transverse eigenfunctions of Section (1). This results in $4N_m$ sets of equations with $4N_m$ unknown coefficients. Coefficient A_1^+ is known and coefficient $A_3^- = 0$ as there is an anechoic termination at the exit plane at $x = L$.

An iterative scheme proposed by Cummings [2] is employed to solve the problem and to avoid problems associated with ill-conditioning of the matrix. The procedure also reduces the number of equations to be solved simultaneously by a factor of two giving a considerable saving in computation time and resources.

5.5.2 Iterative Method

First, substitute Eqs. (5.42) and (5.44) into Eqs. (5.46) and (5.49) and these equations are rewritten in the following partition form:

$$\left\{ \begin{matrix} A_1^- \\ A_2^+ \end{matrix} \right\} = [\mathrm{T}_{1-2}] \left\{ \begin{matrix} A_1^+ \\ A_2^- \end{matrix} \right\} \tag{5.50}$$

$$\left\{ \begin{matrix} A_2^- \\ A_3^+ \end{matrix} \right\} = [\mathrm{T}_{2-3}] \left\{ \begin{matrix} A_2^+ \\ A_3^- \end{matrix} \right\} \tag{5.51}$$

T_{1-2} and T_{2-3} are transfer matrices which relate solutions between Sections (1) and (2) and between Sections (2) and (3) using continuity of momentum flux and mass flux at $x = x_1$ and x_2 respectively. The entries of the matrices are presented in Appendix **A**. In reaching these equations, the coefficients $B_{N,i}^{\pm}$ have been eliminated in terms of the coefficients $A_{N,i}^{\pm}$.

Coefficients A_3^- and A_2^- are then assumed to be zero. Eq. (5.50) is solved for a known A_1^+. The coefficient A_2^+ calculated is then used in Eq (5.51) to calculate A_2^- and A_3^+. The coefficient A_2^- with the known A_1^+ is then used in Eq. (5.50) to compute a new A_2^+. A_2^- in Eq. (5.51) is then recomputed using the A_2^+ computed from Eq. (5.50). The process is repeated until both coefficients A_1^- and A_3^+ or all the coefficients cease to change significantly or converged.

5.5.3 Acoustic Performance

Modal Intensity

There a number of measures of the performance of the acoustic treatment in the duct. A common measure is by the change in the sum of acoustic power in all the cut-on modes at the source and exit planes. The acoustic power in each mode can be summed because the mode eigenfunctions are orthogonal. At the source plane, it is assumed that all the acoustic energy is contained in the incident mode(s). At the exit plane, due to liner scattering, it is anticipated that all the cut-on modes will contain some acoustic energy. The sum of acoustic power in all the cut-on modes at the source and exit planes is $W_{x=0} = \sum_{i=1}^{m1} PWL_i$ and $W_{x=L} = \sum_{i=1}^{m3} PWL_i$ respectively. PWL is the average modal intensity computed using the Morfey expression of acoustic intensity

[102, 103].

The expression for acoustic intensity $I(t)$ proposed by Morfey is defined as:

$$I(t) = p(t)\mathbf{u(t)} + \rho_o(\mathbf{u_o}\cdot\mathbf{u(t)})u(t) + \frac{1}{\rho_o c_o^2}\mathbf{u_o}p^2(t) + \frac{1}{c_o^2}\mathbf{u_o}(\mathbf{u_o}\cdot\mathbf{u(t)})p(t) \tag{5.52}$$

where $p(t)$ is the instantaneous acoustic pressure and $\mathbf{u(t)} = (u, v, w)$ is the instantaneous particle velocity. $\mathbf{u_o} = (u_o, v_o, w_{o,z})$ is the instantaneous particle velocity. The time-averaged acoustic intensity, I in the duct axial direction is defined as:

$$I = < I(t) > = \frac{1}{2}(1 + M_o^2)Re(p^*u) + \frac{M_o}{2\rho_o c_o}|p^2| + \frac{1}{2}\rho_o u_o|u^2| \tag{5.53}$$

where $M_o = u_o/c_o$ is the axial mean flow Mach number. The average modal intensity, PWL is obtained by integrating the local acoustic intensity, I over the width of the duct, h and the contribution of the impedance boundary:

$$PWL = \int_0^h \left[\frac{1}{2}(1 + M_o^2)Re(p^*u) + \frac{M_o}{2\rho_o c_o}|p^2| + \frac{1}{2}\rho_o u_o|u^2|\right] dy + \text{boundary condition term} \tag{5.54}$$

and the boundary condition term is given by [103]:

$$\left[\rho_o M_o c_o \left(\frac{p}{\rho_o} + M_o c_o u\right)\zeta\right]_0^h \tag{5.55}$$

where ζ is the particle displacement of the wall directed into the wall and it is related to the fluid particle velocity in the normal direction of the wall and directed into the wall, $\mathbf{V}\cdot\upsilon$:

$$\mathbf{V}\cdot\upsilon = \left(ik + M_o\frac{\partial}{\partial x}\right)\zeta \tag{5.56}$$

PWL is expressed in decibels (dB) using the following expression:

$$PWL = 10log_{10}\left(\frac{PWL}{I_{ref}}\right) \quad (dB) \tag{5.57}$$

I_{ref} is the reference modal intensity defined by:

$$I_{ref} = \frac{\left(1 + sign(k_x^{\pm})M_o\right)\left(2\times 10^{-5}\right)^2}{\rho_0 c_o} \tag{5.58}$$

The in-duct sound power transmission loss, $\triangle PWL$ defined as the ratio of transmitted to incident sound power in dB and is given by

$$\Delta PWL = -10\log_{10}\left(\frac{\sum_{i=1}^{n_e} PWL_i|_{x=L}}{\sum_{i=1}^{n_i} PWL_i|_{x=0}}\right) \tag{5.59}$$

where n_e and n_i are the number of cut-on modes at the source and exit planes of the duct. A value of zero for the relative ΔPWL corresponds to zero attenuation or no energy loss in the duct.

5.5.4 Duct (B) With An Infinitely Thin Splitter

The revised MM procedure minimises the residual of the mass continuity equation and the axial momentum equation over a duct area enclosing the duct width where the impedance discontinuities and geometrical change occurred at $x = x_1$ and x_2. The residuals are minimised using mode eigenfunctions as weighting functions. At $x = x_1$, the following weak statements are yielded:

$$\int_0^h W\left(u_o U_1^{m1} + \frac{1}{\rho_o} P_1^{m1}\right) dy - \int_0^{h1} W\left(u_o U_2^{m2} + \frac{1}{\rho_o} P_2^{m2}\right) dy - \int_{h1}^h W\left(u_o U_3^{m3} + \frac{1}{\rho_o} P_3^{m3}\right) dy = 0 \quad (5.60)$$

and

$$\begin{aligned}
&\int_0^h W\left(u_o P_1^{m1} + \rho_o c_0^2 U_1^{m1}\right) dy - i\rho_o c_0^2 u_o \omega^{-1}\left[A_{1,y=h} W(h) P_1^{m1}(h) - A_{1,y=0} W(0) P_1^{m1}(0)\right] - \\
&\int_0^{h1} W\left(u_o P_2^{m2} + \rho_o c_0^2 U_2^{m2}\right) dy - i\rho_o c_0^2 u_o \omega^{-1}\left[A_{2,y=h1} W(h1) P_2^{m2}(h1) - A_{2,y=0} W(0) P_2^{m2}(h1)\right] - \\
&\int_{h1}^h W\left(u_o P_3^{m3} + \rho_o c_0^2 U_3^{m3}\right) dy - i\rho_o c_0^2 u_o \omega^{-1}\left[A_{3,y=h} W(h) P_3^{m3}(h) - A_{3,y=h1} W(h1) P_3^{m3}(h1)\right] = 0
\end{aligned} \quad (5.61)$$

where A_1, A_2 and A_3 are acoustic admittances of the boundary of Sections (1) to (3). Matching solutions between Sections (2) to (4) at $x = x_2$ using continuity of mass flux and axial momentum flux yields the following two weak statements:

$$\int_0^{h1} W\left(u_o U_2^{m2} + \frac{1}{\rho_o} P_2^{m2}\right) dy + \int_{h1}^h W\left(u_o U_3^{m3} + \frac{1}{\rho_o} P_3^{m3}\right) dy - \int_0^h W\left(u_o U_4^{m4} + \frac{1}{\rho_o} P_4^{m4}\right) dy = 0 \quad (5.62)$$

and

$$\begin{aligned}
&\int_0^{h1} W\left(u_o P_2^{m2} + \rho_o c_0^2 U_2^{m2}\right) dy - i\rho_o c_0^2 u_o \omega^{-1}\left[A_{2,y=h1} W(h1) P_2^{m2}(h1) - A_{2,y=0} W(0) P_2^{m2}(0)\right] + \\
&\int_{h1}^h W\left(u_o P_3^{m3} + \rho_o c_0^2 U_3^{m3}\right) dy - i\rho_o c_0^2 u_o \omega^{-1}\left[A_{3,y=h} W(h) P_3^{m3}(h) - A_{3,y=h1} W(h1) P_3^{m3}(h1)\right] - \\
&\int_0^h W\left(u_o P_4^{m4} + \rho_o c_0^2 U_4^{m4}\right) dy - i\rho_o c_0^2 u_o \omega^{-1}\left[A_{4,y=h} W(h) P_4^{m4}(h) - A_{4,y=0} W(0) P_4^{m4}(0)\right] = 0
\end{aligned} \quad (5.63)$$

where A_4 is the acoustic admittance of the boundary of Section (4) and $m4$ is the number of truncated modes in Section (4). The total number of modes in Sections (2) and (3) is equal to number of modes in Section (1) or (4), which is in proportion with the width of the duct, $m2 + m3 = m1 = m4$. The theory of relative convergence states that for regions of similar geometry, the ratio of the number of modes is the same as the ratio of the characteristic sizes [104]. When dealing with two circular ducts with a radius ratio of 2 : 1, the number of mode ratio must be 2 : 1.

The testing function, W is selected to be the eigenfunction of Section (1), $W = \psi_1^+$. This leads to $6N_m$ sets of equations with $6N_m$ unknown coefficients. Eqs. (5.60) and (5.63 and Eqs. (5.42) and (5.44) are rearranged into the following partition format and solved using the iterative procedure [2].

$$\begin{Bmatrix} A_1^- \\ A_2^+ \\ A_3^+ \end{Bmatrix} = [\mathbf{T}_{1-2-3}] \begin{Bmatrix} A_1^+ \\ A_2^- \\ A_3^- \end{Bmatrix} \tag{5.64}$$

$$\begin{Bmatrix} A_2^- \\ A_3^- \\ A_4^+ \end{Bmatrix} = [\mathbf{T}_{2-3-4}] \begin{Bmatrix} A_2^+ \\ A_3^+ \\ A_4^- \end{Bmatrix} \tag{5.65}$$

$\mathbf{T}_{1-2-3}$ and $\mathbf{T}_{2-3-4}$ are transfer matrices which relate solutions between Sections (1)-(3) and between Section (2)-(4) using continuity of mass and momentum. Expressions for their component terms are listed in Appendix A. In reaching these equations, the coefficients $B_{N,i}^{\pm}$ have been eliminated in terms of the coefficients $A_{N,i}^{\pm}$.

Coefficients A_4^-, A_2^- and A_3^- are first assumed to be zero. Eq. (5.64) is solved with a known A_1^+. The coefficients A_2^+ and A_3^+ calculated are then used in Eq (5.65) to compute coefficients A_2^- and A_3^-. The coefficients A_2^- and A_3^- calculated from Eq. (5.65) are then used in Eq. (5.64) to recompute new coefficients A_2^+ and A_3^+. These coefficients are then used to calculate the A_2^- and A_3^- in Eq. (5.65). The process is repeated until coefficients A_2^-, A_3^- and A_4^+ or all the coefficients cease to change significantly or converged.

Chapter 6

Finite Element Method

6.1 Introduction

In this chapter, the formulation of an finite element (FE) transmission model is presented. It models the sound field in a domain which extends a finite distance along the duct. Some results of validation and convergence of the FE transmission model are also presented. Factors that affect the FE solutions such the mesh refinement, mesh uniformity and element type are explored. The FE transmission model is to provide a validation for the mode matching results. The formulation of a FE flow model for computing steady compressible mean flow in the duct is also presented.

6.1.1 Outline

In Section 6.2, the problems are posed. Aspects such as the duct geometries, liner impedances and aspects of the computational models are described. Section 6.4 presents the formulation of the FE transmission model followed by some results of validation and convergence of the FE transmission model in Section 6.6. In Section 6.7, results of a numerical study of the effect of splitter thickness on sound propagation in a two-dimensional duct are presented. Section 6.5.2 presents the formulation of the FE flow model followed by some results.

6.2 Problem Specification

A two-dimensional duct consisting of a hard-soft-hard section as shown in Fig. 6.1 is considered in the study. The boundaries Γ_t and Γ_b, at the top and bottom of the duct, are lined with an acoustic liner whose impedance is Z_t and Z_b, respectively. The boundary Γ_h is acoustically hard. The duct inlet Γ_i at $x = 0$ is the plane on which the sound source is defined and the duct outlet Γ_o at $x = L$ is assumed to be anechoically terminated. The acoustic domain ω is bounded by boundaries Γ_i, Γ_h, Γ_b, Γ_o and Γ_t. M_o denotes the flow Mach number in the duct.

The duct is discretized using structured or unstructured meshes constructed from either 8-noded quadrilateral elements or 6-noded triangular elements with an average mesh resolution of 8 to 10 nodes per wavelength.

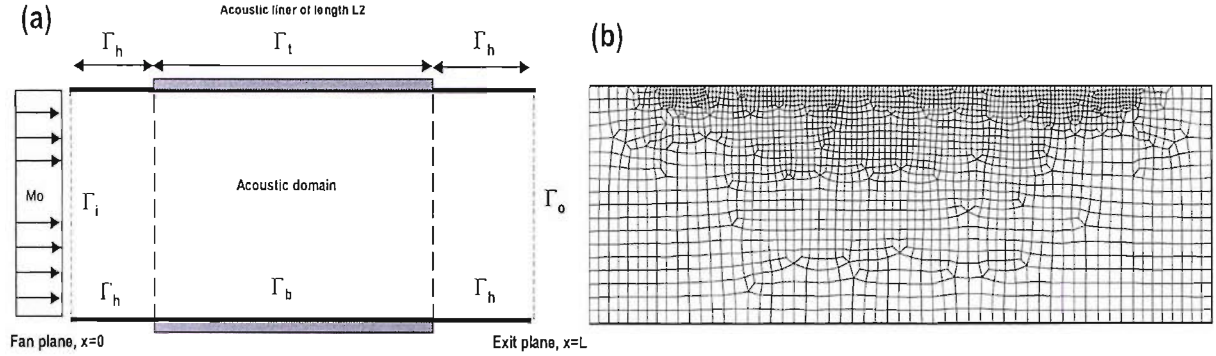

Figure 6.1: (a) A uniform flow duct with a hard-soft-hard-walled section, (b) An FE mesh constructed from 8-noded quadrilateral elements.

The mesh resolution is defined by the number of nodes which are required to represent accurately the solution over one wavelength:

$$N = \frac{c_o}{f\Delta|1 - M_o|} \tag{6.1}$$

where c_o is the speed of sound, f is the frequency in Hertz and Δ is the average distance between nodes. For many engineering purposes, a mesh resolution of 8 to 10 nodes per wavelength is the rule of thumb reference. The resolution of the mesh in the y direction is given by $N = c_o/f\Delta$ as no account is taken for the effect of flow. Fig. 6.1(b) shows a typical example of the mesh constructed in this study. The mesh near to the impedance boundary has been refined.

6.2.1 Benchmark Results

In this research, FE solutions obtained using ACTRAN are used to validate the results obtained using mode matching (MM). ACTRAN is a commercial code produced by Free Field Technologies [105] which is capable of predicting sound propagation in non-uniform ducts with non-uniform mean flow and impedance boundaries. In this research, a FE transmission code similar to ACTRAN but which uses a slightly different matching procedure is written by the author for two-dimensional problems. The in-house FE transmission code is to provide a validation for the mode matching results in addition to the ACTRAN results. It is also desirable to have an in-house code with access to source.

6.3 Derivation of The Converted Wave Equation

In this section, the linearized wave equations that governing the isentropic motion of a non-viscous, non-heat conducting perfect gas in a duct are derived. To reduce the complexity of the problem, the present analysis will be confined to two-dimensions and uniform mean flow is assumed. The field governing equations are:

$$\text{Continuity}: \quad \frac{\partial \rho^*}{\partial t} + \nabla \cdot \rho^* \mathbf{U}^* = 0 \tag{6.2}$$

$$\text{Momentum}: \quad \frac{\partial \mathbf{U}^*}{\partial t} + (\mathbf{U}^* \cdot \nabla)\mathbf{U}^* = -\frac{1}{\rho^*}\nabla p^* = 0 \tag{6.3}$$

$$\text{Equation of state}: \quad p^* = \frac{1}{\gamma}\rho^{*\gamma} \tag{6.4}$$

where p^* is the pressure, $\mathbf{U}^*$ is the velocity, ρ^* is the local fluid density and $\gamma = 1.4$ is the ratio of specific heats at constant pressure and volume. The acoustic equations are obtained by considering small perturbations on a mean state ρ_o, p_o and u_o:

$$\begin{aligned} \rho^* &= \rho_o + \rho \\ p^* &= p_o + p \\ \mathbf{U}^* &= \mathbf{U_o} + \mathbf{U} \end{aligned} \tag{6.5}$$

Substitute Eq. (6.5) into the field governing equations, Eqs. (6.2) to (6.4). Ignore the products of perturbation, the following linearized acoustic field governing equations are obtained:

$$\text{Acoustic Continuity}: \quad \frac{\partial \rho}{\partial t} + \nabla \cdot (\rho_o \mathbf{U} + \rho \mathbf{U_o}) = 0 \tag{6.6}$$

$$\text{Acoustic Momentum}: \quad \frac{\partial \mathbf{U}}{\partial t} + (\mathbf{U_o} \cdot \nabla)\mathbf{U} + \frac{1}{\rho_o}\nabla p + \mathbf{U} \cdot \nabla \mathbf{U_o} - \frac{1}{\gamma p_o \rho_o} p \nabla p_o = 0 \tag{6.7}$$

$$\text{Acoustic Equation of State}: \quad p = c_o^2 \rho \tag{6.8}$$

where c_o is the speed of sound.

6.4 Velocity Potential Formulation

Assuming both the steady and acoustic parts are irrotational, the velocity $\mathbf{U}^*$ can be expressed in terms of a velocity potential, $\hat{\phi}$ where

$$\mathbf{U}^* = \nabla \hat{\phi} \tag{6.9}$$

Acoustic disturbances in the flow can be described by decomposing the velocity potential, $\hat{\phi}$ as

$$\hat{\phi}(\mathbf{x}, t) = \phi_o(\mathbf{x}) + \phi(\mathbf{x}, t) \tag{6.10}$$

where the steady-state mean flow is given by

$$\mathbf{U}_o(\mathbf{x}) = \nabla \phi_o(\mathbf{x}) \tag{6.11}$$

and the harmonic acoustic disturbances are given by

$$\phi(\mathbf{x},t) = \phi(\mathbf{x})e^{i\omega t} \tag{6.12}$$

It is assumed that the acoustic velocity potential $\phi_o >> \phi$. The linearized acoustic mass and momentum equations, Eqs. (6.6) and (6.7), can be written in terms of the velocity potential, ϕ:

$$\text{Acoustic Continuity}: \quad \frac{\partial \rho}{\partial t} + \nabla \cdot (\rho_o \nabla \phi + \nabla \rho \phi_o) = 0 \tag{6.13}$$

$$\text{Acoustic Momentum}: \quad \rho = -\frac{\rho_o}{c_o^2}(\frac{\partial \phi}{\partial t} + \nabla \phi_o \cdot \nabla \phi) \tag{6.14}$$

In reaching these equations, the second and higher order terms in the small perturbations have been ignored. Using the linearized isentropic equation of state, Eq. (6.8), the acoustic pressure, p can be related to the acoustic potential, ϕ by

$$p = -\rho_o(\frac{\partial \phi}{\partial t} + \nabla \phi_o \cdot \nabla \phi) \tag{6.15}$$

On combining Eqs. (6.13) and (6.14), the convected wave equation in ϕ is obtained:

$$\frac{\partial}{\partial t}\left\{-\frac{\rho_o}{c_o^2}(\frac{\partial \phi}{\partial t} + \nabla \phi_o \cdot \nabla \phi)\right\} + \nabla \cdot \left\{\rho_o \nabla \phi - \frac{\rho_o}{c_o^2}(\frac{\partial \phi}{\partial t} + \nabla \phi_o \cdot \nabla \phi)\nabla \phi_o\right\} = 0 \tag{6.16}$$

6.4.1 The FE Transmission Model

The FE transmission model is based on a weak variational statement constructed by multiplying the convected wave equation, Eq. (6.16), by weighting functions, W and integrating over the acoustic domain, Ω:

$$\int_\Omega \rho_o W \left\{\frac{\omega^2}{c_o^2}\phi - \frac{i\omega}{c_o^2}\mathbf{U_o} \cdot \nabla \phi + \nabla \cdot [\nabla \phi - \frac{1}{c_o^2}(i\omega \phi + \mathbf{U_o} \cdot \nabla \phi)\mathbf{U_o}]\right\} d\Omega = 0 \tag{6.17}$$

where $W(\mathbf{x}) \in H(R)$. Apply the divergence theorem to Eq. (6.17) to obtain:

$$\begin{aligned} &\textstyle\int_\Omega \left\{\rho_o W \left[\frac{\omega^2}{c_o^2}\phi - \frac{i\omega}{c_o}\mathbf{M_o} \cdot \nabla \phi\right] - \nabla W \cdot \left[\rho_o \nabla \phi - \rho_o \left(\frac{i\omega}{c_o}\phi + \mathbf{M_o} \cdot \nabla \phi\right)\mathbf{M_o}\right]\right\} d\Omega \\ &+ \textstyle\int_\Gamma W \left\{\rho_o \nabla \phi - \rho_o \left(\frac{i\omega}{c_o}\phi + \mathbf{M_o} \cdot \nabla \phi\right)\mathbf{M_o}\right\} \cdot \mathbf{n}\, d\Gamma = 0 \end{aligned} \tag{6.18}$$

The line integral in the equation is associated with the boundary conditions of the problem. $\mathbf{M_o} = \mathbf{U_o}/c_o$ denotes the flow Mach number in the duct and $\mathbf{n}$ is the normal outward from the boundary, Γ.

The acoustic domain, Ω is then discretized using finite elements which take the form

$$\phi(\mathbf{x}) = \sum_{j=1}^{N} N_j(\mathbf{x})\phi_j \tag{6.19}$$

where ϕ_j is the nodal value of $\phi(\mathbf{x})$ in the FE region and $N_j(\mathbf{x})$ are the element shape functions which have the following property at a nodal point x_j,

$$N_i(x_j) = \begin{cases} 1, & (j = i), \\ 0, & (j \neq i). \end{cases}$$

The shape functions for an 8-noded quadrilateral element are - see Fig. 6.2(a):

$$\begin{aligned}
N_1(\xi,\eta) &= (1/4)\xi(1-\xi)\eta(1-\eta) \\
N_2(\xi,\eta) &= -(1/2)\xi(1-\xi)(1+\eta)(1-\eta) \\
N_3(\xi,\eta) &= (1/4)\xi(1-\xi)\eta(1+\eta) \\
N_4(\xi,\eta) &= -(1/2)(1+\xi)(1-\xi)\eta(1+\eta) \\
N_5(\xi,\eta) &= (1/4)\xi(1+\xi)\eta(1+\eta) \\
N_6(\xi,\eta) &= -(1/2)\xi(1+\xi)(1+\eta)(1-\eta) \\
N_7(\xi,\eta) &= (1/4)\xi(1+\xi)\eta(1-\eta) \\
N_8(\xi,\eta) &= -(1/2)(1+\xi)(1-\xi)\eta(1-\eta)
\end{aligned} \tag{6.20}$$

where ξ and η are the local coordinates. The element shape functions for a 6-noded triangular element are - see Fig. 6.2(b):

$$\begin{aligned}
N_1(\xi,\eta) &= 1-\xi-\eta \\
N_2(\xi,\eta) &= \xi \\
N_3(\xi,\eta) &= \eta \\
N_4(\xi,\eta) &= 4\xi(1-\xi-\eta) \\
N_5(\xi,\eta) &= 4\eta(1-\xi-\eta) \\
N_6(\xi,\eta) &= 4\xi\eta
\end{aligned} \tag{6.21}$$

The Galerkin method selects weighting functions, $W_i(\mathbf{x})$ equal to $N_i(\mathbf{x})$, the element shape functions. Eq. (6.18) is then written in the following discrete form:

$$[\mathbf{A}]\{\phi\} + \{\mathbf{B}\} = \{0\} \tag{6.22}$$

where the $[\mathbf{A}]$ term is assembled from the surface integral term:

$$A_{ij} = \int_{\Omega} \left\{ \rho_o N_i \left[\frac{\omega^2}{c_o^2} N_j - \frac{i\omega}{c_o} \mathbf{M}_0 \cdot \nabla N_j \right] - \nabla N_i \cdot \left[\rho_o \nabla N_j - \rho_o \left(\frac{i\omega}{c_o} N_j + \mathbf{M}_0 \cdot \nabla N_j \right) \mathbf{M}_0 \right] \right\} d\Omega \tag{6.23}$$

and the $\{B\}$ term is assembled from the boundary integral term:

$$B_i = \int_{\Gamma} N_i \left\{ \rho_o \nabla N_j \phi_j - \rho_o \left(\frac{i\omega}{c_o} N_j \phi_j + \mathbf{M}_0 \cdot \nabla N_j \phi_j \right) \mathbf{M}_0 \right\} \cdot \mathbf{n} \, d\Gamma \tag{6.24}$$

An important aspect of the FE analysis is the mapping from local coordinates to global coordinates. This

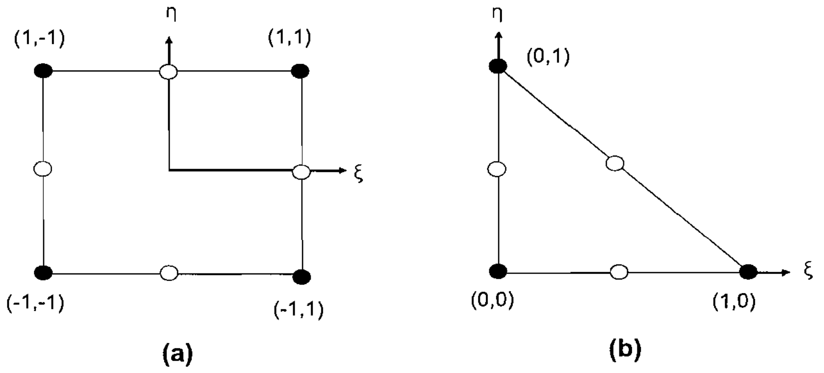

Figure 6.2: (a) 8-noded quadrilateral element, (b) 6-noded triangular element.

is needed for a systematic way of integrating different elements of different sizes and shapes throughout the meshed model. The relation between the local and global coordinates is given by

$$dXdY = |J|d\eta d\xi \tag{6.25}$$

where $|J|$ is the Jacobian which is the determinant of

$$J = \begin{bmatrix} \frac{\partial X}{\partial \xi} & \frac{\partial Y}{\partial \xi} \\ \frac{\partial X}{\partial \eta} & \frac{\partial Y}{\partial \eta} \end{bmatrix} \tag{6.26}$$

X and Y are the global coordinates defined as

$$\mathrm{X} = \sum N_i \mathrm{X_i} \qquad \mathrm{Y} = \sum N_i \mathrm{Y_i} \tag{6.27}$$

N_i is the shape function for node i and X_i and Y_i are the global coordinates x and y of node i.

6.4.2 Admittance Boundary

On boundaries, Γ_l, Γ_b and Γ_h, $\mathbf{M_0} \cdot \mathbf{n} = 0$ and $\nabla\phi \cdot \mathbf{n} = u_n$ as the mean flow is tangential to the boundary. The boundary integral term in Eq. (6.24) becomes

$$\int_\Gamma W\rho_o \nabla\phi \cdot \mathbf{n}\, d\Gamma \tag{6.28}$$

The solution on the boundary must satisfy the Myers boundary condition [95]:

$$\nabla\phi \cdot \mathbf{n} = \mathbf{u_n} \cdot \mathbf{n} = A_n p - \frac{iu_o}{\omega}\frac{\partial}{\partial x}(A_n p) \tag{6.29}$$

where A_n is the acoustic admittance normal to the boundary and u_o is the mean flow in the x direction. On Γ_b substitute Eq. (6.29) into Eq. (6.28). The following expression is obtained:

$$\int_{\Gamma_b} W\rho_o \nabla\phi\cdot\mathbf{n}d\Gamma = -\int_{\Gamma_b} \rho_o W\left\{A_n p - \frac{iu_o}{\omega}\frac{\partial}{\partial x}(A_n p)\right\}d\Gamma \tag{6.30}$$

Using Eq. (6.15), the acoustic pressure in the equation can be replaced by the velocity potential. This leads to

$$A^{Z}_{i,j} = -\int_{\Gamma_b} \rho_o N_i\left\{-A_n\rho_o(i\omega N_j + u_o\frac{\partial N_j}{\partial x}) + \frac{iu_o}{\omega}\frac{\partial}{\partial x}\left(A_n\rho_o(i\omega N_j + u_o\frac{\partial N_j}{\partial x})\right)\right\}d\Gamma \tag{6.31}$$

where $A^{Z}_{i,j}$ is non-zero if i and j correspond to a node on Γ_b. Eq. (6.31) can be further simplified to

$$A^{Z}_{i,j} = \int_{\Gamma_b} \rho_o^2 A_n\left\{N_i i\omega N_j + N_i u_o\frac{\partial N_j}{\partial x} - (u_o\frac{\partial N_i}{\partial x})N_j - \frac{1}{i\omega}(u_o\frac{\partial N_i}{\partial x})(u_o\frac{\partial N_j}{\partial x})\right\}d\Gamma \tag{6.32}$$

6.4.3 Modal Boundary

On boundaries Γ_i and Γ_o, modal boundary conditions are prescribed. Two modal matching procedures are considered in this work; a direct method and a Galerkin weighted residuals method. For both procedures, the accurate matching of the eigenfunctions on the modal boundary is depended on good approximation by the FE interpolation functions. To ensure the duct eigenfunctions are computed accurately in this study, the mesh used must have resolution of 10 to 12 nodes per wavelength.

Modal Matching By A Galerkin Weighted Residuals Method

At $x = 0$, the plane Γ_i is perpendicular to the x axis. Assume that the modal plane is adjacent to the FE region, then $W_i(y) = N_i(y)$. The modal boundary matching term is expressed as:

$$B_{i,j} = \int_{\Gamma_i} N_i\left\{\rho_o\nabla\phi_j - \rho_o\left(\frac{i\omega}{c_o}\phi_j + \mathbf{M_o}\cdot\nabla\phi_j\right)\mathbf{M_o}\right\}\cdot\mathbf{n}d\Gamma \tag{6.33}$$

ϕ_j at $x = 0$ is assumed to have the form:

$$\phi_j(y) = \sum_{j=1}^{m}\left(a_j^+\phi_j^+(y)e^{-ik^{+}_{x,j}x} + a_j^-\phi_j^-(y)e^{-ik^{-}_{x,j}x}\right) \tag{6.34}$$

where the superscripts + and − signs are associated with waves propagating in the positive and negative x directions. $a^{\pm}$ are coefficients of the positive and negative acoustic modes and $\phi(y)^{\pm}_j$ and $k^{\pm}_{x,j}$ are the corresponding duct eigenfunctions and axial wavenumbers respectively. ϕ_j is truncated to number m modes. Substitute Eq. (6.34) and its derivative, $\partial\phi/\partial x$ into Eq. (6.33) and write the equation in the following discrete form:

$$\underset{n\times 1}{\{\mathbf{B}^{\mathbf{inlet}}\}} = \underset{n\times m}{[\mathbf{B}^{+}_{\mathbf{in}}]}\underset{m\times 1}{\{a^+\}} + \underset{n\times m}{[\mathbf{B}^{-}_{\mathbf{in}}]}\underset{m\times 1}{\{a^-\}} \tag{6.35}$$

where n is the number of degrees of freedom and

$$B^{\pm}_{in,i,j} = i\int_{\Gamma_i}\left\{\rho_o N_i\left[(1-M_o^2)k^{\pm}_{x,j}+M_o k\right]\phi^{\pm}_j(y)e^{-ik^{\pm}_{x,j}x}\right\}d\Gamma \tag{6.36}$$

The system is under-determined so m equations are still required for the solutions. The additional equations are provided by implying potential continuity on the plane Γ_i [11, 13, 51]. The residuals $(\phi-\phi_{in})$ are weighted over the duct width by testing functions, F to give

$$\int_{\Gamma_i}\{F(\phi-\phi_{in})\}\,d\Gamma = 0 \tag{6.37}$$

$\phi_{in}(y)$ is assumed to have the form:

$$\phi_{in}(y) = \sum_{j=1}^{m}\left(a^+_j\phi^+_j(y)e^{-ik^+_{x,j}x}+a^-_j\phi^-_j(y)e^{-ik^-_{x,j}x}\right) \tag{6.38}$$

ϕ_{in} has been truncated to number m of modes. Substitute Eq. (6.38) into Eq. (6.37) and the equation is written in the following discrete form:

$$\underset{m\times m}{[\mathbf{D}^+_{\mathbf{in}}]}\underset{m\times 1}{\{a^+\}}+\underset{m\times m}{[\mathbf{D}^-_{\mathbf{in}}]}\underset{m\times 1}{\{a^-\}}+\underset{m\times n}{[\mathbf{E}_{\mathbf{in}}]}\underset{n\times 1}{\{\phi\}} = \{0\} \tag{6.39}$$

where

$$D^{\pm}_{in,i,j} = -\int_{\Gamma_i}F_i\phi^{\pm}_j(y)e^{-ik^{\pm}_{x,j}x}d\Gamma \tag{6.40}$$

and

$$E_{in,i,j} = \int_{\Gamma_i}F_iN_jd\Gamma \tag{6.41}$$

On plane Γ_o at $x=L$, a similar modal matching procedure is applied. The modal matching term is expressed as:

$$B_{i,j} = \int_{\Gamma_o}N_i\left\{\rho_o\nabla\phi_j-\rho_o\left(\frac{i\omega}{c_o}\phi_j+\mathbf{M_o}\cdot\nabla\phi_j\right)\mathbf{M_o}\right\}\cdot\mathbf{n}d\Gamma \tag{6.42}$$

ϕ_j is assumed to be in the form:

$$\phi_j(y) = \sum_{j=1}^{m}\left(b^+_j\psi^+_j(y)e^{-ik^+_{x,j}x}\right) \tag{6.43}$$

where b^+_j are coefficients of the positive acoustic modes and $\psi^+_j(y)$ are the corresponding duct eigenfunctions. The duct is assumed to be anechoically terminated. Substituting Eq. (6.43) into Eq. (6.42) and write the equation in the following discrete form:

$$\underset{n\times 1}{\{\mathbf{B}^{\text{outlet}}\}} = \underset{n\times m}{[\mathbf{B}^+_{\mathbf{out}}]}\underset{m\times 1}{\{b^+\}} \tag{6.44}$$

where,

$$B^{+}_{out,i,j} = -i\int_{\Gamma_o}\left\{\rho_o N_i\left[(1-M_o^2)k^{+}_{x,j}+M_o k\right]\psi_j^{+}(y)e^{-ik^{+}_{x,j}x}\right\}d\Gamma \tag{6.45}$$

The additional equations are obtained by implying continuity of velocity potential. The residuals of $(\phi_{out}-\phi)$ are weighted over the duct width by testing functions, G to give

$$\int_{\Gamma_o}\{G(\phi-\phi_{out})\}\,d\Gamma = 0 \tag{6.46}$$

where G are weighting functions. ϕ_{out} is assumed to have the form:

$$\phi_{out}(y) = \sum_{j=1}^{m}\left(b_j^{+}\psi_j^{+}(y)e^{-ik^{+}_{x,j}x}\right) \tag{6.47}$$

ϕ_{out} has been truncated to number m of modes. Substitute Eq. (6.47) into Eq. (6.46) and write the equation in the following discrete form:

$$\underset{m\times m}{[\mathbf{D}^{+}_{\mathbf{out}}]}\,\underset{m\times 1}{\{b^{+}\}}+\underset{m\times n}{[\mathbf{E}_{\mathbf{out}}]}\,\underset{n\times 1}{\{\phi\}} = \{0\} \tag{6.48}$$

where

$$D^{+}_{out,i,j} = -\int_{\Gamma_o}G_i\psi_j^{+}(y)e^{-ik^{+}_{x,j}x}d\Gamma \tag{6.49}$$

and

$$E_{out,i,j} = \int_{\Gamma_o}G_iN_jd\Gamma \tag{6.50}$$

Eqs. (6.22), (6.35), (6.39), (6.44) and (6.48) are then written as a single matrix equation of the form:

$$\left[\begin{array}{c|c|c} \mathbf{D}^{-}_{\mathbf{in}} & \mathbf{0} & \mathbf{E}_{\mathrm{in}} \\ \hline \mathbf{0} & \mathbf{D}^{+}_{\mathbf{out}} & \mathbf{E}_{\mathrm{out}} \\ \hline \mathbf{B}^{-}_{\mathbf{in}} & \mathbf{B}^{+}_{\mathbf{out}} & \mathbf{A} \end{array}\right]\left\{\begin{array}{c} a^{-} \\ \hline b^{+} \\ \hline \phi \end{array}\right\} = -\left[\begin{array}{c} \mathbf{D}^{+}_{\mathbf{in}} \\ \hline \mathbf{0} \\ \hline \mathbf{B}^{+}_{\mathbf{in}} \end{array}\right]\left\{\, a^{+} \,\right\} \tag{6.51}$$

Weighting functions F are then chosen so that

$$[\mathbf{E}_{\mathbf{in}}] = \left[\mathbf{B}^{-\mathrm{T}}_{\mathbf{in}}\right] \tag{6.52}$$

The matrices in Eq. (6.39) become:

$$D^{\pm}_{in,i,j} = -i\int_{\Gamma_i}\rho_o\phi_i^{-}(y)e^{-ik^{-}_{x,i}x}\left[(1-M_o^2)k^{\pm}_{x,j}+M_o k\right]\phi_j^{\pm}(y)e^{-ik^{\pm}_{x,j}x}d\Gamma \tag{6.53}$$

and

$$E_{in,i,j} = i\int_{\Gamma_i} \rho_o N_i \left[(1-M_o^2)k_{x,j}^- + M_o k\right] \phi_j^-(y)e^{-ik_{x,j}^- x} d\Gamma \tag{6.54}$$

Similarly at $x = L$, weighting functions G in Eq. (6.48) are chosen so that

$$[\mathbf{E}_{\text{out}}] = \left[\mathbf{B}_{\text{out}}^{+\mathrm{T}}\right] \tag{6.55}$$

The matrices in Eq. (6.48) become:

$$D_{out,i,j}^{+} = i\int_{\Gamma_o} \rho_o \psi_i^+(y) e^{-ik_{x,i}^+ x}\left[(1-M_o^2)k_{x,j}^+ + M_o k\right]\psi_j^+(y)e^{-ik_{x,j}^+ x}d\Gamma \tag{6.56}$$

and

$$E_{out,i,j} = -i\int_{\Gamma_o}\rho_o N_i\left[(1-M_o^2)k_{x,j}^+ + M_o k\right]\psi_j^+(y)e^{-ik_{x,j}^+ x}d\Gamma \tag{6.57}$$

The complex sparse linear solver in the IMSL Fortran library is employed to solve the discrete system to yield the field potential, ϕ and the mode coefficients, a^- and b^+ for given a^+.

Direct Modal Boundary Matching

This section describes the direct modal matching procedure. At $x = 0$, the plane Γ_i is perpendicular to the x axis. The modal boundary term is expressed as:

$$B_{i,j} = \int_{\Gamma_i} N_i\left\{\rho_o\nabla\phi_j - \rho_o\left(\frac{i\omega}{c_o}\phi_j + \mathbf{M}_o\cdot\nabla\phi_j\right)\mathbf{M}_o\right\}\cdot\mathbf{n}d\Gamma \tag{6.58}$$

ϕ_j is assumed to be in the form:

$$\phi(y) = \sum_{j=1}^{m}\left(a_j^+\phi_j^+(y)e^{-ik_{x,j}^+ x} + a_j^-\phi_j^-(y)e^{-ik_{x,j}^- x}\right) \tag{6.59}$$

Substitute Eq. (6.59) and its derivative with respect to x into the modal matching integral, Eq. (6.58) and write the equation in the following discrete form:

$$\underset{n\times 1}{\{B_i\}} = \underset{n\times m}{[\mathbf{B}_{\text{in}}^+]}\underset{m\times 1}{\{a^+\}} + \underset{n\times m}{[\mathbf{B}_{\text{in}}^-]}\underset{m\times 1}{\{a^-\}} \tag{6.60}$$

where

$$B_{in,i,j}^{\pm} = i\int_{\Gamma_i}\rho_o N_i\left[(1-M_o^2)k_{x,j}^{\pm}+M_o k\right]\phi_j^{\pm}(y)e^{-ik_{x,j}^{\pm}x}\,d\Gamma \tag{6.61}$$

At the outlet plane Γ_o at $x = L$, the modal boundary term is expressed as:

$$B_{i,j} = -\int_{\Gamma_o} N_i\left\{\rho_o\nabla\phi_j - \rho_o\left(\frac{i\omega}{c_o}\phi_j + \mathbf{M}_o\cdot\nabla\phi_j\right)\mathbf{M}_o\right\}\cdot\mathbf{n}d\Gamma \tag{6.62}$$

ϕ_j is assumed to be in the form:

$$\psi(y) = \sum_{j=1}^{\infty} \left(b_j^+ \psi_j^+(y) e^{-ik_{x,j}^+ x} \right) \tag{6.63}$$

There are no reflected modes at the exit plane as the duct is assumed to be anechoically terminated. Substitute Eq. (6.63) and its derivative with respect to x into the boundary integral term, Eq. (6.62) and write the equation in the following discrete form

$$\underset{n\times 1}{\{B_o\}} = \underset{n\times m}{[\mathbf{B}_{\mathbf{out}}^+]} \underset{m\times 1}{\{b^+\}} \tag{6.64}$$

where

$$B_{out,i,j}^+ = -i \int_{\Gamma_o} \rho_o N_i \left[(1 - M_o^2) k_{x,j}^+ + M_o k \right] \psi_j^+(y) e^{-ik_{x,j}^+ x} \, d\Gamma \tag{6.65}$$

The solution vector, $\{\phi\}$ is partitioned into sub-vectors $\{\phi_i\}$, $\{\phi_o\}$ and $\{\phi_r\}$ which correspond to nodes on plane Γ_i, plane Γ_o and the remaining nodes in the finite element domain. Eq. (6.22) is then written as:

$$\left[\begin{array}{c|c|c} \mathbf{A}_{\mathrm{rr}} & \mathbf{A}_{\mathrm{ri}} & \mathbf{A}_{\mathrm{ro}} \\ \hline \mathbf{A}_{\mathrm{ir}} & \mathbf{A}_{\mathrm{ii}} & \mathbf{0} \\ \hline \mathbf{A}_{\mathrm{or}} & \mathbf{0} & \mathbf{A}_{\mathrm{oo}} \end{array} \right] \left\{ \begin{array}{c} \phi_r \\ \hline \phi_i \\ \hline \phi_o \end{array} \right\} + \left\{ \begin{array}{c} 0 \\ \hline B_i \\ \hline B_o \end{array} \right\} = \left\{ \begin{array}{c} 0 \\ \hline 0 \\ \hline 0 \end{array} \right\} \tag{6.66}$$

and re-written as:

$$\left[\begin{array}{c|c|c} \mathbf{A}_{\mathrm{rr}} & \mathbf{A}_{\mathrm{ri}} & \mathbf{A}_{\mathrm{ro}} \\ \hline \mathbf{A}_{\mathrm{ir}} & \mathbf{A}_{\mathrm{ii}} + \mathbf{B}_{\mathbf{in}}^- \{a^-\} & 0 \\ \hline \mathbf{A}_{\mathrm{or}} & \mathbf{0} & \mathbf{A}_{\mathrm{oo}} + \mathbf{B}_{\mathbf{out}}^+ \{b^+\} \end{array} \right] \left\{ \begin{array}{c} \phi_r \\ \hline \phi_i \\ \hline \phi_o \end{array} \right\} = - \left\{ \begin{array}{c} 0 \\ \hline [\mathbf{B}_{\mathbf{in}}^+] \{a^+\} \\ \hline 0 \end{array} \right\} \tag{6.67}$$

ϕ_o and ϕ_i can be written in the following discrete form:

$$\underset{n\times 1}{\{\phi_i\}} = \underset{n\times m}{[\Phi^+]} \underset{m\times 1}{\{a^+\}} + \underset{n\times m}{[\Phi^-]} \underset{m\times 1}{\{a^-\}} \tag{6.68}$$

$$\underset{n\times 1}{\{\phi_o\}} = \underset{n\times m}{[\Psi^+]} \underset{m\times 1}{\{b^+\}} \tag{6.69}$$

where,

$$\Phi_j^\pm = \phi_j^\pm(y) e^{-ik_{x,j}^\pm x} \tag{6.70}$$

$$\Psi_j^+ = \psi_j^+(y) e^{-ik_{x,j}^+ x} \tag{6.71}$$

Substitute Eqs. (6.68) and (6.69) into Eq. (6.67) and multiply the second row by Φ^- and the third row by Ψ^+, the following expression is obtained:

$$\left[\begin{array}{c|c|c} \mathbf{A}_{\mathbf{rr}} & \mathbf{A}_{\mathbf{ri}}\left(\Phi^{-T}\right) & \mathbf{A}_{\mathbf{ro}}\left(\Psi^{+T}\right) \\ \hline \mathbf{A}_{\mathbf{ir}}\left(\Phi^{-}\right) & \Phi^{-}\left(\mathbf{A}_{\mathbf{ii}}\right)\Phi^{-T}+\Phi^{-}\left(\mathbf{B}_{\mathbf{in}}^{-}\right) & 0 \\ \hline \mathbf{A}_{\mathbf{or}}\left(\Psi^{+}\right) & \mathbf{0} & \Psi^{+}\left(\mathbf{A}_{\mathbf{oo}}\right)\Psi^{+T}+\Psi^{+}\left(\mathbf{B}_{\mathbf{out}}^{+}\right) \end{array}\right]\left\{\begin{array}{c} \phi_r \\ \hline a^- \\ \hline b^+ \end{array}\right\} = - \left[\begin{array}{c} \mathbf{A}_{\mathbf{ri}}\left(\Phi^{+T}\right) \\ \hline \Phi^{-}\left(\mathbf{A}_{\mathbf{ii}}\right)\Phi^{+T}+\Phi^{-}\left(\mathbf{B}_{\mathbf{in}}^{+}\right) \\ \hline \mathbf{0} \end{array}\right]\left\{a^+\right\} \tag{6.72}$$

Although the entries in the system are slightly different to those employing the Galerkin weighted residual method for the modal matching, both FE transmission models should agree with each other for converged solutions.

6.5 Steady Compressible Mean Flow Calculation

In this section, the formulation of a FE model for computing steady compressible flow in two-dimensional ducts is presented. Details of a similar scheme can be found in [20]. To reduce the complexity of the problem, the present analysis will be confined to two-dimensions only.

6.5.1 Problem Specification

A duct contains a finite thickness splitter as shown in Fig. 6.3 is considered. The computational domain, Ω is bounded by boundaries Γ_l, Γ_s and Γ_h. On these boundaries, the mean flow is zero as the flow is perpendicular to the boundary. At plane Γ_i, the mean flow is denoted by U_i and at plane Γ_o, the mean flow is denoted by U_o. It is assumed that Γ_i and Γ_o are located remotely enough from regions of non-uniformity in the duct to allow the mean flow velocity to be uniform at these planes.

6.5.2 The FE Flow Model

In the duct, the mean flow field is governed by the following equations

$$\nabla \cdot (\rho_o \mathbf{U}_o) = 0 \tag{6.73}$$

$$\frac{1}{2}|\mathbf{U}_o|^2 + \frac{c_o^2}{\gamma - 1} = E \tag{6.74}$$

$$c_o^2 = \gamma p/\rho_o = \rho_o^{\gamma-1} \tag{6.75}$$

E is a constant and $\mathbf{U}_o = \nabla\phi_o$ is the mean flow velocity. The subsonic mean flow in the duct is determined by the condition of uniformity upstream, the constant E and a constant axial mass flux πF. The FE flow model is

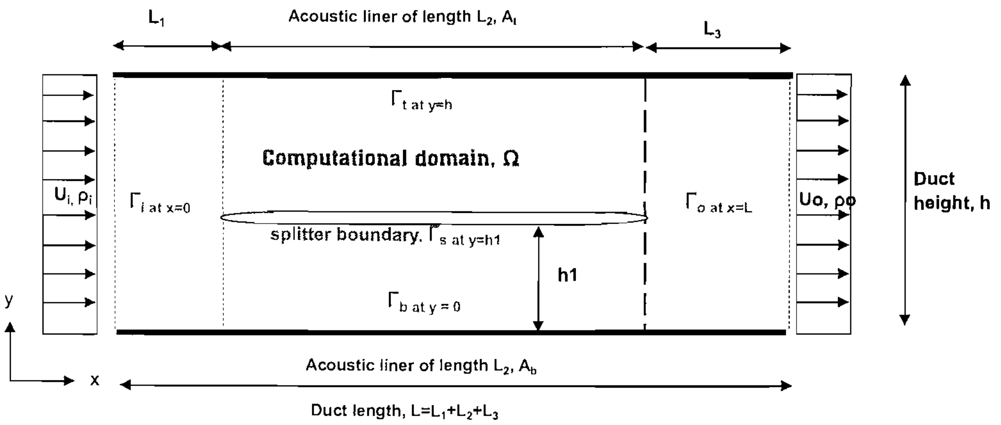

Figure 6.3: Duct model with a finite thickness splitter.

based on a weak formulation of Eq. (6.73):

$$\int_{\Omega} W\{\nabla\cdot(\rho_o\nabla\phi_o)\}d\Omega=0 \tag{6.76}$$

Apply the divergence theorem to Eq. (6.76) to give

$$\int_{\Omega}(\nabla W)\cdot(\rho_o\nabla\phi_o)d\Omega-\int_{\Gamma} W(\rho_o\nabla\phi_o)\cdot\mathbf{n}d\Gamma=0 \tag{6.77}$$

where W are weighting functions. The line integral in the equation is associated with the boundary conditions of the problem.

Boundary Conditions

On boundaries Γ_t, Γ_b and Γ_s, $\nabla\phi_o\cdot\mathbf{n}=0$. On plane Γ_i, $\nabla\phi\cdot\mathbf{n}=U_i$, the line integral becomes

$$\int_{\Gamma_i} W(\rho_o\nabla\phi_o)\cdot\mathbf{n}d\Gamma=\int_{\Gamma_i} W(\rho_oU_i)\,d\Gamma \tag{6.78}$$

and on plane Γ_o, $\nabla\phi_o\cdot\mathbf{n}=-U_o$, the line integral becomes

$$\int_{\Gamma_o} W(\rho_o\nabla\phi_o)\cdot\mathbf{n}d\Gamma=-\int_{\Gamma_o} W(\rho_oU_o)d\Gamma \tag{6.79}$$

U_o is related to U_i by the continuity of mass equation, $\rho_iU_ih_i=\rho_oU_oh_o$ where $\rho_{i,o}$ and $h_{i,o}$ are the fluid density and width of the duct at Γ_i and Γ_o respectively. The weighted residual formulation with the boundary conditions incorporated is:

$$\int_{\Omega}(\nabla W)\cdot(\rho_o\nabla\phi_o)d\Omega-\int_{\Gamma_i} W(\rho_oU_i)d\Gamma+\int_{\Gamma_o} W(\rho_oU_o)d\Gamma=0 \tag{6.80}$$

The acoustic domain, Ω is then discretized using finite elements which take the form

$$\phi_o(\mathbf{x}) = \sum_{j=1}^{N} N_j(\mathbf{x})\phi_{o,j} \tag{6.81}$$

where $\phi_{o,j}$ is the nodal value of $\phi_o(\mathbf{x})$ in the FE region and $N_j(\mathbf{x})$ are the element shape functions. The FE discretization consists of the same mesh with the same element type as used in the acoustic propagation calculation. Meshes constructed from either 8-noded quadrilateral elements or 6-noded triangular elements with an average mesh resolution of 8 to 10 nodes per wavelength are used to discretize the duct- see Fig. 7.2. The splitter is modelled with round edges to ensure smooth flow. The mesh near to the splitter edges is refined for accurate model of the flow in the vicinity. Weighting functions W are assumed from the same functions space, $W(\mathbf{x}) = \sum_{i=1}^{n} N_i(\mathbf{x})$. Eq. (6.80) is then written in the following discrete form:

$$[\mathbf{K} + \mathbf{K}^{\mathbf{B}}]\{\phi_o\} = 0 \tag{6.82}$$

where

$$K_{i,j} = \int_{\Omega} (\nabla N_i) \cdot (\rho_o \nabla N_j) d\Omega \tag{6.83}$$

and

$$K^{B}_{i,j} = -\int_{\Gamma_i} N_i N_j (\rho_o U_i) d\Gamma + \int_{\Gamma_o} N_i N_j (\rho_o U_o) d\Gamma \tag{6.84}$$

6.5.3 Iterative Procedure

An iterative procedure is employed to solve the problem. First, Eq. (6.82) is solved with density $\rho_o = 1$ and speed of sound $c_o = 340$. Then, using Eqs. (6.74) and (6.75), a new density ρ_o and speed of sound c_o are computed. Eq. (6.82) is then solved with the new ρ_o and c_o derived from the previous iteration step. This procedure is repeated until the solution ceases to change significantly.

6.6 Validation of The Finite Element Results

In this section, some results of the validation study of the in-house FE transmission model are presented. The results obtained using the in-house FE models are compared against those obtained using ACTRAN. Two duct models are considered, one with a hard-soft-hard-walled boundary at the top of the duct and the other with an infinitely thin splitter positioned at $y = 0.2$ in the duct - see Fig. 6.4. Duct (B) has the duct walls at $y = 0$ and h lined with acoustic liners. The values of the parameters used in this analysis are detailed in Table 8.3. Fig. 7.2 shows typical examples of the meshes constructed in this study. These meshes are generated using the

Duct length	L	1.6m
Liner length	L_2	1.2m
Hard section length	L_1, L_3	0.2m
Duct height	h	0.5m
Reduced frequency	kh	5, 10
Mean flow	M_o	0.5
Impedance	Z	$3.0-4.97i(kh=5), 3.0-1.29i(kh=10)$
Splitter thickness	t_s	0.001m

Table 6.1: Model duct specification.

ICEMCFD package [101]. At the inlet plane at $x=0$, all cut-on and a few cut-off negative acoustic modes are considered for modal matching. At the exit plane at $x=L$, all cut-on and a few cut-off positive acoustic modes are considered. No negative propagating modes are specified in the latter case as the exit plane is assumed to be an anechoic termination.

Fig. 6.6 presents the absolute acoustic pressure along the duct wall at $y=h$ predicted by the in-house FE model and by ACTRAN for Duct (A). Fig. 6.6(a) presents results for $kh=5$ and Fig. 6.6(b) presents results for $kh=10$. In the plots, impedance discontinuities at $x=0.2$ and 1.4 are indicated by dotted lines. The comparisons show good agreement between the two FE models and both models predict pressure singularities where impedance discontinuities occur.

Figs. 6.7 and 6.8 show the average modal intensity (PWL) of the reflected modes at $x=0$ and of the transmitted modes at $x=L$ plotted against the mode number for Duct (A) at frequency of $kh=5$ and 10. Results predicted by ACTRAN and by the in-house FE code are presented. The mode number is obtained by ordering the duct modes according to their cut-off ratios in a descending order. The PWL is evaluated using the Morfey expression of acoustic intensity [102] with an additional contribution from the wall boundary derived by Eversman [103]. The expression of the modal intensity is presented in Chapter 5. The comparisons show good agreement between the two FE models. Figs. 6.9 and 6.10 present the PWL of the reflected modes at $x=0$ and of the transmitted modes at $x=L$ predicted using ACTRAN and the in-house FE model for Model (B) at frequency of $kh=5$ and 10. The comparisons show good agreement between the two FE solutions with discrepancies less than 1 dB.

6.7 A Numerical Study of Varying Splitter Thickness on Sound Propagation In A Duct

This section presents the results of a numerical study of the effect of varying splitter thickness on sound propagation in the duct. The analysis is carried out using ACTRAN and the mean flow in the duct is computed using the FE flow model presented in Section 6.5. The values of the parameters used in this analysis are detailed in Table 6.2. The flow calculation is carried out on the same grid with the same element type as used in the

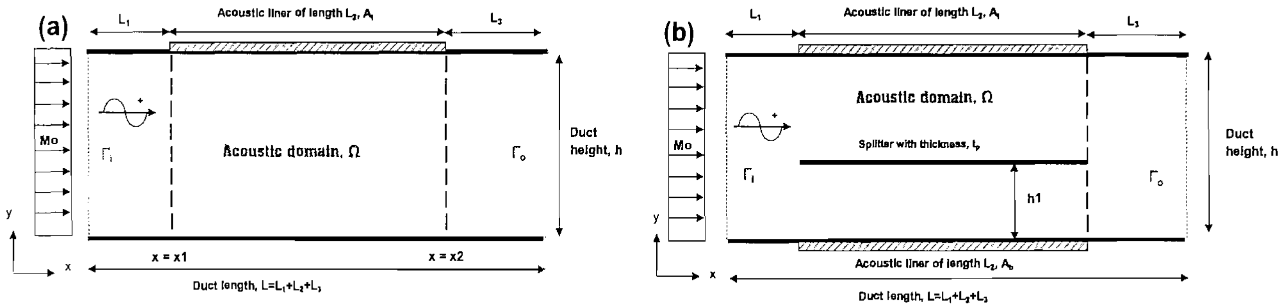

Duct (A)

Duct (B)

Figure 6.4: Duct models.

acoustic propagation calculation.

At the inlet of the duct, flow at $M_o = 0.3$ is specified. The splitter thicknesses considered are $t_p/h = 0.3$, 0.2, 0.1, 0.05, 0.01, 0.005, 0.001, 0.0005 and 0.0001 where t_p is the splitter thickness. The splitter is modelled with round edges to ensure a smooth flow. At the source plane at $x = 0$, a harmonic mode $n_i = 2$ is incident.

Fig. 6.11 presents plots of compressible mean flow computed for splitter thickness, $t_p/h = 0.2$ and 0.01. Figs. 6.11(a) and (b) present the mean flow in the x direction, Figs. 6.11(c) and (d) present the mean flow in the y direction and Figs. 6.11(e) and (f) present the streamlines of the mean flow. The flow in the duct become almost uniform, no flow in the y direction, as the splitter thickness decreases.

In Figs. 6.12 and 6.13, bar charts show the *PWL* of the transmitted modes at $x = L$ and of the reflected modes at $x = 0$ plotted against the mode number for zero and uniform flows. Results obtained by the revised mode matching method (NMMM) model are also presented. The splitter is assumed to be infinitely thin in the MM model.

The results show that, the FE results converge to the MM results of an infinitely thin splitter as the splitter thickness decreases. This is observed for uniform flow and zero flow. The results also show that as the splitter thickness decreases, more acoustic energy is scattered into the high order modes than the low order modes. This is seen as acoustically beneficial as the high the order modes are more easily attenuated by the acoustic liner.

6.8 Conclusions

An in-house FE transmission code has been developed to study transmission of sound in two-dimensional flow ducts. The model is to provide a validation to the MM model. The in-house FE model yields results which show good agreement with those obtained using ACTRAN which is also an FE transmission code but uses a slightly different modal matching procedure. The FE solutions obtained using ACTRAN are used as the benchmark

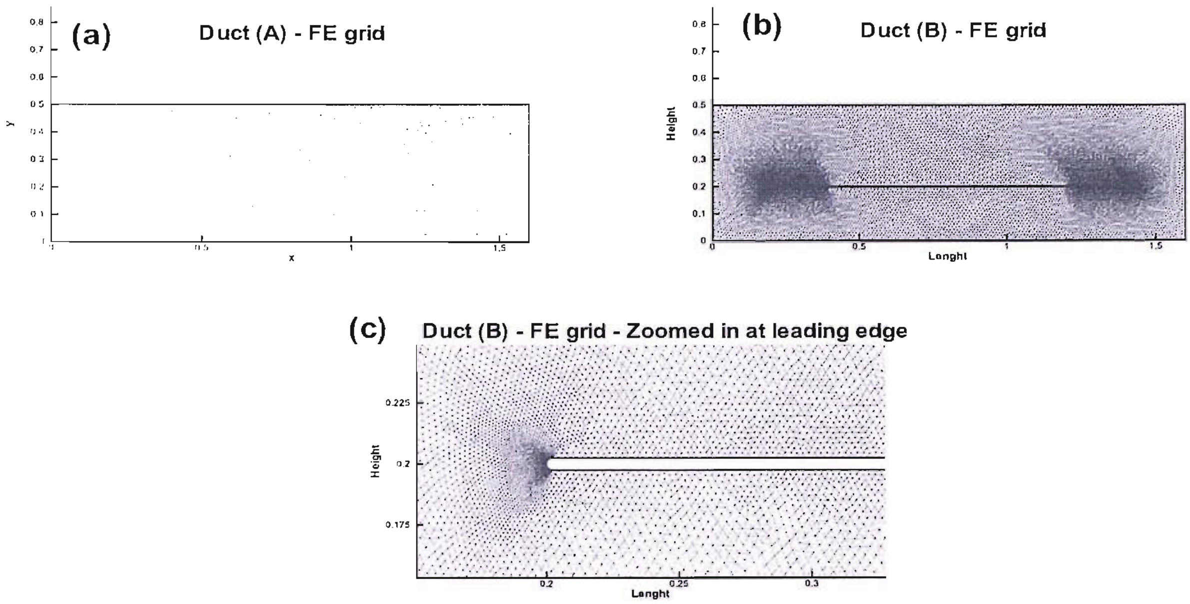

Figure 6.5: FE grids.

Duct length	L	1.6m
Liner length	L_2	1.2m
Duct height	h	0.5m
Splitter position	h_1	0.2m
Splitter thickness	t_p/h	0.3 - 0.0001
Splitter length	L_p	1.2m
Reduced frequency	kh	10
Acoustic impedance	Z	∞, 2-1i
Mean flow Mach number	M_o	0.3M

Table 6.2: Model duct specification - sound diffraction by a splitter in the duct.

solutions to validate the mode matching solutions.

An FE flow model has also been developed to compute steady compressible mean flow in two-dimensional ducts. The flow model have been employed with ACTRAN to investigate the effect of varying splitter thickness on sound propagation in the duct. The study shows that the FE solution converge to the MM solution of an infinitely thin splitter as the splitter thickness decreases. The diffraction at the splitter resulted in more energy been transferred to the high order modes than the low order modes. This is seen as acoustically beneficial as the high order modes are more easily attenuated by the acoustic liner.

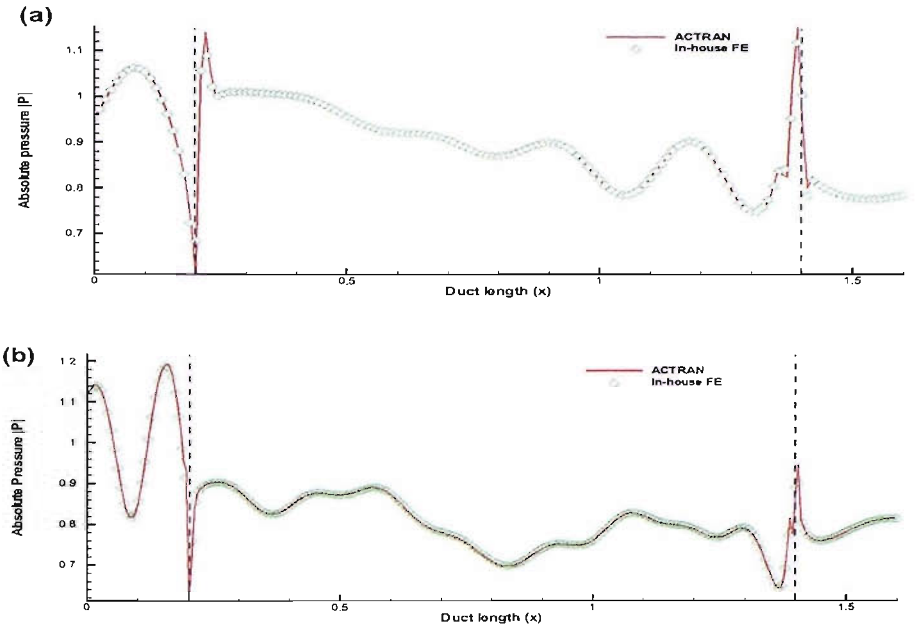

Figure 6.6: Model (A) - Absolute acoustic pressure along the duct wall at $y = h$. Results predicted by ACTRAN and by the in-house FE transmission model are presented. (a) $Z_t = 3 - 4.97i$, $Z_b = \infty + \infty i$, $Mo = 0.5$, $kh = 5$, (b) $Z_t = 3 - 1.29i$, $Z_b = \infty + \infty i$, $M_o = 0.5$, $kh = 10$.

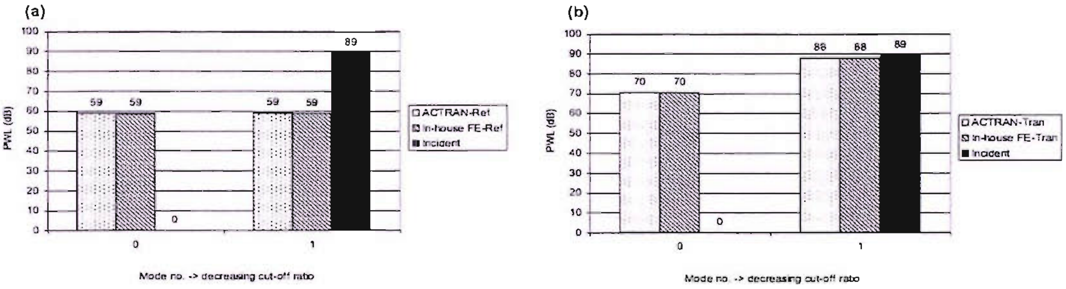

Figure 6.7: Model (A) - *PWL* of the reflected modes at $x = 0$ and of the transmitted modes at $x = L$ predicted by ACTRAN and by the in-house FE transmission model. $kh = 5$, $M_o = 0.5$, $Z_t = 3 - 4.97i$, $Z_b = \infty + \infty i$. (a) Reflected modes, (b) Transmitted modes.

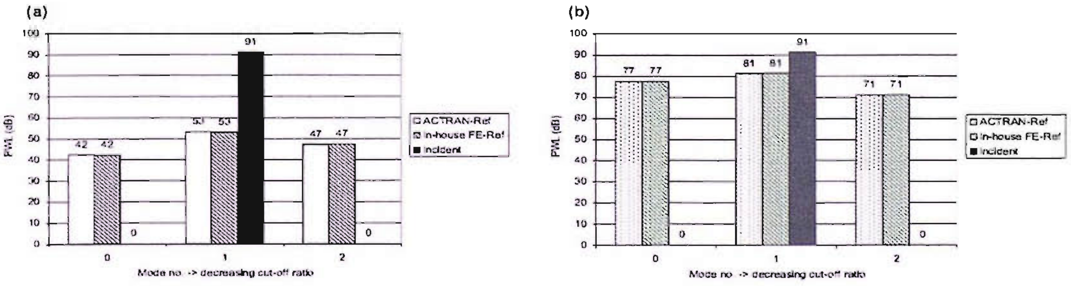

Figure 6.8: Model (A) - *PWL* of the reflected modes at $x = 0$ and of the transmitted modes at $x = L$ predicted by ACTRAN and by the in-house FE transmission model. $kh = 10$, $M_o = 0.5$, $Z_t = 3 - 1.29i$, $Z_b = \infty + \infty i$. (a) Reflected modes, (b) Transmitted modes.

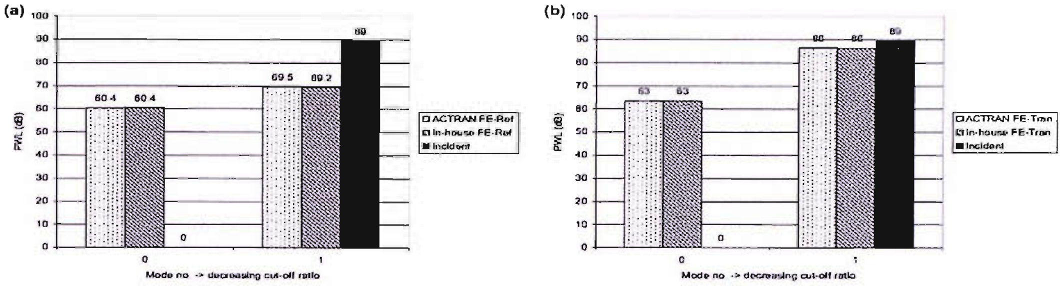

Figure 6.9: Model (B) - PWL of the reflected modes at $x = 0$ and of the transmitted modes at $x = L$ predicted by ACTRAN and by the in-house FE transmission model. $kh = 5$, $M_o = 0.5$, $Z_t = 3 - 4.97i$, $Z_b = 3 - 4.97i$. (a) Reflected modes, (b) Transmitted modes.

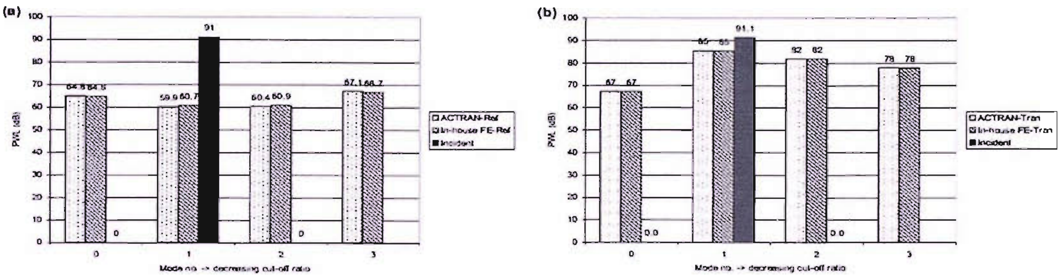

Figure 6.10: Model (B) - PWL of the reflected modes at $x = 0$ and of the transmitted modes at $x = L$ predicted by ACTRAN and by the in-house FE transmission model. $kh = 10$, $M_o = 0.5$, $Z_t = 3 - 1.29i$, $Z_b = 3 - 1.29i$. (a) Reflected modes, (b) Transmitted modes.

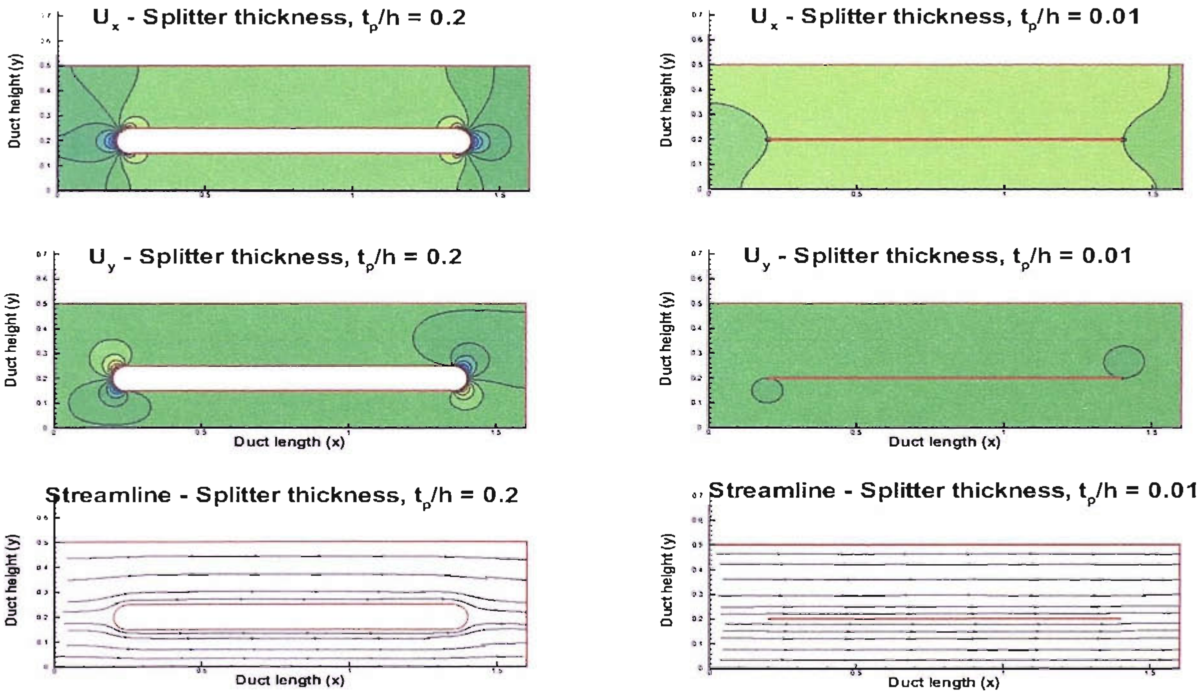

Figure 6.11: Compressible mean flow computed for a duct with splitter thickness, $t_p/h = 0.2$ and 0.01.

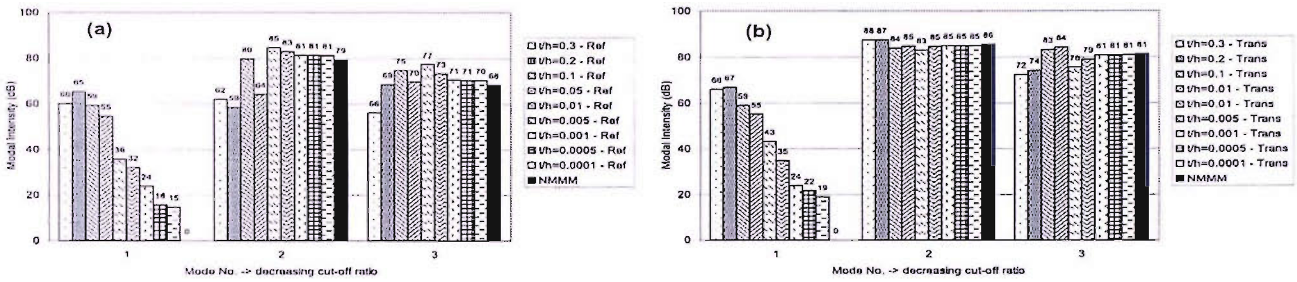

Figure 6.12: Duct (B) - *PWL* of the reflected modes at $x = 0$ and of the transmitted duct modes at $x = L$ for different splitter thickness. Solutions are predicted using ACTRAN. $M_o = 0$ and $kh = 10$. (a) Reflected modes, (b) Transmitted modes.

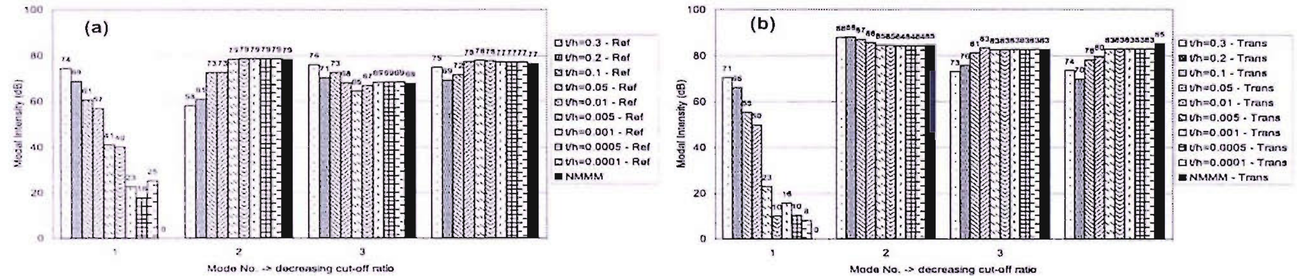

Figure 6.13: Duct (B) - *PWL* of the reflected modes at $x = 0$ and of the transmitted duct modes at $x = L$ for different splitter thickness. $M_o = 0.3$ and $kh = 10$. (a) Reflected modes, (b) Transmitted modes.

Chapter 7

Results: Two-Dimensional Mode Matching Problems - Validation and Application

7.1 Introduction

This chapter presents the results of a study of sound transmission in two-dimensional flow ducts using mode matching (MM) method. The revised MM procedure presented in Chapter 5 is employed to study transmission of sound in two-dimensional flow ducts and the accuracy of the method is examined by comparing with the finite element (FE) transmission analysis. If the results for the two-dimensional problems are favourable then generalization and assessment of the MM scheme for three-dimensional problems would be warranted.

The revised MM procedure or the new mode matching method (NMMM) is different from the existing procedure or the traditional mode matching method (TMMM) which has been employed by Beckmeyer [1], Cummings [2] and Sijtsma [3] in their studies of duct acoustics. Details of the two procedures are described in Chapter 5. Note that when no flow is present in the duct, the NMMM is equivalent to the TMMM.

A series of two-dimensional ducts with and without mean flow in the duct are studied. The results are presented in two parts. The first part of the results is about validation and convergence of the NMMM. In the second part of the results, the NMMM is employed to study (*i*) acoustic scattering by an acoustic impedance discontinuity in the duct, (*ii*) sound propagation in a duct containing surface waves and (*iii*) sound diffraction by a splitter in the duct. In these analyses, comparisons of solutions obtained by the FE transmission analysis, by the TMMM and by the NMMM are presented.

7.1.1 Outline

Section 7.2 details the test problems considered in the study. Aspects such as the duct geometries, liner impedances and aspects of the computational models are described. Results of validation and convergence of the NMMM are then presented in Sections 7.4 and 7.5. This is followed by the case study results in Section 7.7. Section 7.8 presents the results of a performance study of the NMMM compared to the FE transmission

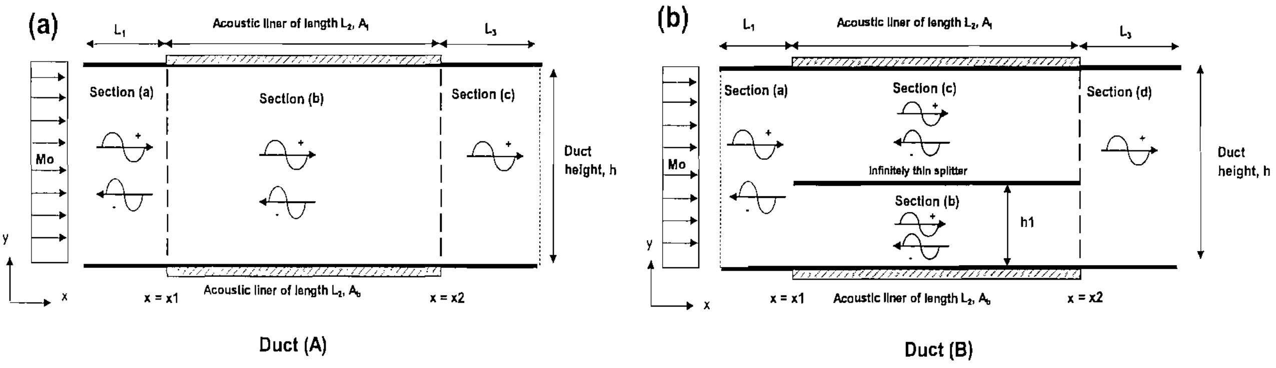

Duct (A)

Duct (B)

Figure 7.1: Duct models.

analysis. The computation times of the two methods are determined using a test problem. Finally in Section 7.9, some conclusions of the study are presented.

7.2 Problem Specification

The results have been presented for two-dimensional models shown in Fig. 7.1. Both Duct (A) and Duct (B) have three sections, a short hard Section (a) with length L_1, a lined Section (b) with impedance Z and length L_2 and another short hard Section (c) with length L_3. In Duct (B), an infinitely thin splitter with length L_2 is positioned at $y = h_1$ in Section (b).

At the inlet of the duct at $x = 0$, a single harmonic mode with mode number, n_i or a multi-mode source with equal energy per mode is incident. For simplicity and for the purpose of validation, the current study only considers single tone analysis. These ducts are studied for reduced frequency, $kh \sim 5$to 10 with and without flow. The acoustic liners are assumed to be locally reacting linings. The resistance is taken to be $R = 2 \sim 3$, and the reactance is taken to be $X = 1 \sim 2$. These acoustic liner values are derived for a simple model for a single cavity liner detailed in Chapter 3. These values are typical for a turbofan aero-engine liner.

7.2.1 Modal Scattering

In Duct (A), the input sound propagates in the positive x direction. It scatters into other cut-on modes when it meets the hard/lined interface at $x = x_1$. Here some of the incident sound is reflected but most of it is transmitted into the lined Section (b). The scattered field in the lined Section (b) comprises of forward-scattered and backward-scattered sound. The forward-scattered sound attenuates along the lined section and then strikes the downstream end of the lined section at $x = x_2$. At here, the sound is partially reflected and transmitted. The sound power that is transmitted into the hard Section (c) is approximately equal to the sound power that is radiated to the far-field. The back-scattered modes in Section (b) that strike the hard/lined interface at $x = x_1$

are transmitted into the hard Section (a) where they travel back to the source plane. Without acoustic lining in the duct, the incident sound propagates un-attenuated through the duct.

In [58], a plot of sound power variation in a hard/lined/hard section circular duct is presented which illustrates clearly the above phenomenon. The duct contains spliced liners and with uniform mean flow.

7.2.2 FE Models

For the FE transmission analysis, the ducts are discretized using meshes constructed from either 8-noded quadrilateral elements or 6-noded triangular elements with an average mesh resolution of 10 to 12 nodes per wavelength. The mesh resolution is defined on the basis of the number of nodes which are required to represent accurately the solution over one wavelength. In the x direction, the mesh resolution, N is defined by:

$$N = \frac{c_o}{f\Delta|1 - M_o|} \tag{7.1}$$

where c_o is the speed of sound, f is the frequency in Hertz, M_o is the mean flow Mach number and Δ is the average distance between nodes. The mesh resolution in the y direction is defined by $N = c_o/f\Delta$ as no flow effect is taken into account. For many engineering purposes, a mesh resolution of 8 to 10 nodes per wavelength is the rule of thumb. Fig. 7.2 shows examples of the meshes constructed in this study. The mesh near to the splitter edges and the acoustic liner is refined. This is to model more accurately the pressure at these regions.

At the inlet plane at $x = 0$, 20 negative propagating modes are assumed for the modal matching. At the exit plane at $x = L$, 20 positive propagating modes are assumed for the modal matching and no negative propagating modes are specified as the exit plane is assumed to be an anechoic termination.

7.2.3 Mode Matching Models

Duct (A) is segmented into three sections; Section (1), Section (2) and Section (3) at $x = x_1$ and x_2 where the wall impedance changes. Duct (B) is segmented into four sections; Section (1), Section (2), Section (3) and Section (4) at $x = x_1$ and x_2 where the wall impedance and duct geometry change - see Fig. 7.3.

In each section, the superposition of positive and negative acoustic modes that represent the harmonic pressure field is truncated to a finite number of modes, n; $m1$ in Section (1), $m2$ in Section (2), $m3$ in Section (3) and $m4$ in Section (4). Typically, to ensure good accuracy, $n >> n_c$, where n_c is the number of cut-on modes in a hardwalled duct [59]. In practice if $n_c < 5$, then $n \geqslant 20$ appears sufficient [59]. The duct modes are computed numerically using the FE eigenvalue model described in Chapter 2. Meshes with an average mesh resolution of 10 nodes per wavelength are used to discretize the duct width. The matching procedures described in Chapter 5 are then carried out to yield a linear system which is solved to obtain the unknown modal coefficients in each duct section.

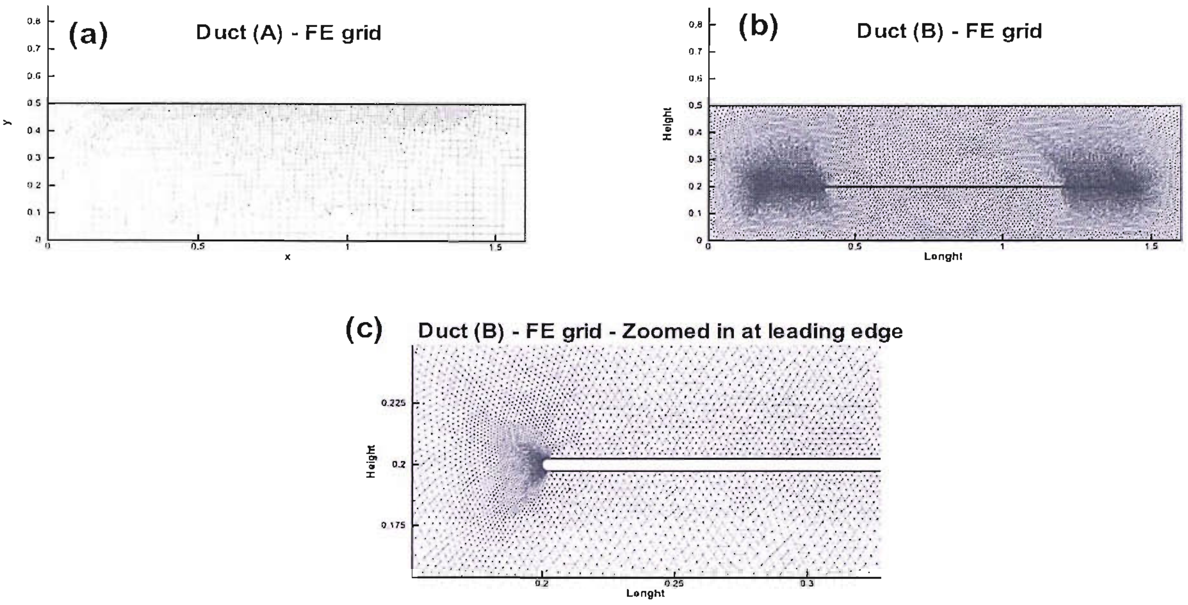

Figure 7.2: FE grids

7.3 Benchmark Results

In this study, to benchmark the MM solutions, FE solutions obtained using ACTRAN are used. ACTRAN is a finite/infinite element (FE/IE) code produced by Free Field Technologies [105] which is capable of predicting sound propagation in non-uniform ducts with non-uniform mean flow and boundaries with finite acoustic impedance. Details of the FE transmission model are presented in Chapter 6.

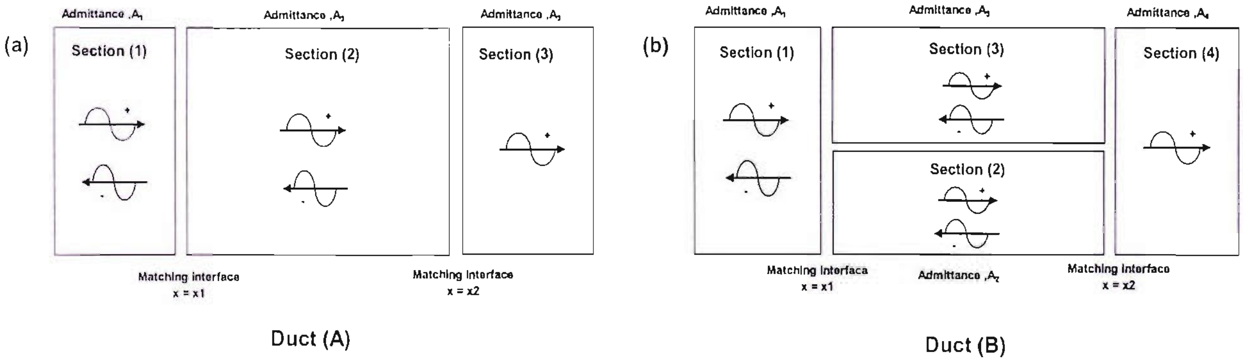

Figure 7.3: Mode matching models. (a) Duct (A), (b) Duct (B)

Duct length	L	1.6m
Liner length	L_2	1.2m
Hard section length	L_1, L_3	0.2m
Duct height	h	0.5m
Reduced frequency	kh	10
Acoustic impedance	Z	∞, 2-1i
Mean flow Mach number	M_o	0.4

Table 7.1: Model duct specification.

7.4 Assessment of Accuracy of the New Mode Matching

This section examines the accuracy of the NMMM by comparing the MM results with those of the FE transmission analysis. A uniform two-dimensional duct as shown in Fig. 7.1(a) is considered. Table 7.1 details the values of the parameters used in this analysis. At the inlet of the duct, a harmonic mode, $n_i = 2$ with modal coefficient of 1 is incident. The number of duct modes considered in Sections (1) to (3), is taken to be the number of hardwalled modes having cut-off ratios greater than 0.7. For the results, the average modal intensities (PWL) of the transmitted and reflected duct modes are obtained.

7.4.1 Hardwalled Duct

Fig. 7.4 shows the acoustic pressure; real and imaginary parts along the duct wall at $y = h$ for a hardwalled duct. Solutions obtained by the FE transmission analysis and by the NMMM using numerical or analytical eigen-modes are presented. The analytical eigen-modes are computed using the integration scheme presented in Chapter 2 [79, 80].

The results are expected as the incident mode propagates un-attenuated along the duct. The two MM results not only agree well with each other but also with the FE results. Fig. 7.5 presents the PWL of the transmitted modes at $x = L$ and of the reflected modes at $x = 0$ plotted against the mode number. The mode number is obtained by ordering the duct modes according their cut-off ratios in descending order. The results show no modal scattering and no energy loss occur in the duct as the relative sound power - defined as the ratio of transmitted to incident sound power in dB, $\triangle PWL$, has a zero value. The results predicted by the two NMMM's are in good agreement with each other and also with the FE transmission analysis. The FE solutions show some reflected energy at $x = 0$. This is due to the numerical error in the calculations and it is relatively small compared to the incident or transmitted energy - see Fig. 7.5.

7.4.2 Softwalled Duct

Fig. 7.6 presents the acoustic pressure; real and imaginary parts along the duct wall at $y = h$ for a softwalled duct. Solutions obtained by the FE transmission analysis and by the NMMM using numerical or analytical

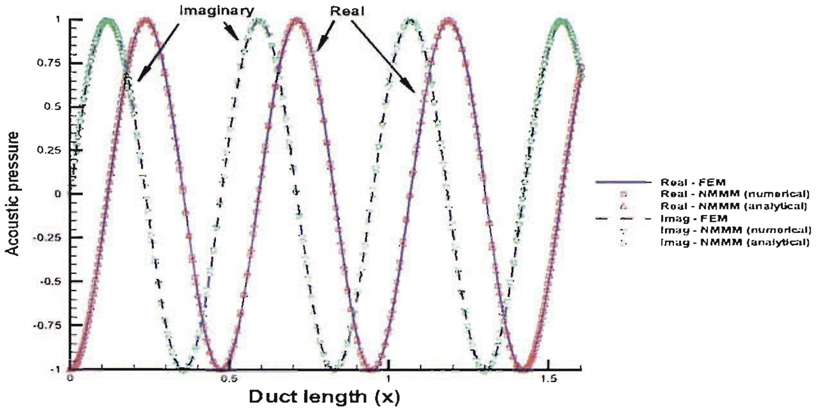

Figure 7.4: Validation study - acoustic pressure along the duct wall at $y = h$. Results obtained by the FE transmission analysis and by the NMMM using analytical and numerical eigen-modes are presented. $kh = 10$, $Z = \infty + \infty i$ and $M_o = 0.4$.

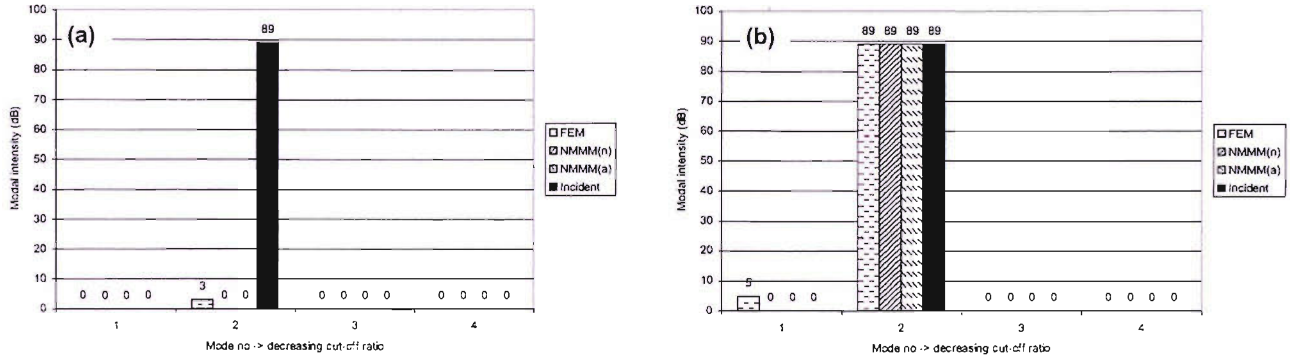

Figure 7.5: Validation study - *PWL* of the reflected modes and of the transmitted modes plotted against mode number. Results obtained by the FE transmission analysis and by the NMMM using analytical or numerical eigen-modes are presented. $kh = 10$, $Z = \infty + \infty i$, $M_o = 0.4$. (a) Reflected modes, (b) Transmitted modes.

eigen-modes are presented. Fig. 7.6 shows that a jump in the pressure is observed where there is a discontinuity in acoustic impedance or impedance mismatch. The pressure amplitude reduces along the acoustically lined duct section. The two NMMM's show good agreement with each other and also with the FE transmission analysis. Both methods indicate that the pressure is singular at an impedance discontinuity.

Fig. 7.7 presents the *PWL* of the transmitted modes at $x = L$ and of the reflected modes at $x = 0$ plotted against the mode number. The results show that the impedance discontinuity causes scattering of acoustic energy to other cut-on modes, both high and low order modes. The performance of the acoustic treatment is evaluated by the in-duct sound power transmission loss, $(\triangle PWL)$ which is defined as the ratio of transmitted

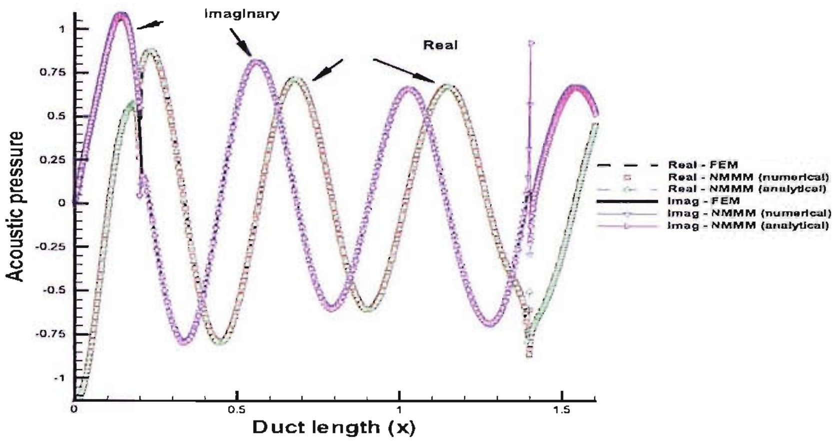

Figure 7.6: Validation study - acoustic pressure along the duct wall at $y = h$. Results obtained by the FE transmission analysis and by the NMMM using analytical or numerical eigen-modes are presented. $kh = 10$, $Z = 2 - 1i$ and $M_o = 0.4$.

to incident sound power:

$$\triangle PWL = 10\log\frac{\sum_{i=1}^{n}\left(W_i^+|_{x=0}\right)}{\sum_{i=1}^{n_i}\left(W_{n_i}^+|_{x=L}\right)} \tag{7.2}$$

where $\sum_{i=1}^{n}\left(W_i^+|_{x=L}\right)$ is the sum of the acoustic power in all the cut-on duct modes at $x = L$ and $\sum_{i=1}^{n_i}\left(W_{n_i}^+|_{x=0}\right)$ is the sum of the acoustic power in all the incident modes at $x = 0$. A $\triangle PWL$ of 3.5 dB is predicted by the FE transmission analysis. The difference between the $\triangle PWL$ predicted by the two NMMM is less than 0.5 dB and less than 1 dB between the NMMM and the FE transmission analysis.

The results presented in this section have shown good agreement between the FE transmission analysis and the NMMM using either numerical or analytical eigen-modes.

7.5 Convergence of the New Mode Matching Method

This section presents the results of a convergence study of the NMMM. The aim of the study is to determine the number of duct modes required for accurate solutions in each duct section. The number of duct modes in each segmented duct section is determined by the number of hardwalled modes having a given cut-off ratio. The test model in Section 7.4.2 with the same parameters is considered.

Fig. 7.8 presents the PWL of the transmitted modes at $x = L$ and of the reflected modes at $x = 0$ plotted against the mode number for different number of duct modes specified in each duct section. The number of duct modes is determined by the number of acoustic modes having cut-off ratios greater than 0.8, 0.7, 0.6, 0.5

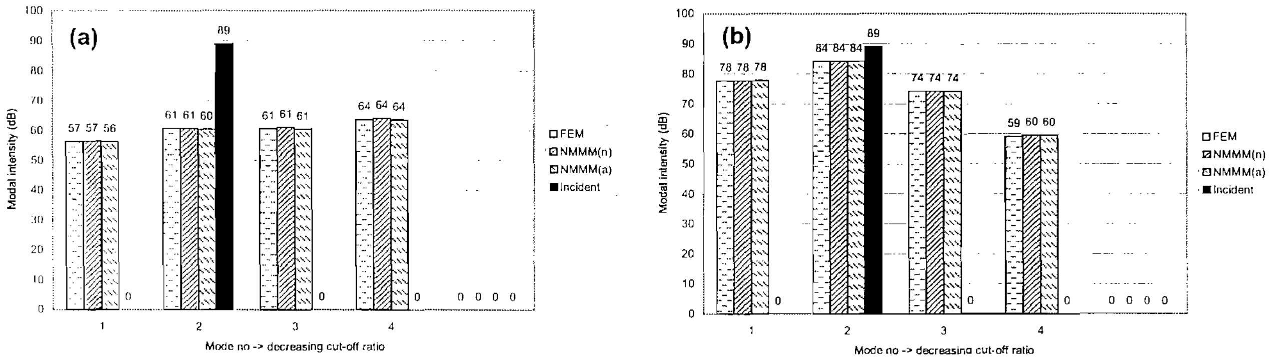

Figure 7.7: Validation study - *PWL* of the reflected modes at $x = 0$ and of the transmitted modes at $x = L$ plotted against mode number. Results obtained by the FE transmission analysis and by the NMMM using numerical or analytical eigen-modes are presented. $kh = 10$, $Z = 2 - 1i$ and $M_o = 0.4$. (a) Reflected modes, (b) Transmitted modes.

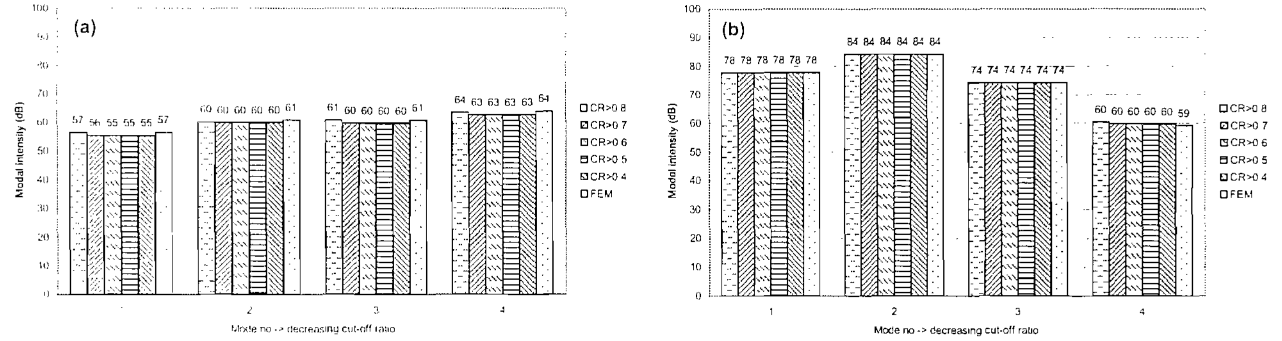

Figure 7.8: Convergence study - *PWL* of the reflected modes at $x = 0$ and of the transmitted modes at $x = L$ plotted against mode number for different numbers of truncated modes in each duct section. $kh = 10$, $Z = 2 - 1i$ and $M_o = 0.4$. (a) Reflected modes, (b) Transmitted modes.

and 0.4. FE solutions are also presented.

Fig. 7.8 shows that only a small number of cut-off modes is adequate for the MM solutions to converge to the FE solutions. The number of hardwalled duct modes having cut-off ratios greater than 0.8 is found to be adequate for converged MM solutions. The results obtained using these modes show discrepancies less than 1 dB with the FE transmission results - see Fig. 7.8.

7.6 Galerkin Weighted Residuals Method and Least Squares Method

This section investigates the accuracy of the MM solution obtained using the Galerkin weighted residuals (GWR) method and using the least squares (LS) method by comparing them with the FE transmission analysis. A softwalled duct with zero flow as shown in Fig. 7.1(a) is considered. The duct is studied for $kh = 10$ and the impedance of the acoustic liner at $y = 0$ and h is $2 - 1i$. The objective here is to establish the accuracy and

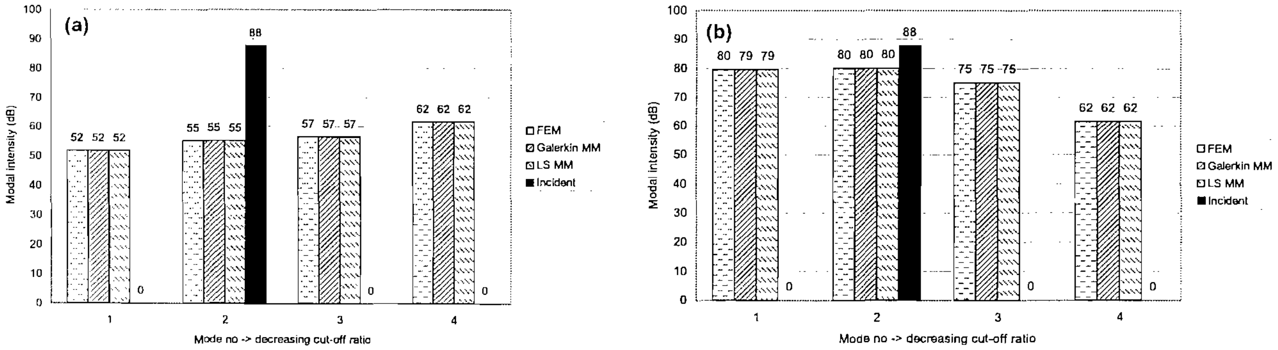

Figure 7.9: Validation study - PWL of the reflected modes at $x = 0$ and of the transmitted modes at $x = L$ plotted against mode number. MM solutions obtained by the GWR method and by the LS methods are presented. $kh = 10$, $Z = 2 - 1i$ and $M_o = 0$. (a) Reflected modes, (b) Transmitted modes.

consistency of the solutions of the two methods. No attempt is therefore made to evaluate the performance of any specific acoustic treatments.

Fig. 7.9 presents bar charts which show the PWL of the transmitted modes at $x = L$ and of the reflected modes at $x = 0$ plotted against the mode number. Solutions obtained by the FE transmission analysis and by the two MM schemes are presented. Good agreement is shown between the two MM schemes with discrepancies less than 0.5 dB. The two MM schemes also agree well with the FE transmission analysis with discrepancies less than 1 dB.

7.7 Case Study Results

The following section presents the results of the case study. First, results of a study of acoustic scattering by a discontinuity in acoustic impedance in the duct are presented. Section 7.7.2 presents the results of a study of sound propagation in a duct containing surface waves and Section 7.7.3 presents the results of a study of sound diffraction by an infinitely thin splitter. The objective of these study is to demonstrate that the MM scheme is capable of studying the problems. No attempt is therefore made to evaluate the performance of any specific acoustic treatments.

7.7.1 Case Study 1: Acoustic Scattering By An Impedance Discontinuity In The Duct

The study is

- to show that the NMMM is capable of studying acoustic scattering by an impedance discontinuity in the duct; and
- to show that the NMMM with an additional boundary condition term yields better accuracy than the TMMM when flow is present in the duct.

Duct length	L	1.6m
Liner length	L_2	1.2m
Hard section length	L_1, L_3	0.2m
Duct height	h	0.5m
Reduced frequency	kh	10
Acoustic impedance	Z	2-1i
Mean flow Mach number	M_o	0, 0.4

Table 7.2: Model duct specification - acoustic impedance discontinuity study.

The test model consisted of a two-dimensional duct with a hard-soft-hard boundary at $y = h$ as shown in Fig. 7.1(a). The duct wall at $y = 0$ is hard. The model is studied for $kh = 10$ with and without flow in the duct. Table 7.2 details the values of the parameters used in this analysis. At the inlet of the duct, a harmonic mode, $n_i = 2$ with a modal coefficient of 1 is incident.

For the no flow case, results obtained by the FE transmission analysis and by the NMMM are presented as the TMMM is equivalent to the NMMM. For the flow case, results obtained by the FE transmission analysis, by the NMMM and by the TMMM are presented.

Zero Flow

In Fig. 7.10, the absolute acoustic pressure along the duct wall at $y = h$ for zero flow is presented. Solutions obtained by the FE transmission analysis and by the MM are presented. In the plot, the matching locations are shown by dotted lines. Fig. 7.10 shows good agreement between the two predictions even in the regions of impedance mismatch.

Fig. 7.11 presents the PWL of the transmitted modes at $x = L$ and of the reflected modes at $x = 0$ plotted against the mode number. Good agreement is shown between the FE and the MM with discrepancies less than 1 dB. The results show that the incident acoustic energy has been scattered into other cut-on modes due to impedance discontinuities at $x = 0.2$ and 1.4. The $\triangle PWL$ predicted by the FE and the MM shows a reduction of 4.22 and 4.21 dB respectively.

Uniform Mean Flow

In Fig. 7.12, the absolute acoustic pressure along the duct wall at $y = h$ is plotted. Uniform mean flow of Mach number 0.4 is considered in the duct. Solutions obtained by the FE transmission analysis, by the NMMM and by the TMMM are presented. In the plot, the matching locations are indicated by dotted lines. The NMMM agrees better with the FE transmission analysis than the TMMM especially at the region of impedance mismatch. The FEM and the NMMM predict very large pressure fluctuations or pressure singularity at the impedance mismatch whilst the TMMM predicts only a smooth pressure variation.

Fig. 7.13 presents the PWL of the reflected and transmitted modes. Discrepancies of 4 to 6 dB are shown

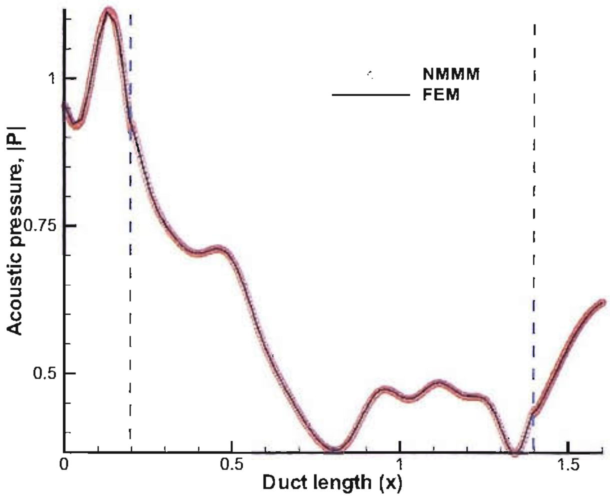

Figure 7.10: Case study 1 - absolute acoustic pressure along the duct wall at $y = h$. Results obtained by the FE transmission analysis and by the NMMM are presented. $kh = 10, Z = 2 - 1i, M_o = 0$.

between the TMMM and the FE transmission analysis, especially the reflected modes. Energy conservation calculation shows that the energy is not conserved for the TMMM. The NMMM show discrepancies of 1 dB with the FE transmission analysis. The $\triangle PWL$ predicted by the FE transmission analysis, by the NMMM and by the TMMM shows 3.50 dB , 3.50 dB and 3.51 dB reduction respectively. Compared to the zero flow case, it is shown that the acoustic lining performance is reduced by approximately 1 dB due to the flow.

In Fig. 7.14, the absolute acoustic pressure along the matching interfaces at $x = x_1$ and x_2 is presented. Again, better agreement is shown between the FEM and the NMMM. The agreement between the FEM and the NMMM is generally good apart from the regions near to the impedance discontinuity at the wall. Further study has shown that the agreement improves as more duct modes are considered in the MM model.

7.7.2 Case Study 2: Sound Propagation In A Duct Containing Surface Waves

This section presents the results of a study of sound propagation in a duct containing surface waves. Computations are made for a uniform two-dimensional duct with a hard-soft-hard boundary at $y = 0$ and h as shown in Fig. 7.1(a). Table 7.3 lists the different combinations of non-dimensionalized acoustic impedances used in this analysis. These impedances are particulary selected to reflect the existence of different types of surface waves in the duct. At the inlet of the duct, a harmonic mode, $n_i = 1$ is incident. The duct is studied for $kh = 10$ with uniform mean flow at Mach number $M_o = 0.5$. The values of the parameters used in the analysis are listed in Table 7.4.

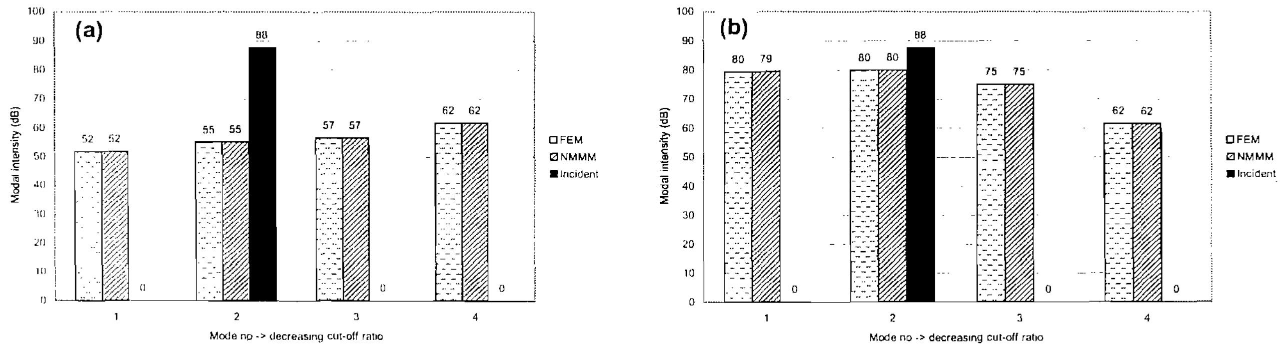

Figure 7.11: Case study 1 - PWL of the reflected modes at $x = 0$ and of the transmitted modes at $x = L$ plotted against mode number. Results obtained by the FE transmission analysis and by the MM are presented. $kh = 10$, $Z = 2 - 1i$ and $M_o = 0$. (a) Reflected modes, (b) Transmitted modes.

No.	Impedance, Z_b at $y = 0$	Region	Impedance, Z_t at $y = h$	Region
Configuration (1)	0.1-3i	V	0.1-3i	V
Configuration (2)	0.1+3i	I	0.1-3i	V

Table 7.3: Acoustic impedances at the top and bottom of the duct.

FE Mesh

For the FE transmission analysis, a fine mesh and a coarse mesh are constructed from 8-noded quadrilateral elements. Both meshes has an average mesh resolution of 10 nodes per wavelength - see Fig. 7.15. The fine mesh has the mesh near to the liner boundaries refined aiming to model the short wavelength surface waves more effectively. Fig. 7.15 presents the absolute acoustic pressure predicted using the coarse and the fine mesh for configuration 2. Both meshes predict the presence of surface waves at $y = h$. However, the solutions obtained using the fine mesh show a better resolution of the surface waves - see Fig. 7.16. Fig. 7.17 presents the PWL of the reflected modes at $x = 0$ and of the transmitted modes at $x = L$ predicted using the two meshes. Almost identical results are shown between the two mesh results even though some deviations are shown in the pressure plots in Fig. 7.15.

In this study, to ensure the surface waves are modelled accurately, meshes used to obtain the FE solutions have the mesh near to the impedance boundary refined.

Duct length	L	1.6m
Liner length	L_2	1.2m
Hard section length	L_1, L_3	0.2m
Duct height	h	0.5m
Reduced frequency	kh	10
Mean flow Mach number	M_o	0.5M

Table 7.4: Surface waves duct model specification.

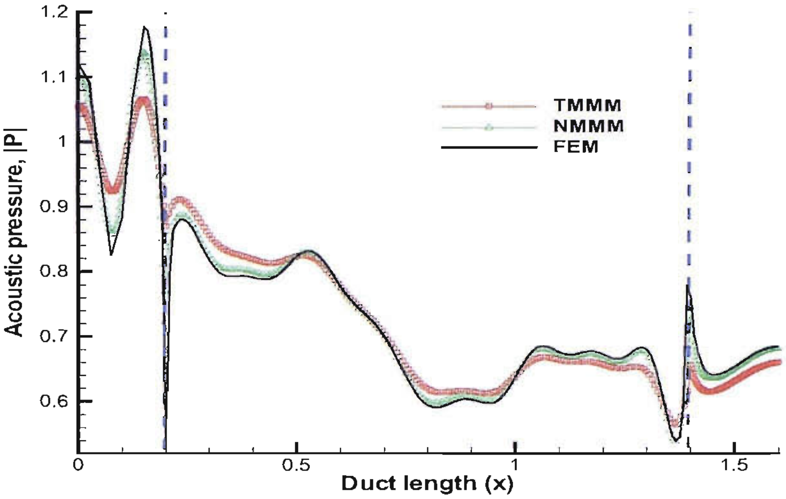

bt

Figure 7.12: Case study 1 - absolute acoustic pressure along the duct wall at $y = h$. Results obtained by the FE transmission analysis, by the TMMM and by the NMMM are presented. $kh = 10$, $Z = 2 - 1i$ and $M_o = 0.4$.

Fig. 7.18 presents contour plots of the absolute acoustic pressure computed by the FE transmission analysis, by the NMMM and by the TMMM for configuration 1 and 2. For configuration 1, only the NMMM and the FEM predict the presence of surface waves at the impedance boundaries at $y = 0$ and h. The same is observed for configuration 2, in which surface waves are predicted at the acoustic boundary at $y = h$.

In Fig. 7.19, bar charts show the *PWL* of the transmitted modes at $x = L$ and of the reflected modes at $x = 0$ plotted against the mode number are presented. Results obtained by the FE transmission analysis, by the NMMM and by the TMMM are presented. The TMMM agrees poorly with the FEM especially the reflected modes with discrepancies as much as 9 dB. The NMMM agrees well with the FEM with discrepancies less than 1 dB.

This study have shown that the NMMM is capable of studying sound propagation in a duct containing surface waves and the NMMM yields solutions with better accuracy than those obtained using the TMMM for the problems considered.

7.7.3 Case Study 3: Sound Diffraction By An Infinitely Thin Splitter In The Duct

This work investigates the effect of sound diffraction by an infinitely thin splitter in the duct. The objectives of the work are to demonstrate that the NMMM is capable of studying the problem and to show any acoustic benefit of having a splitter in the duct. The test case consists of a uniform two-dimensional duct with a rigid splitter located at $y = 0.2$ in the duct - see Fig. 7.1(b). The duct is studied for $kh = 10$ with and without flow. At the inlet of the duct, a harmonic mode of $n_i = 2$ is incident. Table 6.2 details the values of the parameters

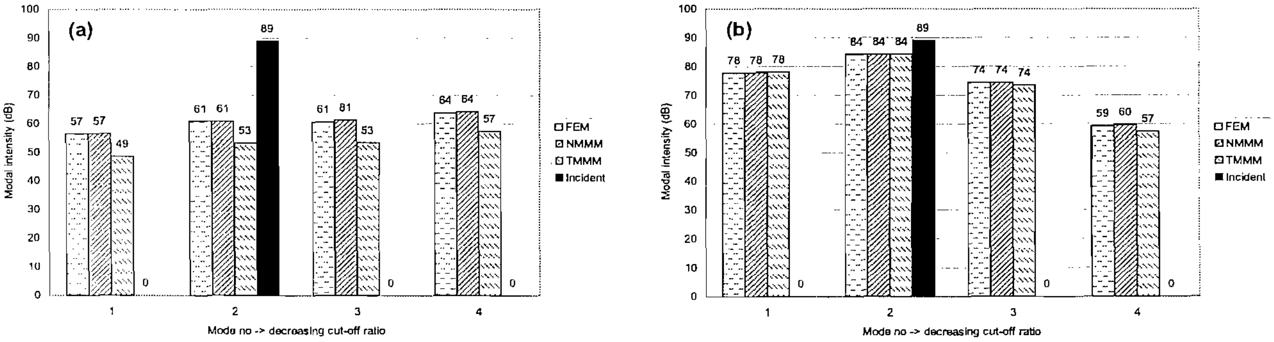

Figure 7.13: Case study 1 - PWL of the reflected modes at $x = 0$ and of the transmitted modes at $x = L$ plotted against mode number. Solutions obtained by the FE transmission analysis, by the TMMM and by the NMMM are presented. $kh = 10$, $Z = 2 - 1i$, $M_o = 0.4$. (a) Reflected modes, (b) Transmitted modes.

used in the analysis.

For the FE transmission analysis, meshes constructed from 6-noded triangular elements with an average mesh resolution of 10 nodes per wavelength are used to discretize the ducts - see Figs. 7.2(b) and (c). The mesh near the splitter edges and the impedance boundaries is refined. The splitter thickness is taken to be $t_p/h = 0.001$. t_p is the splitter thickness and h is the width of the duct.

For the MM analysis, the splitter is assumed to be infinitely thin. The number of duct modes in Sections (1) and (4) is set to equal to the number of hardwalled duct modes having cut-off ratios greater than 0.7. According to the relative convergence theorem, the number of duct modes in Sections (2) and (3) need to set to be equal to $m2 = (h1/h)m1$ and $m3 = (1 - h1/h)m1$, which is in proportion to the width of the duct [104].

Hardwalled Duct with A Splitter

Figs. 7.20 and 7.21 present the PWL of the transmitted modes at $x = L$ and of the reflected modes at $x = 0$ plotted against the mode number for a hardwalled duct with and without flow. Results obtained by the FE transmission analysis and by the NMMM are presented. The results show good agreement between the two methods with discrepancies less than 1 dB for the no flow case and less than 2 dB for the flow case.

The results show that the splitter has scattered the acoustic energy to the other cut-on modes. The high order modes are more affected than the low order modes by the splitter diffraction. The same results were observed by Nijboer and Sijtsma [106] in their study of sound diffraction by an infinitely thin circumferential splitter in a cylindrical duct.

Fig. 7.22 presents contour plots of the absolute acoustic pressure predicted by the FE transmission analysis and by the NMMM for the zero and uniform flow. Fig. 7.22 also shows good agreement between the two methods. For the flow case, the pressure is finite at the trailing edge of the splitter which satisfies the Kutta

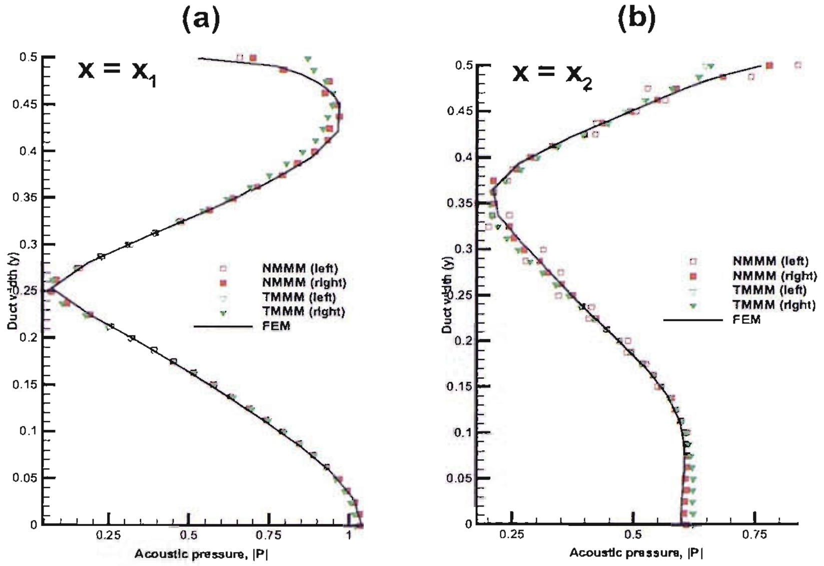

Figure 7.14: Case study 1 - absolute acoustic pressure along the matching interfaces at $x = x_1$ and x_2. $kh = 10$, $Z = 2 - 1i$, $M_o = 0.4$. (a) Acoustic pressure along the matching interface at $x = x_1$, (b) Acoustic pressure along the matching interface at $x = x_2$.

condition - see Figs. 7.22(c) and (d) [60]. At the leading edge of the splitter, pressure singularity is shown.

Softwalled Duct with A Splitter

Figs. 7.23 and 7.24 present the *PWL* of the transmitted modes and of the reflected modes plotted against the mode number for a softwalled duct with and without flow. For the no flow case, good agreement is shown between the NMMM and the FEM with discrepancies less than 2 dB. For the flow case, good agreement is only observed between the NMMM and the FEM with discrepancies less than 3 dB. This can be regarded as good agreement as the splitter is not infinitely thin in the FE model. Again, the TMMM shows considerably poorer

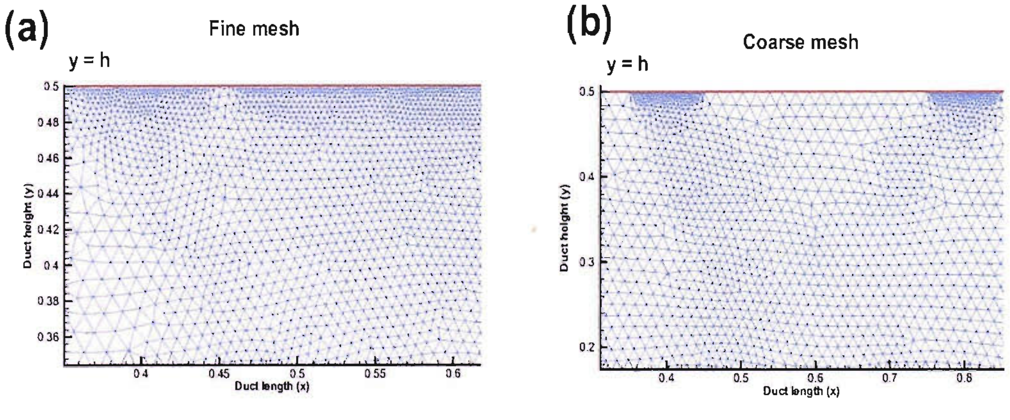

Figure 7.15: Case study 2 - finite element meshes (a) Fine mesh, (b) Coarse mesh.

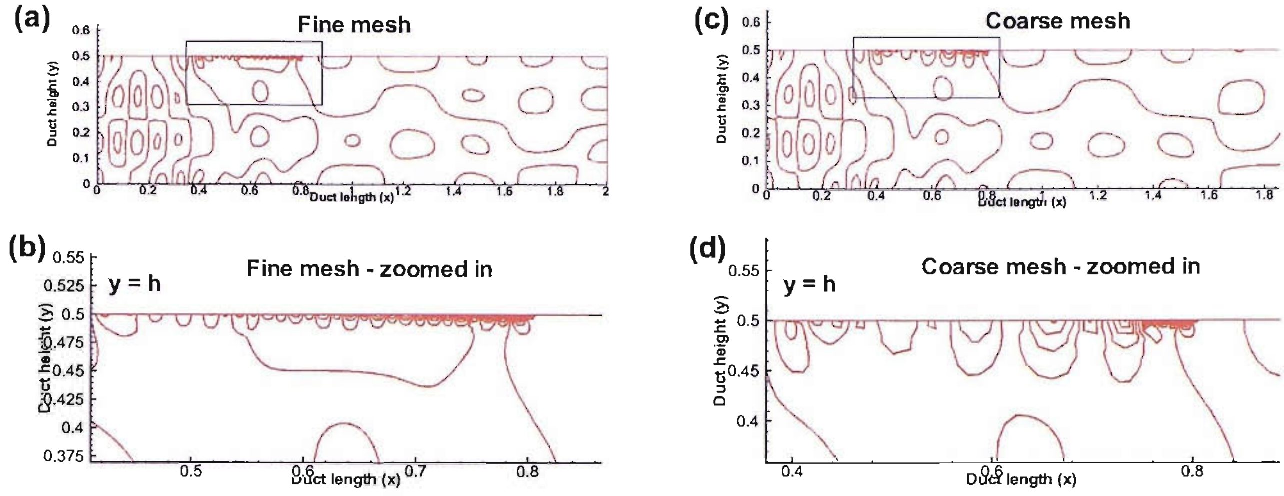

Figure 7.16: Case study 2 - contour plots of the absolute acoustic pressure obtained using the fine and the coarse mesh shown in Fig. 7.15. kh=10 and $M_o = 0.5$. (a) Fine mesh, (b) Coarse mesh.

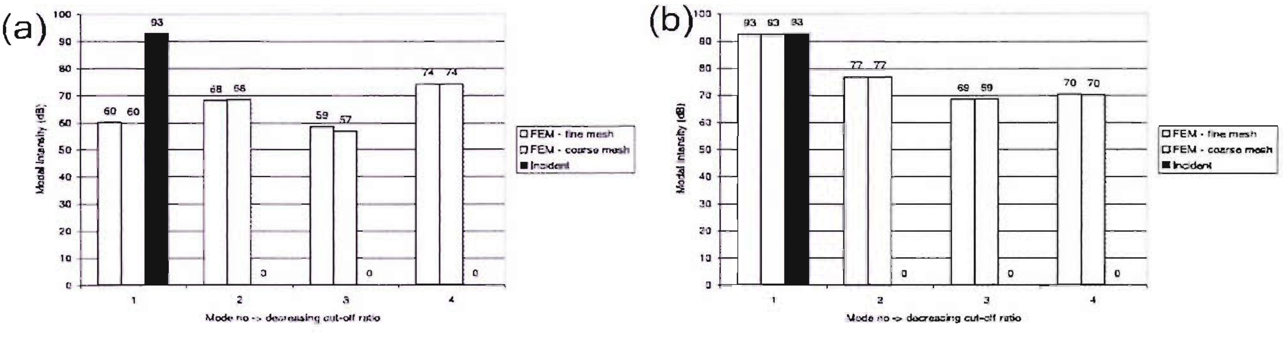

Figure 7.17: Case study 2 - *PWL* of the reflected and transmitted modes predicted by using the fine and coarse FE grids. kh=10, $M_o = 0.5$. (a) Reflected modes, (b) Transmitted modes.

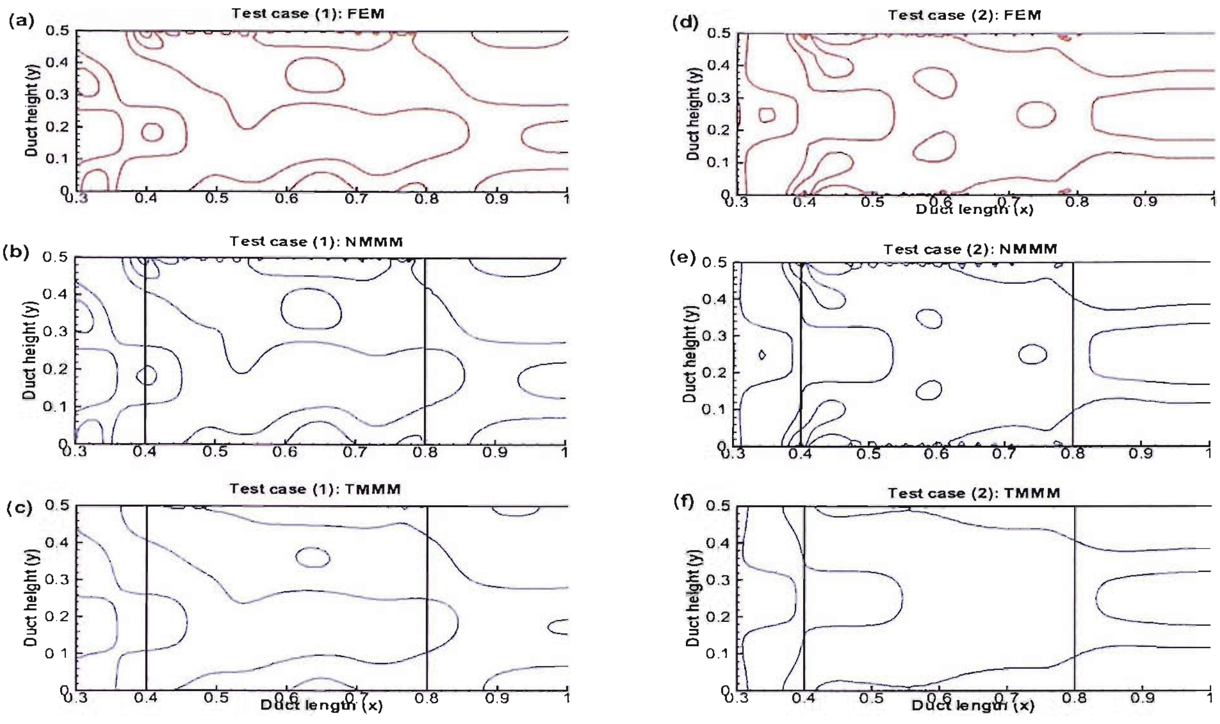

Figure 7.18: Case study 2 - absolute acoustic pressure obtained by the FE transmission analysis, by the NMMM and by the TMMM. $kh = 10$ and $M_o = 0.5$.

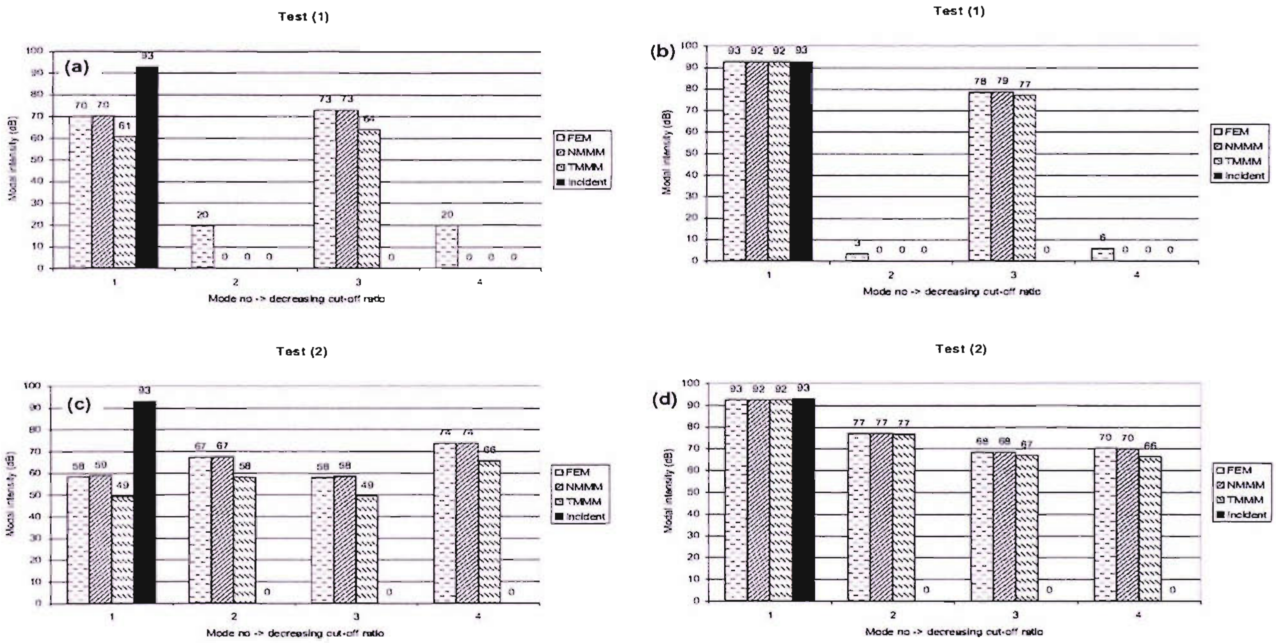

Figure 7.19: Case study 2 - PWL of the reflected modes at $x = 0$ and of the transmitted modes at $x = L$ plotted against mode number. kh=10 and $M_o = 0.5$. (a) Configuration 1 - Reflected modes, (b) Configuration 1 - Transmitted modes, (c) Configuration 2 - Reflected modes, (d) Configuration 2 - Transmitted modes.

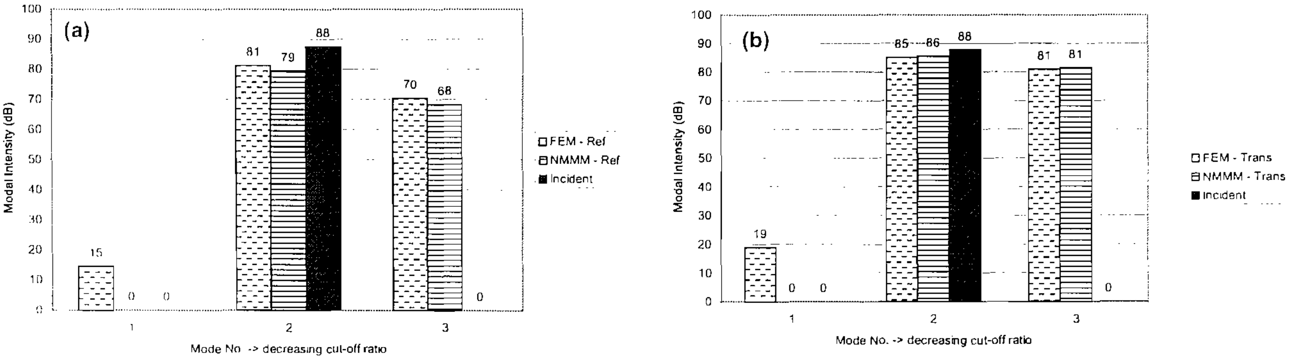

Figure 7.20: Case study 3 - Hardwalled duct with a splitter. *PWL* of the transmitted modes at $x = 0$ and of the reflected modes at $x = L$ plotted against mode number. $M_o = 0$ and $kh = 10$. (a) Reflected modes, (b) Transmitted modes.

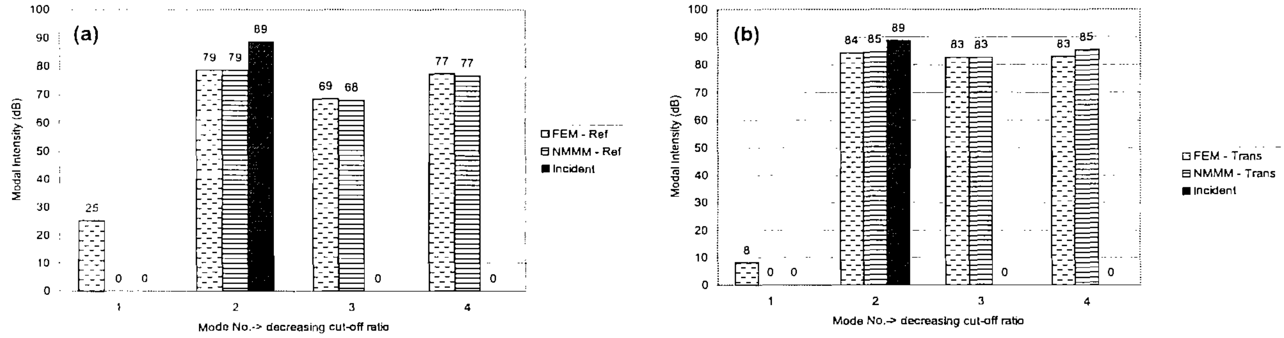

Figure 7.21: Case study 3 - Hardwalled duct with a splitter. *PWL* of the transmitted modes at $x = 0$ and of the reflected modes at $x = L$ plotted against mode number. $M_o = 0.3$ and $kh = 10$. (a) Reflected modes, (b) Transmitted modes.

agreement with the FE results especially the reflected modes - see Fig. 7.24. Fig. 7.27 presents the $\triangle PWL$ predicted by the FEM, by the NMMM and by the TMMM for the flow case. The poor TMMM results has slightly under-predicted the $\triangle PWL$ when compared to the FE results.

Compared to the case of a hardwalled duct without a splitter, the inclusion of the splitter in the duct has improved the $\triangle PWL$ by nearly 2 dB. For the no flow case, the improvement is even greater which is 3 dB. Although splitters help improving the acoustic treatment in the engine duct, they also introduce further weight and disturbances to the aerodynamic of the engine. A compromise between the acoustic benefit and safety is therefore required.

The study shows that the NMMM has correctly model the problem of sound diffraction by a splitter in the duct and the results agreed well with those obtained using the FE transmission model.

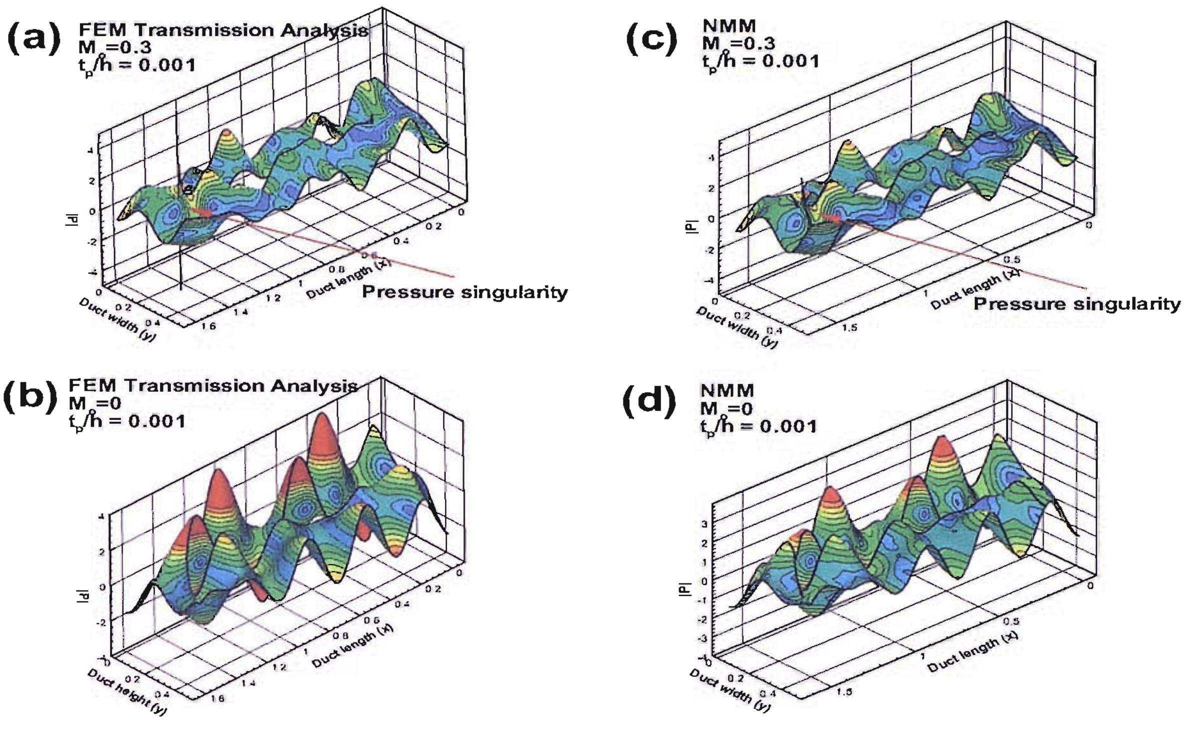

Figure 7.22: Case study 3 - Absolute acoustic pressure fields computed by the FE transmission analysis and by the NMMM. $M_o = 0.3$ and $kh = 10$. (a)-(b) FE transmission analysis (c)-(d) NMMM.

7.8 Computation Time

In this work, the computation time of the FE transmission model and of the NMMM model is evaluated using a uniform rigid duct as shown in Fig. 7.1(a). The duct is studied for $kh = 5$ and 10 with uniform mean flow at $M_o = 0.5$.

For the MM analysis, the number of duct modes in Sections (1) to (3) is set to equal to the number of hardwalled modes having cut-off ratios greater than 0.8. These duct modes are computed numerically using the FE eigenvalue model presented in Chapter 2. A uniform grid constructed from quadratic line elements with an average mesh resolution of 10 nodes per wavelength is used to discretize the duct width. For the FE transmission analysis, meshes constructed from 8-noded quadrilateral elements with an average mesh resolution of 10 nodes per wavelength are used for the discretization of the duct - Fig. 7.15.

The FE solutions are computed using ACTRAN which invokes a very efficient sparse direct solver. The solver has an out-of-core capability so that data is temporarily stored on the computer's hard disk during the solution process. The MM solutions are computed using the NMMM code developed by the author. The code is written in Fortran language operates under Window 2000 system. Both solutions are computed with a 1G Hz Pentium III processor with 1G bytes of RAM.

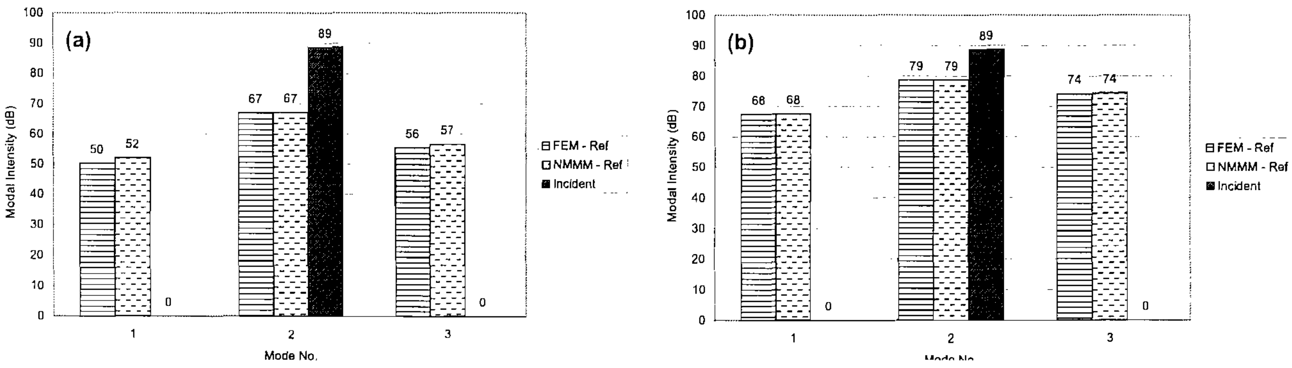

Figure 7.23: Case study 3 - softwalled duct with a splitter. *PWL* of the transmitted modes at $x = 0$ and of the reflected modes at $x = L$ plotted against mode number. $M_o = 0$, $kh = 10$ and $Z = 2 - 1i$. (a) Reflected modes, (b) Transmitted modes.

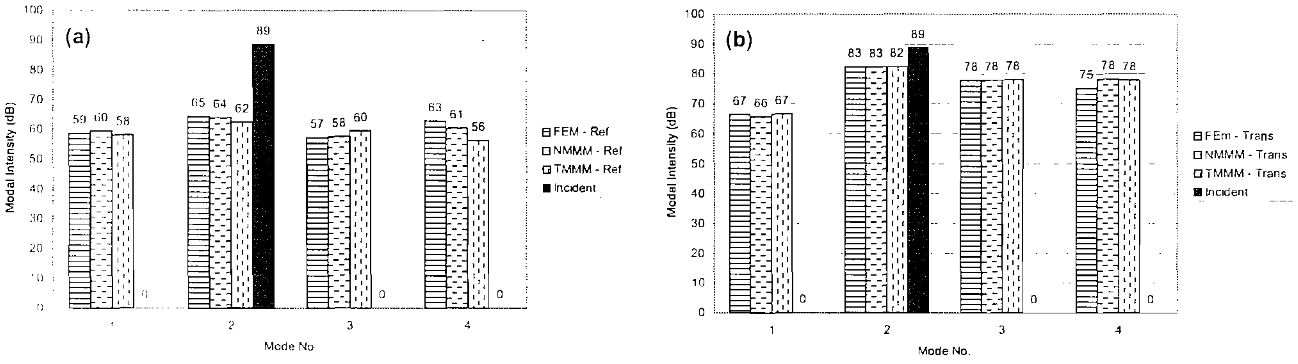

Figure 7.24: Case study 3 - softwalled duct with a splitter. *PWL* of the transmitted modes at $x = 0$ and of the reflected modes at $x = L$ plotted against mode number. $M_o = 0.3$, $kh = 10$ and $Z = 2 - 1i$. (a) Reflected modes, (b) Transmitted modes.

In Fig. 7.28(a), the computation time of the NMMM model is plotted against the number of truncated modes in the duct section. The two curves in the plot correspond to $kh = 5$ and 10 respectively. In Fig. 7.28(b), the problem size and the computation time of the FE transmission model are plotted against the mesh resolution for $kh = 5$ and 10.

Comparison between the two methods show that the NMMM requires significantly less computation time and storage than the FEM. The slopes of the time curves indicate that the difference between the two methods will be more significant for three-dimensional problems and with increasing frequency.

7.9 Conclusions

1. This study have demonstrated that the NMMM is capable of studying acoustic scattering due to impedance discontinuity, sound diffraction by splitters and sound propagation in a duct containing surface

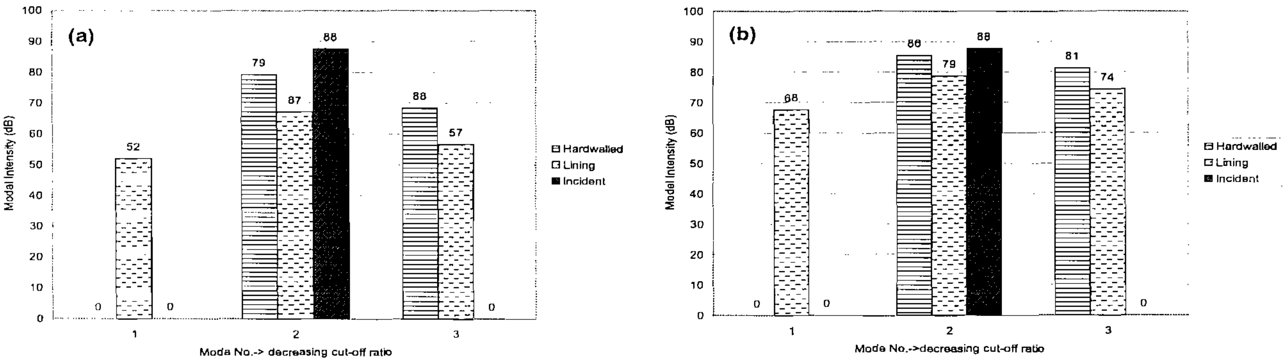

Figure 7.25: Case study 3 - comparison of hard and softwalled ducts with zero flow. *PWL* of the transmitted modes at $x = 0$ and of the reflected modes at $x = L$ plotted against mode number. $M_o = 0$, $kh = 10$ and $Z = 2 - 1i$. (a) Reflected modes, (b) Transmitted modes.

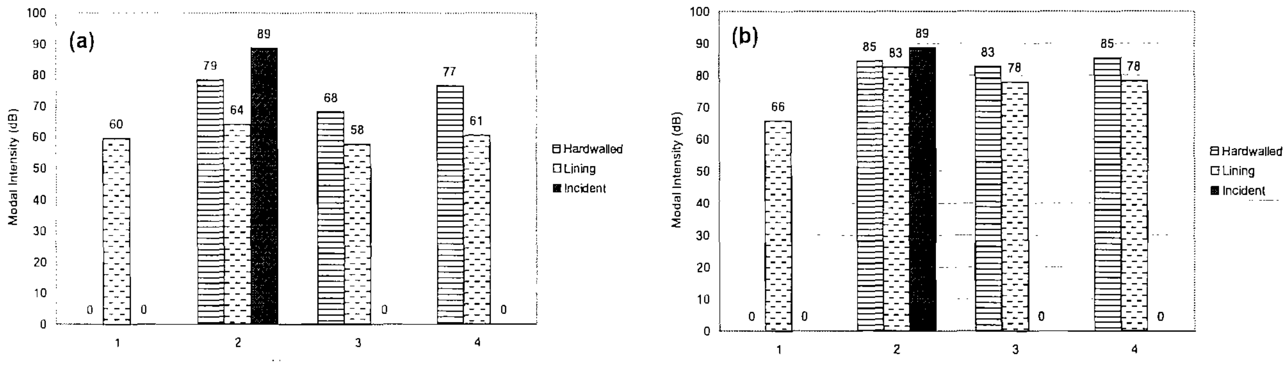

Figure 7.26: Case study 3 - comparison of hard and softwalled ducts with uniform flow. *PWL* of the transmitted modes at $x = 0$ and of the reflected modes at $x = L$ plotted against mode number. $M_o = 0.3$, $kh = 10$ and $Z = 2 - 1i$. (a) Reflected modes, (b) Transmitted modes.

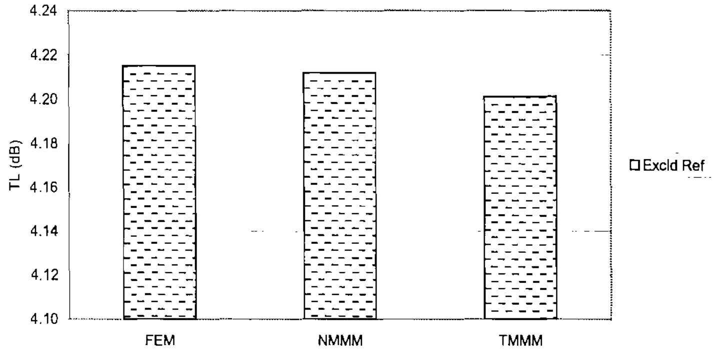

Figure 7.27: Case study 3 - ΔPWL predicted by the FE transmission analysis, by the NMMM and by the TMMM. $M_o = 0.3$, $kh = 10$ and $Z = 2 - 1i$.

waves.

2. When flow is present in the duct, the NMMM yields solutions which give better agreement with the finite

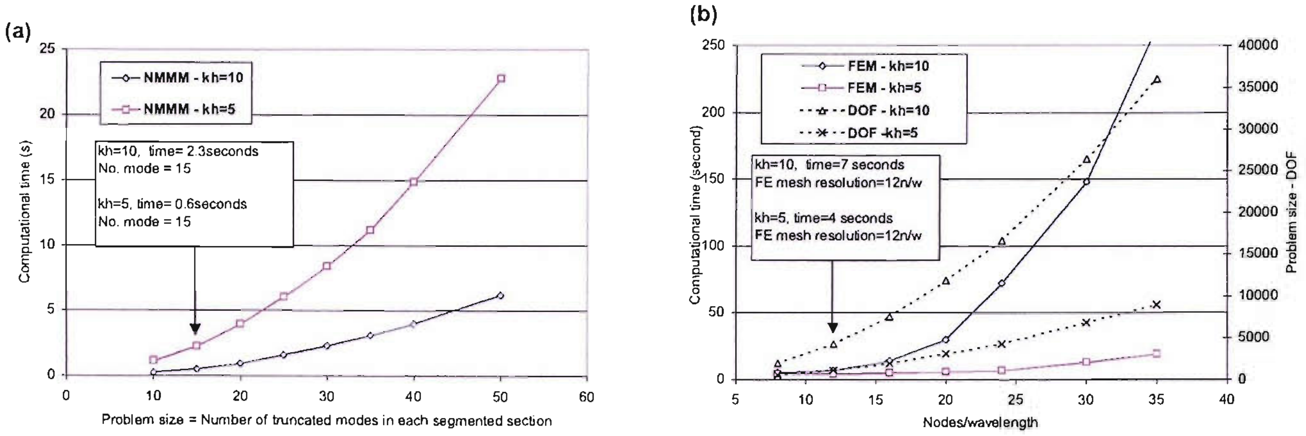

Figure 7.28: Computation time of the NMMM and the FE methods. $kh = 10$ and 5. $M_o = 0.5$.

element transmission analysis than those obtained using the TMMM. This is attributed to the additional boundary condition term derived in the NMMM which gives a better model of the acoustic pressure singularity at the impedance discontinuity.

3. The MM solutions obtained using the Galerkin weighted residuals method and using the least squares method show good agreement with each other and also with the FE transmission analysis.

4. The convergence study shows that the number of duct modes considered in each segment, equal to the number of hardwalled modes having cut-off ratios greater than 0.8, is found to be adequate for MM solutions to converge.

5. Splitters can improve the acoustic performance in lined ducts by scattering the acoustic energy into other high order cut-on modes which may be more easily attenuated by the liner.

6. The NMMM requires significantly less computing time and storage than the FE transmission analysis. The slopes of the time curves indicate that the difference between the two methods will be more significant at high frequencies and for three-dimensional problems. The resulting solution times are such that a parametric study of the geometrical parameters may be performed within an engineering time scale.

The results of the study have indicated that it is worthwhile to assess the performance of the NMMM for studying sound transmission in three-dimensional flow ducts.

Chapter 8

Results: Three-Dimensional Mode Matching Problems - Validation and Application

8.1 Introduction

This chapter presents the results of a study of sound transmission in three-dimensional ducts using the mode matching method (MMM). Chapter 6 has established that the new mode matching method (NMMM) is accurate and robust for two-dimensional problems. The method also requires less computational time and storage than the finite element (FE) transmission analysis. The aim of the present study is to examine the validity of the NMMM to study transmission of sound in three-dimensional ducts with non-uniform impedance boundaries.

The reduced frequency range covered in this study is $15 \leq kR \leq 30$ where k is the acoustic wavenumber and R is the characteristic size of the duct radius. This frequency range corresponds approximately to the blade passing frequency (BPF) in the intake or bypass duct of an aero-engine at maximum power. In Table 8.1, the relationship between flight condition, engine speeds and BPF for approach, cut-back and sideline for a typical high bypass ratio turbofan aero-engine is shown. Depending on the engine operation conditions, either the engine order (EO) or broadband propagation is of interest according to Table 8.2.

Engine order is related to modes generated by pressure disturbances rotating with the shaft frequency. For EO analysis, the propagating modes are locked with the rotor and are generated by the supersonic tip speed of the fan. The modes and frequencies to be considered are given by:

$$m = EO.nr = 1 \text{ and } f = EO/NB \times BPF \tag{8.1}$$

where m is the azimuthal mode order, nr is the radial mode order and NB is the number of blades in the rotor.

In this study, only the first radial mode is considered assuming that all the energy is concentrated at the first radial mode. However, in practice, the rotor-alone pressure field attached to a supersonic ducted fan will contain acoustic energy over a range of harmonics based on the engine shaft rotational speed. These EO harmonics are known as 'Buzz-saw' or 'Multiple Pure' tones. These tones are generated because of blade-to-blade variations.

Flight condition	BPF (Hz)	kR	Fan tip Mach No.
Approach	800	18	0.7
Cutback	1250	29	1.1
Sideline	1500	34	1.3

Table 8.1: Engine operating conditions for approach, cutback and sideline.

Analysis type	Approach	Cutback	Sideline
Engine order		x	x
Broadband	x	x	

Table 8.2: Flight conditions and analysis types.

For an ideal ducted fan, all the fan blades are identical and rotating in the presence of a uniform mean flow, the only generated tones are those of harmonics of BPF. In the study, the problem is simplified by neglecting the buzz-saw tones. The incident sound field generated by the fan is assumed to consist of a single tone which is the rotor-alone BPF tone.

Under less extreme engine operating conditions, the fan tip speed is subsonic, or just supersonic. The acoustic shock waves generated by the fan will be weak or non existent. Under these conditions, the acoustic sources many be generated by any part of the fan blade; the blade may be considered to be a broadband source. There are many ways to characterize the broadband source. The common one is to assume all possible modes are generated with equal energy and are uncorrelated [107, 32].

In this study, a series of simplified aero-engine ducts is considered for different engine operating conditions. Both EO and broadband analyses are performed.

Results are presented in two parts. The first part is about validation and convergence of the NMMM for three-dimensional problems. These studies are conducted by comparing the NMMM results with the FE transmission analysis results. In the second part, results of a parametric study of acoustic scattering by liner splices in a circular cylindrical duct is presented.

8.1.1 Outline

In Section 8.2, the problems are posed. Aspects such as the duct geometries, liner impedances and aspects of the computational models are described. Sections 8.3 and 8.4 present the results of validation and convergence of the NMMM. This is followed by Section 8.5 which presents the results of a parametric study of acoustic scattering by liner splices in a circular cylindrical duct. Three flying conditions are considered; approach, cut-back and sideline. In Section 8.6, the conclusions of the study are presented.

8.2 Problem Specification

Although a real engine duct has a three-dimensional geometry and flow, this noise transmission problem can be simplified , to a first approximation, by assuming that the inlet duct has an axisymmetric circular-section containing a uniform mean flow and the bypass duct has an axisymmetric annular-section containing a uniform mean flow as described in Chapter 1.

The results presented in this chapter have been carried out for the three-dimensional ducts shown in Fig. 8.1. These models can be viewed as the three-dimensional representations of simplified turbofan aero-engine inlet ducts. Both ducts have three sections, a short hard Section (a) with length, L_1, a lined Section (b) with impedance, Z and length, L_2 and another short hard Section (c) with length, L_3. At the inlet of the duct at $z = 0$, a single harmonic mode or a multi-mode source with equal energy per mode is specified as the input source.

In Duct (A), a uniform liner is considered in Section (b) and in Duct (B) two spliced liners are considered in Section (b). In the validation and convergence study, the acoustic impedance values are taken from the known test cases in [59].T he acoustic liners values are derived for a simple model for a single cavity liner. In the liner splices study, the acoustic impedance is taken to be $Z = 2 - 1i$, which is a typical value for a turbofan inlet liner. Although uniform mean flow is considered in the study, the new mode matching (NMM) model is capable of considering any flow profile over the duct cross section.

At the inlet of the duct at $z = 0$, for engine order analysis, the input source is specified as a rotor-alone BPF tone with a modal coefficient of 1. For broadband analysis, the input source consists of all the cut-on modes with equal energy per mode. The amplitude of each cut-on mode is determined using the expression of modal energy presented in Chapter 5.

8.2.1 Modal Scattering

In Duct (A), a sound source (m,nr) propagates in the positive z direction will scatter into other radial modes, nr of the same azimuthal order, m, when it meets the hard/lined interfaces at $z = z_1$ and z_2. In Duct (B), the liner splices will cause scattering of acoustic energy into other radial, nr and circumferential, m modes which are cut-on. The scattered modes will consist of azimuthal modes with $m = iB \pm jN_s$, where j and i are integers, B is the BPF azimuthal mode number and N_s is the number of splices. More explanations about modal scattering by an acoustic liner are presented in Chapter 5.

8.2.2 Mode Matching Models

To carry out MM analysis, both Duct (A) and Duct (B) are segmented into three sections; Section (1), Section (2) and Section (3), at the change of impedance at $z = z_1$ and z_2 - see Fig. 8.2. In each section, the superposition of positive and negative acoustic modes that represent the acoustic field are truncated into a finite number of

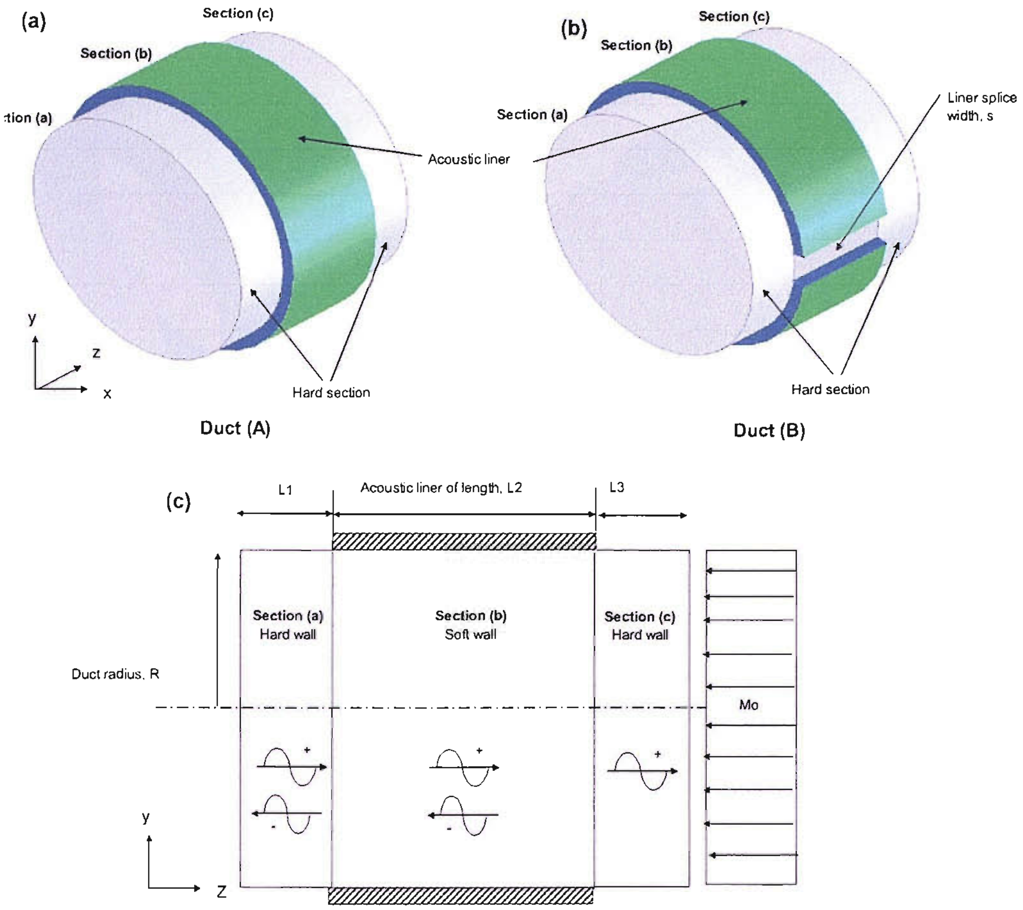

Figure 8.1: Duct models.

acoustic modes, n. The mode truncation is based on the number of hardwalled acoustic modes having a given cut-off ratio. The duct modes in each duct section are computed numerically using the FE eigenvalue model presented in Chapter 2. Meshes constructed from 6-noded triangular elements with an average mesh resolution of 8 to 10 nodes per wavelength are used to discretize the duct cross-sections. For the duct with liner splices, the mesh is refined near to the splices - see Fig. 8.3.

8.2.3 FE Models

As Duct (A) is axisymmetric along the z-axis, the problem can be simplified to a two-dimensional problem. The duct is discretized using grids constructed from 8-noded quadrilateral elements as shown in Fig. 8.3(b). The average mesh resolution is set at 14 nodes per wavelength and the mesh near to the liner is refined. The mesh resolution defines the number of nodes which are required to represent the solution over one wavelength.

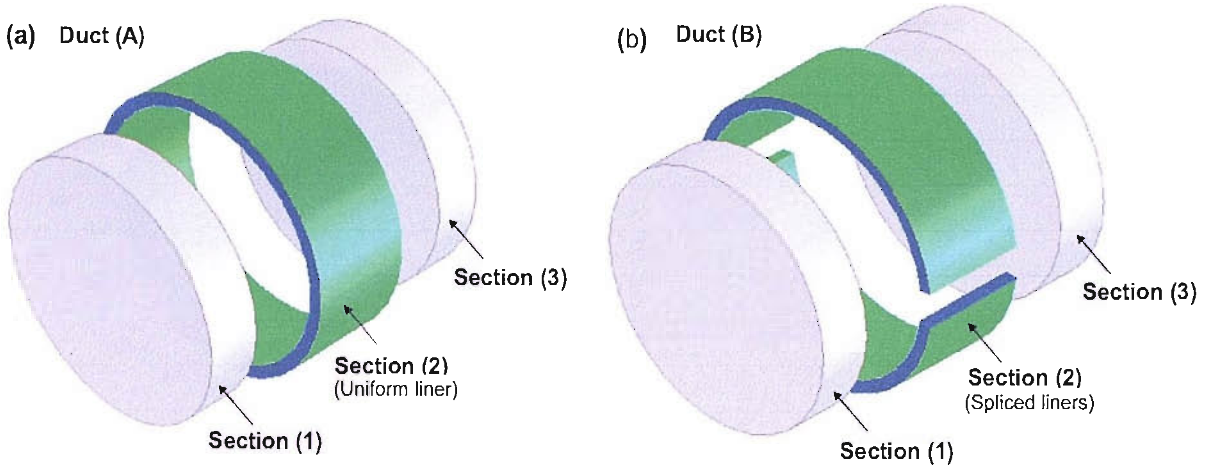

Figure 8.2: Mode matching models.

In the z direction, the resolution of the grid, N is defined as:

$$N = \frac{c_o}{f\Delta|1 - M_o|} \tag{8.2}$$

where c_o is the speed of sound, f is the frequency in Hertz and Δ is the average distance between two nodes. The mesh resolution in the y direction is given by $N = c_o/f\Delta$ as no flow effect is taken into account. Duct (B) is discretized using meshes constructed from quadratic pentahedral and hexahedral elements with an average mesh resolution of 8 to 10 nodes per wavelength as shown in Fig. 8.3(a).

At the inlet plane, for the modal matching, all the cut-on and a few cut-off negative propagating duct modes are considered. At the exit plane, all the cut-on and a few cut-off positive propagating duct modes are considered. No negative duct modes are specified as the exit plane is assumed to be an anechoic termination.

In this study, FE results obtained using ACTRAN [105] are used as the benchmark solutions for comparison with the MM results. Details of the FE transmission model are presented in Chapter 6.

8.3 Assessment of Accuracy of the New Mode Matching

This study examines the accuracy of the NMMM by comparing with the FE transmission analysis. The model used in this analysis consists of a circular cylindrical duct with a hard-soft-hard section as shown in Fig. 8.1. In the soft section, Section (b), a uniform liner or two spliced liners of widths 3.8 cm, 5.7 cm, 7.6 cm, 9.5 cm and 11.9 cm are considered. These models are studied for $kR = 14$ and 16. Table 8.3 details the values of the parameters used in this analysis. These parameters are taken from the known test cases in [59]. At the inlet of

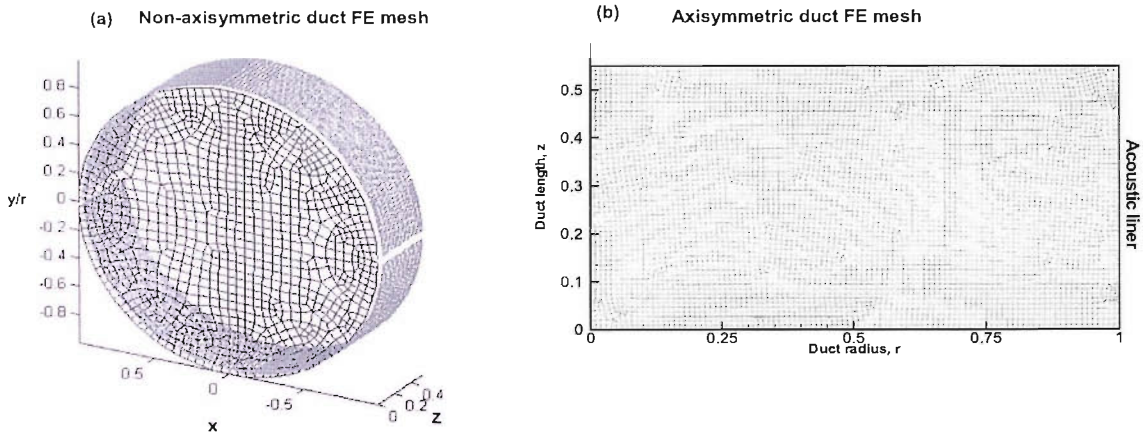

Figure 8.3: FE meshes. (a) Non-axisymmetric duct FE mesh, (b) Axisymmetric duct FE mesh.

the duct at $z = 0$, a harmonic tone (m=12,nr=1) with a modal coefficient of 1 is incident. Fig. 8.4 shows the duct cross-sectional meshes constructed for the FE and MM models. The mesh used for the computation of duct eigenvalues and eigenfunctions for the MM has the mesh near to the liner splices refined.

For the result, the in-duct sound power transmission loss, $\triangle PWL$ is computed by using the following expression:

$$\triangle PWL = 10 \log \frac{\sum_{i=1}^{n} W_i^+|_{z=0}}{\sum_{i=1}^{n_i} W_{n_i}^+|_{z=L}} \tag{8.3}$$

where $\sum_{i=1}^{n} W_i^+|_{z=L}$ is the sum of the acoustic power in all the cut-on positive acoustic modes at the exit plane and $\sum_{i=1}^{n_i} W_{n_i}^+|_{z=0}$ is the sum of the acoustic power of the incident modes at the source plane.

Figs. 8.5(a) and 8.6(a) present the $\triangle PWL$ predicted by the FE transmission analysis, by the NMMM and by the TMMM plotted against different splice widths for $kR = 14$ and 16. Figs. 8.5(b) and 8.6(b) present the discrepancies between the TMMM and NMMM predictions compared to the FE transmission analysis predictions for $kh = 14$ and 16.

The results show that the NMMM and the TMMM agree well with the FE transmission analysis with discrepancies less than 0.5 dB. However, the NMMM shows better agreement with the FEM than the TMMM. This is credited to the additional boundary condition term derived in the NMMM which gives a better model of the acoustic pressure singularity at the impedance discontinuity. Details of the MM models are presented in Chapter 5. Fig. 8.7 presents contour plots of the real part of the acoustic pressure at the inlet ($z = 0$) and outlet ($z = L$) of the duct for different splice widths and fan speeds. The results are obtained using the NMM model. In the plots, acoustic scattering by the liner splices is clearly shown and the scattering becomes more apparent

		$kh = 14$	$kh = 16$
Duct radius	R	1.0m	1.0m
Duct length	L	1.1m	1.1m
Hard section length	L_1, L_3	0.15m	0.15m
Liner length	L_2	0.8m	0.8m
Reduced frequency	kR	14.01	16.35
Acoustic impedance	Z	2.12+0.01i	4.49+2.29i
Mean flow Mach number	M_o	-0.4M	-0.5M

Table 8.3: Model inlet duct specification - validation and convergence study.

as the splice width increases. In the case of $kR = 16$, the spinning pattern of the incident mode is still visible at the outlet of the duct because the incident mode is well cut-on and is not well attenuated by the acoustic liner. It is not the case for $kR = 14$, as the incident mode is just cut-on and is well attenuated by the liner.

In Fig. 8.8, the averaged modal intensities, PWL of all the cut-on modes at the exit plane for different splice widths are presented. The PWL of the incident mode is also presented in the plots. The results presented show that the acoustic energy of the incident mode (12,1) has been scattered into other cut-on modes of different radial and azimuthal orders due to the liner splices. The scattered fields are made up of modes with circumferential order, $m = 12 \pm j2$ where j=1,2,... . If no splice is present in the duct, the scattered fields will be made up of cut-on modes with circumferential order, $m = 12$. The results also show that the number of scattered modes increases with the splice width. For $kR = 16$, the incident mode (12,1) dominates the total sound field and for $kR = 14$, the scattered tones dominate the total sound field. This is consistent with the results presented in Fig. 8.7. The large variation in the effective attenuation occurs with the splice width indicates that large acoustic benefit can be gained by having thin splice or no splices in the duct.

The study has shown that the NMMM yields solutions which agree with the FE transmission analysis. The NMMM yields solution with better accuracy than the TMMM. The study has also shown that the NMMM offers significant savings in computational time and storage compared to the FE transmission analysis. The resulting solution times are such that a parametric study of the geometrical parameters may be performed within an engineering time scale.

8.4 Convergence of the New Mode Matching Method

The aim of this study is to determine the number of truncated modes required in each duct section in the MM model to produce convergence of the solution. The test model in Section 8.3 with the same parameters is considered here. The duct is studied for $kR = 14$.

Fig. 8.9 shows the $\triangle PWL$ predicted by considering different numbers of duct modes, n in each duct section in the MM model. The number of modes truncated in each section is determined by the number of hardwalled

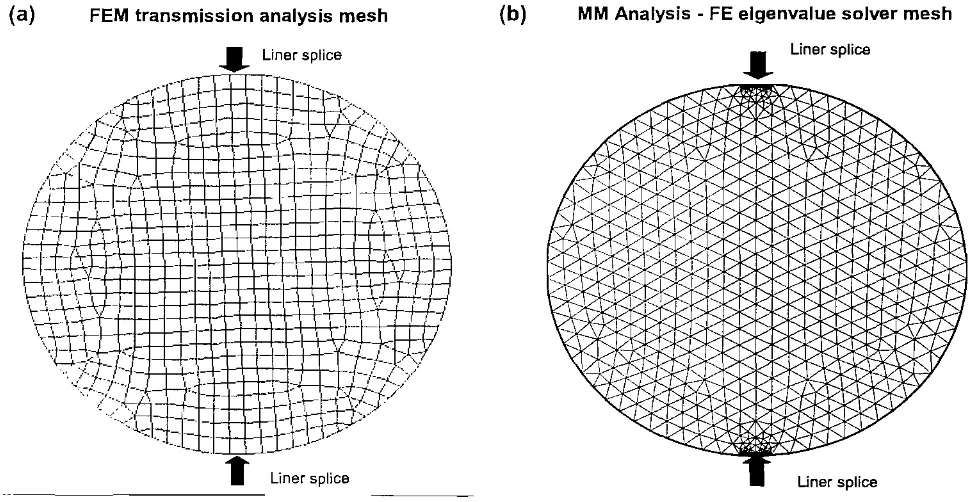

Figure 8.4: Duct cross-sectional meshes. (a) FE model mesh, (b) MM model mesh.

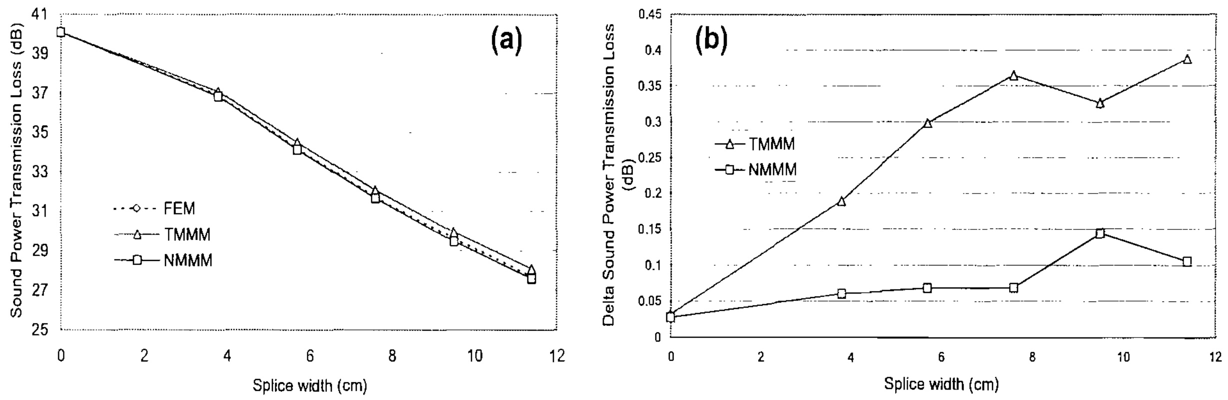

Figure 8.5: Validation study: Variation in $\triangle PWL$ with splice width for $kR = 14$, $M_o = -0.4$, $Z = 2.12 + 0.01i$. (a) $\triangle PWL$ plotted against different splice widths, (b) Discrepancies between TMMM and NMMM predicted $\triangle PWL$ with the FE transmission analysis predictions.

duct modes having cut-off ratios greater than 0.9, 0.8 and 0.7. Results of the FE transmission analysis are also presented.

The results show that a relatively small number of cut-off modes are required for the MM solutions to converge. The discrepancies between the solutions obtained by using the number of duct modes having cut-off ratios greater than 0.9, 0.8 and 0.7 are less than 1 dB. This indicates that the results are well converged. The converged MM results show discrepancies less than 1 dB with the FE transmission analysis.

The convergence study has shown that the number of duct modes considered in each duct section equals to the number of hardwalled duct modes having cut-off ratios greater than 0.8 is found to be adequate for converged solutions.

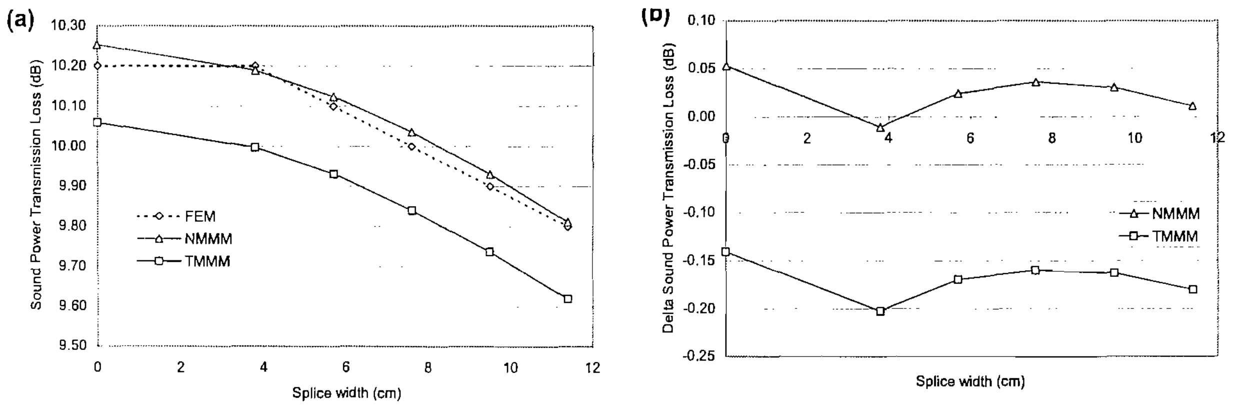

Figure 8.6: Validation study: Variation in $\triangle PWL$ with splice width for $kR = 16$, $M_o = -0.5$, $Z = 4.49 + 2.29i$. (a) $\triangle PWL$ plotted against different splice widths, (b) Discrepancies between TMMM and NMMM predicted $\triangle PWL$ with the FE transmission analysis predictions.

8.5 Acoustic Scattering By Liner Splices

This section presents the results of a parametric study of the effects of acoustic scattering by liner splices in a simplified engine inlet using the NMMM. The objectives of the study are to investigate how the liner attenuation is affected by the fan speed, the splice width and to illustrate the potential benefit that could be gained by manufacturing a uniform lining with no splices. Numerical results are presented to demonstrate how the rotor-alone BPF tone is scattered by the liner splices and also to show how the broadband noise attenuation is affected by the liner splices.

The test model consists of an infinite cylindrical duct containing two spliced liners as shown in Fig. 8.1(b). The splice width, s varies from 0 cm to 11.9 cm or 0 inch to 5 inch where 0 cm corresponds to no splices. Depending on the engine operation conditions, EO or broadband analysis is performed. The values of the parameters used for the different engine operation conditions are listed in Table 8.4.

For the broadband calculation, all the cut-on modes are uncorrelated and carry equal sound power. For the EO calculation, the rotor-alone BPF tone (26, 1) of modal coefficient 1 is incident at the fan plane at $z = 0$.

The meshes constructed for the MM and FE models for the cutback case are presented in Fig. 8.10. For the MM model, the duct cross-section meshes used for the computation of duct eigenvalues and eigenfunctions are constructed from 6-noded triangular elements with an average mesh resolution of 8 to 10 nodes per wavelength. The mesh near to the splices is refined such that there are at least four elements for the smallest splice width. For the FE model, the three-dimensional mesh is constructed from quadratic pentahedral and hexahedral elements and the mesh resolution is such that the splice is only one element wide. These meshes are generated using the ICEM CFD package [101].

		Approach	Cutback	Sideline
Duct radius	R	1.27m	1.27m	1.27m
Duct length	L	1.6m	1.6m	1.6m
Hard section length	L_1, L_3	0.2m	0.2m	0.2m
Reduced frequency	kR	18	28	34
Acoustic impedance	Z	2-1i	2-1i	2-1i
Mean flow Mach number	M_o	-0.2M	-0.4M	-0.5M

Table 8.4: Model inlet duct specification.

8.5.1 Broadband Analysis

For the broadband analysis, two engine operation conditions of approach and cutback are considered. The length of the liner considered is 0.8 m, a typical length for an inlet liner. Fig. 8.11(a) presents the in-duct sound power transmission loss, $\triangle PWL_{BB}$ plotted against different splice widths for approach and cut-back. The $\triangle PWL_{BB}$ is defined by

$$\triangle PWL_{BB} = 10\log\frac{\sum_{i=1}^{n} W_i^+|_{z=0}}{\sum_{j=1}^{n_t} W_j^+|_{z=L}} \tag{8.4}$$

where $\sum_{i=1}^{n} W_i^+|_{z=L}$ is the sum of the acoustic power in all the transmitted modes at the exit plane at $z = L$. $\sum_{j=1}^{n_t} W_j^+|_{z=0}$ is the sum of the acoustic power in all the incident acoustic modes at the inlet plane at $z = 0$.

The results show that the $\triangle PWL_{BB}$ decreases with increasing splice width, s. This is expected as the splice width increases, the effective lining area decreases. However, the reduction in the acoustic power due to the liner splices is relatively small. For both approach and cutback, only 0.5 dB reduction in the $\triangle PWL_{BB}$ between a uniform liner with no splice and the one with two 11.9 cm splices.

Fig. 8.11(b) also shows that the reduction in acoustic power varies exponentially with the splice width whilst the liner splice area varies linearly with the splice width. The general assumption of linear reduction in acoustic power with the splice area will over-predict the liner performance. The results also show that the broadband attenuations are greater for the cutback case. It might be the present acoustic liner is not optimized for approach. There are also more cut on modes which might not be well attenuated by the present acoustic liner.

The results show that for broadband source, the variations in $\triangle PWL_{BB}$ due to the presence of liner splices are relatively small.

8.5.2 Engine Order Tone Analysis

The effect of varying the length of the acoustic lining on the in-duct sound power transmission loss, $\triangle PWL$ for different splice liner widths is examined in this study. Cutback and sideline flying conditions are considered. The expression of the $\triangle PWL$ is:

$$\triangle PWL = 10\log\frac{\sum_{i=1}^{n} W_i^+|_{z=0}}{W^+|_{z=L}} \tag{8.5}$$

where $\sum_{i=1}^{n} W_i^+|_{z=L}$ is the sum of the acoustic power in all the positive acoustic modes at the exit plane at $z = L$. The sum of the acoustic power of the incident modes at the inlet plane at $z = 0$ is given by $W^+|_{z=0}$. The length of the lining considered is $L/D = 0.1$ to 4.0 where D is the diameter of the duct and L is the length of the liner.

Figs. 8.12(a) and 8.13(a) present three-dimensional plots of the $\triangle PWL$ plotted against the splice width, s and the liner length, L/D for cutback and sideline. Figs. 8.12(b) and 8.13(b) present the same results viewing from a different angle. In the plots, the typical lengths of fan case and inlet liners are highlighted which is $D/L = 0.03$ to 0.06 for the fan case liner and $D/L = 0.4$ to 0.5 for the inlet liner.

The results show that increasing the splice width has significant effects on the $\triangle PWL$ for cutback. The $\triangle PWL$ varies from 110 dB to 24 dB as the splice width reduces from 11.9 cm to 0 cm for a liner length of $L/D = 0.6$. The benefit of having smaller splice width is greater than having longer liner. For sideline, the effect of decreasing the splice width on the $\triangle PWL$ is relatively small. The $\triangle PWL$ only improved by 1 dB as the splice width reduces from 11.9 cm to 0 cm for a liner length of $L/D = 0.6$. The reason being the rotor-alone BPF tone (26,1) is well cut-on and is not well attenuated by the liner. For cutback, the rotor-alone BPF tone (26,1) is just cut-on and therefore is well attenuated by the liner. Fig. 8.14 presents curves of the $\triangle PWL$ plotted against the liner length for different splice widths and flying conditions. The results show that the liner attenuations are significantly greater for cutback than sideline.

Figs. 8.13 and 8.12 show that the benefit of doubling the length of the exiting fan case and inlet liner is small for sideline. However, for cutback, significant improved in the $\triangle PWL$ is shown; 7 to 10 dB for the inlet liner and 5 to 8 dB for the fan case liner - see Fig. 8.12. For sideline, 2 to 3 dB for the inlet liner and of 6 to 7 dB for the fan case liner are shown by doubling the liner length - see Fig. 8.13.

The cutback results also show that the $\triangle PWL$ increases linearly with the liner length until the scattered tones dominate the rotor-alone attenuation in the duct [58] - see Fig. 8.12(b). The $\triangle PWL$ curves flatten out when the scattered tones dominate the rotor-alone attenuation.

In Fig. 8.15, contour plots showing the real part of the acoustic pressure at the inlet ($z = 0$) and at the outlet ($z = L$) of the duct for different splice widths and engine operating conditions are presented. The results are obtained using the NMMM and the length of the liner is set to $L/D = 0.48$. Acoustic scattering by the liner splices is clearly shown in the contour plots and the scattering effect becomes more significant as the splice width increases especially for cutback. For the sideline case, the spinning pattern of the rotor-alone mode is still visible at the outlet of the duct because the rotor-alone mode is well cut-on and is not well attenuated by the liner as in the cutback case. This is consistent with the results presented in Figs. 8.12 - 8.14.

Fig. 8.16 presents the modal solutions at the outlet plane of the duct to illustrate the effect of acoustic scattering by liner splices of different widths and at different engine operating conditions. The *PWL* of all the cut-on modes at the exit plane is shown. The results demonstrate that the liner splices cause scattering of acoustic energy from the incident modes into other cut-on modes. The scattered fields are only made up of duct modes with azimuthal order, $m = 26 \pm j2$ where $j = 1, 2...$. At this stage there is no simple or obvious explanation for the complex patterns which are observed in these modal distributions, but the current method provides a useful tool for exploring this phenomenon.

The results show that the *PWL* of the scattered modes decreases with decreasing splice width. For sideline, the incident rotor-alone mode dominates the total sound field and for cutback, the scattered tones dominate the total sound field. Therefore, reducing the *PWL* of the scattered modes by having thinner splices is predicted to increase the $\triangle PWL$ only for cutback.

For high fan speed, (e.g. sideline) in order to increase the overall sound power transmission loss, it will be necessary to increase the attenuation of the rotor-alone tones before there is any benefit of having thinner splices. In [59], the use of an axially segmented liner is being suggested to reduce the well cut-on rotor-alone tone for the sideline case. This is to scatter the rotor-alone mode into other modes which are more readily attenuated by the liner. For the broadband source, as the benefit of having thinner splices is relatively small, a better noise reduction method is therefore required before there is any benefit of having thinner splices.

8.6 Conclusions

The main conclusions from this chapter are:

1. The NMMM yields results which agree well with the FE transmission analysis for the three-dimensional ducts considered in this study.
2. The NMMM yields results with better accuracy than the TMMM when compared with the FE transmission analysis. This is credited to the additional boundary condition term in the NMMM.
3. The convergence study showed that the number of duct modes considered in each duct section equal to the number of hardwalled modes having cut-off ratios greater than 0.8 is found to be adequate for converged MM solutions.

4. Reducing the splice width has significant benefits for rotor-alone propagation for cutback, where the propagating mode is not well cut-on. However, these benefits are smoothed out when the engine is running at sideline conditions where the rotor-alone mode is well cut-on. For cutback, doubling the length of the existing fan case and inlet liners also shows significantly acoustic benefits. However, the benefit is not as great as having thinner splices.

5. The broadband analysis results show that reducing the splice width gives small acoustic benefits. Better noise reduction methods are therefore required to reduce the broadband noise before there is any benefit of having thinner splices.

6. The NMMM offers significant savings in computational time and storage compared to the FE transmission analysis. This is because of reduced problem size. The study has indicated that a parametric study of the geometrical parameters may be performed within an engineering time scale.

(a) kR=14 - splice width 0 cm

(e) kR=16 - splice width 0 cm

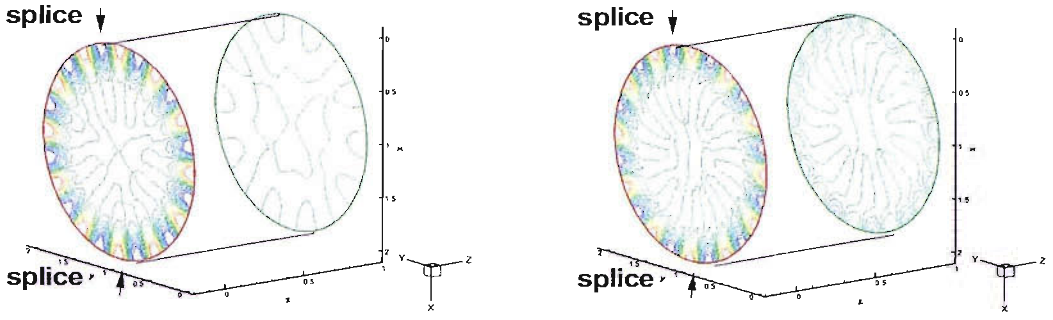

(b) kR=14 - splice width 3.798 cm

(f) kR=16 - splice width 3.798 cm

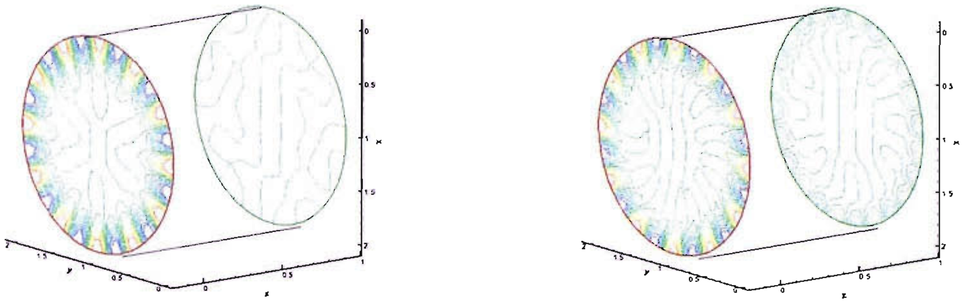

(c) kR=14 - splice width 7.596 cm

(g) kR=16 - splice width 7.596 cm

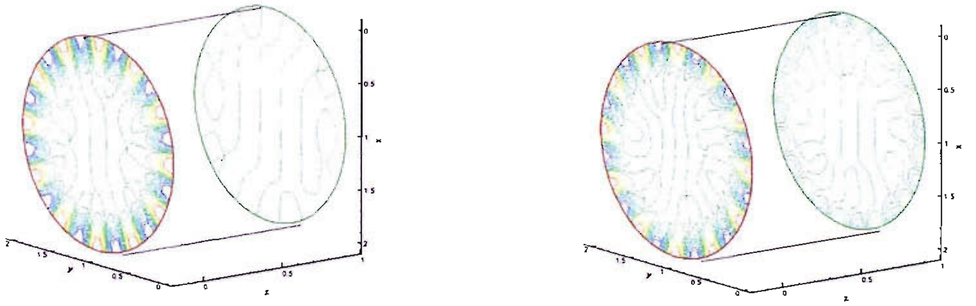

(d) kR=14 - splice width 11.940 cm

(h) kR=16 - splice width 11.940 cm

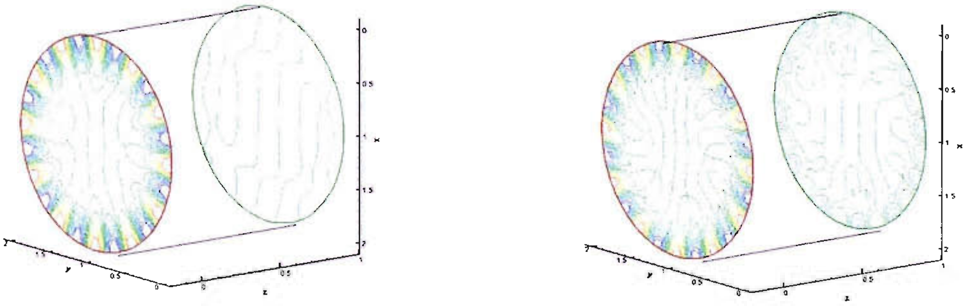

Figure 8.7: Validation study: Contour plots of the real part of the acoustic pressure at the inlet and exit of the duct for different splice widths. $kR = 14$ and 16, $M_o = -0.4$ and -0.5, $Z = 2.21+0.01i$ and $Z = 4.49+2.29i$.

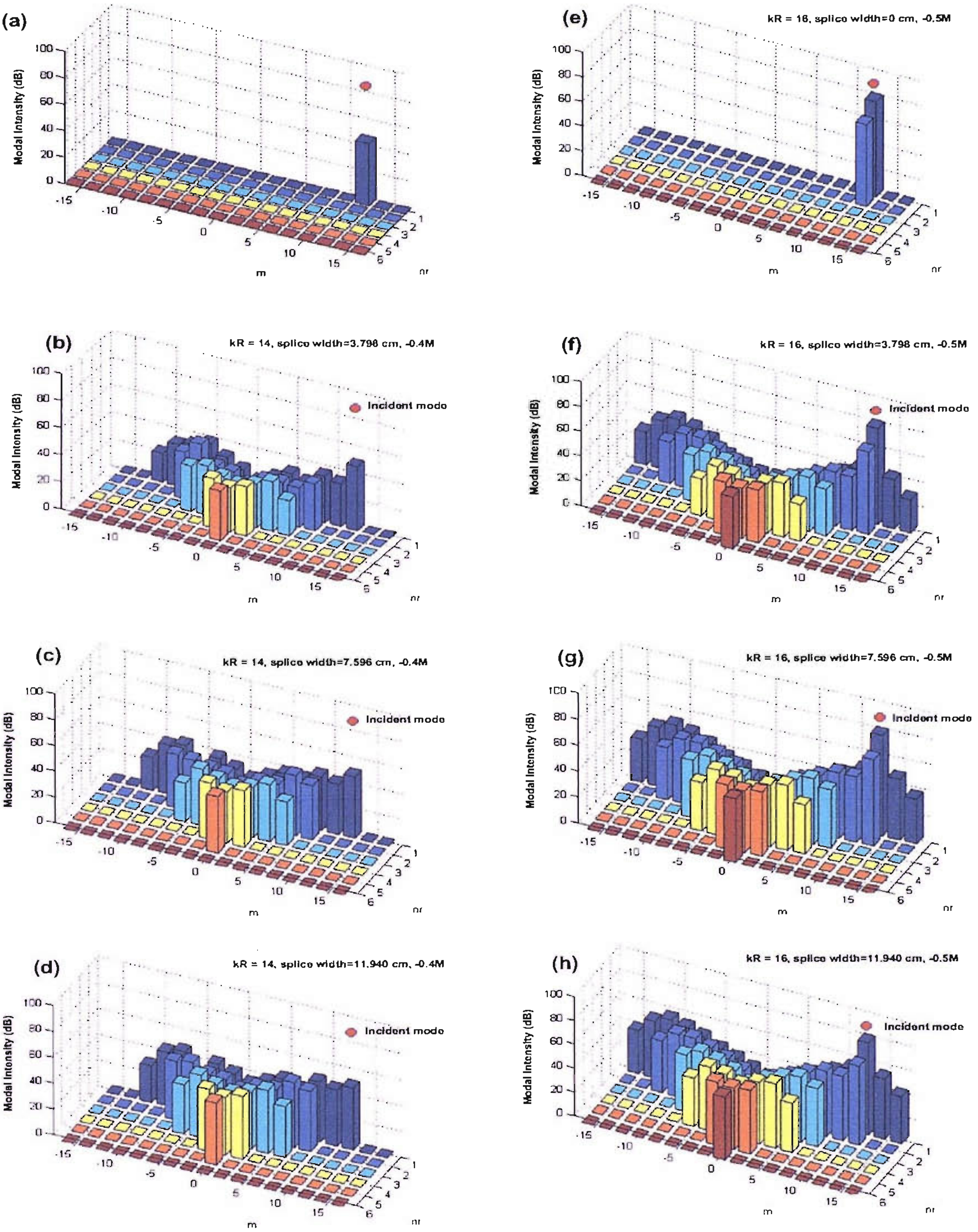

Figure 8.8: Validation study: (a)-(d) *PWL* of all the cut-on modes at the exit plane for $kR = 14$, $M_o = -0.4$, $Z = 2.21 + 0.01i$, (e)-(h) *PWL* of all the cut-on modes at the exit plane for $kR = 16$, $M_o = -0.5$, $Z = 4.49 + 2.29i$.

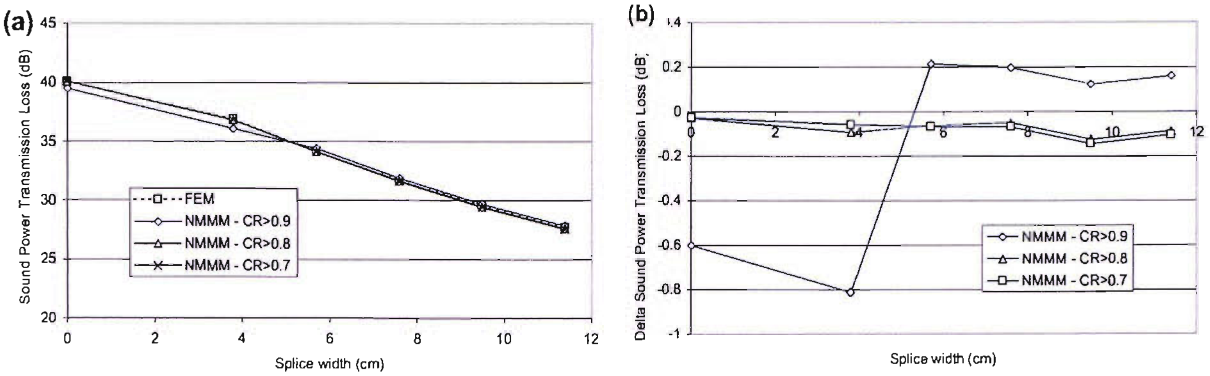

Figure 8.9: Convergence study: (a) $\triangle PWL$ predicted by considering different number of truncated modes in each segmented section in the MM model. (b) Difference between NMMM and FE predicted $\triangle PWL$. $kR = 14$, $M_o = -0.4, Z = 2.12 + 0.01i$.

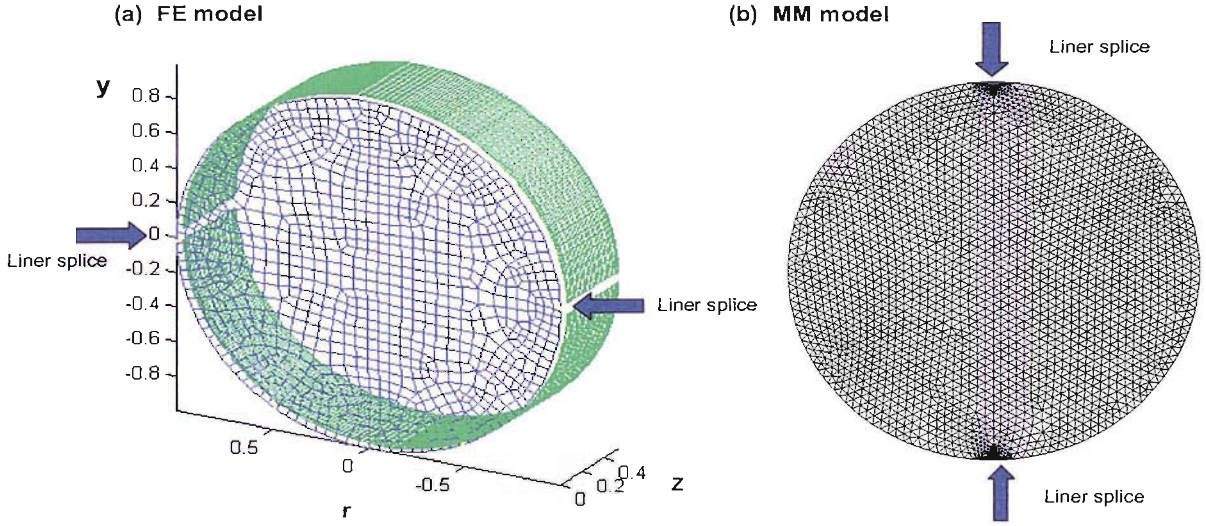

Figure 8.10: FE meshes constructed for the FE and MM models. (a) FE model, (b) MM model.

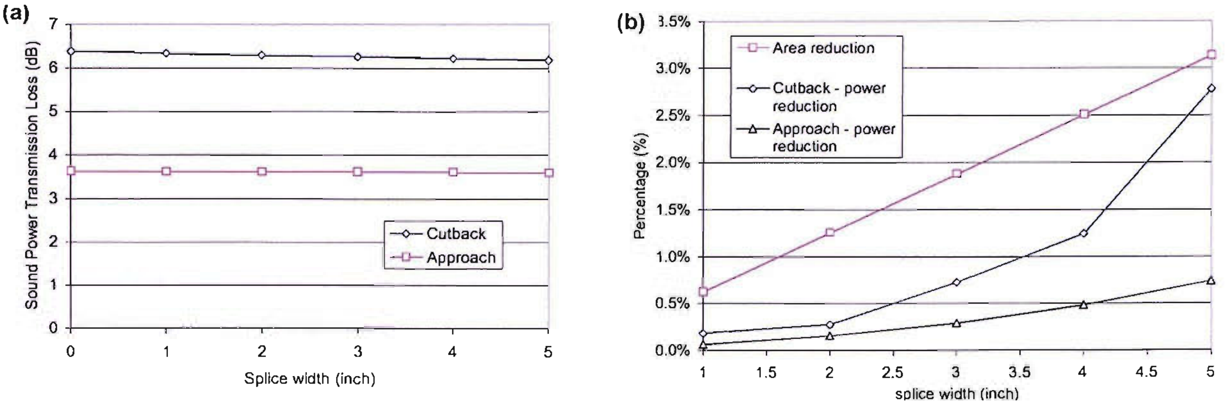

Figure 8.11: (a) Variation in $\triangle PWL_{BB}$ over a range of splice width for approach and cutback. (b) Acoustic power reduction and increment in liner splice area plotted against splice width.

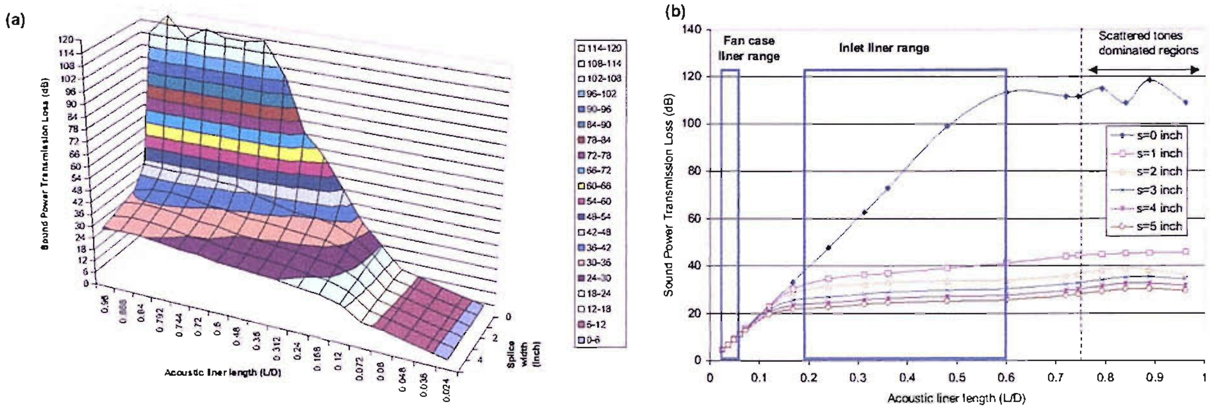

Figure 8.12: $\triangle PWL$ plotted against splice width and liner length for cutback. $kR = 28$, $M_o = -0.4$ and $Z = 2 - 1i$. (a) Three-dimensional plot, (b) Two-dimensional plot.

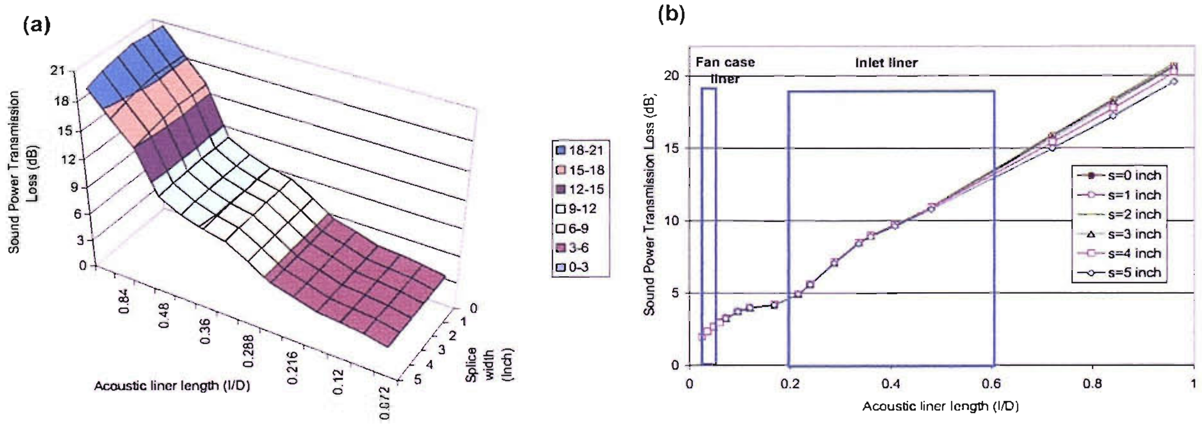

Figure 8.13: $\triangle PWL$ plotted against splice width and liner length for sideline. $kR = 34$, $M_o = -0.5$ and $Z = 2 - 1i$. (a) Three-dimensional plot, (b) Two-dimensional plot.

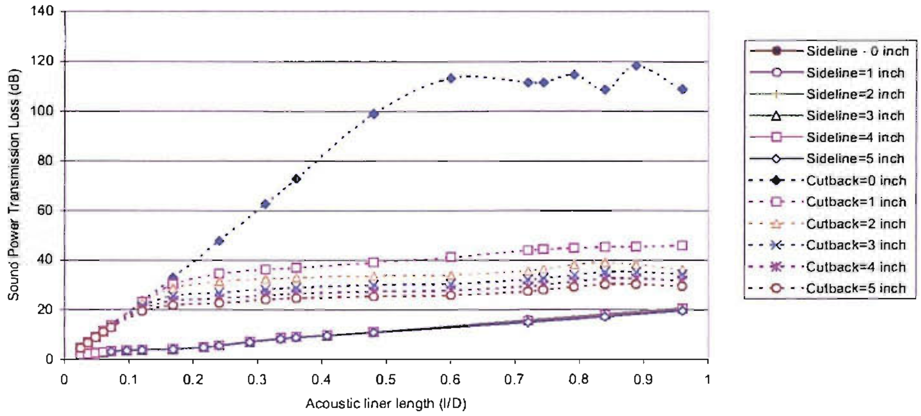

Figure 8.14: $\triangle PWL$ plotted against liner length for cutback and sideline. Results are obtained using the NMM model.

(a) Cutback - splice width 0 inch

(d) Sideline - splice width 0 inch

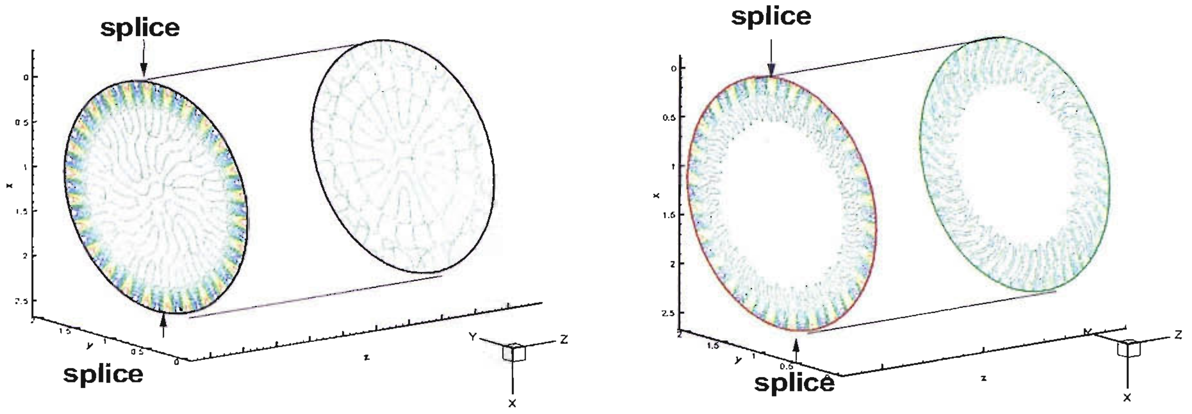

(b) Cutback - splice width 2 inch

(e) Sideline - splice width 2 inch

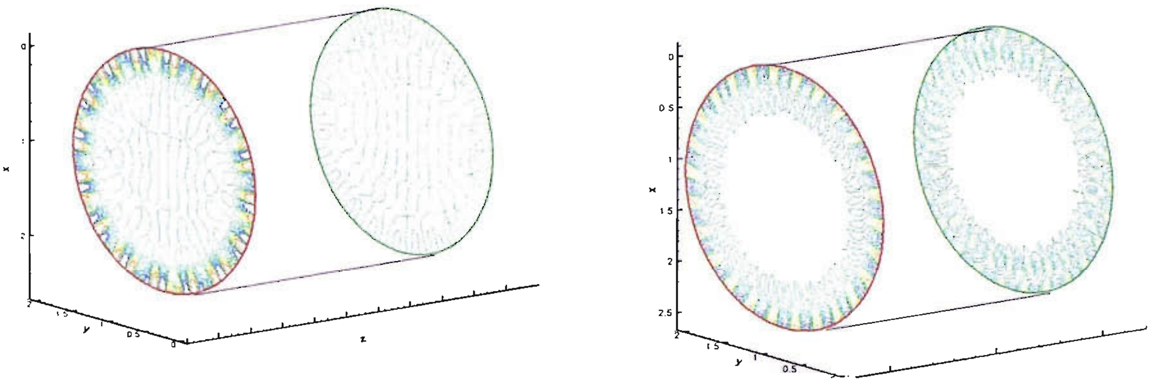

(c) Cutback - splice width 5 inch

(f) Sideline - splice width 5 inch

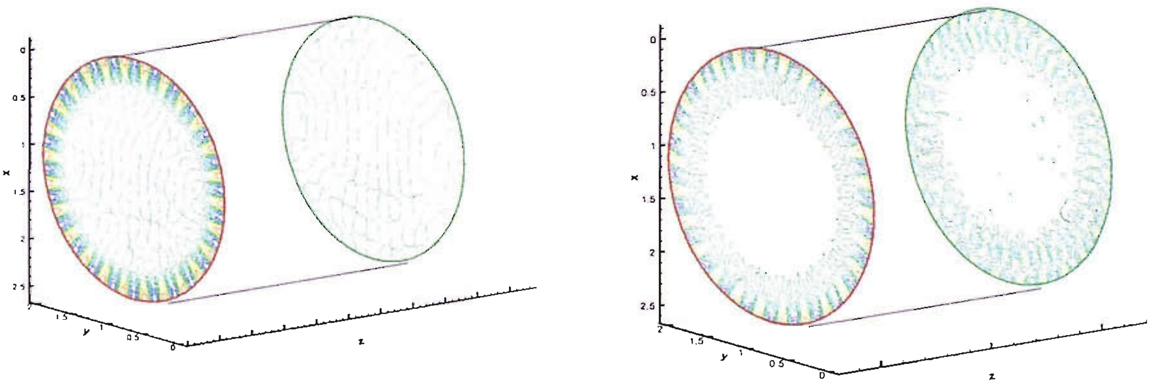

Figure 8.15: Contour plots showing the real part of the acoustic pressure at the inlet and exit of the duct for different engine operating conditions and splice widths. NMMM results. (a)-(c) Cutback, (d)-(f) Sideline.

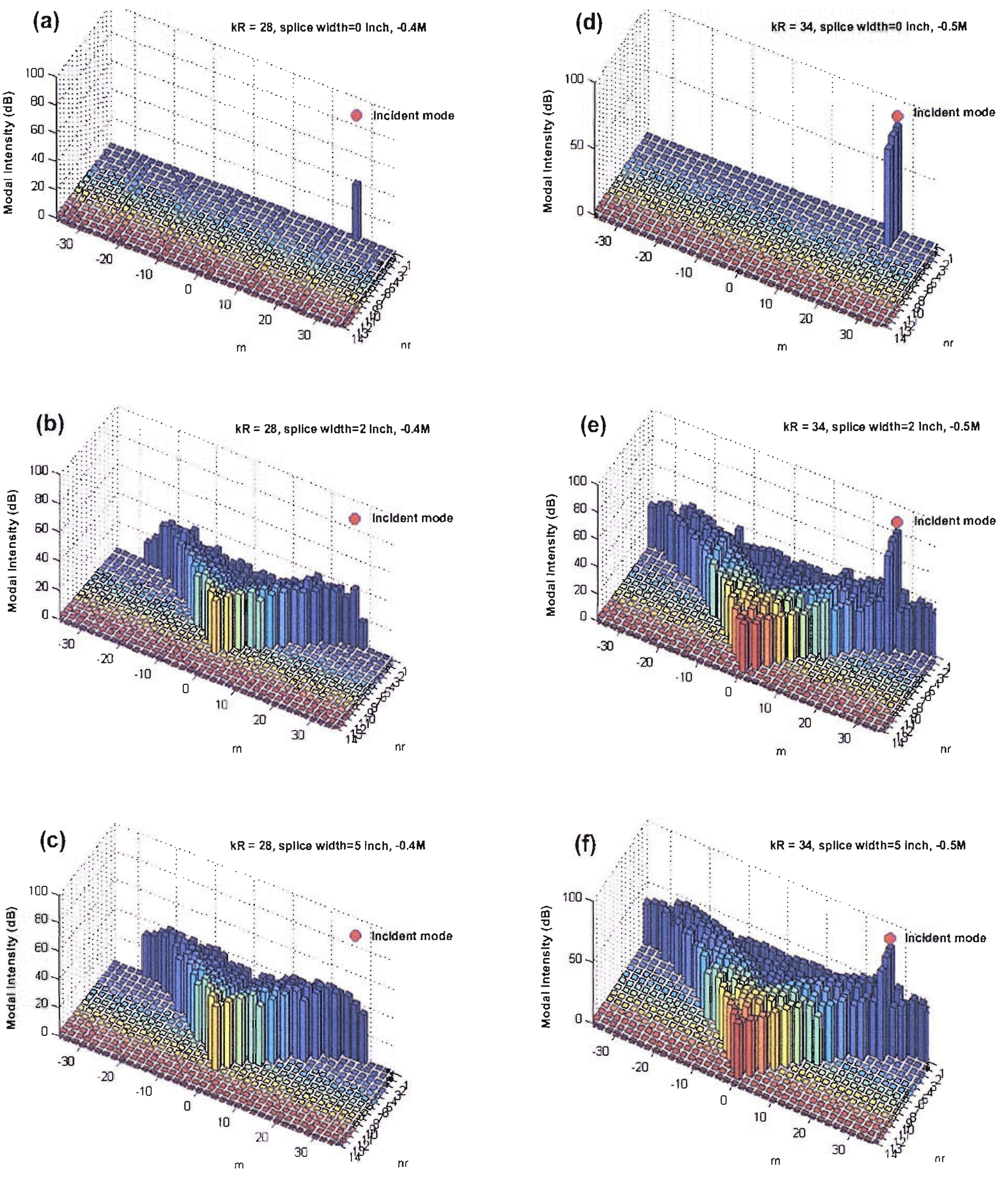

Figure 8.16: *PWL* of all the cut-on modes at the exit plane for different splice widths and engine operating conditions. NMMM results. (a)-(c) Cutback, (d)-(f) Sideline.

Chapter 9

Summary of Conclusions

9.1 Conclusions Arising From The Work

In the accomplishment of the research objectives the following original contributions have been made in this thesis:

- A numerical scheme using finite elements has been developed to solve for the duct eigenvalues and eigenfunctions in flow ducts. The FE eigenvalue model is capable of considering any arbitrary duct cross-sections with non-uniform flow and impedance boundaries. The duct modes of different types are being identified unambiguously and no modes are repeated. There is also no occurrence of spurious modes in the results. An mesh resolution of 8 to 10 nodes per wavelength is found be adequate to resolve duct modes of interest (modes having cut-off ratios greater than 0.8) to the design and acoustic treatment of aircraft engine bypass ducts.

- The FE eigenvalue model has been employed to study the effect of liner splices on the modal sound field in a circular cylindrical duct. The results of the study show that the overall liner performance decreases with increasing splice width. The results show no occurrence of spurious modes or additional duct modes in the spliced duct.

- For large three-dimensional problems, an iterative eigenvalue routine (ARPACK) has been employed to solve the eigenvalue problems. The iterative solver has demonstrated large savings in solution times compared to a direct eigenvalue solver.

- The new mode matching method (NMMM) has been shown to give solutions which agree better with the FE transmission analysis than those obtained using the traditional mode matching method (TMMM). The NMMM uses continuity of mass flux and momentum flux to match solutions between different uniform duct sections at the interface. The TMMM uses continuity of acoustic pressure and velocity to match solutions between different duct sections at the interface. The convergence study shows that the number of duct modes considered in each duct section equals to the number of hardwalled modes having cut-off ratios greater than 0.8 is found to be adequate for converged solution.

- The NMMM has been demonstrated to be capable of studying acoustic scattering due to an impedance discontinuity, sound diffraction by splitters and sound propagation in a duct containing surface waves. In general, the NMMM is capable of studying acoustic effects in axially straight ducts of arbitrary cross section with non-uniform flow and impedance boundaries. The NMMM also offers significant savings in computational time and storage compared to the FE transmission analysis. The resulting solution times are such that a parametric study of the geometrical parameters may be performed within an engineering design time scale.
- The NMMM has been employed to study sound diffraction by a infinitely thin splitter in a two-dimensional flow duct. The splitter causes scattering of acoustic energy to other cut-on modes and the high order modes are more affected than the low order modes.
- The NMMM has been employed to study transmission of sound in an idealised aircraft engine intake with spliced liners at a frequency of practical interest. The study shows that reducing the splice width has significant acoustic benefit for just cut-on modes.
- The NMMM has been employed to conduct a broadband analysis of the effect of liner splices in a circular cylindrical duct with uniform flow. The study shows that reducing the splice width gives small acoustic benefits. Better noise reduction methods are therefore required to reduce the broadband noise before there is any benefit of having thinner splices.

The research has shown that the NMMM offers a computationally efficient alternative to other currently available methods of analysis for flow duct acoustic problems.

9.2 Future Research

Previous studies have indicated that the duct modal spectrum can be considerably altered by variations in the duct geometry, flow and the present of splitters in the duct [13, 46, 60]. The next stage of the research will be to apply the MM model to study more practical problems such as ducts with non-uniform duct cross sections, non-uniform mean flow and sound diffraction by radial and circumferential splitters in the duct.

In order to employ the MM model for analysing realistic problems in aeroacoustics, the following avenues of future research have been suggested.

Integration with a radiation model

The use of modal representation within the duct lends itself to integration with analytical radiation model at the duct exit [108]. Models of this type are currently being developed. The models can be used to investigate the effect on far field directivity of non-axisymmetric liner placement within intake and bypass duct. The models will also be less computationally demanding than other numerical models such as the finite element transmission model and the computational aeroacoustic schemes.

Integration with a ray acoustic model

The ray theory has been shown to be an effective technique for studying sound propagation in turbofan engine ducts in the high-frequency regime where a large number of modes are excited [49, 109]. By integrating the current MM scheme to a ray acoustic model, this will enable a wider range of frequency to be considered in a more efficient and effective way.

Validation against experimental measured data

For the current MM scheme to be used to optimise the next generation of engine ducts, true validation between the measured data in the presence of mean flow against which the predictions can be assessed is therefore required. Engine and rig tests which should provide data of this type are currently in progress within the SILENCE(R) and TURNEX projects.

Appendix A

The following presents the terms of the transfer matrices T_{1-2} and T_{2-3}, which relate solutions in Sections (1) and (2) and Sections (2) and (3) using continuity of momentum flux and mass flux at $x = x_1$ and x_2 in Chapter 5.

$$T_{1-2} = \begin{bmatrix} a^- & b^+ \\ g^- & f^+ \end{bmatrix}^{-1} \begin{bmatrix} a^+ & b^- \\ g^+ & f^- \end{bmatrix} \quad ; \quad T_{2-3} = \begin{bmatrix} c^- & d^+ \\ s^- & t^+ \end{bmatrix}^{-1} \begin{bmatrix} c^+ & d^- \\ s^+ & t^- \end{bmatrix} \tag{A.1}$$

where

$$\begin{aligned}
a^\pm_{i,j} &= \left(\frac{k^\pm_{x,1,j}}{\rho_o(\omega - u_o k^\pm_{x,1,j})} + \frac{1}{\rho_o}\right)\int_0^h \psi^+_{1,i}\psi^\pm_{1,j}e^{-ik^\pm_{x,1,j}x_1}dy \quad ; \quad b^\pm_{i,j} = \left(\frac{k^\pm_{x,2,j}}{\rho_o(\omega - u_o k^\pm_{x,2,j})} + \frac{1}{\rho_o}\right)\int_0^h \psi^+_{1,i}\psi^\pm_{2,j}e^{-ik^\pm_{x,2,j}x_1}dy \quad ; \\
c^\pm_{i,j} &= \left(\frac{k^\pm_{x,2,j}}{\rho_o(\omega - u_o k^\pm_{x,2,j})} + \frac{1}{\rho_o}\right)\int_0^h \psi^+_{1,i}\psi^\pm_{2,j}e^{-ik^\pm_{x,2,j}x_2}dy \quad ; \quad d^\pm_{i,j} = \left(\frac{k^\pm_{x,3,j}}{\rho_o(\omega - u_o k^\pm_{x,3,j})} + \frac{1}{\rho_o}\right)\int_0^h \psi^+_{1,i}\psi^\pm_{3,j}e^{-ik^\pm_{x,3,j}x_2}dy \quad ; \\
g^\pm_{i,j} &= \left(\frac{k^\pm_{x,1,j}c_o^2}{(\omega - u_o k^\pm_{x,1,j})} + u_o\right)\int_0^h \psi^+_{1,i}\psi^\pm_{1,j}e^{-ik^\pm_{x,1,j}x_1}dy - \left[i\rho_o c_o^2 u_o \omega^{-1} A_1 \psi^+_{1,i}\psi^\pm_{1,j}e^{-ik^\pm_{x,1,j}x_1}\right]_0^h \quad ; \\
f^\pm_{i,j} &= \left(\frac{k^\pm_{x,2,j}c_o^2}{(\omega - u_o k^\pm_{x,2,j})} + u_o\right)\int_0^h \psi^+_{1,i}\psi^\pm_{2,j}e^{-ik^\pm_{x,2,j}x_1}dy - \left[i\rho_o c_o^2 u_o \omega^{-1} A_2 \psi^+_{1,i}\psi^\pm_{2,j}e^{-ik^\pm_{x,2,j}x_1}\right]_0^h \quad ; \\
s^\pm_{i,j} &= \left(\frac{k^\pm_{x,2,j}c_o^2}{(\omega - u_o k^\pm_{x,2,j})} + u_o\right)\int_0^h \psi^+_{1,i}\psi^\pm_{2,j}e^{-ik^\pm_{x,2,j}x_2}dy - \left[i\rho_o c_o^2 u_o \omega^{-1} A_2 \psi^+_{1,i}\psi^\pm_{2,j}e^{-ik^\pm_{x,2,j}x_2}\right]_0^h \quad ; \\
t^\pm_{i,j} &= \left(\frac{k^\pm_{x,3,j}c_o^2}{(\omega - u_o k^\pm_{x,3,j})} + u_o\right)\int_0^h \psi^+_{1,i}\psi^\pm_{3,j}e^{-ik^\pm_{x,3,j}x_2}dy - \left[i\rho_o c_o^2 u_o \omega^{-1} A_2 \psi^+_{1,i}\psi^\pm_{3,j}e^{-ik^\pm_{x,3,j}x_2}\right]_0^h \quad ;
\end{aligned} \tag{A.2}$$

The following presents the terms of the transfer matrices T_{1-2-3} and T_{2-3-4}, which relate solutions in Sections (1), (2) and (3) and Sections (2), (3) and (4) using continuity of momentum flux and mass flux at $x = x_1$ and x_2 in Chapter 5.

$$T_{1-2-3} = \begin{bmatrix} a^- & b^+ & c^+ \\ d^- & e^+ & f^+ \end{bmatrix}^{-1} \begin{bmatrix} a^+ & b^- & c^- \\ d^+ & e^- & f^- \end{bmatrix} \quad ; \quad T_{2-3-4} = \begin{bmatrix} p^- & q^- & r^+ \\ s^- & t^- & u^+ \end{bmatrix}^{-1} \begin{bmatrix} p^+ & q^+ & r^- \\ s^+ & t^+ & u^- \end{bmatrix} \tag{A.3}$$

where

$$
\begin{aligned}
a^{\pm}_{i,j} &= \left(\frac{k^{\pm}_{x,1,j}}{\rho_o(\omega-u_o k^{\pm}_{x,1,j})}+\frac{1}{\rho_o}\right)\int_0^h \psi^{+}_{1,i}\psi^{\pm}_{1,j}e^{-ik^{\pm}_{x,1,j}x_1}dy \quad ; \quad b^{\pm}_{i,j} = \left(\frac{k^{\pm}_{x,2,j}}{\rho_o(\omega-u_o k^{\pm}_{x,2,j})}+\frac{1}{\rho_o}\right)\int_0^{h1} \psi^{+}_{1,i}\psi^{\pm}_{2,j}e^{-ik^{\pm}_{x,2,j}x_1}dy \quad ; \\
c^{\pm}_{i,j} &= \left(\frac{k^{\pm}_{x,3,j}}{\rho_o(\omega-u_o k^{\pm}_{x,3,j})}+\frac{1}{\rho_o}\right)\int_{h1}^h \psi^{+}_{1,i}\psi^{\pm}_{3,j}e^{-ik^{\pm}_{x,3,j}x_1}dy \quad ; \quad p^{\pm}_{i,j} = \left(\frac{k^{\pm}_{x,2,j}}{\rho_o(\omega-u_o k^{\pm}_{x,2,j})}+\frac{1}{\rho_o}\right)\int_0^{h1} \psi^{+}_{1,i}\psi^{\pm}_{2,j}e^{-ik^{\pm}_{x,2,j}x_2}dy \quad ; \\
q^{\pm}_{i,j} &= \left(\frac{k^{\pm}_{x,3,j}}{\rho_o(\omega-u_o k^{\pm}_{x,3,j})}+\frac{1}{\rho_o}\right)\int_{h1}^h \psi^{+}_{1,i}\psi^{\pm}_{3,j}e^{-ik^{\pm}_{x,3,j}x_2}dy \quad ; \quad r^{\pm}_{i,j} = \left(\frac{k^{\pm}_{x,4,j}}{\rho_o(\omega-u_o k^{\pm}_{x,4,j})}+\frac{1}{\rho_o}\right)\int_0^{h} \psi^{+}_{1,i}\psi^{\pm}_{4,j}e^{-ik^{\pm}_{x,4,j}x_2}dy \quad ; \\
d^{\pm}_{i,j} &= \left(\frac{k^{\pm}_{x,1,j}c_o^2}{(\omega-u_o k^{\pm}_{x,1,j})}+u_o\right)\int_0^h \psi^{+}_{1,i}\psi^{\pm}_{1,j}e^{-ik^{\pm}_{x,1,j}x_1}dy - \left[i\rho_o c_o^2 u_o \omega^{-1} A_1 \psi^{+}_{1,i}\psi^{\pm}_{1,j}e^{-ik^{\pm}_{x,1,j}x_1}\right]_0^h \quad ; \\
e^{\pm}_{i,j} &= \left(\frac{k^{\pm}_{x,2,j}c_o^2}{(\omega-u_o k^{\pm}_{x,2,j})}+u_o\right)\int_0^{h1} \psi^{+}_{1,i}\psi^{\pm}_{2,j}e^{-ik^{\pm}_{x,2,j}x_1}dy - \left[i\rho_o c_o^2 u_o \omega^{-1} A_2 \psi^{+}_{1,i}\psi^{\pm}_{2,j}e^{-ik^{\pm}_{x,2,j}x_1}\right]_0^{h1} \quad ; \\
f^{\pm}_{i,j} &= \left(\frac{k^{\pm}_{x,3,j}c_o^2}{(\omega-u_o k^{\pm}_{x,3,j})}+u_o\right)\int_{h1}^h \psi^{+}_{1,i}\psi^{\pm}_{3,j}e^{-ik^{\pm}_{x,3,j}x_1}dy - \left[i\rho_o c_o^2 u_o \omega^{-1} A_3 \psi^{+}_{1,i}\psi^{\pm}_{3,j}e^{-ik^{\pm}_{x,3,j}x_1}\right]_{h1}^h \quad ; \\
s^{\pm}_{i,j} &= \left(\frac{k^{\pm}_{x,2,j}c_o^2}{(\omega-u_o k^{\pm}_{x,2,j})}+u_o\right)\int_0^{h1} \psi^{+}_{1,i}\psi^{\pm}_{2,j}e^{-ik^{\pm}_{x,2,j}x_2}dy - \left[i\rho_o c_o^2 u_o \omega^{-1} A_2 \psi^{+}_{1,i}\psi^{\pm}_{2,j}e^{-ik^{\pm}_{x,2,j}x_2}\right]_0^{h1} \quad ; \\
t^{\pm}_{i,j} &= \left(\frac{k^{\pm}_{x,3,j}c_o^2}{(\omega-u_o k^{\pm}_{x,3,j})}+u_o\right)\int_{h1}^h \psi^{+}_{1,i}\psi^{\pm}_{3,j}e^{-ik^{\pm}_{x,3,j}x_2}dy - \left[i\rho_o c_o^2 u_o \omega^{-1} A_3 \psi^{+}_{1,i}\psi^{\pm}_{3,j}e^{-ik^{\pm}_{x,3,j}x_2}\right]_{h1}^h \quad ; \\
u^{\pm}_{i,j} &= \left(\frac{k^{\pm}_{x,4,j}c_o^2}{(\omega-u_o k^{\pm}_{x,4,j})}+u_o\right)\int_0^h \psi^{+}_{1,i}\psi^{\pm}_{4,j}e^{-ik^{\pm}_{x,4,j}x_2}dy - \left[i\rho_o c_o^2 u_o \omega^{-1} A_4 \psi^{+}_{1,i}\psi^{\pm}_{4,j}e^{-ik^{\pm}_{x,3,j}x_2}\right]_0^h \quad ;
\end{aligned}
\tag{A.4}
$$

List of References

[1] R.J. Beckemeyer and D.T. Sawdy. Boundary conditions for mode matching analyses of coupled acoustic fields in duct. *AIAA Journal*, 16(9):912–918, 1978.

[2] A. Cummings. High frequency ray acoustics models for duct silencers. *J. Sound Vib.*, 221(4):681–708, 1999.

[3] P. Sijtsma. A study of non-locally reacting liners: modelling, validation and application to a full-size engine. Technical report, 2001.

[4] http://www.hq.nasa.gov/office/pao/History/SP-468/ch10 3.htm.

[5] S.W. Rienstra. A classification of duct modes based on surface waves. In *AIAA-2001-2180*. AIAA, 2001.

[6] S.W. Rienstra. A classification of duct modes based on surface waves. *Wave Motion*, 37:119–135, 2003.

[7] W. Eversman. The boundary condition at an impedance wall in a non-uniform duct with potential mean flow. *J. Sound Vib.*, 246(1):63–69, 2001.

[8] W. Eversman and Astley R.J. Acoustic transmission in non-uniform ducts with mean flow, part 1: The method of weighted residualss. *J. Sound Vib.*, 74(1):89–101, 1981.

[9] W. Eversman and D. Ukunbor. Aft fan duct acoustic radiation. *J. Sound Vib.*, 213(2):235–257, 1998.

[10] R.J. Astley and A. Cummings. A finite element scheme for attenuation in ducts lined with porous material: Comparison with experiment. *J. Sound Vib.*, 116(2):239–263, 1987.

[11] R.J. Astley and W. Eversman. A finite element method for transmission in non-uniform ducts without flow: Comparison with the method of weighted residualss. *J. Sound Vib.*, 57(3):367–388, 1978.

[12] R.J. Astley and W. Eversman. A finite element formulation of the eigenvalue problem in lined ducts with flow. *J. Sound Vib.*, 65(1):61–74, 1979.

[13] B. Regan and J. Eaton. Modelling the influence of acoustic liner non-uniformities on duct modes. *J. Sound Vib.*, 219(5):859–879, 1999.

[14] C.L. Rumsey, R.T. Biedron, F. Farassat, and P.L. Spence. Ducted fan engine acoustic predictions using a navier stokes code. *J. Sound Vib.*, 213(4):643–664.

[15] Y. Ozyoruk, V. Ahuja, and L.N. Long. Euler predictions of forward and aft radiated noise of a turbofan. In *8th AIAA/CEAS Aeroacoustics Conference & Exhibit*, Breckenridge, Colorado, June 2002. AIAA.

[16] V. Ahuja, Y. Ozyoruk, and L. Long. Computational simulations of fore and aft radiation. In *AIAA*, 2000-1943.

[17] Y. Ozyoruk, V. Ahuja, and L.N. Long. Time domain simulations of radiation from ducted fans with liners. In *7th AIAA/CEAS Aeroacoustics Conference & Exhibit*, Maastricht, The Netherlands, May 2001. AIAA.

[18] B.J. Tester. Ray models for sound propagation and attenuation in ducts, in the absence of mean flow. *J. Sound Vib.*, 27(4):515–531, 1973.

[19] R.P. Dougherty. Nacelle acoustic design by ray tracing in three dimensions. AIAA 96-1773, 1996.

[20] S.W. Rienstra and W. Eversman. A numerical comparison between the multiple-scales and finite-element solutions for sound propagation in lined flow ducts. *J. Fluid Mechanics*, 437:367–384, 2001.

[21] S.W. Rienstra. Sound transmission in slowly varying circular and annular lined ducts with flow. *J. Fluid Mechanics*, 380:279–296, 1999.

[22] R.P. Dougherty. A parabolic approximation for flow effects on sound propagation in nonuniform, softwall ducts. AIAA 99-1822, 1999.

[23] R.P. Dougherty. A wave-splitting technique for nacelle acoustic propagation. AIAA 97-1652, 1997.

[24] Laurent Dallois and Philippe Blanc-Benon. Wide angle parabolic equations in moving media: Sound diffraction by a core vortex. AIAA - 2001-2256, 2001.

[25] F.Q. Hu, M.Y. Hussaini, and P. Rasetarinera. An analysis of the discontinuous galerkin method for wave propagation problems. *Journal of Computational Physics*, 151:921–946, 1999.

[26] P.L. David and H. Atkins. An application of the quadrature free discontinuous galerkin method. Research report.

[27] F.Q. Hu and H.L. Atkins. Eigensolution analysis of the discontinuous galerkin method with non-uniform grids, part i: One space dimension. NASA contract report 2001-211269, NASA, NASA, 2001.

[28] Wenping Bi. *Sound Propagation In Varying Cross-section Waveguides With Non-uniform Boundary Conditions.* PhD thesis, University of Maine, June 2004.

[29] V. Pagneux, N. Amir, and J. Kergomard. A study of wave propagation in varying cross-section waveguides by modal decomposition. part i. theory and validation. *J. Acoust. Soc. Am.*, 100:2034–2048, 1996.

[30] N. Amir, V. Pagneux, and J. Kergomard. A study of wave propagation in varying cross-section waveguides by modal decomposition. part ii. results. *J. Acoust. Soc. Am.*, 101(5):2504–2517, 1997.

[31] J.M. Tyler and T.G. Sofrin. Axial flow compressor studies. *SAE transaxtions*, 70:309–332, 1962.

[32] J.A. Hamilton and R.J. Astley. Fe/ie acoustic analysis of lip liners in turbofan inlets. Technical report, Institute of Sound and VIbration, 2002.

[33] J.A. Reed and A.A. Afjeh. Computational simulation of gas turbines: Part 1 - foundations of component-based models. In *International Gas Turbine and Aeroengine Congress and Exhibition*, 99-GT-346, Indianapolis, Indiana, June 1999.

[34] R.J. Alfredson. The propagation of sound in a circular duct of continuously varying cross sectional area. *J. Sound Vib.*, 23(4):433–442, Aug 1972.

[35] D.L. Lansing and W.E. Zorumski. Effects of wall admittance changes on duct transmission and radiation of sound. *J. Sound Vib.*, 27(1):85–100, 1973.

[36] M.C. Joshi, R.E. Kraft, and S.Y. Son. Analysis of sound propagation in annular ducts with segmented treatment and sheared flow. In *AIAA-82-0123*. AIAA, 1982.

[37] S. Lidoine, H. Batard, S. Troyes, and A. Delnevo. Acoustic radition modelling of aeroengine intake comparison between analytical and numerical methods. In American Institute Of Aeronautics and Astronautics, editors, *7th AIAA/CEAS Aeroacoustics Conference & Exhibit*, AIAA-2001-2140, Maastricht, Netherlands, May 2001.

[38] T. Elnady. *Modelling and characterization of perforates in lined ducts and mufflers.* Doctoral thesis, KTH Aeronautical and Vehicle Engineering, Stockholm, Sweden, September 2004.

[39] A.J. Cooper and N. Peake. Wave propagation in a slowly varying duct with mean vortical swirling flow. Number 2001-2124, 7th AIAA/CEAS Aeroacoustics coference, Maastricht, Netherlands, 2001.

[40] Ali Hasan Nayfeh and Demetri P. Telionis. Acoustic propagation in ducts with varying cross section. *J. Acoust. Soc. Am.*, 54(6):1654–1661, 1973.

[41] S.W. Rienstra. Sound propagation in slowly varying lined flow ducts of arbitrary cross-section. *J. Fluid Mechanics*, 495:157–173, 2003.

[42] S.W. Rienstra. Cut-on, cut-off transition of sound in slowly varying flow duct. 2001. downloaded from internet.

[43] N.C. Ovenden. Near cut-on/cut-off transition in lined ducts with flow. In *8th AIAA/CEAS aeroacoustics conference*, Breckenridge, Colorado, June 2002. AIAA.

[44] N.C. Ovenden. A uniformly valid multiple scales solution for cut-on cut-off transition of sound in flow ducts. *J. Sound Vib.*, 286:403–416, 2005.

[45] J.M. Mendoza, B. Schuster, and J. Lan. Prediction of aft fan duct lining attenuation for a turbofan engine. In American Institute Of Aeronautics and Astronautics, editors, *9th AIAA/CEAS Aeroacoustics Conference & Exhibit*, AIAA-2003-3241, Hilton Head, South Carolina, May 2003.

[46] M.D. Nark, F. Farassat, D.S. Pope, and V. Vatsa. Effects of bifurcations on aft fan engine nacelle noise. In American Institute Of Aeronautics and Astronautics, editors, *10th AIAA/CEAS Aeroacoustics Conference & Exhibit*, AIAA-2004-2988, Manchester, United Kingdom, May 2004.

[47] D. Lee, A.D. Pierce, and EC Shang. Parabolic equation development in the twentieth century. *Journal of Computational Acoustics*, 8(4):527–637, 2000.

[48] J.H. Lan. Turbofan duct propagation model - parabolic approximation. Contractor Report NASA/CR-2001-211245, NASA, NASA, 2001.

[49] A.J. Kempton and M.G. Smith. Ray theory predictions of the sound radiated from realistic engine intakes. In *7th Aeroacoustics Conference*, Paper 81-1982, 1981.

[50] I. Danda Roy and W. Eversman. Improved finite element modelling of the turbofan engine inlet radition problem. *Journal of Vibration and Acoustics*, 117:109–115, 1995.

[51] W. Eversman, A.V. Parrett, J.S. Preisser, and R.J. Silcox. Contributions to the finite element solution of the fan noise radiation problem. *Journal of Vibration, Acoustics, Stress, and Reliability in Design*, 107:216–223, 1985.

[52] R.J. Astley, G.J. Macaulay, and J-P. Coyette. Mapped wave envelope elements for acoustical radiation and scattering. *J. Acoust. Soc. Am.*, 170:97–118, 1994.

[53] R.J. Astley. Mapped spheroidal elements for unbounded wave problems. *Int. J. Numer. Meth. Eng.*, 41:1235–1254, 1998.

[54] R.J. Astley, G.J. Macaulay, J-P. Coyette, and L. Cremers. Three dimensional wave-envelope elements of variable order for acoustic radiation and scattering. part 1. formulation in the frequency domain. *J. Acoust. Soc. Am.*, 103:49–63, 1998.

[55] R.J. Astley, J-P. Coyette, and L. Cremers. Three dimensional wave-envelope elements of variable order for acoustic radiation and scattering. part 2. formulation in the time domain. *J. Acoust. Soc. Am.*, 103:64–72, 1998.

[56] R.J. Astley. A finite element, wave envelope formulation for acoustical radiation in moving flows. *J. Sound Vib.*, 103(4):471–485, 1985.

[57] R.J. Astley and W. Eversman. A finite element, wave envelope formulation for acoustical radiation in moving flows. *J. Sound Vib.*, 88(1):47–64, 1983.

[58] B.J. Tester, N.J. Baker, A.J. Kempton, and M.C. Wright. Validation of an analytical model for scattering by intake liner splices. In *10th AIAA/CEAS Aeroacoustics Conference & Exhibit*, 2004-2906, Manchester, UK, 2004.

[59] A. McAlpine and M.C.M Wright. Acoustic scattering by a turbofan inlet duct liner at supersonic fan speeds. part 1: Spliced liner. *To be submitted for publication*, 2004.

[60] R. Sugimoto and R.J. Astley. Modelling of flow effects on propagation and radiation from bypass ducts. In AIAA, editor, *11th AIAA/CEAS Aeroacoustics Conference (26th AIAA Aeroacoustics Conference)*, AIAA 2005-3011, Monterey, California, 23-25 May, 2005.

[61] J.E. Dean and R. Glowinski. Domain decompositions of wave problem using a mixed finite element method. In *Ninth International conference on domain decomposition methods.*, number 38, downloaded from internet, 1998.

[62] J.A. Hamilton. *Transient Finite/Infinite Element Solutions For Unbounded Wave Problems.* Phd thesis, University of Southampton, Institute of Sound and Vibration Research, March 2003.

[63] E. Listerud and W. Eversman. Finite element modeling of acoustics using high order elements. part 1: Nonuniform duct propagation. *Journal of Computational Acoustics*, 12(3):397–429, 2004.

[64] E. Listerud and W. Eversman. Finite element modeling of acoustics using high order elements. part 2: Turbofan acoustic radiation. *Journal of Computational Acoustics*, 12(3):431–446, 2004.

[65] C.K.W. Tam. Computational aeroacoustics: Issues and methods. *AIAA Journal*, 33(10):1788–1796, 1995.

[66] K. Christopher Tam and Jay C. Webb. Dispersion-relation-preserving finite difference schemes for computational acoustics. *J. Comput. Phys.*, 107:262–281, 1993.

[67] Sanjiva K. Lele. Computational aeroacoustics: A review. 97-0018, Reno, NV, 1997. AIAA/CEAS Aeroacoustics Conference & Exhibit.

[68] X. Zhang, X.X. Chen, C.L. Morfey, and B.J. Tester. Computation of fan noise radiation through a realistic engine exhaust geometry with flow. In *AIAA*, Hilton Head, South Carolina, USA, May 2003. 9th AIAA/CEAS Aeroacoustics Conference & Exhibit.

[69] J. Astley. An introduction to computational aeroacoustics (caa). ISVR Short courses - lecture note, 2004.

[70] Christophe Bailly and Danial Juve. Numerical solution of acoustic propagation problems using linearised euler equation (lee). *AIAA Journal*, 38(1), 2000.

[71] J.M.C. Pereira, M.H. Kobayashi, and J.C.F. Pereira. A fourth-order-accurate finite volume compact method for the incompressible navier-stokes solutions. *Journal of Computational Physics*, 167:317–243, 2001.

[72] I.A. Abalakin, A.V. Alexandrov, V.G. Bobkov, and T.K. Kozubskaya. High accuracy methods and software development in computational aeroacoustics. *Journal of Computational Methods*, 2(3):1–14, 2003.

[73] X.G. Zhang, G.A. Blaisdell, and A.S. Lyrintzis. High-order compact schemes with filters on multi-block domains. *Journal of Scientific Computing*, 21(3):321–339, 2004.

[74] Y.M. Chung and P.G. Tucker. Accuracy of higher-order finite difference schemes on non-uniform grids. *AIAA Journal*, 41(8):1–3, 2003.

[75] C. Bogey and C. Bailly. Three-dimensional non-reflective boundary conditions for acoustic simulations: far field formulation and validation test cases. *ACTA Acustica united with Acustica*, 88:463–471, 2002.

[76] W.N. E and J.G. Liu. Essentially compact schemes for unsteady viscous imcompressible flows. *Journal of Computational Physics*, 126:122–138, 1996.

[77] R.J. Astley. The finite element duct eigenvalue problem: An improved formulation with hermitian elements and no-flow condensation. *J. Sound Vib.*, 69(1):13–25, 1980.

[78] R.J. Nijboer. Eigenvalues and eigenfunctions of ducted swirling flows. Technical Report NLR-TP-2001-141, National Aerospace Laboratory NLR, 2001.

[79] W. Eversman. Computation of axial and transverse wave numbers for uniform two dimensional ducts with flow using a numerical integration scheme. *J. Sound Vib.*, 41(2):252–255, 1975. Errata.

[80] W. Eversman. Intial values for the integration scheme to compute the eigenvalues for propagation in ducts. *J. Sound Vib.*, 50(1):159–162, 1977.

[81] Sung-Hwan Ko. Sound attenaution in lined rectangular ducts with flow and its application to the reduction of aircraft engine noise. *J. Acoust. Soc. Am.*, 50(6(Part 1)):1418–1432, 1971.

[82] D.C. Pridmore-Brown. Sound propagation in a fluid flowing through an attenuating duct. *J. Fluid Mechanics*, 4, pt4:393–406, 1958.

[83] K.A. Kousen. Eigenmode analysis of ducted flows with radially dependent axial and swirl components. In *16th AIAA Aeroacoustics Conference*, pages 1085–1094, Munich, Germany, June 1995.

[84] P. Mungur and M.L. Gladwell. Acoustic wave propagation in a sheared fluid contained in a duct. *J. Sound Vib.*, 9(1):28–48, 1969.

[85] A.S. Hersh and I. Catto. Effect of shear flow on sound propagation in rectangular ducts. *J. Acoust. Soc. Am.*, 50:992–1003, 1970.

[86] D.H. Tack and R.F. Lambert. Influence of shear flow on sound attenuation in a lined duct. *J. Acoust. Soc. Am.*, 38:655–666, 1965.

[87] A.A. Syed and S.C. Bennett. Comparison of measured broadband noise attenuation spectra from circular flow ducts and from lined engine intakes with predictions. *jsv*, 56(4):531–564, 1978.

[88] J.F. Unruh and W. Eversman. The transmission of sound in an acoustically treated rectangular duct with boundary layer. *J. Sound Vib.*, 25(3):371–382, 1972.

[89] J.F. Unruh and W. Eversman. The utility of the galerkin method for the acoustic transmission in an attenuating duct. *J. Sound Vib.*, 23(2):187–197, 1972.

[90] W Eversman. Effect of boundary layer on the transmission and attenuation of sound in an acoustically treated circular duct. *J. Acoust. Soc. Am.*, 49(5, part 1):1372–1380, 1970.

[91] P.T. Vo and W. Eversman. A method of weighted residuals with trigonometric basis functions for sound transmission in circular ducts. *J. Sound Vib.*, 56(2):243–250, 1978.

[92] S.D. Savkar. Propagation of sound in ducts with shear flow. *J. Sound Vib.*, 19(3):355–372, 1971.

[93] J.F. Unruh and W. Eversman. The utility of the galerkin method for the acoustic transmission in an attenuation duct. *J. Sound Vib.*, 23(2):187–197, 1972.

[94] W. Eversman. Theoretical models for duct acoustic propagation and radiation. WRDC technical report 90-3052, Aeroacoustics of flight vehicles: Theory and Practice. Noise Control NASA reference publication 1258, NASA.

[95] M.K. Myers. On the acoustic boundary condition in the presence of flow. *J. Sound Vib.*, 71(3):429–434, 1980.

[96] O.C. Zienkiewicz and R.L. Taylor. *The Finite Element Method.* Butterworth, London, 5th edition, 2000.

[97] D.C. Sorensen. Numerical methods for large eigenvalue problems. *Acta Numerica*, pages 519–584, 2002.

[98] R.B. Lehoucq. D.C. Sorensen. and C. Yang. Implicitly restarted arnoldi method for computing a partial schur decomposition corresponding to a selected subset of eigenvalues. symmetric, nonsymmetric, generalized and *svd* problems solved. 1998.

[99] Visual Numerics Inc. *IMSL Fortran 90 MP Library Version 4.01 User's Manual.*, 1999.

[100] S.W. Rienstra and A. Hirschberg. *An Introduction to Acoustics.* 2002.

[101] ICEM CFD 4.2 Users' Guide. *ICEM CFD Engineering.*, 2002.

[102] C.L. Morfey. Sound transmission and generation in ducts with flow. *J. Acoust. Soc. Am.*, 14(1):37–55, 1971.

[103] W. Eversman. Acoustic power in lined ducts. In *10th AIAA/CEAS Aeroacoustics Conference & Exhibit*, 2004-2904, Manchester. UK, June 2004. AIAA/CEAS.

[104] R.T. Muehleisen. *Reflection, radition, and coupling of higher order modes at discontinuities in finite length rigid walled rectangular ducts.* Phd thesis. The Pennsylvania State University, 1996.

[105] Free Field Technologies. *ACTRAN Rev 2.0. Users' Guide.* Louvain-la-Neuve, Begium, 2002.

[106] R.J. Nijboer and P. Sijtsma. Sound diffraction by the splitter of a turbofan engine. Technical report NLR-TP-99133, National Aerospace Laboratory NLR. 1999.

[107] L. Lafronza. A. McAlpine. A.J. Keane, and R.J. Astley. Computer-aided liner optimization for broadband noise. In *AIAA*. 2004.

[108] G. Gabard and Astley R. Theoretical model for sound radiation from aeroengine exhausts. In 11th AIAA-CEAS Aeroacoustics Conference, editor. *AIAA paper 2005-3064*. Monterey, CA, 23-25 May 2005.

[109] A.J. Kempton. Ray theory and mode-theory predictions of intake-liner performance: a comparison with engine measurements. In *8th Aeroacoustics Conference*. Paper 83-0711, 1983.